UNIVERSITY OF OKLAHOMA

GRADUATE COLLEGE

DEVELOPMENT AND PRECLINICAL EVALUATION OF ENZYME PRODRUG THERAPIES TARGETED TO THE TUMOR VASCULATURE

A DISSERTATION

SUBMITTED TO THE GRADUATE FACULTY

in partial fulfillment of the requirements for the

Degree of

DOCTOR OF PHILOSOPHY

By

JOHN J. KRAIS
Norman, Oklahoma
2014

DEVELOPMENT AND PRECLINICAL EVALUATION OF ENZYME PRODRUG THERAPIES TARGETED TO THE TUMOR VASCULATURE

A DISSERTATION APPROVED FOR THE
DEPARTMENT OF BIOMEDICAL ENGINEERING

BY

_____
Dr. Roger Harrison, Chair

_____
Dr. Matthias Nollert

_____
Dr. Vassilios Sikavitsas

_____
Dr. Rajagopal Ramesh

_____
Dr. Barbara Safiejko-Mroczka

Acknowledgements

I would like to thank my committee, Dr. Nollert, Dr. Sikavitsas, Dr. Ramesh, Dr. Safiejko-Mroczka, and Dr. Harrison, for the support and guidance throughout this project. The courses, project assistance, and laboratory equipment have all been incredibly valuable. Dr. Harrison has been an excellent advisor and a pleasure to work under. I am very thankful for all the insight and support provided throughout the entire project.

I greatly appreciate the Stephenson Cancer Center and its core facilities, specifically the Tissue Pathology Laboratory and the Molecular Imaging Core. Dr. Kar-Ming Fung and Sheeja Aravindan were instrumental in all of the tissue processing and immunohistochemistry. Dr. Rajagopal Ramesh and his laboratory have provided great assistance with use of the imaging equipment as well as other aspects of the project, including the transfection of the 4T1 cells to express TdTomato and Luciferase. I would also like to thank the Noble Microscopy Laboratory at the Norman campus of the University of Oklahoma, particularly Dr. Ben Smith for enormous support with the confocal microscopy studies. The core facilities at the University of Oklahoma and the Health Sciences Center have been hugely beneficial towards the collection of strong data, and I would like to thank all of the people involved. In addition, I would like to thank Dr. Carla Kurkjian of the Stephenson Cancer Center for the guidance she provided. The staff of the Chemical, Biological, and Materials Engineering office also deserves recognition for all of the assistance provided throughout the duration of the project, particularly when orders did not go as planned.

Colleagues in the Harrison laboratory, specifically Brent Van Rite, Yoann Royet, Needa Virani, and Q Nguyen have provided significant assistance at various points throughout this project and I am very grateful for their help. Additionally, Brandon Engebretson, Mathilde Mouchiroud, Alex Houzelle, and Etienne Bendjebbar went out of their way to provide training and an extra set of hands on a number of occasions for which I am also incredibly thankful. Many of my colleagues were also great friends among others at the University of Oklahoma, back home in Pennsylvania, and abroad without whose support I would not have been able to succeed. In addition to those that helped directly with the labwork, I would especially like to thank the friends at OU that helped me through the long hours and weekend work: Marine Le Ray, Theresa Ashley, Jaclyn Brennan, Arthur Wendling, Fabien Pariot, Ginn Lefeuvre, Jon Gersinger, Matt Wulfers, Rachel Dreher, Jeff Fontenot, Alex Xausa, Sam Papus, Victor Vayssiere, Aurelien Collange, and others. Finally, I would like to thank my parents, John and Janelle, and sisters, Ryann and Julie, for the continuous love, support, and encouragement.

Table of Contents

Acknowledgements iv

List of Tables xiv

List of Figures xvi

Abstract xxi

Chapter I: Introduction 1

Breast Cancer Landscape and Project Overview 1

Impact and Treatment of Breast Cancer 1

Directed Enzyme Prodrug Strategy 2

Enzyme Prodrug Therapies 6

Cytosine Deaminase and 5-Fluorocytosine 6

Purine Nucleoside Phosphorylase and Fludarabine Phosphate 7

Methionine-γ-Lyase and Selenomethionine 11

Targeting Cancer Therapeutics to Phosphatidylserine 13

Phosphatidylserine Externalization 14

Annexin Protein Family 15

Clinical Relevance of Phosphatidylserine Targeted Therapies 16

Summary of Targeting Strategy 17

Overcoming Protein Immunogenicity 17

Use of Combination Therapies for Enhanced Response 21

Docetaxel Enhanced Phosphatidylserine Targeting 22

Countering the Hypoxic Response with Rapamycin 22

Immunostimulation with Cyclophosphamide Depletion of Regulatory T Cells 25

Project Summary and Experimental Overview 26
Chapter II: Materials and Methods 28
Fusion Gene Construction and Transformations 28
Construction of Recombinant Expression Plasmid for PNP-AV 28
Construction of Recombinant Expression Plasmids for mCGL Fusions 30
Protein Expression and Purification 31
BL21(DE3) Expression of CD-AV, PNP-AV, Met-AV, and mCGL-AI 31
T7 Express lysY (DE3) Expression of mCGL-AV 32
IMAC Purification 32
Enzyme Activity Assays 33
Cytosine Deaminase Activity Assay 33
Purine Nucleoside Phosphorylase Activity Assay 34
Methionine-γ-Lyase Activity Assay 34
Reducing Immunogenicity 35
PEGylation 35
mCGL Design 36
Mammalian Cell Culture 36
HAAE-1 Endothelial Cells 36
MCF-7 Human Breast Cancer Cells 37
MDA-MB-231 Human Triple-Negative Breast Cancer Cells 38
4T1 Murine Triple-Negative Breast Cancer Cells 38
In Vitro Binding Studies 39
Binding Strength 39

Binding Stability 40
Binding Visualization 41
In Vitro Cytotoxicity 42
In Vivo Tumor Models 43
MDA-MB-231 Implantation in SCID Mice 43
4T1 Implantation in BALB/cJ Mice 44
Non-terminal *In Vivo* Procedures and Follow-up Analysis 44
Mass and Tumor Volume 44
Fluorescence Live Animal Imaging 45
Antibody Titer 45
Terminal *In Vivo* Procedures and Follow-up Analysis 46
Fusion Protein Clearance 46
Measurement of Metastatic Nodules in Lungs 46
Tumor Section Immunohistochemistry 47
Quantification of Regulatory T Cells in Spleen 51
Statistical Analysis 51
Chapter III: Results and Discussion 53
Cytosine Deaminase and 5-Fluorocytosine 53
In Vivo CD-AV Plasma Clearance 53
Evaluation of CD-AV System In Vivo 54
Summary of CD-AV System 57
Purine Nucleoside Phosphorylase and Fludarabine 58
Fusion Protein Construction, Expression, and Purification 58

In Vitro Binding 61
In Vitro Cytotoxicity 66
In Vivo PNP-AV Plasma Clearance 72
In Vivo Evaluation of PNP-AV System and Combination with Docetaxel 72
Summary of PNP-AV System 79
Methionine-γ-Lyase and Selenomethionine 80
In Vivo Met-AV Plasma Clearance 80
In Vivo Evaluation of Met-AV System 80
Transition to Orthotopic Tumor Models 82
In Vivo Evaluation of Docetaxel Combination with Met-AV System 85
Preliminary In Vivo Investigation of Rapamycin Combination Therapy 88
Summary of Met-AV System 89
PEGylation 90
Mouse Mutant Cystathionine-γ-Lyase and Selenomethionine 93
Fusion Gene Constructions with Annexin I and Annexin V 93
Protein Expression and Purification 94
Enzyme Activity 95
In Vitro Binding 95
In Vitro Cytotoxicity 99
In Vivo Comparison of Annexin I and Annexin V Therapy Efficacy 103
In Vivo Comparison of Protein Administration Method 105
In Vivo mCGL-AV Plasma Clearance 106
Efficacy and Immunogenicity of Met-AV vs. mCGL-AV 107

Rapamycin and Cyclophosphamide Combination Therapies 110
Therapeutic Contributions of Combination Constituents 116
Commentary on 4T1 Mouse Model 130
Analysis of Combination Therapies for Synergism 131
Summary of mCGL System and Combination Therapies 136
Chapter IV: Conclusions and Future Directions 138
References 143
Appendix A: Supplemental Data 172
PNP-AV *In Vitro* Binding Data 172
mCGL-AI, mCGL-AV, and Met-AV *In Vitro* Binding Data 174
Appendix B: Laboratory Protocols 177
Protein Design and Vector Construction 177
PNP-AV Fusion Gene Construction and Transformation 177
mCGL-AI, mCGL-AV Fusion Gene Constructions and Transformations 181
Plasmid Miniprep 183
PCR Product Purification 184
DNA Gel Electrophoresis and Extraction 185
NovaBlue Gigasingles Competent Cell Transformation 187
BL21(DE3) Competent Cell Transformation 189
NEB 5-alpa Competent Cell Transformation 189
T7 Express lysY Competent Cell Transformation 190
Protein Expression and Purification 192
BL21(DE3) Expression of CD-AV, PNP-AV, Met-AV, and mCGL-AI 192

T7 Express lysY (DE3) Expression of mCGL-AV 193
Fusion Protein Purification 195
Protein Analysis 201
Bradford Protein Concentration Assay 201
SDS-PAGE 202
Cytosine Deaminase Activity Assay 205
Purine Nucleoside Phosphorylase Activity Assay 206
Methionine-γ-Lyase Activity Assay 207
Chromogenic Limulus Amebocyte Lysate Endotoxin Assay 210
Protein Conjugations 212
Biotinylation 212
DyLight 680 Conjugation 213
In Vitro Studies 215
Binding Stability Assay 215
Binding Strength Assay 217
Fixed Cell Confocal Microscopy 220
Live Cell Confocal Microscopy 221
Cytotoxicity Assay 222
In Vivo Studies and Follow-up Analysis 223
Protein Specific Antibody Titers 223
Fusion Protein Plasma Clearance 225
Fluorescent Lung Metastasis Image Processing and Quantification 227
Immunohistochemistry Image Processing and Quantification 230

Quantification of Regulatory T Cells in Spleen 233
Appendix C: Fusion Gene Construction 235
PNP-AV Primers 235
PNP and AV Amplification Primers 235
PNP-AV Fusion Primers 235
PNP-AV Sequences 236
PNP-AV DNA Sequence 236
PNP-AV Amino Acid Sequence (Pre-Cleavage) 237
PNP-AV Amino Acid Sequence (Post-Cleavage) 237
PNP-AV NCBI BLAST Results 237
Mutant CGL Sequences 238
Engineered Mouse and Human CGL Sequence Comparison 238
Mutant mCGL Sequence and NCBI BLAST Results 239
mCGL Fusions Gibson Fragments 240
mCGL-AI Gibson Fragments 241
mCGL-AV Gibson Fragments 242
mCGL Fusions Sequencing Primers and Sequences 243
mCGL-AI Sequencing Primers and DNA Sequence 244
mCGL-AV Sequencing Primers and DNA Sequence 245
mCGL-AV Amino Acid Sequence (Pre-cleavage) 246
mCGL-AI Amino Acid Sequence (Pre-cleavage) 246
mCGL-AV Amino Acid Sequence (Post-cleavage) 247
mCGL-AI Amino Acid Sequence (Post-cleavage) 247

mCGL-AV NCBI BLAST Results 248

mCGL-AI NCBI BLAST Results 248

List of Tables

Table 1. Features of an ideal enzyme prodrug combination summarized from Greco and Dachs [17] 3

Table 2. Enzyme prodrug systems targeted to phosphatidylserine. 6

Table 3. Size-relationship to immunogenicity of foreign proteins adapted from [164] 19

Table 4. Fusion protein molecular weights 20

Table 5. CGL Mutation Summary for Methioninase Activity 36

Table 6. Immunohistochemistry antibody staining details 50

Table 7. Dissociation constant of PNP-AV binding to cells. 62

Table 8. Metastases in SCID mice with orthotopic MDA-MB-231 tumors..... 84

Table 9. Dissociation constants of mCGL-AI, mCGL-AV, and Met-AV on MDA-MB-231 and HAAE-1 cells..... 96

Table 10. Fusion protein specific IgG + IgM titers in BALB/cJ mice improved with daily administration of mCGL-AV over Met-AV (10 mg/kg IP) 109

Table 11. Median mouse survival and log-rank *p*-values of Kaplan-Meier survival curves with indicated significance (*). 116

Table 12. Synergism assessment factors for tumor growth inhibition 133

Table 13. PNP-AV Fusion Gene Amplification PCR Components 177

Table 14. PNP-AV Fusion Gene Amplification PCR Conditions..... 178

Table 15. PNP-AV Restriction Digest Components 179

Table 16. pET303/CT-His Backbone Restriction Digest Components 179

Table 17. Components for PNP-AV Ligation into pET303/CT-His 180

Table 18. SDS-PAGE gel casting components 204

Table 19. Gel selection based on monomer molecular weight 204

Table 20. PNP activity assay components 206

Table 21: LAL Endotoxin Assay Standard Curve 211

Table 22. NCBI BLAST Result Summary for PNP-AV 237

Table 23. mCGL and hCGL NCBI BLAST Results and Sequences with Highlighted Site of Mutation 238

Table 24. Mutant mCGL NCBI BLAST Results and Sequence with Highlighted Mutations 239

Table 25. NCBI BLAST Result Summary for mCGL-AV 248

Table 26. NCBI BLAST Result Summary for mCGL-AI 248

List of Figures

Figure 1. Outline of enzyme prodrug system targeted to phosphatidylserine. 5

Figure 2. PNP-AV mechanism of action. 10

Figure 3. Ribbon structures of fusion protein components. 19

Figure 4. Schematic of fusion protein binding quantification. 40

Figure 5. Placement of flank and fat pad tumor grafts. 44

Figure 6. Outline of process for automated quantification of DAB staining of tumor sections with activated caspase-3 and ki-67. 49

Figure 7. Outline of process for quantification of DAB staining of tumor sections with HIF-1α. 50

Figure 8. CD-AV clears from the circulation of SCID mice in <8 h. 54

Figure 9. Poor efficacy of CD-AV and 5-FC against MDA-MB-231 tumors on the flank of SCID mice. 55

Figure 10. Minimal effect of CD-AV system on mouse weight. 55

Figure 11. PNP hexamer model with highlighted terminals. 59

Figure 12. PNP-AV protein model. 59

Figure 13. SDS-PAGE of purified PNP-AV indicates >90% purity. 60

Figure 14. PNP-AV enzyme assay kinetic absorbance measurements over 5 min. 61

Figure 15. Binding stability data for PNP-AV. 63

Figure 16. Fixed cell confocal imaging of PNP-AV binding. 65

Figure 17. Cytotoxic effect of PNP-AV enzyme prodrug therapy on non-confluent HAAE-1 cells. 68

Figure 18. Cytotoxic effect of PNP-AV enzyme prodrug therapy on MCF-7 cells. 69

Figure 19. Cytotoxic effect of PNP-AV enzyme prodrug therapy on MDA-MB-231 cells. 70
Figure 20. Lack of cytotoxic effect of PNP-AV enzyme prodrug therapy on confluent HAAE-1 cells. 71
Figure 21. PNP-AV clears from the circulation of SCID mice in <8 h. 72
Figure 22. Mild antitumor effect of PNP-AV and fludarabine against MDA-MB-231 tumors on the flank of SCID mice. 73
Figure 23. Minimal effect of PNP-AV system on weight of SCID mice. 74
Figure 24. PNP-AV and fludarabine mathematical modeling of plasma levels based on dosing regimen. 75
Figure 25. Enhanced antitumor effect of PNP-AV and fludarabine in combination with docetaxel against MDA-MB-231 tumors on the flank of SCID mice. 76
Figure 26. Hematoxylin stained MDA-MB-231 tumor section from PNP-AV and fludarabine + docetaxel treated mouse shown with 4x magnification. 78
Figure 27. PNP-AV staining of MDA-MB-231 tumor section. 78
Figure 28. Met-AV clears from the circulation of SCID mice in <8 h. 80
Figure 29. Met-AV and selenomethionine reduce MDA-MB-231 tumor growth on the flank of SCID mice. 82
Figure 30. Met-AV and selenomethionine reduce orthotopic MDA-MB-231 tumor growth in mammary fat pad of SCID mice. 84
Figure 31. Minimal effect of Met-AV system on SCID mouse weight. 85
Figure 32. Docetaxel combination has no apparent enhancement of antitumor effect of Met-AV and selenomethionine for orthotopic MDA-MB-231 tumors in SCID mice. .. 87

Figure 33. Preliminary enzyme prodrug combination therapy with rapamycin produces antitumor effect on large orthotopic MDA-MB-231 tumors in SCID mice. 89
Figure 34. Met-AV Maleimide PEGylation at 25°C. 92
Figure 35. Met-AV Maleimide PEGylation at 4°C. 93
Figure 36. Binding stability of mCGL-AI, mCGL-AV, and Met-AV on MDA-MB-231 cells for 3 days. 97
Figure 37. Live cell confocal microscopy confirms membrane binding of mCGL-AI and mCGL-AV. 98
Figure 38. Comparison of the cytotoxic effect of mCGL-AI, mCGL-AV, and Met-AV enzyme prodrug therapy on MDA-MB-231 cells. 100
Figure 39. Comparison of the cytotoxic effect of daily administration of mCGL-AI and mCGL-AV enzyme prodrug therapy on MDA-MB-231 cells. 101
Figure 40. Comparison of the cytotoxic effect of mCGL-AI, mCGL-AV, and Met-AV enzyme prodrug therapy on 4T1 cells. 102
Figure 41. Comparison of efficacy of AV and AI targeted mCGL enzyme prodrug therapy with selenomethionine on orthotopic 4T1 tumors in BALB/cJ mice. 104
Figure 42. Intraperitoneal route of administration of fusion protein produces stronger antitumor effect than tail vein administration for orthotopic 4T1 tumors in BALB/cJ mice. 105
Figure 43. mCGL-AV clears from the circulation of BALBC/cJ mice in <10 h. 106
Figure 44. Comparison of efficacy of mCGL-AV and Met-AV enzyme prodrug therapy with selenomethionine on 4T1 tumors in BALB/c mice. 109

Figure 45. Combination therapy effects on orthotopic 4T1 tumor volume in BALB/cJ mice. 114
Figure 46. Minimal effect of mCGL-AV system and combination therapies on BALB/cJ mouse weight. 115
Figure 47. Kaplan-Meier survival curves for combination therapies. 115
Figure 48. Representative immunohistochemistry images. 117
Figure 49. Enzyme prodrug treatment for 3 weeks results in increased staining of apoptosis marker activated caspase-3 in mice with orthotopic 4T1 tumors. 119
Figure 50. Enzyme prodrug treatment for 3 weeks results in decreased staining of proliferation marker ki-67 in mice with orthotopic 4T1 tumors. 120
Figure 51. Rapamycin reduces percent necrosis in 4T1 tumor sections. 122
Figure 52. Rapamycin reduces percent of tumor expressing HIF-1α. 123
Figure 53. Cyclophosphamide reduces number of pulmonary metastasis in orthotopic 4T1-TdTomato BALB/cJ model. 125
Figure 54. Flow cytometry gating of regulatory T cells from the spleens of BALB/cJ mice. 126
Figure 55. Effects of combination treatments of regulatory T cell levels in the spleen. 127
Figure 56. Low vasculature density in untreated 4T1 tumors in BALB/cJ mice. 131
Figure 57. Fixed cell confocal imaging with differential interference contrast (DIC). 172
Figure 58. PNP-AV dissociation constant binding data on non-confluent HAAE-1 cells. 172
Figure 59. PNP-AV dissociation constant binding data on MCF-7 cells. 173

Figure 60. PNP-AV dissociation constant binding data on MDA-MB-231 cells. 173
Figure 61. mCGL-AI dissociation constant binding data on MDA-MB-231 cells. 174
Figure 62. mCGL-AV dissociation constant binding data on MDA-MB-231 cells.... 174
Figure 63. Met-AV dissociation constant binding data on MDA-MB-231 cells. 175
Figure 64. mCGL-AI dissociation constant binding data on non-confluent HAAE-1 cells. 175
Figure 65. mCGL-AV dissociation constant binding data on non-confluent HAAE-1 cells. 176
Figure 66. Bradford protein concentration assay calibration curve using bovine serum albumin. 201
Figure 67. Standard curve for methioninase assay using α-ketobutyrate and MTBH. 209

Abstract

Breast cancer is a global health concern of high prevalence that lacks safe and effective therapies for advanced cases. A targeted enzyme prodrug therapy aims to address this issue using an enzyme localized to the tumor to convert a systemically administered nontoxic prodrug into a toxic anticancer agent exclusively in the tumor. The target of the presented enzyme prodrug systems, phosphatidylserine, exists on cancer cells and the cells of the tumor vasculature. Annexin V binds to phosphatidylserine with high affinity and was successfully fused to three enzymes for the targeted delivery of the enzyme prodrug systems to the tumor. Development of the purine nucleoside phosphorylase fusion with annexin V is described, and results showing strong *in vitro* binding and promising cytotoxicity are presented. This system is compared *in vivo* with targeted cytosine deaminase and targeted methioninase enzyme prodrug systems. The methioninase system produced the strongest antitumor results showing tumor regression for the duration of treatment. Further engineering of the system resulted in the generation of a mammalian cystathionine-γ-lyase protein with methioninase activity to prevent the immune response anticipated against foreign methioninase. Successful transition to immune competent models without incurring an immune response led to studies with combination therapies to achieve an enhanced therapeutic effect. Antitumor synergism was observed when the enzyme prodrug therapy was combined with rapamycin to address the hypoxic response. Combination with immunostimulatory levels of cyclophosphamide produced an anti-metastatic response and enhanced survival. Combination of the enzyme prodrug therapy with both

rapamycin and cyclophosphamide effectively reduced tumor volumes, inhibited metastatic progression, and enhanced survival.

Chapter I: Introduction

Breast Cancer Landscape and Project Overview

Impact and Treatment of Breast Cancer

Despite advancing technologies and enormous public health campaigns, one in eight women are still diagnosed with breast cancer [1, 2] and over 40,000 women die each year in the United States [3]. Breast tumor metastasis rather than primary tumor burden causes mortality in over 90% of cases; therefore, early detection should improve survival rates [1, 4]. While there is an inarguable decline in breast cancer death rates in recent decades [5], the relevance of these statistics and the standards of care responsible are a topic of debate. A recent study claims 30% of breast cancer patients are overdiagnosed and overtreated, resulting in one to three deaths for every one life saved [1, 6, 7]. An improved breast cancer landscape depends upon enhanced diagnostic abilities as well as the development of revolutionary treatment regimens as safe and effective alternatives to the current standards of care.

Oncologists utilize response rates specific to tumor type and stage to prescribe treatment regimens that attempt to find a middle ground between inadequate treatment efficacy and overtreatment, both of which have potentially fatal consequences. Current standards of care include surgery, sentinel lymph node biopsy and surgery, radiation therapy, chemotherapy, hormone therapy, and targeted therapy [8]. Surgical options range from lumpectomy to radical mastectomy and are often dependent on lymph node biopsy. Surgical procedures are frequently preceded by neoadjuvant chemotherapy or followed by adjuvant radiation therapy, chemotherapy, or hormone therapy. Difficulty in removing every cancer cell and recurrence limits the success of surgical resection [9,

10]. Radiation therapy uses high-energy radiation from either internal or external sources to kill cancer cells. Chemotherapy drugs kill cancer cells or inhibit growth, either through systemic or regional administration. The FDA has approved dozens of chemotherapeutic agents and drug combinations for the treatment of breast cancer [8]. Tumor access, drug sensitivity, local and systemic toxicities, and development of resistance constrain chemotherapy and radiotherapy efficacies [11-13]. Targeted therapies attempt to identify and attack cancer cells without impacting normal cells. Exploitation of the hormone dependence of a subset of breast cancers, specifically estrogen dependence, has led to the development of hormone therapies including tamoxifen and aromatase inhibitors [8]. Other targeted approaches for breast cancer treatment include monoclonal antibodies, tyrosine kinase inhibitors, and poly(ADP ribose) polymerase (PARP) inhibitors. Most FDA approved targeted drugs for breast cancer (Trastuzumab, Pertuzumab, Ado-trastuzumab emtansine, Lapatinib) are only indicated for HER2-positive breast cancer (20% of cases) [5, 8]. Recent approval of mTOR-targeted Everolimus expands targeted breast cancer treatment to HER2-negative breast cancer, though it is only indicated in advanced hormone receptor-positive breast cancer in combination with exemestane and after failed responses to letrozole or anastrozole [8].

Directed Enzyme Prodrug Strategy

As research continues to unravel the "molecular circuitry" behind cancers and identifies more specific targets, targeted therapies will likely enhance the duration and quality of life of cancer patients beyond the current achievable levels with creative

approaches including toxic payload delivery, signaling attenuation, immune stimulation, and combination strategies [14-16]. One targeted adaptation of a toxic payload delivery with promising results involves the local activation of chemotherapeutic prodrugs to limit toxicity to the tumor environment using enzyme prodrug therapies [11, 17]. Enzyme prodrug strategies localize an enzyme to the tumor microenvironment either through gene delivery (gene-directed enzyme prodrug therapy; GDEPT) [18, 19], antibody targeting (antibody-directed enzyme prodrug therapy; ADEPT) [20, 21], local administrations, or even with cellular delivery systems [11, 22, 23]. Once the enzyme is localized to the tumor environment, a relatively nontoxic prodrug is administered that is then enzymatically converted to a toxic drug in the tumor. Table 1 lists the features exhibited by an ideal enzyme prodrug combination.

Table 1. Features of an ideal enzyme prodrug combination summarized from Greco and Dachs [17]

Enzyme	Prodrug	Drug
Non-toxic (in absence of prodrug)	No activation by processes in normal tissue	>100x more cytotoxic than prodrug
Non-immunogenic (even with prolonged administration)	Freely diffusible throughout tumor	Cytotoxicity should be cell-cycle and proliferation independent
Efficient prodrug activation (high K_{cat}, low K_m) in physiological conditions	Suitable stability for systemic administration	Suitable stability to allow for diffusion and bystander effect (half-life should be >1 min to allow diffusion 100-200 μm in tumor [24])

Enzyme prodrug therapies attempt to achieve a high therapeutic index and therapeutic selectivity through the generation of toxic levels of drug from inert prodrug at the tumor cells [18, 19]. Current enzyme prodrug systems face limitations, particularly GDEPT and its derivative VDEPT (virus-directed enzyme prodrug

therapy). Most significantly, gene delivery strategies suffer from poor gene expression *in vivo*; however selective delivery, insertional mutagenesis, and immunogenicity are persistent concerns as well [25-27]. Delivery of active enzyme (as in ADEPT strategies) circumvents expression issues; however antibody-enzyme conjugate accessibility to the tumor antigen limits antibody delivery approaches [25, 28]. Another drawback of ADEPT systems is the cost involved in producing and purifying sufficient quantities of antibody conjugates [25].

The projects discussed in this dissertation are enzyme prodrug systems targeted to phosphatidylserine, expressed externally on cancer cells and tumor vasculature, through the fusion of the enzyme to annexin V or annexin I, both of which bind to phosphatidylserine with high affinity. Figure 1 outlines the scheme of a phosphatidylserine targeting enzyme prodrug therapy. Our target, phosphatidylserine, allows for delivery of active enzyme to the tumor vasculature, overcoming the permeability issues plaguing most ADEPT approaches. Fusions of enzyme to annexin I or annexin V allow for high affinity targeting of phosphatidylserine on the tumor vasculature using well established and inexpensive bacterial expression systems. Delivery of cytotoxic payloads to the vascular wall results in destruction of tumor endothelial cells and vessel occlusion, hence cutting off the nutrient and oxygen supply to the tumor. The membrane diffusibilty of the small molecule cytotoxic agents allows for permeation into the tumor and a bystander killing effect of the surrounding tumor cells [29-35].

Three targeted enzyme prodrug systems, summarized in Table 2, were developed and evaluated *in vitro* (two previously [36, 37]) and *in vivo*. Binding

strength, stability, and cytotoxicity were the primary criteria evaluated *in vitro* using several breast cancer cell lines and endothelial cells. Tumor progression and survival were the primary criteria evaluated *in vivo* using immune-deficient SCID mice and immune-competent BALB/cJ mice. The most efficient system, methionine-γ-lyase fused to annexin V (Met-AV) was then adapted to an immune competent model using engineered mouse cystathionine-γ-lyase (mCGL).

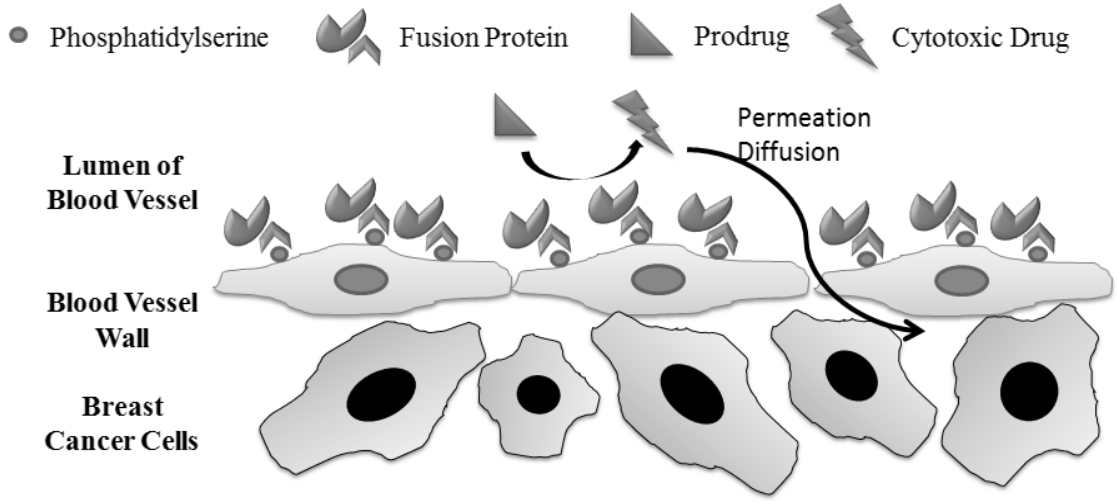

Figure 1. Outline of enzyme prodrug system targeted to phosphatidylserine. The first phase of the treatment is to administer the targeted enzyme. The fusion protein, containing annexin I (AI) or annexin V (AV) at the carboxy terminus, will be localized to tumor and tumor vasculature. AI and AV bind to externally expressed phosphatidylserine (PS) expressed on the endothelial cells of tumor vasculature and tumor cells. The second step, following plasma clearance of the fusion protein, is the administration of a non-toxic dose of prodrug. The prodrug will be converted to toxic drug at site of tumor.

Table 2. Enzyme prodrug systems targeted to phosphatidylserine.

Enzyme	Species	Substrate (Prodrug)	Products (Cytotoxic Drug *)
Cytosine Deaminase (CD)	*Saccharomyces cerevisiae*	5-fluorocytosine	5-fluorouracil*
Purine Nucleoside Phosphorylase (PNP)	*Escherichia coli*	fludarabine	2-fluoroadenine* ribose-1-phosphate
Methionine-γ-lyase (Met)	*Pseudomonas putida*	selenomethionine	methylselenol* α-ketobutyrate ammonia
		methionine	methanethiol α-ketobutyrate ammonia
Cystathionine-γ-lyase (CGL) **[58-N, 118-L, 338-V mutant]**	*Mus musculus*	selenomethionine	methylselenol* α-ketobutyrate ammonia
		methionine	methanethiol α-ketobutyrate ammonia

Enzyme Prodrug Therapies

Cytosine Deaminase and 5-Fluorocytosine

Mammalian cells exposed to 5-fluorouracil (5-FU) convert the molecule to the toxic pyrimidine antimetabolites, 5-FdUMP, 5-FdUTP, and 5-FTUP. These antimetabolites inhibit thymidylate synthase and misincorporate into RNA and DNA resulting in 5-FU RNA/DNA complex formations and eventual cell death [17, 38, 39]. Though a high dose is required for tumor response, 5-FU is currently used as a chemotherapeutic and radiosensitizer for the treatment of some solid tumors, including breast, gastrointestinal, ovary, head, and neck tumors [40, 41]. The high systemic chemotherapeutic dose administered causes a range of side effects, primarily

gastrointestinal and hematological, supporting the advantages of 5-FU localization to the tumor as in the enzyme prodrug therapies [42, 43].

Cytosine deaminase (CD) is a component of the pyrimidine salvage pathway in bacteria and yeast [44]. The enzyme catalyzes the hydrolytic deamination of cytosine to uracil, as well as 5-fluorocytosine (5-FC) to 5-FU which does not occur with the mammalian pyrimidine salvage enzyme, cytidine deaminase [17, 44]. The prodrug, 5-FC, is fairly nontoxic and is approved for use as an antifungal/antimicrobial agent [17, 45]. Cell and tumor sensitivity to the drug, 5-FU, is up to 2000x greater than the sensitivity to 5-FC [46]. 5-FU readily diffuses across cell membranes through non-facilitated diffusion [30, 47, 48], resulting in significant bystander effects without the requirement of cell to cell contact [48].

The lack of human cytosine deaminase and the cytotoxicity of 5-FU has generated significant interest in CD for a number of ADEPT [49-51] and GDEPT [52-54] strategies. More recent enzyme prodrug applications utilize yeast CD, as it was found to have a 22x stronger binding affinity to its substrate and a 4x faster reaction rate than bacterial CD when 5-FC is used as the substrate [55]. Though primarily a cell cycle dependent mechanism and a relatively low potency compared to other enzyme prodrug strategies, 5-FU generation within a tumor using an enzyme prodrug approach has shown significant promise for the treatment of multiple types of cancer.

Purine Nucleoside Phosphorylase and Fludarabine Phosphate

Fludarabine phosphate (9-β-D-arabinofuranosyl-2-fluoroadenine 5'-monophosphate, 2-Fluoro-ara-AMP, F-ara-AMP), a purine nucleoside analogue, is an

approved treatment for chronic lymphocytic leukemia [56-59]. Fludarabine phosphate has undergone numerous clinical trials for treatment of both solid tumors and leukemia; however success was hindered by dose limiting factors including myelosuppression and neurotoxicity when treating solid tumors [59, 60].

More recently, fludarabine phosphate has become the subject of study as the prodrug for enzyme prodrug systems as therapies for cancers such as glioma [61], prostate [62, 63], bladder [64], and liver [65] and is currently undergoing a phase 1 clinical trial for local administrations of adenovirus delivered purine nucleoside phosphorylase (PNP) for head and neck cancers. *In vivo* PNP gene delivery studies used intraperitoneal fludarabine doses ranging from 37.5 mg/kg/day [62, 65] to 450 mg/kg/day [66] in mouse models. Minimal effect was attained by fludarabine alone, but results were positive with the conversion to 2-fluoroadenine by the enzyme prodrug therapies. No signs of systemic toxicity or negative side effects were reported at these doses in either the groups with fludarabine or fludarabine with PNP. The GDEPT clinical trial has reported no serious adverse events or toxicities and a pronounced effect on tumor volumes in some patients using only 60% of the standard prescribed fludarabine doses [67]. Despite early successes, the current untargeted GDEPT approach requires local gene administration, leaving distant sites primarily unaffected and severely limiting future clinical utility.

The *Escherichia coli* enzyme PNP cleaves the ribose-1-phosphate group from fludarabine, resulting in 2-fluoroadenine [68, 69] which inhibits protein, RNA, and DNA synthesis [70]. Fludarabine is not a substrate for the human PNP [44, 68, 71, 72]; therefore undesired systemic production of 2-fluoroadenine from fludarabine is not a

concern. 2-fluoroadenine toxicity to cancer cells occurs at a concentration several orders of magnitude below that required for the same effect from fludarabine [73], partially stemming from the requirement of membrane transport carriers to allow fludarabine to cross the cell membrane in contrast to the free diffusion of 2-fluoroadenine across membranes. This allows for the systemic administration of fludarabine significantly below problematic levels while improving the cytotoxic effect at the site of the tumor. Figure 2 summarizes the treatment mechanism for a PNP molecule targeted to the outside of a cell using annexin V, with fludarabine as the prodrug.

One advantage of this enzyme prodrug therapy is that there is a significant bystander effect of the 2-fluoroadenine generated against both proliferating and non-proliferating cells [70, 74]. The bystander effect results from the ability of 2-fluoroadenine to freely diffuse across cell membranes, eliminating the need for PNP to be present in each individual cell. This property helps to alleviate transfection efficiency problems of studies using suicide gene-directed enzyme prodrug therapies (GDEPT) [63] and viral-directed enzyme prodrug therapies (VDEPT) [61, 62, 65]. Additionally, unlike the products of some other enzyme prodrug systems, 2-fluoroadenine is toxic to proliferating and non-proliferating cells [70]. A PNP based enzyme prodrug system therefore addresses two limitations of many systems: bystander effect requirements and cell cycle dependent cytotoxicity.

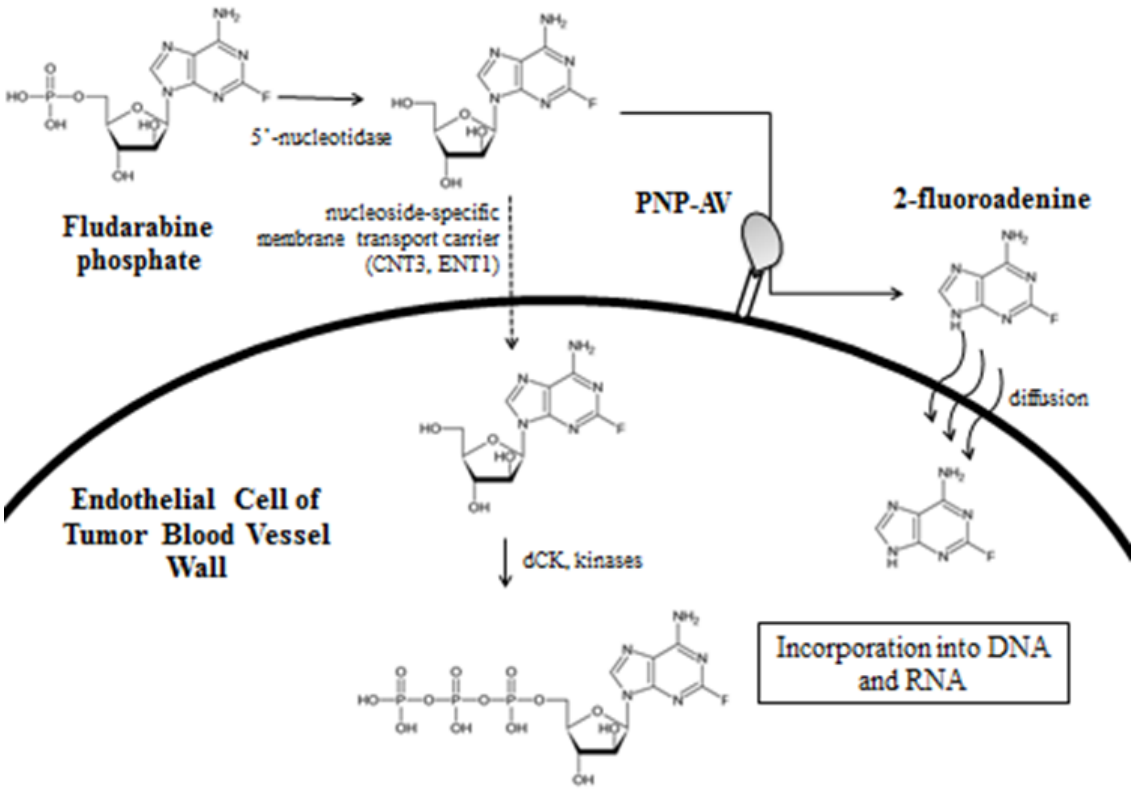

Figure 2. PNP-AV mechanism of action.
Fludarabine monophosphate is converted in serum to a dephosphorylated form by a 5' nucleotidase [75]. PNP attached to the cell surface via annexin V, and phosphatidylserine binding then cleaves the ribose-1-phosphate group, resulting in 2-fluoroadenine [68, 69]. The freely diffusible molecule enters the cell and inhibits protein, RNA, and DNA synthesis [70]. Nucelotide-specific membrane transport carriers transport the dephosphorylated form across the cell membrane, where it is then phosphorylated into a cytotoxic triphosphate [58, 75]

Methionine-γ-Lyase and Selenomethionine

Methionine-γ-lyase (methioninase, Met) catalyzes the production of methanethiol, α-ketobutyrate, and ammonia from L-methionine [76] and methylselenol, α-ketobutyrate, and ammonia from L-selenomethionine [77]. The most active methioninases have been purified from *Brevibacterium linens BL2*, *Psuedomonas putida* and *Aeromonas* sp., though *P. putida* showed maximum catalytic efficiency [78-81]. The enzyme from *P. putida* has been utilized in two anti-cancer capacities: using methionine as the substrate for methionine depletion therapies, and selenomethionine as the substrate for enzyme prodrug therapies.

Asparaginase and glutaminase successfully treat some forms of L-glutamine and L-asparagine dependent leukemias [80, 82, 83], with a similar strategy in development for L-methionine dependent tumors. Methioninase anticancer therapies were first developed as an effective tool for L-methionine depletion of tumors with success found both *in vitro* and *in vivo* [84-88]. Methioninase-aided depletion of L-methionine enhances the effects of dietary replacement of methionine with homocysteine which results in normal growth of healthy cells [89] but restricted growth of cancer cells [88, 90, 91]. These therapies function on the basis that healthy cells are capable of manufacturing methionine from homocysteine and therefore are methionine independent [92-94]; however, many cancer cells are methionine dependent including some bladder, brain, colon, kidney, lung, hematological, neurological, and breast cancers [90, 92, 95-98]. Reduced levels of methionine synthase, responsible for the methylation of homocysteine in the methionine synthesis process, results in methionine dependence of some cancer cells and sensitivity to methionine depletion therapies [99,

100]. Further studies have reported additional mechanisms for the development of methionine dependence of cancer cells, including loss of the methionine salvage pathway enzyme methylthioadenosine phosphorylase, which is genetically located in close proximity to the *p15* and *p16* tumor suppressor genes and frequently co-deleted [101].

Methioninase is found in nearly every organism except mammals [80, 102], and its products are significantly more toxic than its substrate, making it a strong candidate for an enzyme prodrug therapy. Methylselenol, a product of the reaction with selenomethionine, is 200-1000 times more cytotoxic to cancer cells than selenomethionine [87, 103] and diffuses through membranes, producing a significant bystander effect [80, 103]. The presence of methylselenol in cancer cells causes cell cycle arrest and apoptosis primarily through the oxidation of thiols and generation of superoxides [103-109]. The reactive oxygen species cause mitochondrial swelling resulting in increased permeability, loss of membrane potential, and release of cytochrome c which activates the caspase cascade and induces apoptosis [103, 110-112]. Alone, selenomethionine is relatively non-toxic to mammalian cells because it is not converted to selenol [113, 114] and is one form of dietary selenium supplementation [115]. The lack of a mammalian methioninase, strong cytotoxic effect of methylselenol, and significant bystander effect suggest a methioninase-based system would be a strong candidate for directed enzyme prodrug therapy.

Targeting Cancer Therapeutics to Phosphatidylserine

Phosphatidylserine, a cell membrane constituent, is found primarily on the inside of cells except on cancer cells and the tumor vasculature, where it has been externalized. Philip Thorpe's group at the University of Texas Southwest Medical Center in Dallas initiated phosphatidylserine targeting as an anti-cancer strategy and with Peregrine Pharmaceuticals developed the anti-phosphatidylserine monoclonal antibody bavituximab. Clinical trials have been performed or are currently undergoing with lung, breast, and pancreatic cancers primarily in combination with a cytotoxic agent (gemcitabine, docetaxel, or paclitaxel and carboplatin). Our lab has instead utilized the smaller native protein, annexin V (AV), which has a strong affinity for phosphatidylserine and coupled it to an enzyme for use in enzyme prodrug therapies. Additionally, preliminary studies with annexin I (AI) targeted to phosphatidylserine have been conducted. The annexins bind to phosphatidylserine expressed externally on tumor cells [116-118] and endothelial cells of tumor vasculature, but not normal vascular endothelial cells [119, 120]. Expression of the target on both the cancer cells and tumor vascular endothelium provides a significant advantage because the tumor is affected through the targeted cytotoxic mechanism as well as nutrient and oxygen deprivation resulting from vessel infarction [121]. Additionally, the endothelium does not exhibit the severe genetic instability that frequently results in acquisition of chemotherapeutic resistance among the tumor cell population [122].

Phosphatidylserine Externalization

Phosphatidylserine is an anionic membrane phospholipid that constitutes 8 to 15% of cellular phospholipid content [123]; however it is maintained almost exclusively on the inner leaflet of the cell membrane in healthy mammalian cells [124, 125]. A series of enzymes maintains the asymmetric localization of phosphatidylserine within the cell membrane. A family of ten aminophospholipid translocases (flippases) transports lipids (primarily the anionic phospholipids phosphatidylserine, phosphatidylethanolamine, phosphatidic acid, and phosphoinositides) to the internal leaflet in an ATP-dependent manner, transporting polar phospholipid heads through the hydrophobic membrane core against concentration gradients [126, 127]. A different family of enzymes (floppases) is responsible for transport of lipids (primarily cationic phospholipids) to the external membrane leaflet [116, 128]. Scramblase promotes the collapse of asymmetry through bidirectional transport of both cationic and anionic phospholipids and is typically activated when a cell undergoes apoptosis or upon cellular Ca^{2+} influx [123]. Under normal conditions flippases are highly efficient and quickly shift anionic phospholipids to the internal membrane leaflet, particularly phosphatidylserine which found exclusively on the inner leaflet [125, 129-132].

Phosphatidylserine externalization does occur in several processes including platelet activation, cell aging, degranulation, apoptosis, necrosis, and malignancy and has also been associated with sickle cell anemia, thalassemia, malaria, uremia, diabetes, pre-eclampsia, hepatitis C, HIV, and measles [123, 133-137]. Targeting anti-cancer therapeutics to phosphatidylserine has generated research interest since a number of tumor cells have been found to significantly increase levels of externalized

phosphatidylserine, possibly through dysfunction of the pathways responsible for maintenance of membrane asymmetry [116, 117, 119, 138-144]. The altered regulatory pathways resulting in phosphatidylserine externalization provide benefit to cancer cells and tumors as a whole, as phosphatidylserine externalization is a natural mechanism for immune suppression to allow clearance of dying cells without inflammation [145-147]. Additionally, tumor vascular endothelium externalizes phosphatidylserine [148], likely resulting from the tumor microenvironment. Acidity, hypoxia, reactive oxygen species, and inflammatory conditions are associated with the tumor microenvironment and have been found to increase phosphatidylserine externalization *in vitro* in endothelial cells [119, 120, 148].

Annexin Protein Family

The annexin superfamily consists of 13 proteins that bind calcium and phospholipid and exhibit significant structural and biological homologies [149-151]. To some degree most annexins bind phosphatidylserine, phosphatidic acid, and phosphatidylinositol, but minimal binding is seen with phosphatidylethanolamine, phosphatidylcholine, and sphingomyelin [150]. The C terminal of the protein core is a 34 kDa domain conserved among the annexins and is responsible for both membrane and calcium binding [150, 152]. The N terminal domain varies among the family of proteins and can provide differing functionalities. The project discussed in this dissertation primarily uses annexin V as the targeting component of the fusion protein; however annexin I has also been evaluated.

Annexin I is one of the longer annexins and has been shown to form aggregates on membranes. Specifically, once the core protein has bound a phosphatidylserine molecule, the N terminal domain is capable of binding a second phosphatidylserine, another annexin I molecule, and a different calcium binding protein, S100 [149, 150]. The resulting enhanced avidity may improve overall binding of the complexes [152]. When excreted, annexin I will bind externally to anionic phospholipids in the cell membrane causing anti-migratory and anti-inflammatory responses [149]. The capability of annexin I to bind multiple phosphatidylserine molecules has been theorized to play a role in tethering apoptotic cells to phagocytes [149, 153].

Annexin V is one of the smallest members of the annexin family and has only a few amino acids in the N terminal variable region of the protein [150]. Annexin V has been implicated as an anti-inflammatory molecule, an anticoagulant, and plays a role in ion channel activity and membrane fusion [150, 154]. Fusions and tagging of annexin V have been performed and are available commercially, primarily for its utility in detecting apoptotic cells [155, 156]. The annexin V binding to phosphatidylserine may also be involved in promoting the non-inflammatory clearance of apoptotic cells.

Clinical Relevance of Phosphatidylserine Targeted Therapies

While the annexin targeted enzyme prodrug therapies possess the capacity to bind to phosphatidylserine on the cancer cells, data suggests the localization of the enzyme and annexin fusion protein primarily on the tumor vasculature [157]. Vascularization is crucial for progression of tumors beyond 1-2 mm^3 due to the limits of diffusion for the oxygen and nutrients necessary for cell survival [158-160]. The

dependence of nearly all solid tumors (including colon, lung, breast, cervix, bladder, prostate, and pancreas) on vascularization [160] indicates that phosphatidylserine targeted therapies are not limited to breast cancer (the focus of this work) and could be applied to other solid tumor-forming cancers and for the treatment of metastatic lesions [118].

Summary of Targeting Strategy

Significantly enhanced phosphatidylserine exposure on cancer cells and tumor vasculature presents a unique therapeutic target present both in the tumor, its supporting vasculature, and possibly metastatic sites of multiple types of cancer. The annexin family of proteins, most commonly used in research for detection of apoptotic cells, exhibit strong binding properties to phosphatidylserine and similar anionic phospholipids. Annexin I and annexin V were selected as targeted delivery vehicles for enzyme prodrug systems, which, through the fusion of the enzyme to the annexin protein, allows for localization of the enzyme to the tumor.

Overcoming Protein Immunogenicity

Immunogenicity is a major concern for therapeutic protein products. Generation of an immune reaction results from a number of subject-specific and product-specific factors. Adverse immunological reactions can be unpredictable and can result in neutralizing antibodies that render a therapy ineffective, produce anaphylactic responses potentially leading to death, or elicit cross-reactive responses that turn the immune system against native proteins [161].

The subject-specific response can be dependent on the route of administration, dose, frequency of administration, allergy, immune competency, and prior sensitization or tolerance [161]. Product or protein-specific factors include protein origin, size and structure, product purity, and presence of post-translational modification [161]. Subject-specific responses are addressed primarily through appropriate development of dosing regimens and recognition of therapeutic contraindications. The protein-specific factors require significant attention and development primarily during the preclinical phases of evaluation.

FDA approval of biologics includes human, murine, chimeric, and humanized antibodies, as well as recombinant, recombinant human, and even bovine products [162]. Approved therapeutic proteins fall in a large range of sizes using varied production systems and purification techniques; however large non-mammalian proteins present major obstacles preventing clinical use (though possible, as evidenced by FDA approved PEGylated forms of bacterial asparaginase and adenosine deaminase [163]). Table 3 summarizes the expected degree of immune response to foreign proteins based on size, emphasizing a strong expected immune response for foreign proteins over 100 kDa. The large structures of the enzyme component of the enzyme prodrug systems, shown in the models in Figure 3 and summarized in Table 4, combined with the non-mammalian origin of CD, PNP, and Met suggest a strong degree of immunogenicity. To ultimately progress beyond the preclinical phase, enzyme prodrug therapies must address the immunogenicity concerns stemming from the need to use enzymes not present in normal tissue to avoid off-target prodrug activation. Two major strategies exist to address immunogenicity, both of which have been utilized for current FDA

approved products: PEGylation and protein engineering to exhibit stronger similarities to human proteins. Both PEGylation and protein engineering strategies were pursued to reduce the immunogenicity of the enzyme prodrug systems.

Table 3. Size-relationship to immunogenicity of foreign proteins adapted from [164]

Molecular Weight	Amino Acids	Immunogenicity
< 1 kDa	**1-10**	**Rare**
1-10 kDa	**10-100**	**Weak**
10-100 kDa	**100-1000**	**Immunogenic**
> 100 kDa	**> 1000**	**High**

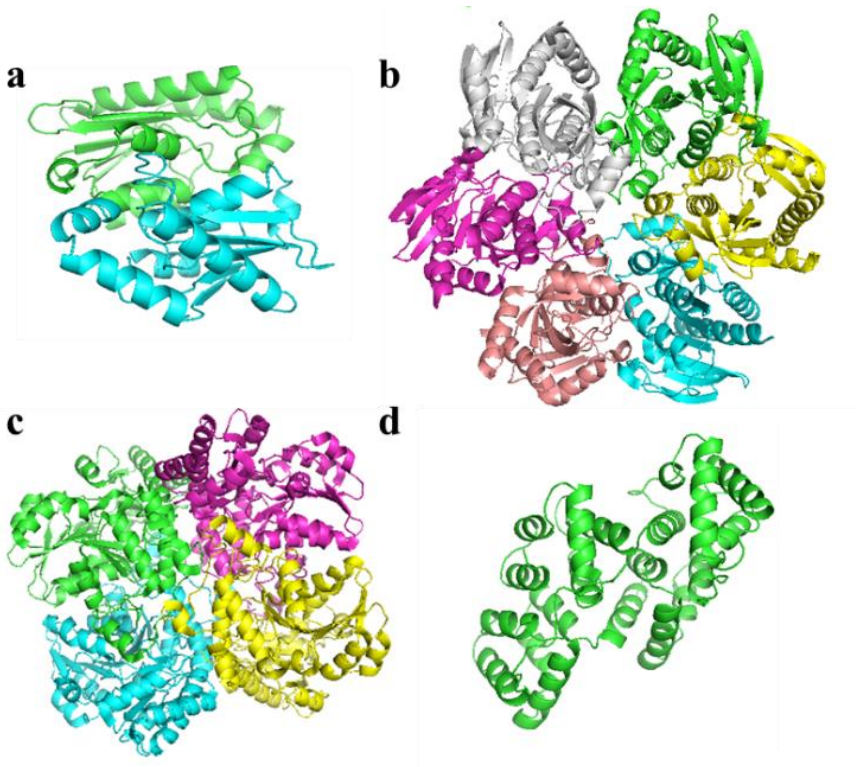

Figure 3. Ribbon structures of fusion protein components.
The PyMOL Molecular Graphics System (version 1.2r3pre; Schrödinger, LLC) generated protein ribbon structures using data files obtained through the Protein Data Bank Europe for (a) CD, (b) PNP, (c) Met, and (d) AV.

Table 4. Fusion protein molecular weights

Fusion Protein	Monomer	Subunits	Multimer
CD-AV	**53 kDa**	**dimer**	**106 kDa**
PNP-AV	**65 kDa**	**hexamer**	**390 kDa**
Met-AV	**80 kDa**	**tetramer**	**320 kDa**
mCGL-AI	**83 kDa**	**tetramer**	**332 kDa**
mCGL-AV	**80 kDa**	**tetramer**	**320 kDa**

Conjugation of hydrophilic poly(ethylene glycol) (PEG) to therapeutic proteins has been utilized to enhance circulation time, prevent protein aggregation, decrease proteolysis, and reduce immunogenicity [165-167]. In general, PEG is considered to be safe, nontoxic, and non-immunogenic with normal clearance mechanisms through renal filtration and liver uptake [163, 167]. Conjugation of PEG occurs through many strategies targeting different reactive sites including those present on amino acid side chains for protein PEGylation. PEG molecules conjugated to therapeutics range from <10 kDa linear chains to >40 kDa branching PEG units and reduce immunogenicity through a steric hindrance effect [163].

Elimination of antigenic sites from protein structure through a protein engineering approach acts as a viable alternative to the steric blockage of antigenic sites on therapeutic agents through chemical conjugation of PEG. The protein engineering approach can rely on identification and direct removal of antigenic epitopes, replacement of some foreign domains with native human protein as in the case of chimeric or humanized antibodies, or modification of native proteins to obtain desired bioactivities [168, 169]. In general, increasing the human sequence content of a therapeutic protein minimizes the possibility of epitope detection and an immune reaction [168].

Use of Combination Therapies for Enhanced Response

The hallmarks of cancer describe a set of biological capabilities acquired during tumor development, specifically: resistance to cell death, sustained proliferation, evasion of growth suppressors, induction of angiogenesis, replicative immortality, activation of metastasis and invasion, reprogramming of energy metabolism, and immune evasion [170, 171]. Genomic instability causes the development of these traits which produce an adaptable tumor microenvironment that challenges anti-cancer strategies. Tumor heterogeneity and genetic changes among and within cancers allude to the potential for successful treatment using combination therapies rather than a single agent approach. Combination strategies attempt to combine agents with different killing mechanisms, sometimes addressing a different tier in the hallmark biological capabilities of cancer cells without causing an overlap in toxicity [172].

Initial efforts with combination therapies focused on increasing the presence of our targeted enzymes through the use of docetaxel; however the most recent studies have included the addition of rapamycin to target the hypoxic response and the use of cyclophosphamide for immune stimulation. This three-pronged anti-cancer approach includes the targeted delivery of a cytotoxic agent, antitumor immune stimulation, and modulation of the hypoxic response within the tumor microenvironment. Together, this strategy addresses many of the hallmark traits of cancer while still minimizing any impact on healthy tissue.

Docetaxel Enhanced Phosphatidylserine Targeting

Docetaxel, an FDA approved anti-mitotic chemotherapeutic, targets microtubules with a high therapeutic index, in a similar fashion to paclitaxel [173]. Docetaxel is used primarily as an adjuvant therapy for patients with high risk breast cancer as a result of problems with cumulative systemic toxicity after prolonged high dose therapies [174]. Several chemotherapeutics, including docetaxel, have been found to significantly increase externalization of phosphatidylserine without inducing apoptosis in multiple cell types when used at low doses [175]. Additional studies examined the possibility of using sub-toxic levels of chemotherapeutic to increase phosphatidylserine externalization within a tumor with particular focus on the tumor vasculature endothelial cells, of which only about 10-40% externalize phosphatidylserine [176]. Low dose docetaxel was found to successfully increase external phosphatidylserine positive tumor vessels by 70% with no reported systemic impacts or effects on normal vasculature [146, 176]. Increased exposure of the target with minimal systemic effect is highly desirable, particularly with a targeted enzyme prodrug system as it allows a higher concentration of localized enzyme and an exponential increase in generation of cytotoxic agents.

Countering the Hypoxic Response with Rapamycin

Aggressive cancers can outgrow the blood supply and surpass angiogenic requirements resulting in a hypoxic tumor microenvironment. In fact, necrotic cancer sections, commonly found in solid tumors, indicates severe intratumoral hypoxia resulting in insufficient oxygenation and decreased cell viability [177]. Hypoxia-

inducible factors (HIF) activate mechanisms to improve oxygenation as well as reprogram metabolic processes to enhance cell survival under oxygen deprivation [178]. HIF-1 and HIF-2 regulate over 1000 genes involved in cancer biology, including the pro-angiogenic vascular endothelial growth factors (VEGF) and enzymes responsible for matrix remodeling and cellular migration [4, 179, 180]. The hypoxic tumor microenvironment activates this cellular survival mechanism which cascades and ultimately plays a role in the development of a number of the hallmark traits of cancer, including angiogenesis, metastasis and invasion, altered metabolism, and apoptotic resistance.

The hypoxic response involves a vast number of molecules and pathways potentially intertwined with vital non-cancer related processes, making complete inhibition difficult. Rapamycin, an inhibitor of mammalian/mechanistic target of rapamycin (mTOR), acts as an upstream downregulator of HIF-1α and subsequently angiogenesis. The subunits HIF-1α and HIF-1β comprise HIF-1 (with similar constituents for HIF-2), though the β unit is constitutively expressed and only the α subunit undergoes oxygen-dependent regulation [181, 182]. Rapamycin and analogues CCI-779, RAD001 (Everolimus), and AP23573 have undergone clinical trials for various cancer treatments and are generally well tolerated [178]. Despite its origins as an immunosuppressive drug, reduced VEGF levels and the anti-angiogenic properties of rapamycin and its analogues generate interest in oncology research because it acts significantly upstream from many of the available anti-angiogenic agents and affects not only angiogenesis but also cell growth, proliferation, and survival [183]. Most anti-

angiogenic drugs act downstream of the cell proliferation pathways, focusing primarily on VEGF (bevacizumab) and its receptors (sorafenib, sunitinib) [184, 185].

mTOR regulates a signaling cascade through control of phosphorylation of proteins S6K1 and 4E-BP-1, important for translation of mRNAs involved in cell growth and proliferation processes including HIF [186, 187]. Inhibition of mTOR results in decreased translation of HIF-1α and possibly HIF-2α [181, 187, 188]. Generally HIF-2 is not considered to be rapamycin sensitive as rapamycin only inhibits one of the two mTOR complexes (rapamycin inhibits mTORC1, and HIF-2 is mTORC2 dependent); however some studies show reduced levels of HIF-2α mRNA translation and inhibition of mTORC2 with rapamycin in some conditions [187-189].

HIF-1α expression increases vascular permeability, promotes intravasation of cancer into circulation, and results in increased metastasis [4, 180]. Additionally, HIF-1 signaling is theorized to play a role in tumor cell repopulation following cytotoxic therapies [190]. Effective reduction of HIF-1α levels with rapamycin could significantly reduce the pro-survival signaling of the hypoxic response and inhibit tumor progression. Combination therapy with rapamycin and the vascular-targeted enzyme prodrug therapies may be especially complementary, as the enzyme prodrug therapy has been shown by this research group to result in necrotic tumor cores and reduced blood flow [157] (and likely oxygen diffusion) in the tumor environment which is already plagued by abnormal vasculature.

Immunostimulation with Cyclophosphamide Depletion of Regulatory T Cells

Regulatory T cells are a subset of CD4+ T cells that help to establish peripheral tolerances to self-antigens and are often classified by the expression of CD25 and the transcription factor forkhead box P3 (FoxP3) [191-194]. The peripheral tolerances established by regulatory T cells are of particular interest in regards to cancer due to the resultant immune evasion capabilities, one of the hallmark biological traits of cancer. Regulatory T cells have been shown to exhibit direct suppressive activity against tumor antigen-specific immune responses. The secretion of immunosuppressive cytokines IL-10, TGF-β, IL-35, and VEGF and results in suppression of helper and effector T cells [191, 192, 195]. Depletion of regulatory T cells reduces immune evasion capabilities of tumors, enhances antitumor immunity, and facilitates tumor rejection [196, 197].

Numerous strategies exist for inhibition of regulatory T cells, including cyclophosphamide, gemcitabine, mitoxantrone, fludarabine, thalidomide analogues, COX-2 inhibitors, and anti-CTLA-4 antibodies [191]. In particular, low dose cyclophosphamide has been shown to selectively deplete regulatory T cells. Cyclophosphamide acts by alkylating DNA, creating inter-strand and intra-strand crosslinks that ultimately result in cell death [198, 199]. Increased apoptosis and decreased immunosuppressive activity of regulatory T cells upon low dose cyclophosphamide treatment results from a hypersensitivity possibly related to a decreased capacity for DNA damage repair [199]. Combined with other antitumor therapies, low dose cyclophosphamide can enhance the antitumor immune response, leading to tumor rejection and improved survival [198, 200-202]. Previously, we have shown that low dose cyclophosphamide combined with tumor thermal ablation using an

annexin V targeted system likely allows for direct antigen release into circulation and results in improved survival compared to thermal ablation alone [203]. Additionally, the apoptosis induced by the enzyme prodrug systems is expected to enhance tumor antigen presentation, and when combined with cyclophosphamide, could tip the balance away from tolerance and augment an antitumor immune response [204].

Project Summary and Experimental Overview

The overarching goal of this project is to develop a targeted enzyme prodrug therapy through the fusion of an enzyme to annexin V for the treatment of breast cancer in an immune competent mouse model. The first objective of this work was to develop the PNP-AV enzyme prodrug system by first constructing, producing, and purifying the PNP-AV fusion protein. The PNP-AV enzyme prodrug system would then be characterized *in vitro* in a similar fashion to the previously developed systems using CD-AV and Met-AV.

The second objective is the assess the three enzyme prodrug systems in immune deficient mice bearing human breast tumors with the primary evaluation criteria being a reduction in tumor volume without introducing negative side effects. The most successful candidate among the three enzyme prodrug systems is to be selected for further development for immune competent models, either through PEGylation or protein engineering strategies.

Upon performing *in vivo* trials with all three systems and selecting a candidate for immune competent models, the third objective is to reduce the immunogenicity of the fusion protein and maximize antitumor efficacy and survival in immune competent

mice bearing breast tumors. A combination therapy approach will be utilized to maximize therapeutic efficacy.

Chapter II: Materials and Methods

Fusion Gene Construction and Transformations

Construction of Recombinant Expression Plasmid for PNP-AV

The PNP (gift of Dr. Joanne Turnbull, Concordia University Department of Chemistry and Biochemistry, Montreal, Canada) and AV (gift of Dr. Stuart Lind, University of Colorado, Denver, CO) genes were amplified separately with the Expand High Fidelity PCR system from Roche Applied Sciences (Madison, WI). The oligonucleotide PCR primers were synthetically produced (Integrated DNA Technologies, Coralville, IA) and are displayed below. The bold regions on the primers indicate the sequences complementary to the genes. BamHI restriction enzyme sites are shown as the boxed regions with the cut sites indicated. The underlined segment in the PNP antisense primer is a linker region.

PNP gene sense primer:

5'-GAC GAC GAC AAG ATG CCC **GCT ACC CCA CAC ATT AAT GCA G**- 3'

PNP gene antisense primer:

5'-CGC G|GA TCC AGA ACC GGA GCC **CTC TTT ATC GCC CAG CAG AAC**-3'

Annexin V sense primer:

5'-CGC G|GA TCC **GCA CAG GTT CTC AGA GGC**-3'

Annexin V antisense primer:

5'-GA GGA GAA GCC CGG **TTA GTC ATC TTC TCC ACA GAG C**-3'

The PCR products were purified using a QIAquick PCR purification kit (Qiagen, Valencia, CA; 28104) and separately digested with BamHI restriction enzyme (New England Biolabs, Ipswich, MA; R0136S). The digested genes were purified and ligated with T4 DNA ligase (New England Biolabs; M0202S). The fusion gene was amplified via PCR with the following sense and antisense primers:

Fusion gene sense primer:

5'-CGC T|CT AGA ATG **GCT ACC CCA CAC ATT AAT GCA G**-3'

Fusion gene antisense primer:

5'-CGC C|TCGAG *CGG ACC CTG GAA CAG AAC TTC CAG* **GTC ATC TTC TCC ACA GAG CAG C**-3'

The bold regions indicate the complementary sequences for the start of the PNP gene for the sense primer and the end of the AV gene on the antisense primer. Restriction enzyme sites were incorporated, shown as the boxed regions with the cut site indicated. The sense strand site is for Xba1 and the antisense strand site is for Xho1. The antisense strand also includes a cleavage site for the protease HRV-3C, shown in italics, to allow for separation of the protein from the C-terminal 6x His-tag using immobilized metal affinity column chromatography (IMAC). PCR was performed with the Phusion High Fidelity PCR kit (New England Biolabs; E0553S).

The PCR products were again purified using a QIAquick PCR purification kit, run on an agarose gel, and extracted with a QIAquick gel extraction kit (Qiagen; 28704). A restriction enzyme digest was performed on the purified PNP-AV gene and

pET303/CT-His vector (Life Technologies, Grand Island, NY; K630203) with Xho1 (New England Biolabs; R0146S) and Xba1 (New England Biolabs; R0145S). Ligation was performed with T4 DNA ligase (New England Biolabs; M0202S). Plasmids were sent for sequence verification (Oklahoma Medical Research Foundation, Oklahoma City, OK) following transformation and culture of NovaBlue Gigasingles competent cells (EMD Chemicals, Gibbstown, NJ; 71227-4). *E. coli* BL21(DE3) cells (EMD Chemicals; 69450-3) were then transformed and cultured for the protein expression.

Construction of Recombinant Expression Plasmids for mCGL Fusions

mCGL, AV, and AI gene fragments were synthesized (Life Technologies) with each fusion, mCGL-AV and mCGL-AI, consisting of three fragments. Fragment sizes ranged from 371 to 1000 amino acids with 40 bp overlapping regions on each end of the fragment. Gene ends were designed with a 40 bp overlap with the ligation independent cloning sites in pET-30 Ek/LIC (EMD Chemicals; 69077) for direct assembly of gene fragments into the vector using the Gibson Assembly method [205, 206]. Codons were optimized for protein production in *E. coli* using DNAWorks software (Helix Systems, National Institutes of Health). Gene fragment sequences as well as the final construct and translated sequences are available in Appendix C: Fusion Gene Construction.

Gibson assembly uses exonuclease activity that creates 3' overhangs on double-stranded DNA and allows annealing of complimentary fragments. Polymerase and ligase activity then fills in and seals the assembled DNA. Gibson assembly master mix (New England Biolabs; E5510S) was held at 50°C for 60 min in a thermocycler with the gene fragments and vector. The assembled product was transformed into NEB 5-

alpha competent *E. coli*, expanded, and cultured on kanamycin plates. Colonies were sequenced (Oklahoma Medical Research Foundation) using sequencing primers (Integrated DNA Technologies) designed for mCGL-AI and mCGL-AV. The plasmid miniprep for mCGL-AI in pET-30 Ek/LIC was transformed into BL21(DE3) competent cells for expression. The plasmid miniprep for mCGL-AV in pET-30 Ek/LIC was transformed into T7 Express lysY competent cells (New England Biolabs; C010I) for protein expression, which yielded more protein than BL21(DE3) expression of mCGL-AV.

Protein Expression and Purification

BL21(DE3) Expression of CD-AV, PNP-AV, Met-AV, and mCGL-AI

BL21(DE3) cells harboring the vector for CD-AV, PNP-AV, Met-AV, or mCGL-AI were grown in LB medium at 37°C and 200 rpm to an $OD_{600\ nm}$ of 0.6. LB medium contained 100 µg/ml carbenicillin (VWR, Radnor, PA; 97063-144) for PNP-AV expression or 35 µg/ml kanamycin (Fisher Scientific, Pittsburgh, PA; BP906-5) for CD-AV, Met-AV, and mCGL-AI expression. Growth occurred in two steps; initially at 10 ml and then expanded to 1 L. Isopropyl β-D-thiogalactopyranoside (IPTG) (VWR; EM-5810) was added to a concentration of 0.4 mM to induce protein expression. Induction occurred for 6 h at 30°C with shaking at 180 rpm. Note that both vectors used, pET-30 Ek/LIC (CD-AV, Met-AV, mCGL-AI, mCGL-AV) and pET303/CT-His (PNP-AV), utilize the T7 lac promoter and could potentially benefit from increased induction concentrations up to 1 mM IPTG.

T7 Express lysY (DE3) Expression of mCGL-AV

T7 Express lysY (DE3) cells harboring the vector with mCGL-AV were grown in TB medium with 35 µg/ml kanamycin at 37°C and 220 rpm to an $OD_{600\ nm}$ of 1.2. Growth occurred in two steps; initially at 10 ml and then expanded to 1 L. IPTG was added to a concentration of 1 mM to induce protein expression. Induction occurred for 19 h at 25°C at 200 rpm. The increase of cells resultant from the use of TB medium and growth to $OD_{600\ nm}$ of 1.2 was necessary for sufficient yields of mCGL-AV.

IMAC Purification

Recombinant fusion proteins were purified using immobilized metal affinity chromatography (IMAC) with immobilized Ni^{2+} to isolate the fusion protein [207]. *E. coli* cells were harvested with centrifugation, lysed through sonication, and cell debris removed through further centrifugation. The supernatant was loaded into a 5 ml HisTrap HP column (GE Healthcare Life Sciences, Piscataway, NJ; 17-5248-02) with 40 mM imidazole and 500 mM NaCl added to reduce non-specific protein binding. For Met and mCGL fusion proteins all buffers also contain 0.02 mM pyridoxal phosphate to maintain enzyme activity. The column was washed with a 20 mM sodium phosphate buffer with 40 mM imidazole and 500 mM NaCl followed by an endotoxin removal wash which also includes 1.0% Triton X-114, both at pH 7.4. Elution of the fusion protein from the column was performed at pH 7.0 in 20 mM sodium phosphate buffer with 500 mM imidazole and 500 mM NaCl.

Following elution, the fusion protein was dialyzed into 20 mM sodium phosphate buffer at pH 7.4 to allow for cleavage of the His-tag with HRV-3C protease

(Thermo Scientific Pierce, Rockford, IL; 88946). A Bradford assay (Bio-Rad Laboratories Inc., Hercules, CA; 500-0205) was utilized to determine protein concentration (see Appendix B: Laboratory Protocols for details). Protease was added at 10 U/mg protein with 10X cleavage buffer as recommended by the manufacturer and incubated for 18 h at 4°C with shaking at 30 rpm. The solution was then loaded onto a 5 ml HisTrap HP column with 40 mM imidazole and 500 mM NaCl, and the flow-through was collected. Protease and uncleaved protein remain bound to the column and elute under the previously described elution conditions. Cleaved protein was dialyzed into 20 mM sodium phosphate and 100 mM NaCl at pH 7.4. The protein solution was passed through a 0.2 µm cellulose-acetate filter for sterilization, flash frozen, lyophilized, and stored at -80°C.

Prior to *in vivo* work, endotoxin levels are assessed through a chromogenic Limulus Amebocyte Lysate assay (Lonza, Walkersville, MD; 50-647U) according to manufacturer instructions with details available in Appendix B: Laboratory Protocols. Purity is assessed through a densitometric analysis with ImageJ (FIJJ build, National Institutes of Health) of SDS-PAGE gels with Coomassie staining of protein samples [208].

Enzyme Activity Assays

Cytosine Deaminase Activity Assay

Cytosine deaminase activity was measured as previously described [37, 209] using the conversion of 5-fluorocytosine (5-FC) to 5-fluorouracil (5-FU) and spectrophotometric properties at 255 nm and 290 nm. 5-FC is incubated with dilutions

of cytosine deaminase at 37°C and pH 7.4 for 30 min. The reaction is quenched with HCl, and then absorbances are measured in a BioTek Synergy HT microtiter plate reader (BioTek Instruments Inc., Winooski, VT). Activity, with one unit defined as 1 µmol 5-FU formed per min at 37°C, is calculated according to the formula determined by Senter *et al* [209].

Purine Nucleoside Phosphorylase Activity Assay

The purine nucleoside phosphorylase activity assay was adapted from Sigma Aldrich protocol EC 2.4.2.1 for nucleoside phosphorylase activity and is previously described [210]. Hypoxanthine is generated from the nucleoside phosphorylase from the substrate inosine. Xanthine oxidase then catalyzes the conversion of hypoxanthine to uric acid, which can be measured with absorbance at 293 nm. A microtiter plate reader is used to perform kinetic measurements at 293 nm for 3 min or until values are constant of a mixture of inosine (Sigma Aldrich, St. Louis, MO; I4125) and xanthine oxidase (Sigma Aldrich; X4500). The maximum rate of change for the linear region of change is considered to be the slope of the blank sample. PNP is added and additional measurements are performed for 5 min to determine the maximum rate of change for the linear region with enzyme. One unit is defined as the phosphorolysis of 1.0 µmol of inosine to hypoxanthine and ribose 1-phosphate per min at pH 7.4 and 25°C.

Methionine-γ-Lyase Activity Assay

The methioninase assay is performed as previously described [36, 76]. Dilutions of enzyme samples were incubated with L-methionine (Sigma Aldrich;

M9625) or L-selenomethionine (Fisher Scientific; AC25996-0010) for 10 min at 37°C to catalyze the production of α-ketobutyrate. Trichloro-acetic acid (50%, w/v) was used to terminate the enzymatic reaction, followed by 2 min of centrifugation at 15000 x *g*. The supernatant was added to sodium acetate buffer and 0.1% 3-Methyl-2-benzo-thiazolinone hydrazine hydrochloride hydrate (MBTH) for color development. Development proceeded for 30 min at 50°C in a PCH02 Peltier Cooler/Heater (Grant Instruments Ltd., Cambridge, UK). Absorbance was read in a microtiter plate reader at 320 nm. One unit of enzyme is defined as the amount that catalyzes the formation of 1 μmol of α-ketobutyrate per minute.

Reducing Immunogenicity

PEGylation

PEGylation was performed using 10 kDa 4-arm branched PEG with a single maleimide functional group (NOF America Corporation, White Plains, NY; SUNBRIGHT PTE-100MA) or a 20 kDa 2-arm branched PEG with a single aldehyde functional group (NOF America Corporation; SUNBRIGHT GL2-200AL3) or a linear 10 kDa PEG with single aldehyde functional group (NOF America Corporation; SUNBRIGHT ME-100AL) or a linear 10 kDa PEG with a single NHS active ester functional group (NOF America Corporation; SUNBRIGHT ME-100TS). Conjugations were performed in 20 mM sodium phosphate, 100 mM NaCl buffer or 100 mM borate buffer for varied times, temperatures, molar ratios, and pH. PEGylation was performed on Met-AV and PNP-AV proteins and assessed for degree of PEGylation with SDS-PAGE and protein function with enzyme activity assays.

mCGL Design

Wild type human CGL displays no activity toward L-methionine or L-selenomethionine; however three mutations impart methionine-γ-lyase activity to human CGL [169]. Since pre-clinical testing will occur in immune competent mice, NCBI BLAST was used to align human and mouse CGL sequences to determine comparable mutations. NCBI BLAST alignments of the human and mouse CGL amino acid sequences can be found in Table 23 of Appendix C: Fusion Gene Construction. The mutations were located in conserved regions of sequence, presumably an area involved in substrate binding, and therefore theorized to impart similar activity upon the mouse CGL. The works in this document refer to mouse CGL with the mutations outlined in Table 5. Gene construction is described in the section "Fusion Gene Construction and Transformations" with detailed protocols in Appendix B: Laboratory Protocols.

Table 5. CGL Mutation Summary for Methioninase Activity

Mutation	Human CGL Position	Mouse CGL Position
E → N	59	58
R → L	119	118
E → V	339	338

Mammalian Cell Culture

HAAE-1 Endothelial Cells

Human abdominal aorta endothelium (HAAE-1) cells (Coriell Insitute for Medical Research, Camden, NJ; AG09799) originated from healthy, non-fetal human

tissue and is an accepted model for normal vascular endothelium [211-213]. When grown *in vitro,* non-confluent HAAE-1 cells are actively dividing, as opposed to a monolayer culture, and have been shown to externalize phosphatidylserine as in tumor vasculature [36, 37, 212]. The endothelial cells were subcultured to a maximum passage of six and maintained in a non-confluent state. F12K (ATCC; Manassas, VA; 30-2004) culture medium was supplemented with 10% FBS (Atlanta Biologicals, Flowery Branch, GA; S11150), 30 µg/ml endothelial cell growth supplement (Fisher Scientific; CB-4006B), 17.5 U/ml heparin (Polysciences, Inc., Warrington, PA; 01491-100), 100 U/ml penicillin, and 100 µg/ml streptomyocin (Atlanta Biologicals; B21210). Tissue culture treated plasticware were also precoated with 0.1% gelatin for 15 min prior to plating cells. Cell cultures were maintained at 37°C and 5% CO_2 until 70% confluence, at which point standard trypsinization subculture procedures were followed using a one to three split ratio.

MCF-7 Human Breast Cancer Cells

MCF-7 cells (ATCC; HTB-22) are estrogen receptor (ER) positive and human epidermal growth factor receptor 2 (HER-2) overexpression negative and are a part of the standard repertoire of models used in testing breast cancer therapeutics. MCF-7 cells were cultured and maintained in Eagle's Minimum Essential Medium (ATCC; 30-2003) supplemented with 10% FBS, 0.01 mg/ml insulin (Life Technologies; 12585-014), 100 U/ml penicillin, and 100 µg/ml streptomyocin at 37°C without CO_2. Subculturing was performed with standard trypsinization procedures with a subculture ratio of one to three once reaching 70% confluence.

MDA-MB-231 Human Triple-Negative Breast Cancer Cells

The MDA-MB-231 cell line (ATCC; HTB-26) is one of the most common models for human triple negative (ER negative, PR negative, HER-2 overexpression negative) breast cancers. This model has poor responsiveness to standard therapies and results in aggressive metastasis, representative of a poor prognosis breast cancer in patients [4, 178]. MDA-MB-231 cells were cultured and maintained in Leibovitz's L-15 medium (ATCC; 30-2008) supplemented with 10% FBS, 100 U/ml penicillin, and 100 µg/ml streptomyocin at 37°C without CO_2. Subculturing was performed with standard trypsinization procedures with a subculture ratio of one to three once reaching 70% confluence. Some applications required use of MDA-MB-231/GFP cells (Cell Biolabs, Inc., San Diego, CA; AKR-201) as specified.

4T1 Murine Triple-Negative Breast Cancer Cells

The 4T1 cell line is a triple-negative, highly metastatic, and poorly immunogenic murine model that is representative of advanced breast cancer in humans and derived from BALB/cJ mice [214, 215]. Pulmonary metastasis is the primary cause of death in 4T1 mouse models; however spontaneous metastasis to lymph nodes, blood, liver, lung, brain, and bone has also been observed [216-218]. A 4T1 orthotopic graft in BALB/cJ mice is recognized as one of the most challenging breast tumor models for immunotherapies [214, 219]. 4T1 cells (ATCC; CRL-2539) were cultured and maintained in RPMI-1640 medium supplemented with 10% FBS, 100 U/ml penicillin, and 100 µg/ml streptomyocin at 37°C and 5% CO_2. Subculturing was performed with

standard trypsinization procedures with a subculture ratio of one to four once reaching 80% confluence. Some applications required use of 4T1/TdTomato/Luciferase (gift of Dr. Rajagopal Ramesh Laboratory, University of Oklahoma Health Sciences Center, Oklahoma City, OK).

In Vitro Binding Studies

Binding Strength

Cells were grown in 24 well plates and fixed with 0.25% glutaraldehyde once 70-80% confluent. Cells were incubated for 2 h with biotinylated fusion protein then washed. See Appendix B: Laboratory Protocols for biotinylation protocol with SureLINK Chromophoric Biotin (KPL, Gaithersburg, MD; 86-00-03). Bound fusion protein was quantified by incubation with streptavidin-horseradish peroxidase (HRP) (KPL; 71-00-38), washed, incubated with the chromogenic substrate *O*-phenylenediamine (OPD) and hydrogen peroxide, and the absorbance measured at 450 nm on a BioTek Synergy HT microtiter plate reader (Winooski, VT). At each concentration of fusion protein, the specific binding was obtained by subtracting the non-specific binding (no $CaCl_2$ present, 5 mM EDTA added) from the total binding (2 mM $CaCl_2$ added). The dissociation constant was determined using a hyperbolic regression with GraphPad Prism software (GraphPad Software Inc., La Jolla, CA).

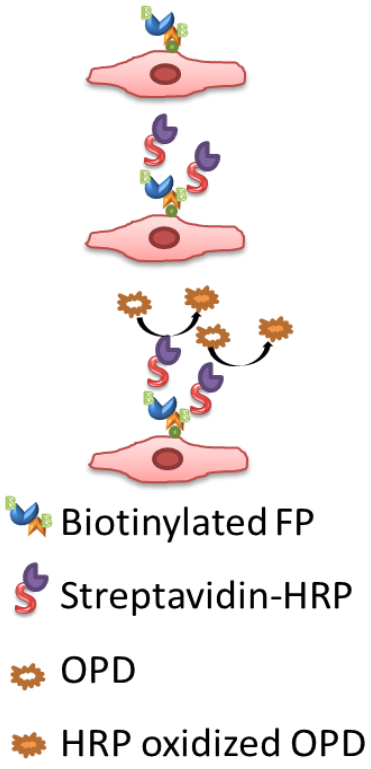

Figure 4. Schematic of fusion protein binding quantification.
Biotinylated fusion protein is incubated with cells and binds to phosphatidylserine on the external leaflet of the cellular membrane. Horseradish peroxidase, conjugated to streptavidin, localizes to the fusion protein through strong biotin-streptavidin binding. Horseradish peroxidase then catalyzes the development of chromogenic substrate OPD, which can then be measured at 450 nm.

Binding Stability

Cells were grown in 24 well plates to 70-80% confluence and incubated with fusion protein for 2 h then washed. On days 0, 1, 2, and 3 separate sets of cells were assessed for viability using an Alamar Blue assay as described in the cytotoxicity test methods and for bound protein. Quantification of bound fusion protein was performed using a chromogenic assay as described for evaluating binding strength.

Binding Visualization

Multiple microscopy methods were utilized for evaluation of fusion protein binding. Fixed cell microscopy involved growth of cells on a coverslip followed by glutaraldehyde fixation to preserve the cell morphology while allowing the exposure of membrane binding sites [220]. Cells were incubated with biotinylated fusion protein for 1 h at 37°C in growth medium with 2 mM supplemental Ca^{2+}. After washing, streptavidin-conjugated green Alexa Fluor 488 (Life Technologies; S-11223) was added to the cells at 5 µg/ml for 30 min in order to visual biotinylated fusion protein on the membrane surface (streptavidin does not internalize into formerly viable cells after fixation [221]). Cells were counterstained with 5 µg/ml Hoechst 33258 dye (Sigma-Aldrich; B2883) for nucleic acids for 30 min and with 1 µg/ml CellMask Deep Red plasma membrane stain (Life Technologies; C10046) using three 5 min incubations followed by washes. The coverslip was attached to the slide with fluoro-gel with TES buffer (Fisher Scientific). Slides were viewed immediately following preparation with a Leica Microsystems SP8 confocal laser scanning microscope (Leica Microsystems Inc., Buffalo Grove, IL) in both x-y and x-z planes at the Noble Microscopy Facility (University of Oklahoma, Norman, OK).

Live cell microscopy was performed with Dylight 680 (Thermo Scientific Pierce; 46418) labeled fusion protein (see Appendix B: Laboratory Protocols for conjugation protocol) to minimize phototoxic effects. Cells transfected to express fluorescent protein (MDA-MB-231/GFP or 4T1/TdTomato) were grown in 35 mm Corning petri dishes (Corning, Tokyo, Japan; 430165) in growth medium that does not require additional CO_2 (L-15 medium). Prior to imaging, the growth medium was

supplemented with 2 mM Ca^{2+} to allow fusion protein binding and 10 µg/ml Hoechst 33258, which is non-membrane permeable nucleic acid stain that acts as a marker for dead cells during live-cell imaging. The dish was then held at 37°C on the microscope with a Peltier Cooling stage and imaged prior to addition of protein. Cells were imaged with Leica's HyD detection system to allow use of low laser power to minimize phototoxic effects. Fusion protein was added to the samples and allowed to incubate for 2 h while continuing to obtain live images. Cells were then washed to remove unbound protein and live-imaging continued for 2 h.

In Vitro Cytotoxicity

Cytotoxicity assays were performed over 3 days (mCGL fusion proteins) or 6 days (PNP-AV) as one or two 3-day cycles in 24-well plates under standard culture conditions with calcium supplemented medium (2 mM Ca^{2+}). On the first day of each cycle (day 0, day 3) cells were incubated with 100 nM fusion protein for 2 h at 37°C. The plates were washed and medium containing varying concentrations of the prodrug, selenomethionine (Fisher Scientific; AC25996-0010) or fludarabine phosphate (VWR; 101095-016), was added. Controls of prodrug with no protein were included, as well as a control with the enzymatic product, 2-fluoroadenine (Fisher Scientific; 50-012-2249), for the PNP-AV study. The medium containing the prodrug or drug was replaced daily for the two subsequent days of each cycle. An Alamar Blue assay [222-224] was performed to determine viability on days 0, 2, 4, and 6 for the PNP-AV studies or on days 0, 1, 2, and 3 for the mCGL studies. Alamar Blue reagent (Life Technologies; DAL1100) was added at 10% to growth medium and incubated with cells for 4 h at

37°C. Fluorescence was measuring using a microtiter plate reader with an excitation wavelength of 530 nm and emission wavelength of 590 nm after the solutions had been transferred to an opaque 96-well plate.

In Vivo Tumor Models

All animal studies were performed in accordance with protocols approved by the Institutional Animal Care and Use Committee at the University of Oklahoma Health Sciences Center. Animals were housed in the Rodent Barrier Facility, a pathogen-free facility, at the University of Oklahoma Health Sciences Center and monitored daily.

MDA-MB-231 Implantation in SCID Mice

Six to eight week old female SCID mice (The Jackson Laboratory; Bar Harbor, ME; 001303) were injected with 6-8 x 10^6 MDA-MB-231/GFP cells per mouse subcutaneously in the flank [157] or 1-2 x 10^6 MDA-MB-231/GFP cells per mouse in mammary fat pad number four. Tumor locations are illustrated in Figure 5. Injections were performed with 25 G needles with 50% Matrigel (Fisher Scientific; CB-40234A) and 50% cell suspension in PBS for total volumes of 200 µL for flank injections and 100 µL for fat pad injections.

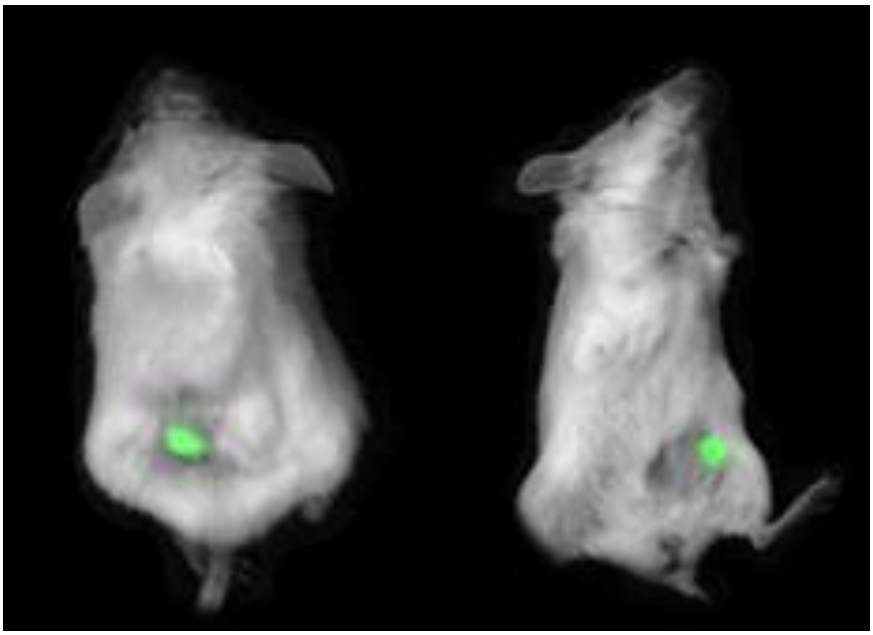

Figure 5. Placement of flank and fat pad tumor grafts.

4T1 Implantation in BALB/cJ Mice

Six to eight week old BALB/cJ mice (The Jackson Laboratory; 000651) were injected with 10^5 4T1/TdTomato/Luciferase cells in the fourth mammary fat pad as described by Lou *et al* [225]. Injections were performed as with the MDA-MB-231 fat pad model using 50% Matrigel and 50% cell suspension in PBS.

Non-terminal *In Vivo* Procedures and Follow-up Analysis

Mass and Tumor Volume

Mass and tumor volume were measured every 3 to 4 days through the duration of the studies. Volume was determined from the modified ellipsoid formula ($Volue = \frac{length * width^2}{2}$) [225] using caliper measurements of the longest axis for the length and the perpendicular measurement for width.

Fluorescence Live Animal Imaging

To perform live fluorescence imaging of mice bearing fluorescent tumors, mice were first anesthetized with isofluorane and maintained under anesthesia for the duration of imaging. An IVIS Spectrum (Perkin Elmer, Waltham, MA) imaging system from the Molecular Imaging Core at the Stephenson Cancer Center of the University of Oklahoma Health Sciences Center collected images. Perkin Elmer software performed spectral unmixing of the tumor fluorescence from tissue fluorescence and overlaid the data on images of the mice.

Antibody Titer

Protein specific antibody titers were determined based on modified protocols from [226-228]. Blood samples were collected from mice at 0, 1, 2, and 3 weeks of treatment. Approximately 150 µL of blood were collected in 3 drops from submandibular bleeds, and plasma was isolated using capiject collection tubes (VWR; TETMG) with centrifugation at 3500 x *g* for 90 s and stored at -80°C.

A sandwich ELISA assay was performed to determine protein specific antibody titers. A 0.1 M carbonate coating buffer and 20 µg/mL fusion protein were incubated overnight at 4°C on high binding capacity ELISA 96 well plates (VWR; 82050-740). Plates were then washed and blocked with fetal bovine serum and plasma dilutions were incubated overnight at 4°C. Following additional washes, goat anti-mouse IgG and IgM conjugated to HRP (Jackson ImmunoResearch Laboratories, Inc., West Grove, PA; 315-035-044) was used to develop OPD as described in the *in vitro* binding assays. Antibody titers are presented as the greatest dilution that produces a positive result.

Terminal *In Vivo* Procedures and Follow-up Analysis

Fusion Protein Clearance

Fusion protein was biotinylated and administered by intraperitoneal (IP) injection into mice at 10 mg/kg IP in PBS. The biotinylation protocol is detailed in Appendix B: Laboratory Protocols. At appropriate time intervals between 0 and 24 h post injection, three to four mice per time point were euthanized and blood collected through cardiac draw. A capiject blood collection vial was used to isolate plasma with centrifugation at 3500 x *g* for 90 s and stored in cryovials at -80°C. Control mice at time point 0 h were not injected with protein.

An ELISA assay was used to determine fusion protein concentration in the plasma. A calibration curve using biotinylated protein was constructed with each assay. Plasma samples were incubated in wells of a streptavidin-coated 96 well plate (Thermo Scientific Pierce; 15500) to bind biotinylated fusion protein in the samples. After washing the plates, rabbit polyclonal anti-annexin V antibody (Abcam, Cambridge, MA; ab14196) was added and incubated for 1 h at 37°C. After further washes, anti-rabbit IgG conjugated to HRP (Jackson ImmunoResearch Laboratories, Inc.; 111-035-003) was incubated for 1 h at 37°C. Following additional wash steps, OPD development and absorbance at 450 nm allowed quantification of bound fusion protein.

Measurement of Metastatic Nodules in Lungs

Immediately following euthanasia, mice were dissected using standard procedure and organs were removed. Organs were placed on ice and stored at -80°C. A Leica stereomicroscope was used to obtain light and fluorescence images of the organs.

An automated image processed macro was developed for ImageJ to remove background fluorescence and quantify fluorescent nodules in the lung, recording number and size. User input was required for thresholding purposes of each image. The macro code is available in Appendix B: Laboratory Protocols.

Tumor Section Immunohistochemistry

Immediately following euthanasia, mice were dissected using standard procedure and organs and tumor were removed. The tumor was placed in 10% neutral buffered formalin and fixed for 24 h at room temperature. Tumors were then sliced to appropriate size and oriented in cassettes for paraffin embedding and fixation by the Tissue Pathology Core of the Stephenson Cancer Center at the University of Oklahoma Health Sciences Center. Hematoxylin and eosin (H + E) stained sections were produced by the Tissue Pathology Core for evaluation of histology and tumor necrosis. Slides were viewed on a Nikon Eclipse E800 compound microscope (Nikon Corporation, Tokyo, Japan) and whole slide images were collected with a Leica stereomicroscope at the Noble Microscopy Facility (University of Oklahoma). Necrotic sections were quantified with ImageJ.

Immunohistochemistry slides were produced using DAB staining for activated caspase-3, ki-67, and HIF-1α with hematoxylin counter staining. Details of the antibodies and staining procedure are included in Table 6. Tumor sections for activated caspase-3 and ki-67 staining were imaged at 20X using a Nikon Eclipse E800 microscope collecting 15 images per section from the non-necrotic portion of the tumor. An automated ImageJ macro was developed for quantification of DAB staining. A

color deconvolution was used to separate the hematoxylin and DAB stains, and cells were counted as DAB positive or DAB negative. User input was required for each image for thresholding purposes. ImageJ macro code is available in Appendix B: Laboratory Protocols with the process outlined in Figure 6. HIF-1α images were collected with a Leica stereomicroscope to capture the entire tumor section in a single image, as the HIF-1α staining was more disperse than the other stains. Instead, HIF-1α was quantified as a percentage of tumor area expressing HIF-1α using the same color deconvolution method previously described. A median filter was applied to the whole section images to reduce noise without affecting the boundaries of the regional staining. The HIF-1α image processing scheme is outlined in Figure 7. The antibody details and staining conditions utilized in the immunohistochemistry studies are displayed in Table 6.

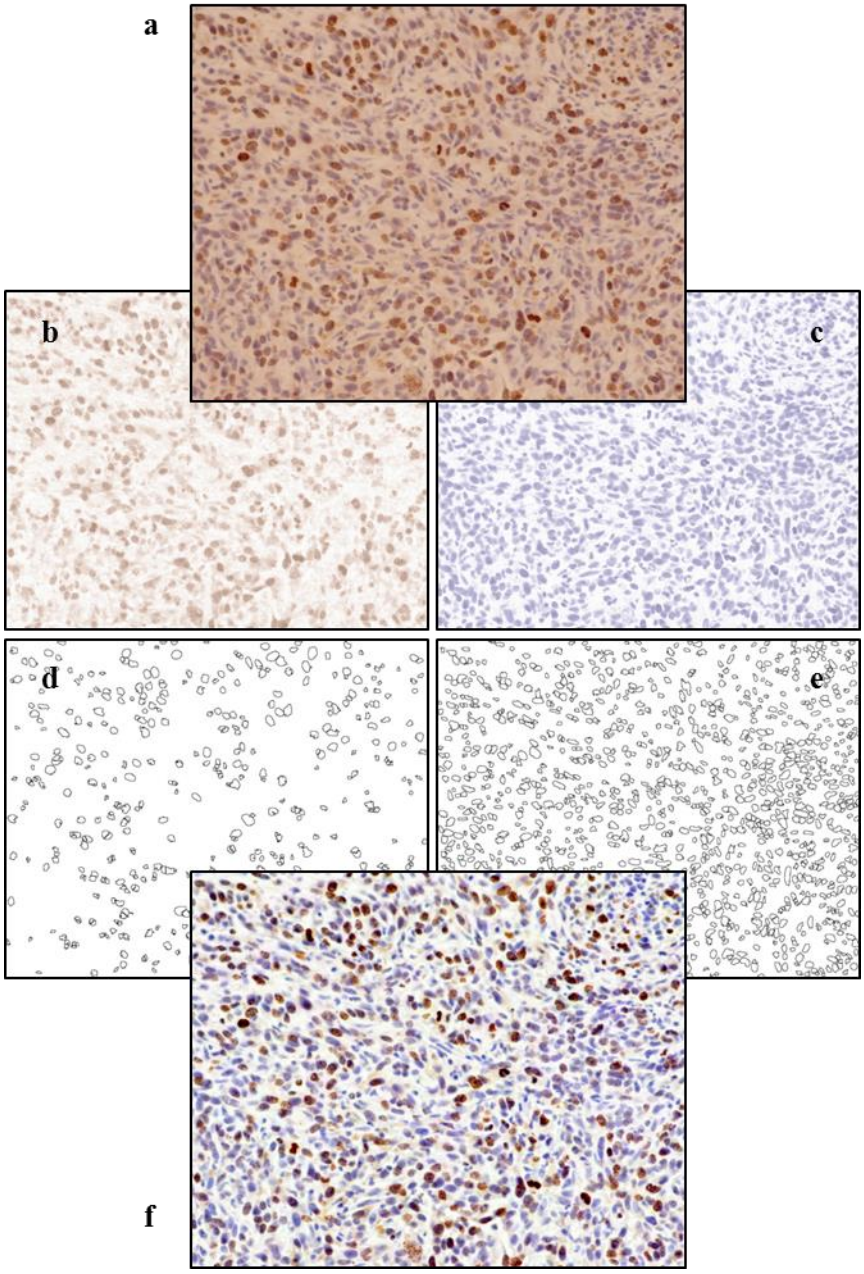

Figure 6. Outline of process for automated quantification of DAB staining of tumor sections with activated caspase-3 and ki-67.
A hematoxylin and DAB stained image is input (a) into the ImageJ macro, background is subtracted, and color deconvolution is performed resulting in a DAB (b) and hematoxylin (c) image. User thresholding is used to generate a mask for each image, and then cell counting is performed with each DAB (d) and hematoxylin (e) stained cell outlined. An overlay of stained regions outlined and counted is shown (f) for comparison to original input image.

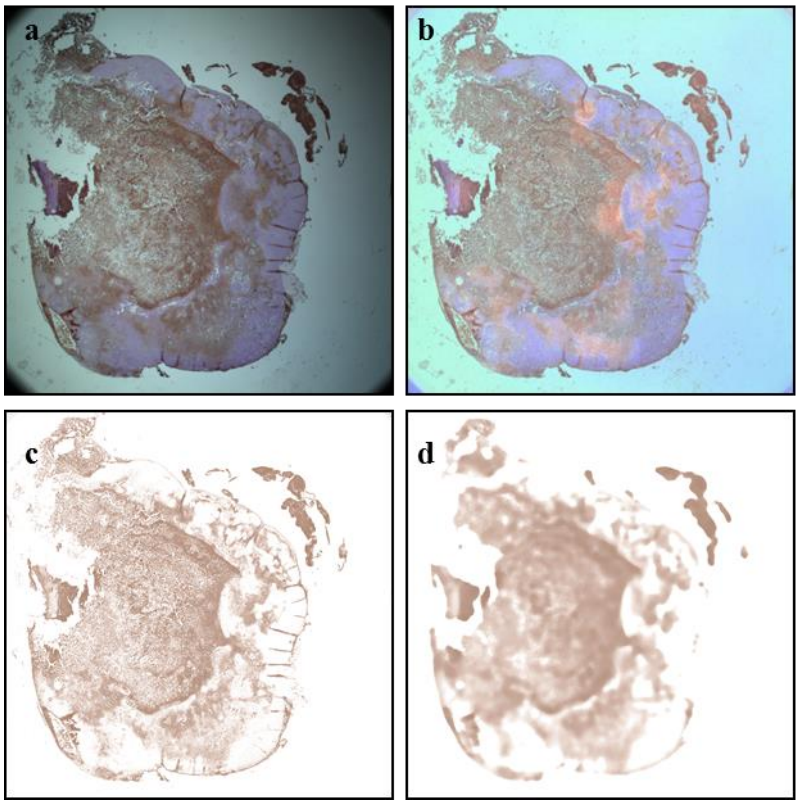

Figure 7. Outline of process for quantification of DAB staining of tumor sections with HIF-1α.
Whole tumor section images were obtained on a Leica stereomicroscope. The DAB image with hematoxylin counterstain (a) undergoes background subtraction (b), and then color deconvolution to isolate DAB signal (c). A median filter is applied to remove noise without blurring the boundary of the stained region (d).

Table 6. Immunohistochemistry antibody staining details

Target	Type	Source	Catalog	Concentration	Epitope Retrieval
Ki-67	Rabbit polyclonal	Abcam	Ab115580	5 µg/mL (1/200)	Heat mediated, pH 6
Activated caspase-3	Rabbit polyclonal	Abcam	Ab2302	0.8 µg/mL (1/250)	Heat mediated, pH 6
HIF-1α	Rabbit polyclonal	Abcam	Ab82832	4 µg/mL (1/250)	Heat mediated, pH 6
CD-31	Rabbit polyclonal	Abcam	Ab28364	(1/50)	Heat mediated, pH 6

Quantification of Regulatory T Cells in Spleen

Immediately following euthanasia, mice were dissected using standard procedures and organs were removed. Cells of the spleen were mechanically dissociated from the organ in FACS buffer and passed through a 70 µm cell strainer (VWR; 10054-456) to obtain single cell suspensions.

A mouse regulatory T cell staining kit (eBioscience, Inc., San Diego, CA; 88-8111) was used to stain splenocytes for flow cytometry according to manufacturer instructions. A BD Accuri C6 flow cytometer (BD Biosciences, San Jose, CA) was used for data acquisition and analysis. The detailed staining protocol is available in Appendix B: Laboratory Protocols. Cells were first blocked, then stained for CD4 and CD25, and then fixed and permeabilized for intracellular staining of FoxP3. CD4+ CD25+ Foxp3+ cells were considered to be regulatory T cells and quantified as a percentage of total spleen lymphocytes [229-231].

Statistical Analysis

Results are expressed as mean ± standard error (SE). Statistical significance of cytotoxicities, tumor volumes, and section staining was assessed using a one-way ANOVA and Tukey-Kramer multiple comparisons test with GraphPad Prism software.

Assessment for synergism of combination therapies was performed using the Bliss independence model on primary tumor growth inhibition [232, 233]. The probability of additivity of the measured percent inhibition of the individual constituents was subtracted from the measured percent inhibition of the combination therapy undergoing analysis for synergism. For example, to evaluate the synergism of

mCGL combined with selenomethionine, the predicted inhibition was calculated using probability theory as the product of the inhibition of the mCGL group alone and the selenomethionine group alone, subtracted from the sum of the two inhibitions. The predicted inhibition is subtracted from the inhibition exhibited by the group treated with mCGL and selenomethionine together. Positive values are indicative of synergism.

Statistical significance for survival was assessed based on Kaplan Meier survival curves using the log-rank (Mantel-Haenszel) test with a 0.05 significance level corrected for family-wise significance based on the number of comparisons according to the Bonferroni corrected threshold (significance level/number of comparisons).

Chapter III: Results and Discussion

Cytosine Deaminase and 5-Fluorocytosine

In Vivo CD-AV Plasma Clearance

Prior to conducting a study to evaluate the efficacy of the CD-AV system *in vivo*, plasma levels of the CD-AV fusion protein were evaluated to ensure that the protein would be cleared from circulation before administration of the prodrug (5-FC). It is necessary for complete clearance of the enzyme from circulation prior to prodrug administration to eliminate off-target activation of the prodrug, as generation of 5-FU in the general circulation could produce negative effects and renders the idea of a targeted enzyme prodrug system ineffective. Blood drawn at various time points and measured for CD-AV indicate complete clearance from circulation within 8 hours of administration, shown in Figure 8. The clearance data suggests that prodrug administration could occur as early as 8 h post fusion protein injection.

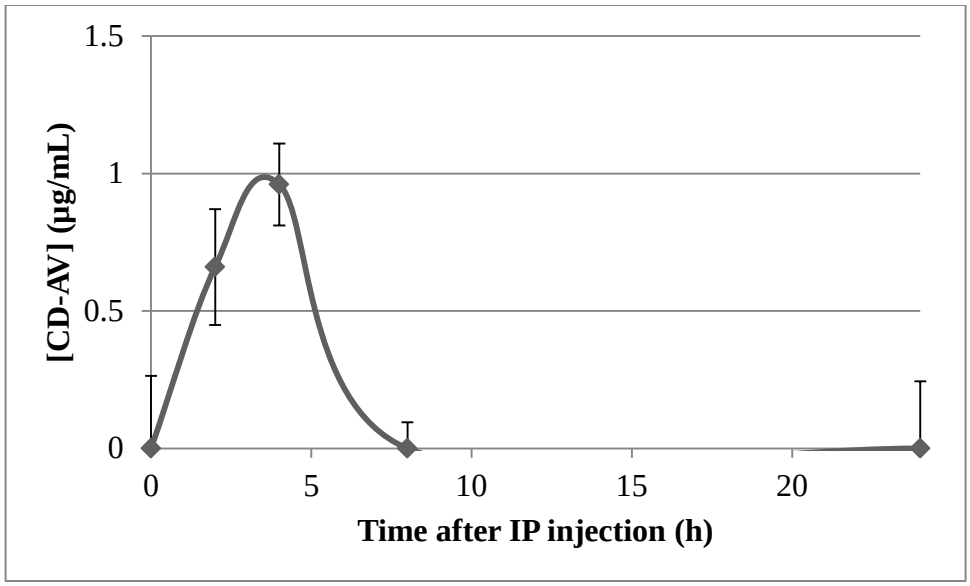

Figure 8. CD-AV clears from the circulation of SCID mice in <8 h.
An ELISA assay for CD-AV was performed on serum samples at intervals following administration of CD-AV at 10 mg/kg IP. Data is presented as mean ± standard error (n = 3).

Evaluation of CD-AV System In Vivo

The volume of subcutaneous MDA-MB-231 tumors grown on the flank of SCID mice was the primary means for the evaluation of efficacy of the CD-AV and 5-FC enzyme prodrug system in vivo. Four consecutive cycled treatments, one day of fusion protein administration followed by three days of prodrug administration, were conducted in an effort to replicate successful in vitro cytotoxicity experiments using the same scheme [37]. Unfortunately in contrast to the in vitro work with MDA-MB-231 cells, the CD-AV enzyme prodrug system had negligible effects on tumor volume in SCID mice, shown in Figure 9. As expected, the CD-AV system did not produce any negative side effects in the mice or result in any weight loss over the duration of the study, shown in Figure 10.

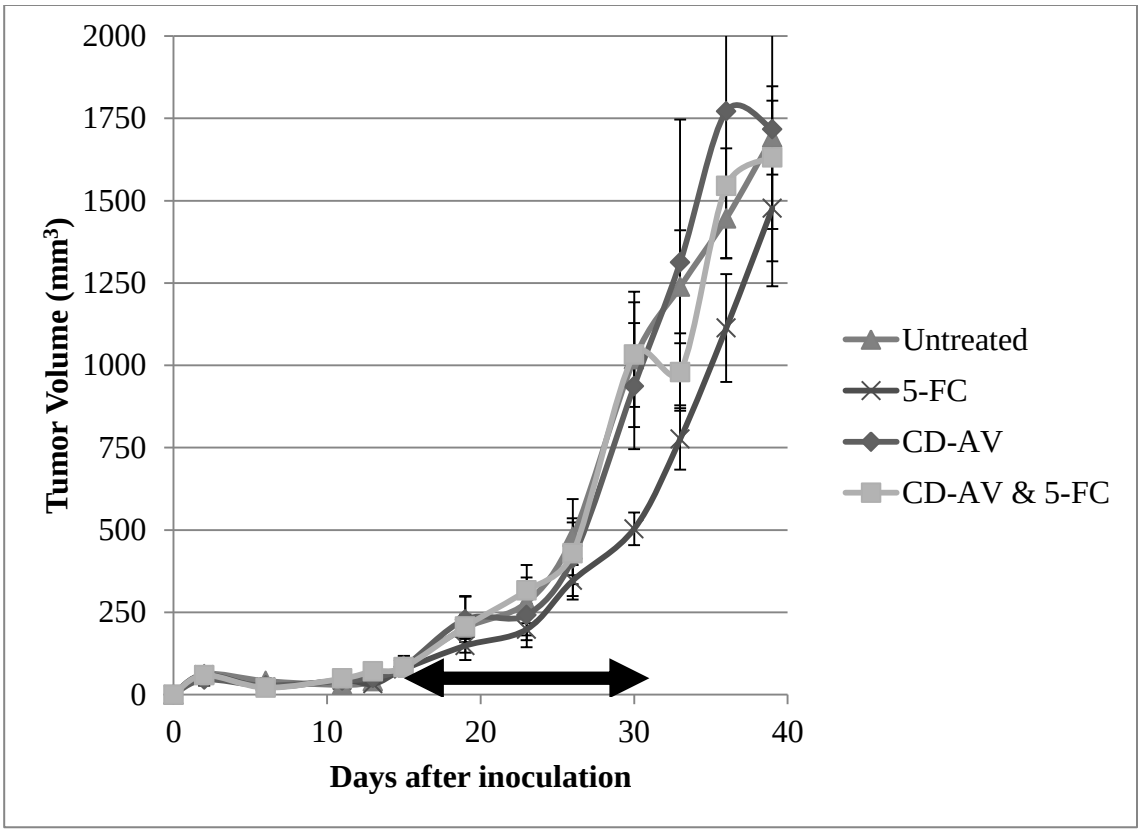

Figure 9. Poor efficacy of CD-AV and 5-FC against MDA-MB-231 tumors on the flank of SCID mice.
CD-AV was administered every 4 days (10 mg/kg IP) with 5-FC administered (500 mg/kg IP) each of the subsequent 3 days of the cycle for 4 cycles. Treatment period is indicated by the arrow. Data is presented as mean ± standard error (n = 6-7). No statistical significance was observed.

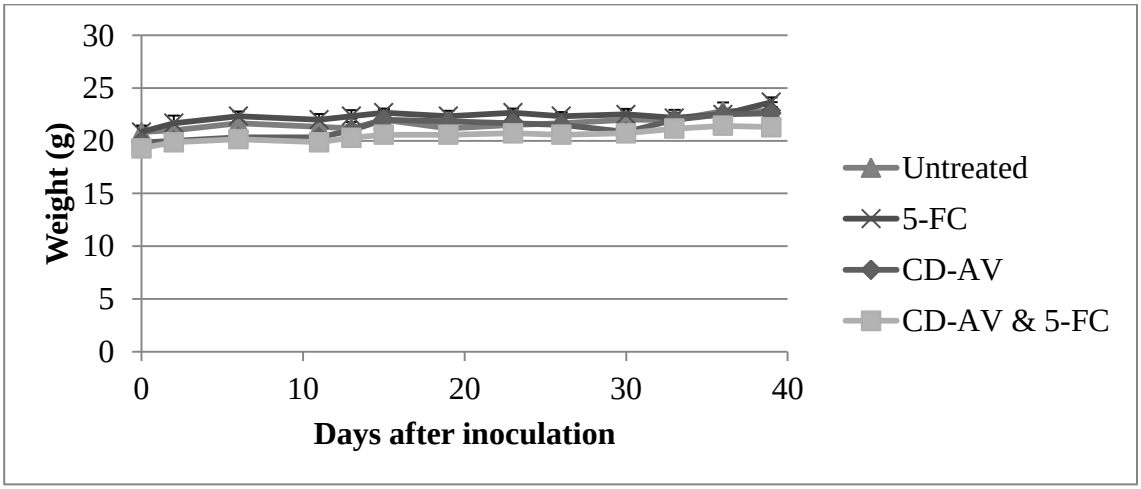

Figure 10. Minimal effect of CD-AV system on mouse weight.

The experimental design of the CD-AV *in vivo* studies aimed to follow up *in vitro* studies and allow for comparison among the three enzyme prodrug systems, CD-AV, PNP-AV, and Met-AV. Certain aspects of the *in vitro* work are not directly translatable to *in vivo* studies in mice, specifically the dosing of the fusion protein and prodrug. Fusion protein dosing of 10 mg/kg was selected based on plasma clearance tests that suggest saturating levels of fusion protein enter the blood stream and are cleared in a reasonable time frame and with no apparent side effects. A study previously performed by our research group also evaluated plasma levels of fusion protein (Met-AV) at 1 mg/kg, which yielded plasma levels an order of magnitude below those observed at a dose of 10 mg/kg. The 5-FC dose of 500 mg/kg was selected based on other enzyme prodrug evaluations [55] and a known LD_{50} of >1000 mg/kg [234].

A comparable study with the Met-AV system using the same MDA-MB-231 tumor model on the flank of SCID mice and using the same dosing scheme with a single fusion protein administration followed by three days of prodrug injections yielded much more promising results [157]. After only three treatment cycles with the Met-AV system, tumor growth was inhibited by 84%; whereas the CD-AV system achieved 0% tumor growth inhibition after three and four treatment cycles (see Figure 9).

Further optimization of the enzyme prodrug system may enhance therapeutic efficacy; however *in vitro* cytotoxicity results suggest that while the CD-AV system can be successful, other systems are likely to have a stronger antitumor effect. The *in vitro* cytotoxicity of the CD-AV system achieved acceptable cancer cell viability reductions following 9 days of treatment, as opposed to 6 days and 3 days for the PNP-AV and Met-AV systems, respectively [37, 210]. Similar *in vitro* efficacy against MDA-MB-

231 cells and MCF-7 cells suggests that poor *in vivo* results is unlikely a cell dependent issue and possibly a function of the required duration of treatment time and 5-FU concentrations necessary to achieve cell death. Death through achievable levels of the generated drug, 5-FU, may simply be too slow to produce a beneficial effect *in vivo*. Additionally, the primary *in vivo* mechanism of action is suspected to act more directly on the tumor endothelium (supported by the *in vivo* data of Van Rite et al. using the Met-AV system [157]) and *in vitro* results show that effect on endothelial cell viability is less significant than the treatment on MCF-7 or MDA-MB-231 cells. This therapy could possibly be more effective if the fusion protein and prodrug were injected daily, more than 8 hours apart. Other delivery mechanisms of cytosine deaminase for enzyme prodrug treatment utilizing either gene directed or cell directed strategies may allow for greater accumulation of protein and hence greater accumulation of 5-FU, rendering those strategies more effective in the case of this particular system *in vivo* [235, 236].

The primary objective for the *in vivo* evaluation of the CD-AV system was to obtain comparative results to allow for selection of one of the three systems for optimization and transition to immune competent models. An alternative dosing schedule may have been more successful; however given the success of Met-AV and selenomethionine with a similar dosing schedule [157], we opted out of further *in vivo* testing of CD-AV.

Summary of CD-AV System

The CD-AV and 5-fluorocytosine enzyme prodrug system failed to produce a therapeutic effect in SCID mice bearing MDA-MB-231 tumors, despite promising *in*

vitro work. Further optimization of the system could certainly enhance results; however pre-existing data for the Met-AV enzyme prodrug system suggest that the CD-AV system would be unlikely to surpass the efficacy of the other systems *in vivo*. Lack of any comparable *in vivo* effect eliminated the CD-AV system as a candidate for further work to transition to a non-immunogenic system.

Purine Nucleoside Phosphorylase and Fludarabine

Fusion Protein Construction, Expression, and Purification

The PNP-AV fusion gene was successfully constructed into an expression plasmid (pET303/CT-His) bearing ampicillin/carbenicillin resistance, as confirmed through sequencing. Protein modeling was utilized in the design of the fusion gene, as previous efforts yielded poor results suspected to be related to the orientation of the protein chains and purification tag. Examination of PNP subunit termini, shown in Figure 11, suggests that fusion to the exposed C-termini of the subunit may have less structural impact than N-terminal fusions. Additionally, previous success with fusion to the N-terminal of AV [36, 37] supported gene construction utilizing the following orientation (written N to C): PNP – linker – AV – HRV-3C protease site – 6X His-tag. Additional modeling of the PNP-AV fusion is shown in Figure 12. Incorporation of a flexible glycine-serine ($[GS]_3$) linker between the PNP and AV genes is standard in protein fusions to maximize appropriate folding of proteins and for maintenance of bioactivity of the two fusion components.

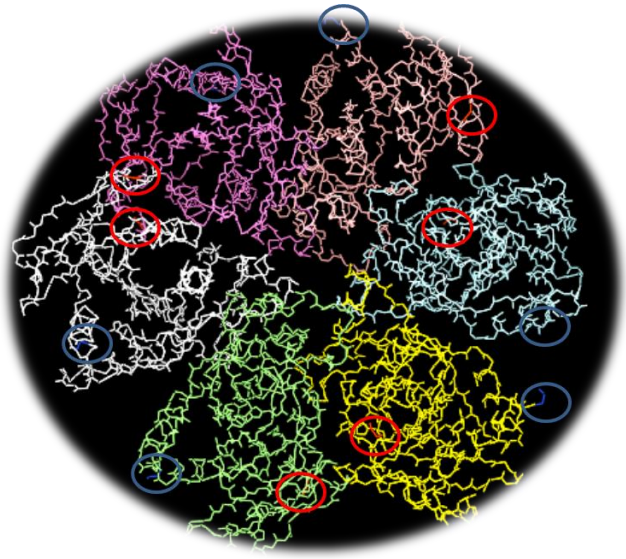

Figure 11. PNP hexamer model with highlighted terminals.
The PyMOL Molecular Graphics System (version 1.2r3pre; Schrödinger, LLC) generated an image of a PNP hexamer using crystal structure data files obtained through the Protein Data Bank Europe. C-termini of each subunit were highlighted and circled in blue and N-termini were highlighted and circled in red.

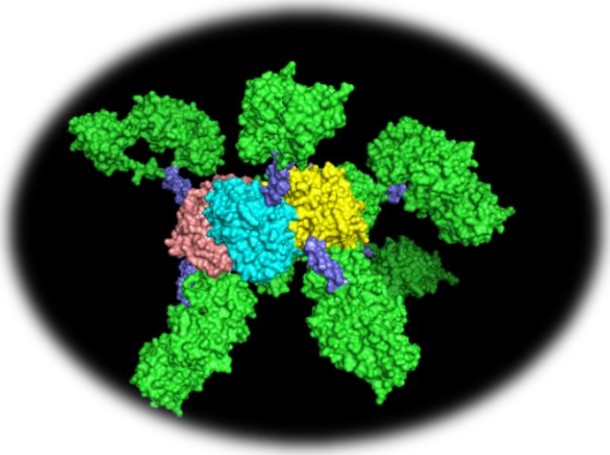

Figure 12. PNP-AV protein model.
The PyMOL Molecular Graphics System (version 1.2r3pre; Schrödinger, LLC) generated a mesh image of a model PNP-AV hexamer using data files obtained through the Protein Data Bank Europe.

The purification process regularly yields in excess of 60 mg purified PNP-AV per liter of culture. The PNP-AV monomers were confirmed with SDS-PAGE, shown in Figure 13, to be approximately 65 kDa as expected based on the known monomeric

PNP size of 26 kDa [237, 238], AV size of 36 kDa, and amino acid linker size of 3 kDa. Densitometric analysis of SDS-PAGE results determined a purity of >93%.

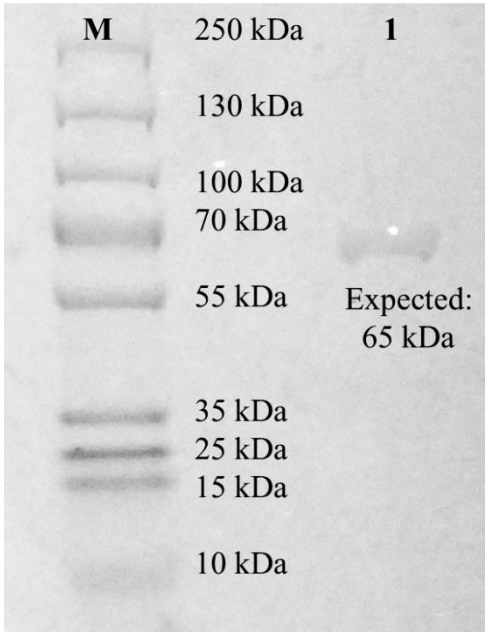

Figure 13. SDS-PAGE of purified PNP-AV indicates >90% purity.
M, marker proteins; lane 1, purified PNP-AV.

Enzymatic activity of PNP-AV was determined to be 35 U/mg PNP-AV. The kinetic absorbance measurements of the enzymatic reaction are shown in Figure 14. A specific activity of PNP-AV of 35 U/mg corresponds to a PNP specific activity of 87.5 U/mg when accounting only for the PNP portion of the fusion. Recombinant PNP production in other studies has yielded enzyme activities between 27 and 180 U/mg [68].

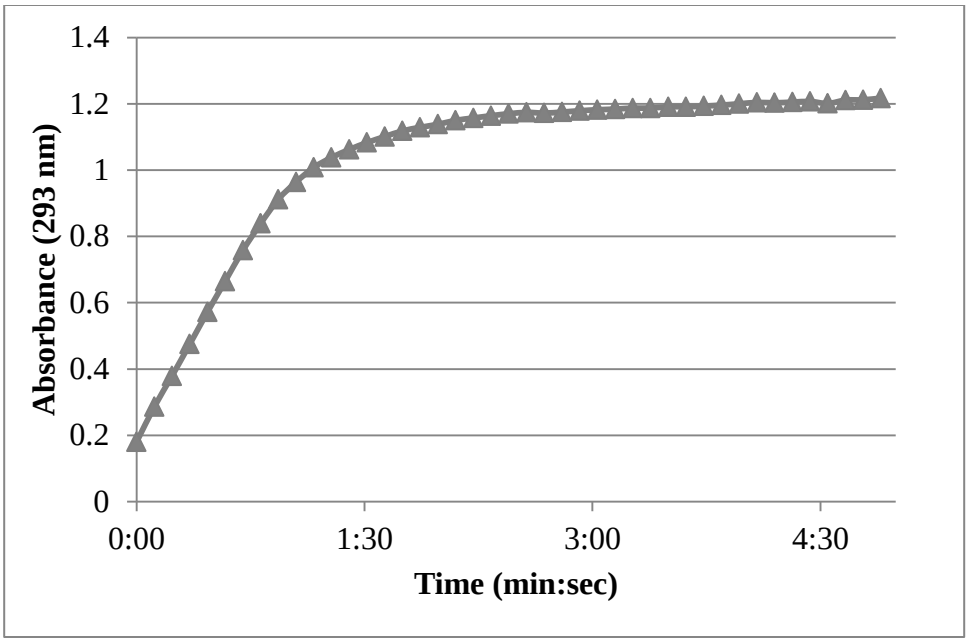

Figure 14. PNP-AV enzyme assay kinetic absorbance measurements over 5 min.

Acceptable yields, purity, and enzyme activity were obtained with PNP-AV, allowing for further characterization and potential therapeutic efficacy using *in vitro* models.

In Vitro Binding

Using the calcium dependent nature of specific AV binding to phosphatidylserine, total, nonspecific, and specific binding curves were obtained on non-confluent HAAE-1, MCF-7, and MDA-MB-231 cells. Removal of calcium from the medium, using the chelator EDTA, allows for the quantification of only nonspecific protein binding. Subtracting the nonspecific binding from the total binding in medium containing calcium allows for the quantification of the specific binding of AV to phosphatidylserine. Dissociation constants were calculated from the hyperbolic

regression of the binding curves (data can be found in Figure 58, Figure 59, and Figure 60 of Appendix A: Supplemental Data) and is summarized in Table 7.

Table 7. Dissociation constant of PNP-AV binding to cells.

Cell Line	Dissociation Constant (K_d) ± standard error (n = 3)
HAAE-1	18.3 pM ± 16.4 pM
MCF-7	51.6 pM ± 18.0 pM
MDA-MB-231	75.3 pM ± 52.3 pM

PNP-AV binding to non-confluent endothelial cells and MCF-7 and MDA-MB-231 breast cancer cells was determined to be relatively strong, with all dissociation constants in the picomolar range. In fact, the dissociation constants were determined to be stronger for PNP-AV than the other annexin targeted enzymes Met and CD, which both had dissociation constants for the same cell lines in the nanomolar range [36, 37]. Enhanced binding of the PNP-AV system over Met-AV and CD-AV is likely a function of avidity (binding of a complex, enhanced with multiple binding sites) rather than improved affinity (binding interactions at a single site) as the AV protein is identical with each system and the hexameric PNP-AV has six AV per molecule as opposed to four AV for Met-AV and two AV for CD-AV. The additional AV present on the PNP-AV molecule increase the number of binding sites per molecule, increasing the capacity to bind to phosphatidylserine compared to Met-AV and CD-AV and lowering the dissociation constant values.

An analysis of binding stability of PNP-AV on endothelial cells and breast cancer cells, shown in Figure 15, confirms presence of protein on cells after 3 days as seen with the CD-AV and Met-AV fusion proteins [36, 37]. Presented as a percentage

of the amount of protein bound to the cells on day 0, there is an expected drop over time.

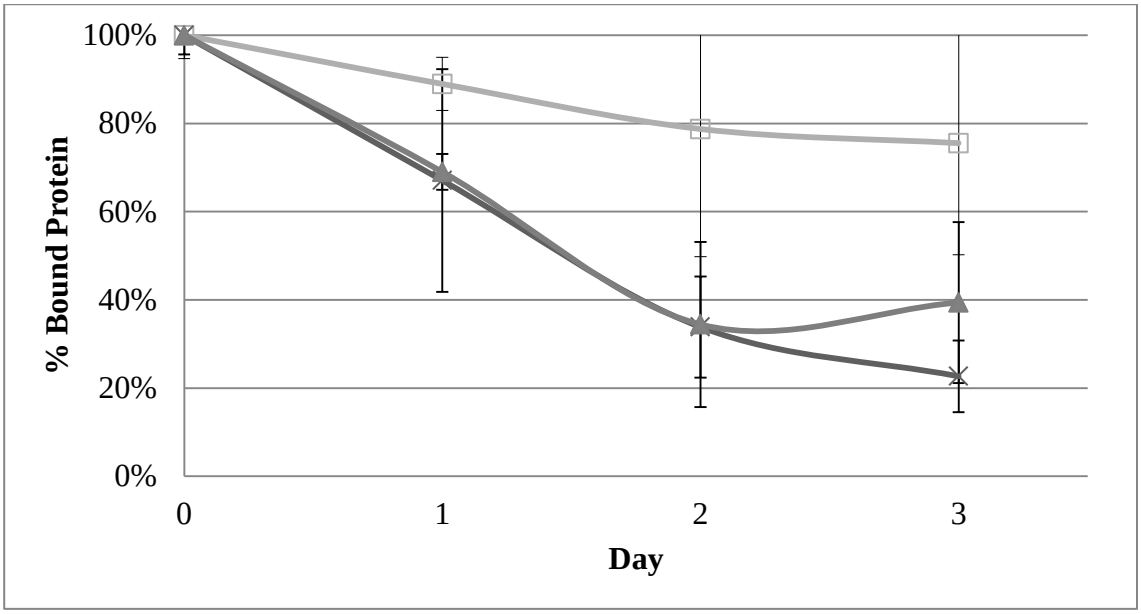

Figure 15. Binding stability data for PNP-AV.
Biotinylated PNP-AV was incubated with cells for 2 h at 37°C and excess was washed away. For three days binding on different cell types was quantified with streptavidin conjugated peroxidase. (□), non-confluent HAAE-1; (▲), MDA-MB-231; and (x) MCF-7 cells. Data is presented as a percentage of fusion protein present immediately after the initial wash and is shown as mean ± standard error (n = 3).

Confocal microscopy confirms that the fusion protein is bound to the cell membrane but does not continuously cover the membrane, shown in Figure 16. Discontinuous exposure of phosphatidylserine has been observed by other studies specifically with MDA-MB-231 breast cancer cells and is expected, as externalized phosphatidylserine exists primarily in patches of lipid rafts [138, 239]. Epifluorescence microscopic approaches have also confirmed cellular association of AV fusion proteins; however our confocal approach utilizes secondary staining with a streptavidin conjugated fluorophore to allow detection of only fusion protein exposed on the cell surface. Presence of PNP-AV on the external surface of the cells is vital to the success

of the enzyme prodrug therapy as the prodrug fludarabine requires transporters to move it across the cell membrane whereas the drug, 5-fluoroadenine, is freely diffusible across the membrane, seen in Figure 2.

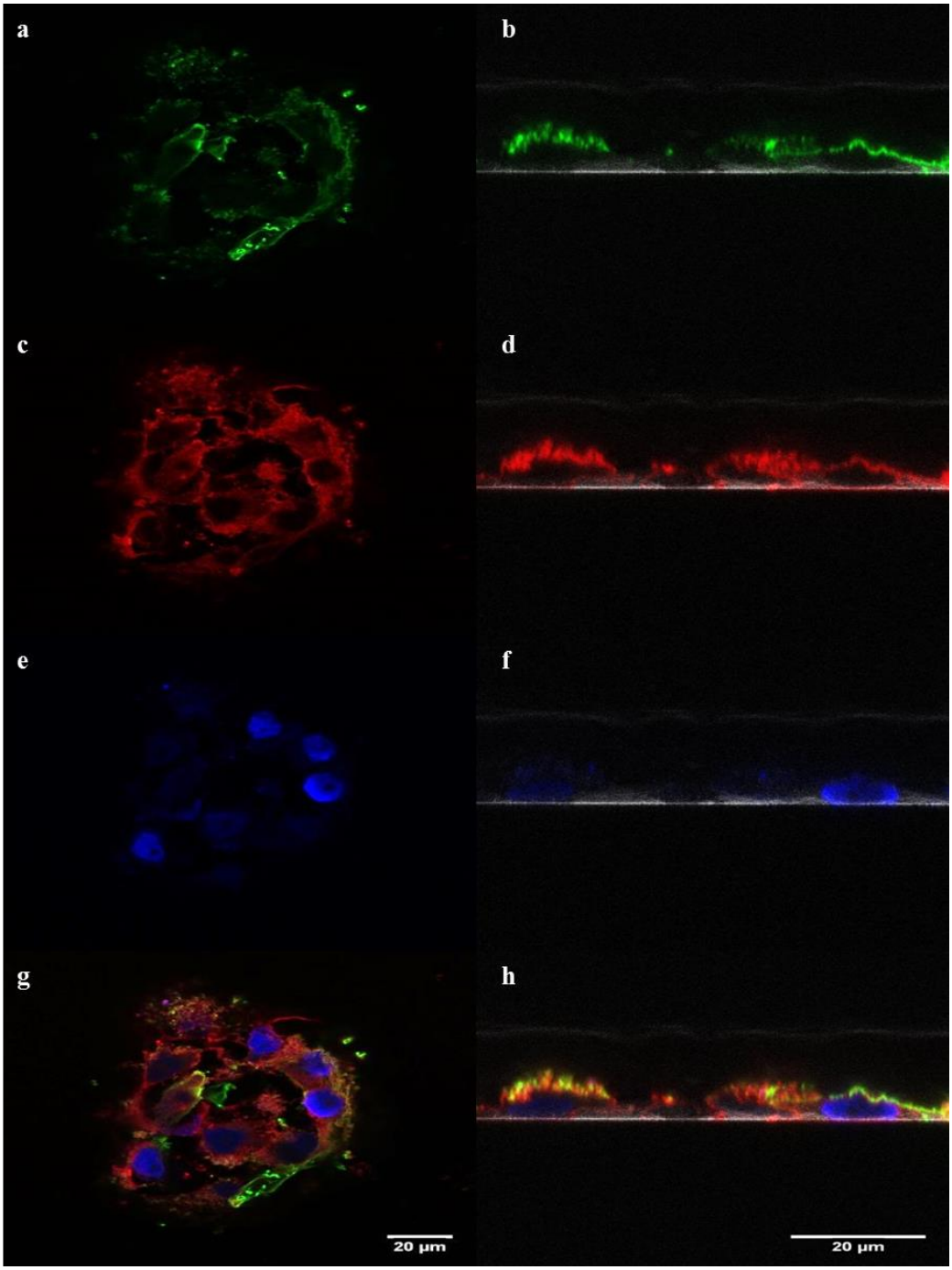

Figure 16. Fixed cell confocal imaging of PNP-AV binding.
Confocal microscopy of MCF-7 cells confirms the presence of externally bound biotinylated PNP-AV, with streptavidin-conjugated Alexa Fluor 488 in green (a, b), red CellMask plasma membrane stain (c, d), and blue Hoechst 33258 nucleic acid stain (e, f). Images a, c, and e show the color channels of an x-y confocal image with the composite shown in g. Images b, d, and f show the color channels of an x-z cross-section of cells with the composite shown in h and the coverslip indicated by the white in each image. Images were obtained on a Leica SP8 scanning confocal microscope.

In Vitro Cytotoxicity

Cytotoxicity studies indicate a significant cytotoxic effect of the PNP-AV enzyme prodrug system on breast cancer cell lines MCF-7 and MDA-MB-231 and endothelial cells representative of the tumor vasculature, non-confluent HAAE-1. Cell viability over two treatment cycles, each with a duration of 3 days, is shown for the three cell lines in Figure 17, Figure 18, and Figure 19. A 6-day incubation period is clearly relevant for the enzyme prodrug treatment for all three cell lines tested, since the cell viability declined after each 2-day interval in every case. The enzyme prodrug treatment was particularly effective for the MCF-7 cancer cells and the non-confluent endothelial cells, where greater than 95% cytotoxicity was obtained after 6 days of treatment. The lack of significant effect on confluent endothelial cells, Figure 20, is a further indication that no binding of the fusion protein had occurred and that confluent endothelial cells are representative of the normal vasculature.

The *in vitro* cytotoxic effect of fludarabine alone on breast cancer cells confirms work in another study that found significant cell killing between 2.5 and 10 μM fludarabine, particularly with the MCF-7 cell line [58]. This effect could potentially result from active transport across the cell membrane and an increased capacity to retain nucleoside analogue triphosphates in tumor cells and is not of significant concern for further testing as the same effect is not observed in confluent HAAE-1 cells, which are representative of normal vasculature [240]. These findings are not surprising given that fludarabine has undergone clinical evaluation as a chemotherapeutic agent for solid tumors.

The presence of PNP-AV does provide enhanced cell killing over fludarabine alone as expected since the conversion of fludarabine to 2-fluoroadenine increases the compound's toxicity, affecting dividing and non-dividing cells and allowing for a bystander killing effect due to free diffusion across cell membranes [65]. Fludarabine alone is clinically limited as a result of dose dependent myelosuppression, so enhancement of the cytotoxic effect only at the site of the tumor using PNP-AV could potentially enhance fludarabine efficacy and reduce the necessary therapeutic dose if evaluated in clinical trials.

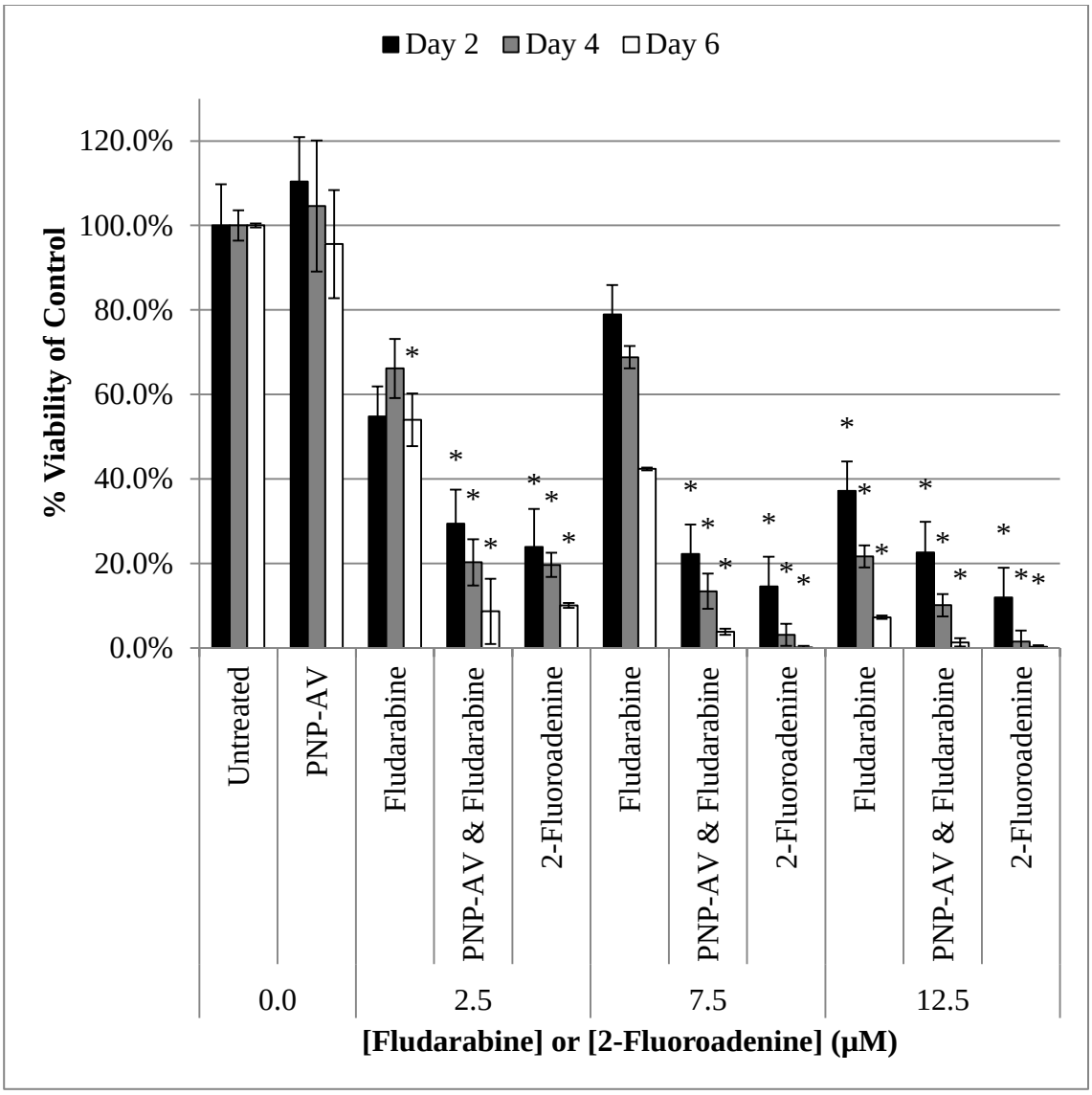

Figure 17. Cytotoxic effect of PNP-AV enzyme prodrug therapy on non-confluent HAAE-1 cells.

The effects of fludarabine, 2-fluoroadenine, and fludarabine converted to 2-fluoroadenine by PNP are shown. Groups that received PNP-AV were treated on days 0 and 3 of the study. Fludarabine and 2-fluoroadenine were administered daily. Viability was determined by the Alamar Blue assay on days 2, 4, and 6 (black, gray, and white bars, respectively), and each sample was represented as a percentage of untreated control on each day. Statistical analysis was performed with a one-way ANOVA test with data presented as mean ± standard error (n = 3). Statistical significance vs. untreated control on the same day is denoted by *($p < 0.001$).

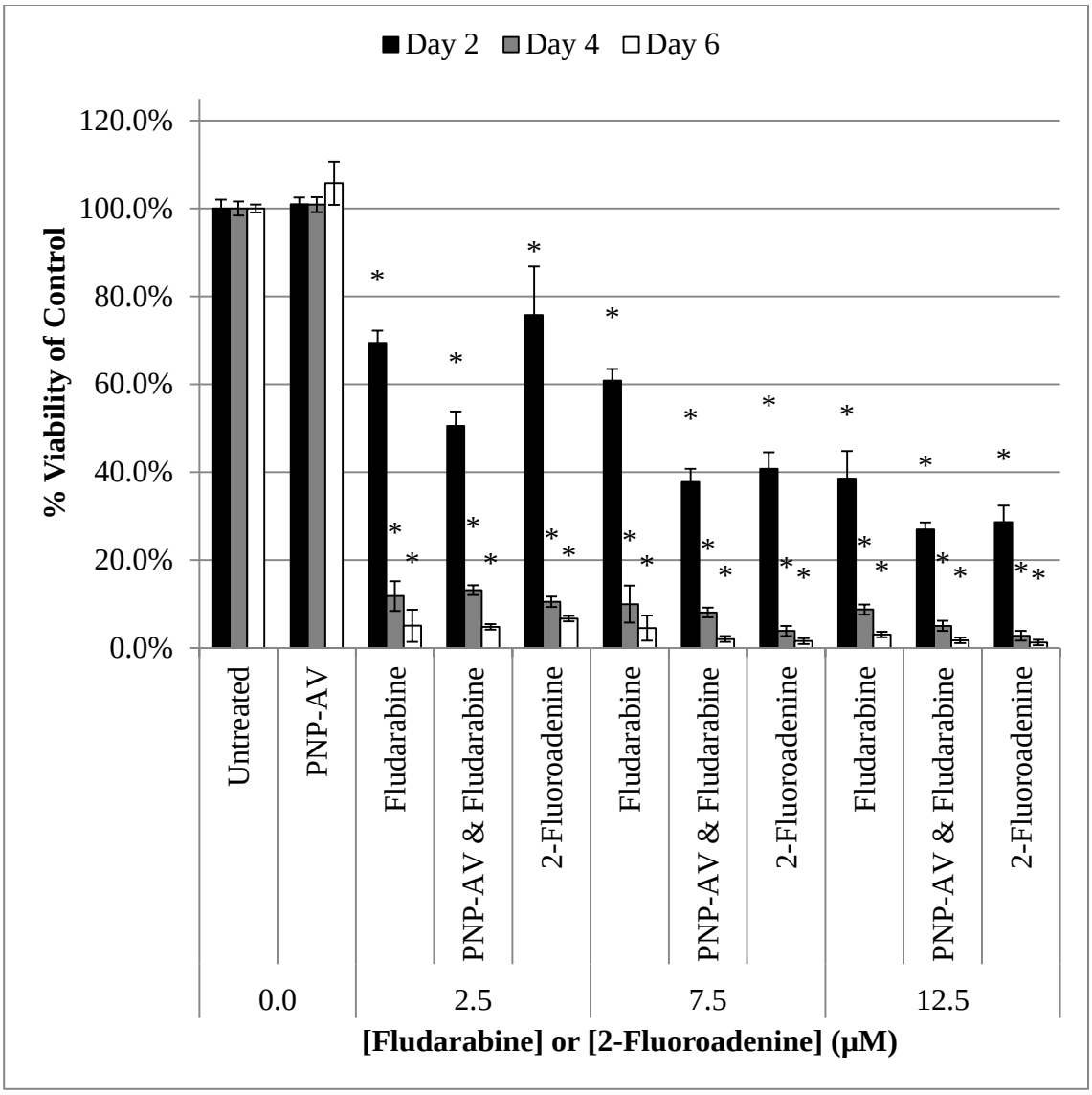

Figure 18. Cytotoxic effect of PNP-AV enzyme prodrug therapy on MCF-7 cells. The effects of fludarabine, 2-fluoroadenine, and fludarabine converted to 2-fluoroadenine by PNP are shown. Groups that received PNP-AV were treated on days 0 and 3 of the study. Fludarabine and 2-fluoroadenine were administered daily. Viability was determined by the Alamar Blue assay on days 2, 4, and 6 (black, gray, and white bars, respectively), and each sample was represented as a percentage of untreated control on each day. Statistical analysis was performed with a one-way ANOVA test with data presented as mean ± standard error (n = 3). Statistical significance vs. untreated control on the same day is denoted by *($p < 0.001$).

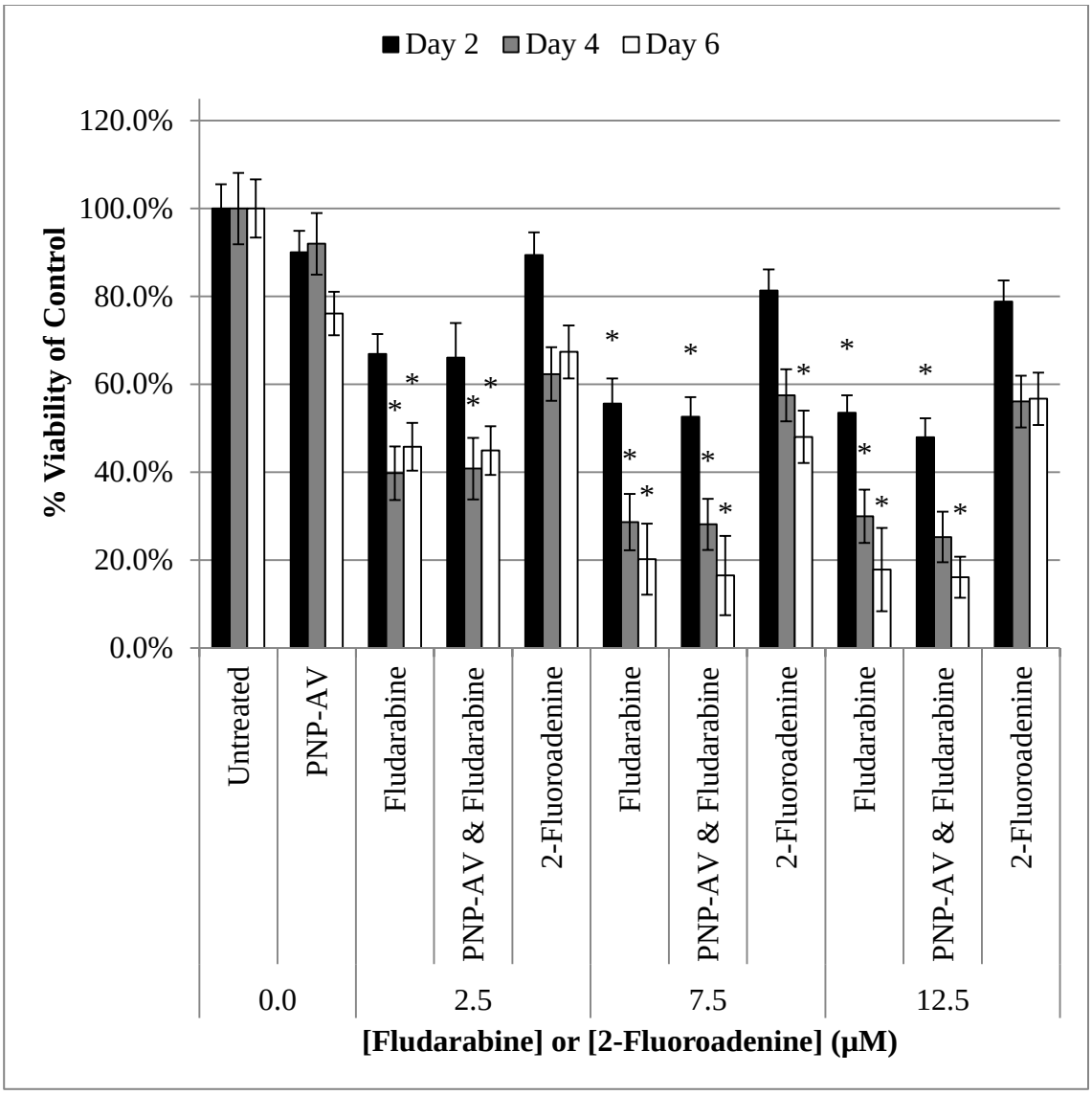

Figure 19. Cytotoxic effect of PNP-AV enzyme prodrug therapy on MDA-MB-231 cells.

The effects of fludarabine, 2-fluoroadenine, and fludarabine converted to 2-fluoroadenine by PNP are shown. Groups that received PNP-AV were treated on days 0 and 3 of the study. Fludarabine and 2-fluoroadenine were administered daily. Viability was determined by the Alamar Blue assay on days 2, 4, and 6 (black, gray, and white bars, respectively), and each sample was represented as a percentage of untreated control on each day. Statistical analysis was performed with a one-way ANOVA test with data presented as mean ± standard error (n = 3). Statistical significance vs. untreated control on the same day is denoted by *($p < 0.001$).

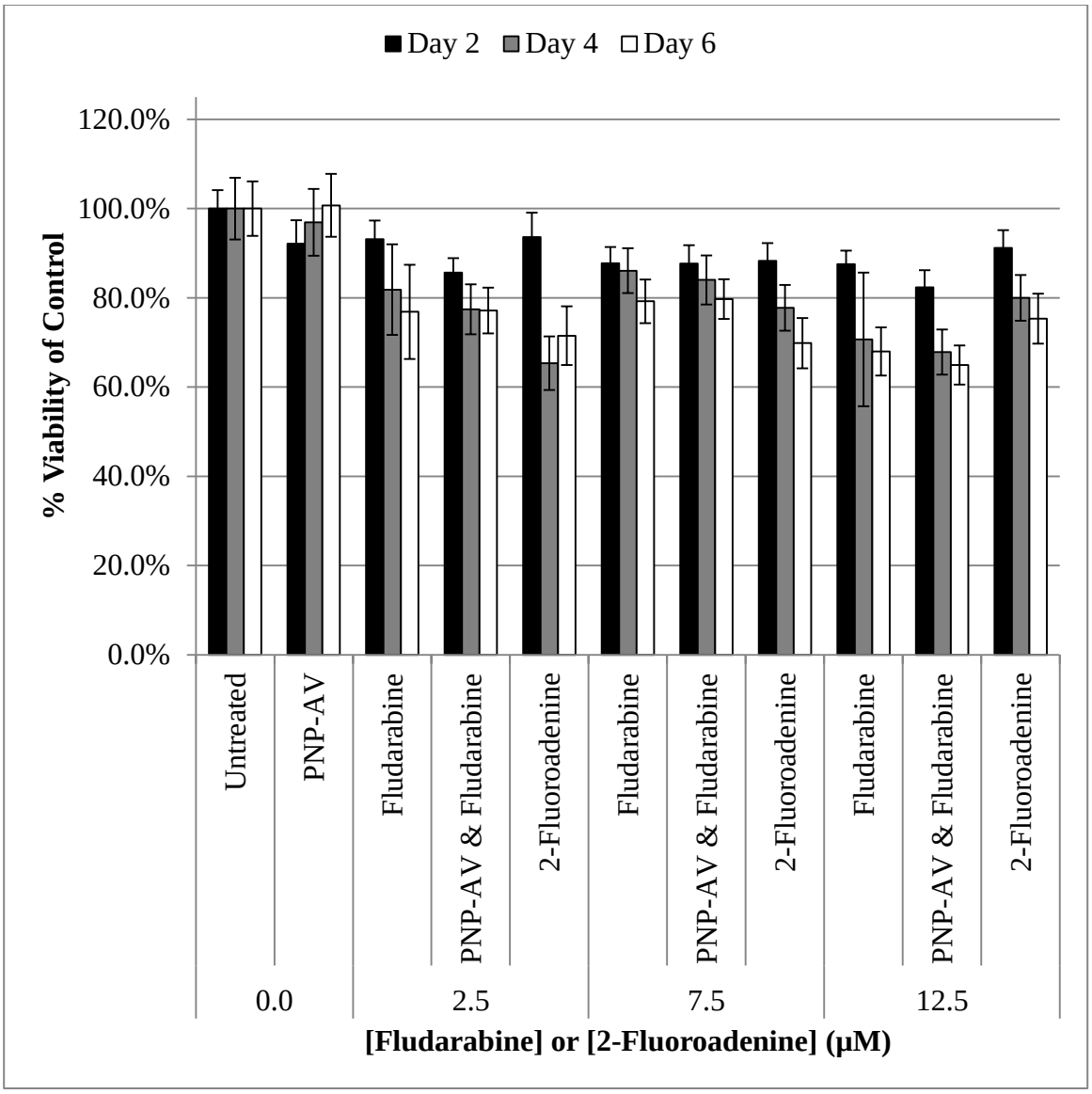

Figure 20. Lack of cytotoxic effect of PNP-AV enzyme prodrug therapy on confluent HAAE-1 cells.

The effects of fludarabine, 2-fluoroadenine, and fludarabine converted to 2-fluoroadenine by PNP are shown. Groups that received PNP-AV were treated on days 0 and 3 of the study. Fludarabine and 2-fluoroadenine were administered daily. Viability was determined by the Alamar Blue assay on days 2, 4, and 6 (black, gray, and white bars, respectively), and each sample was represented as a percentage of untreated control on each day. Statistical analysis was performed with a one-way ANOVA test with data presented as mean ± standard error (n = 3). Statistical significance vs. untreated control on the same day is denoted by *($p < 0.001$).

In Vivo PNP-AV Plasma Clearance

The pharmacokinetic profile of PNP-AV was similar to the other fusion proteins, with plasma clearance occurring within 8 h of intraperitoneal administration, as shown in Figure 21. Clearance within 8 h suggests the prodrug fludarabine could be safely administered as early as 8 h post fusion protein administration. The peak plasma concentration of PNP-AV was higher than for CD-AV (Figure 8), so the increased size of PNP-AV does not appear to inhibit movement from the peritoneal cavity into the circulation.

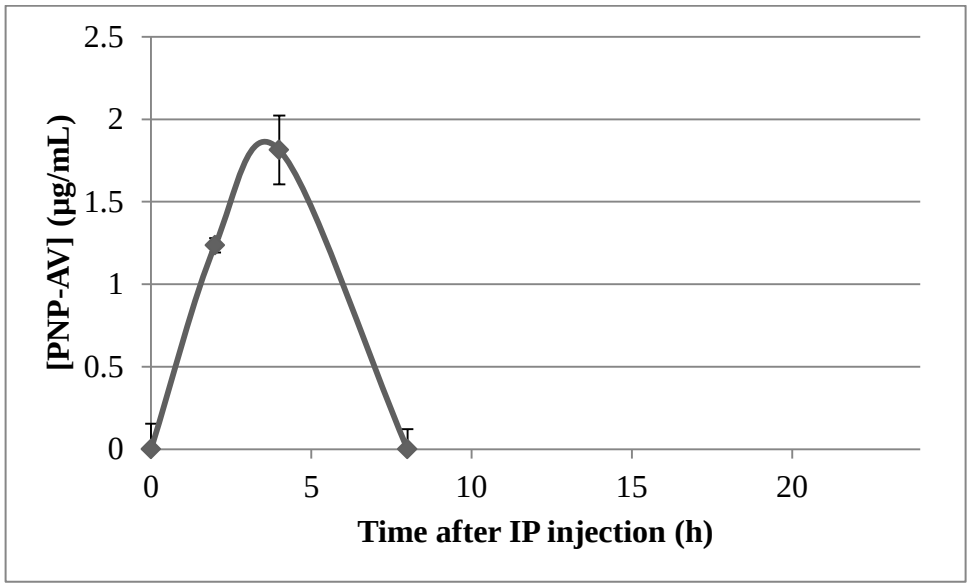

Figure 21. PNP-AV clears from the circulation of SCID mice in <8 h. An ELISA assay for PNP-AV was performed on serum samples at intervals following intraperitoneal administration of PNP-AV at 10 mg/kg. Data is presented as mean ± standard error (n = 3).

In Vivo Evaluation of PNP-AV System and Combination with Docetaxel

The PNP-AV enzyme prodrug system was evaluated in SCID mice bearing subcutaneous MDA-MB-231 tumors placed on the flank. Tumor volumes were assessed every 3-4 days throughout the study, as shown in Figure 22. Treatment was

administered on a daily basis, with PNP-AV administration in the morning and fludarabine administration following 12 h later in the evening. Fludarabine was administered at 100 mg/kg, as the concentration was found to be safe and effective in mice given as an intraperitoneal bolus injection [62, 65, 66, 241].

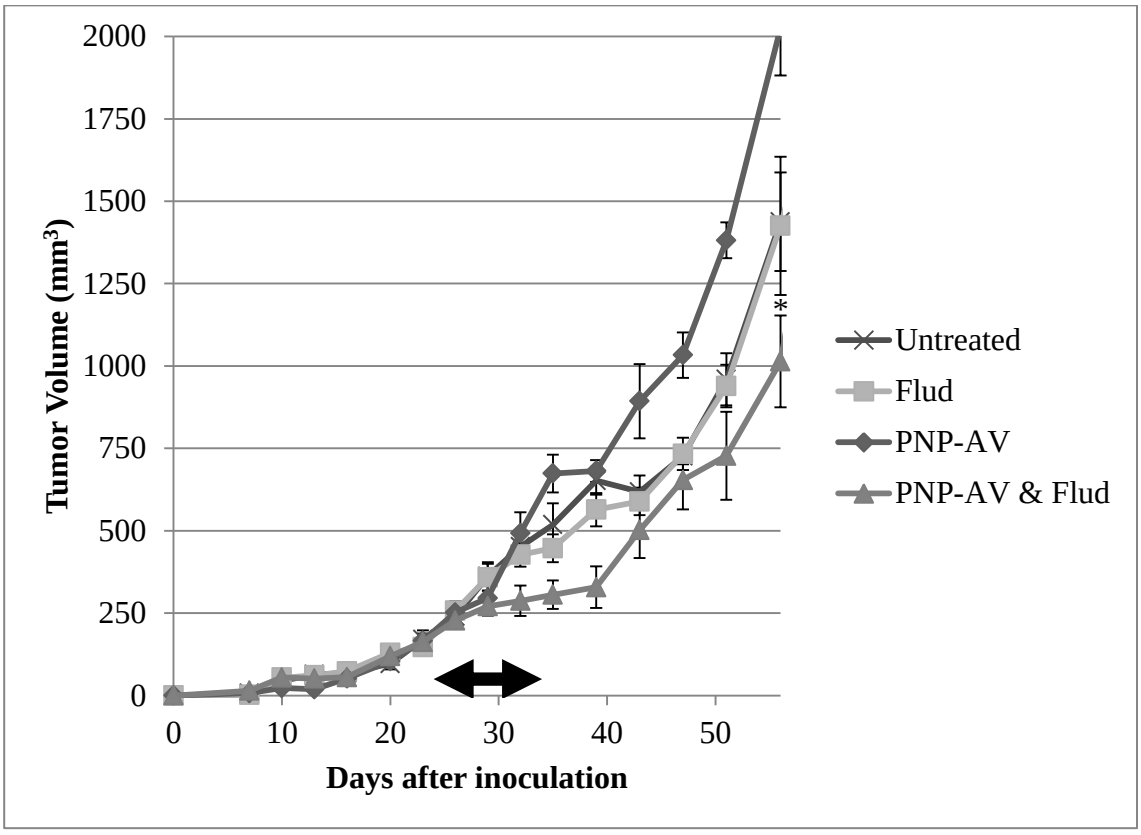

Figure 22. Mild antitumor effect of PNP-AV and fludarabine against MDA-MB-231 tumors on the flank of SCID mice.
PNP-AV was administered daily at 10 mg/kg IP followed 12 h later by the administration of fludarabine at 100 mg/kg IP. Treatment occurred for 10 days and is indicated by the arrow. Data is presented as mean ± standard error (n = 6-7). Statistical significance compared to the untreated group is indicated by *($p < 0.01$).

The enzyme prodrug therapy produced a mild antitumor effect, with suppression of tumor growth achieved during the treatment period and for a brief time following the conclusion of the treatment. As expected, the fusion protein alone and the prodrug alone had minimal effect on tumor volume. None of the groups exhibited signs of

negative reaction to the treatment nor displayed significant weight loss, as shown in Figure 23.

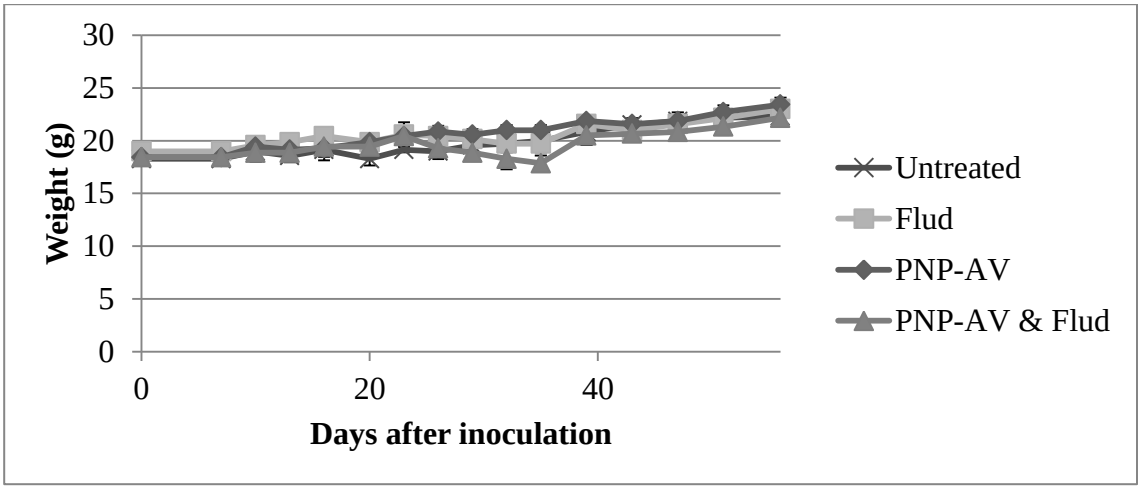

Figure 23. Minimal effect of PNP-AV system on weight of SCID mice.

A stronger antitumor effect may have been observed with increased concentrations of fludarabine. PNP enzyme prodrug therapies dose fludarabine ranging from 12.5 mg/kg three times daily [65, 242] up to 160 mg/kg three times daily [243]. Reports of differing tolerances of up to 8-fold between strains of mice suggest that optimization for each model may be necessary [241]. Additionally, multiple fludarabine injections throughout the day may increase bioavailability, though mathematical modeling of plasma levels of fludarabine, shown in Figure 24, suggest our dosing regimen may be nearly optimized based on the requirement that circulating fludarabine drop below that of the lethal level of 2-fluoroadenine prior to the administration of PNP. The plasma concentrations were estimated based on a fludarabine plasma half-life of 185 minutes [244] and experimentally determined levels of PNP-AV, shown in Figure 21. Stability of the fusion protein bound within the tumor is unknown, so daily administration of the protein may be unnecessary, in which case

fludarabine could potentially be administered at higher doses or with higher frequency, potentially enhancing therapeutic efficacy.

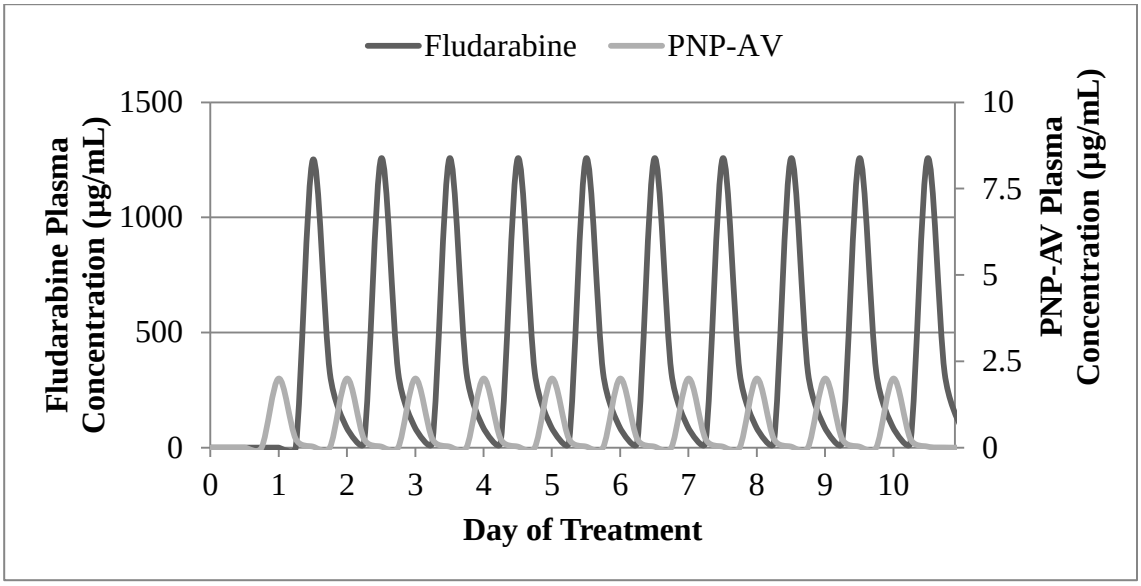

Figure 24. PNP-AV and fludarabine mathematical modeling of plasma levels based on dosing regimen.

Combination with docetaxel was evaluated alongside the PNP-AV enzyme prodrug system to cause greater externalization of phosphatidylserine and increase the presence of PNP-AV within the tumor. Docetaxel was used at 5 mg/kg, below the typical therapeutic level (30-60 mg/kg [245-247]), to minimize systemic effects yet enhance tumor phosphatidylserine exposure. As expected, docetaxel alone caused no significant effects compared to the untreated tumors, shown in Figure 25. Docetaxel combined with the enzyme prodrug treatment resulted in significant tumor regression during the treatment period, however regrowth did occur following the conclusion of the treatment. The enhanced therapeutic efficacy with docetaxel was theorized to be a result of increased externalization of phosphatidylserine; however there are also reports

of some synergy between docetaxel treatment and the PNP and fludarabine enzyme prodrug system [248].

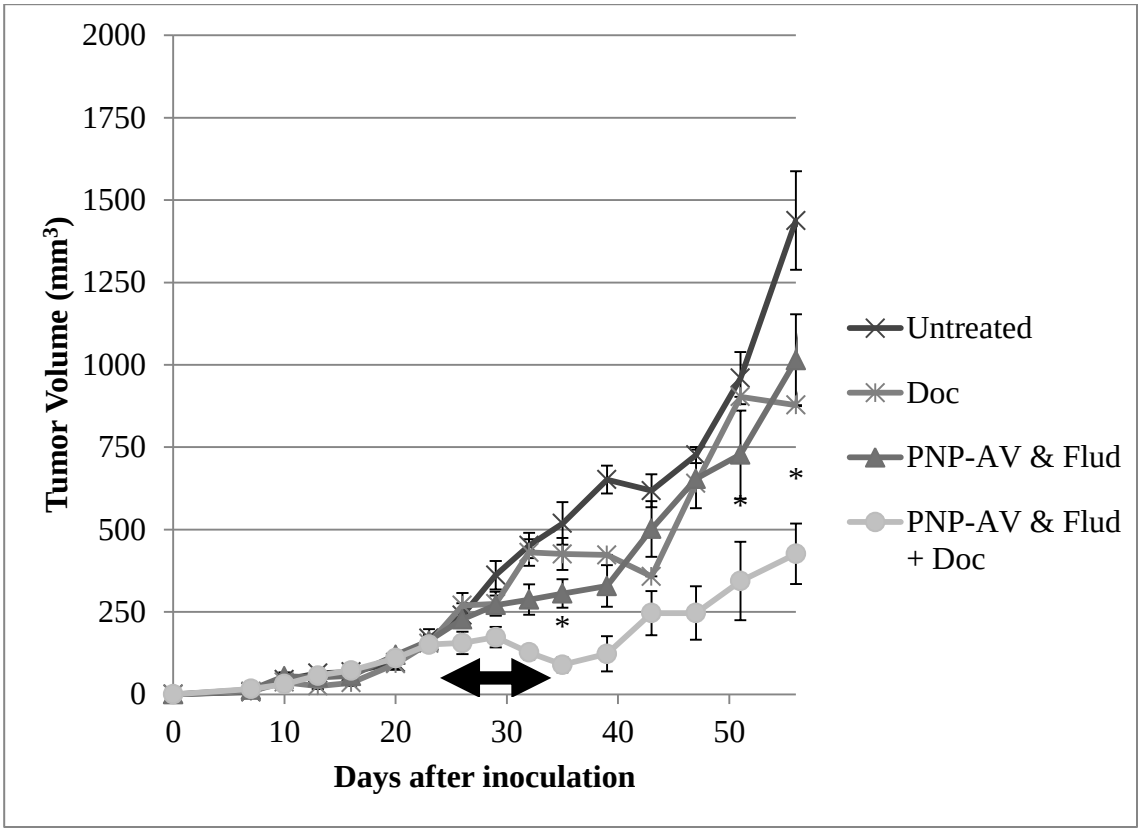

Figure 25. Enhanced antitumor effect of PNP-AV and fludarabine in combination with docetaxel against MDA-MB-231 tumors on the flank of SCID mice. PNP-AV was administered daily at 10 mg/kg IP followed 12 h later by the administration of Flud at 100 mg/kg IP. Docetaxel (Doc) was administered at 5 mg/kg IP every third day, beginning one day prior to the start of the enzyme prodrug treatment. Treatment occurred for 10 days and is indicated by the arrow. Data is presented as mean ± standard error (n = 6-7). Statistical significance compared to the untreated group is indicated by *($p < 0.001$). No significant differences were observed between treatment groups.

Tumor regrowth was theorized to initiate from a viable rim of cells near the edge of the tumor, shown with the darker hematoxylin staining of the intact nuclei of viable cells in Figure 26. Figure 27 confirms the presence of some PNP-AV bound within the tumor after administration of the protein to an untreated mouse bearing an MDA-MB-231 tumor. A central necrotic core and viable periphery are characteristic of vascular targeted agents as observed, whereas direct antitumor chemotherapeutics are most effective against the periphery of the tumor, which is typically well oxygenated and consists of rapidly dividing cells [249] [138]. Presence of cellular death both at the core and at the periphery suggest the therapy may exhibit some properties of both vascular directed and proliferation directed therapies, which may result from phosphatidylserine expression both on the vasculature and tumor cells. Immunohistochemical detection of PNP-AV may only be possible on the tumor vasculature due to higher exposure to protein, but cell death within the tumor may result from free diffusion of 2-fluoroadenine or from the targeted elimination of the blood vessels.

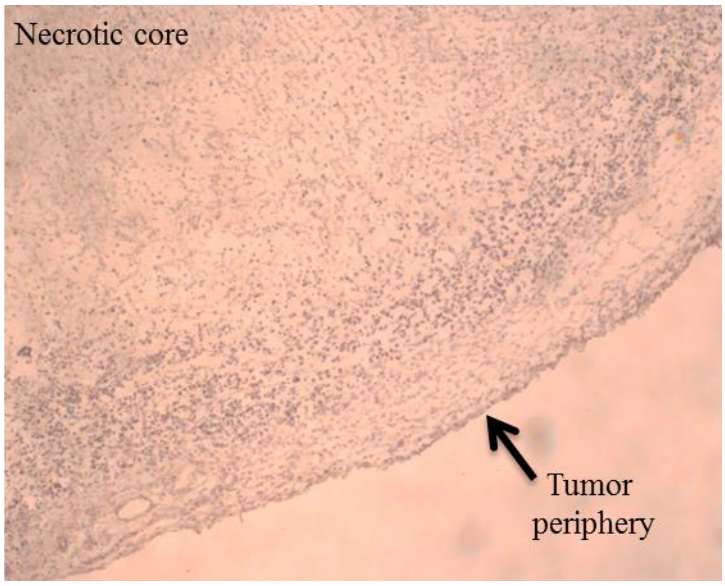

Figure 26. Hematoxylin stained MDA-MB-231 tumor section from PNP-AV and fludarabine + docetaxel treated mouse shown with 4x magnification.

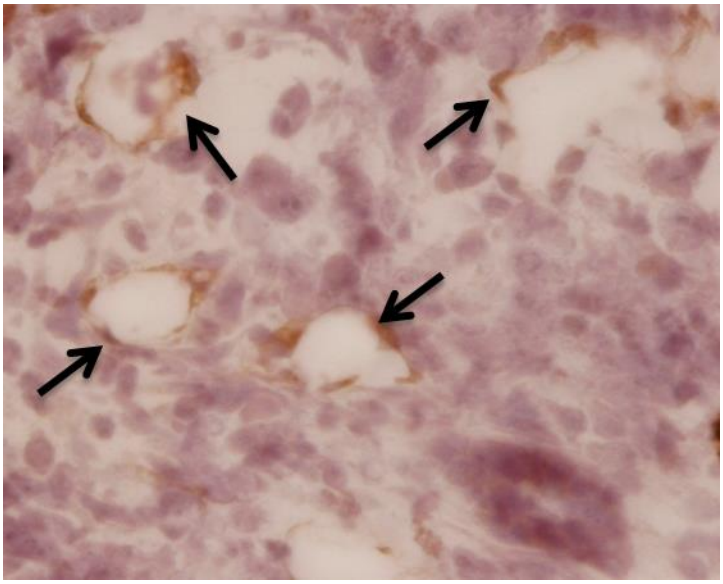

Figure 27. PNP-AV staining of MDA-MB-231 tumor section.
Untreated mice were injected with PNP-AV and then sacrificed after 8 h. Tumors were harvested and cryopreserved. PNP-AV staining was developed with DAB (brown) and is indicated with the arrows. A hematoxylin counterstain (purple) was included for nuclei. Images were obtained on a Nikon Eclipse E800 microscope at 40x magnification.

Summary of PNP-AV System

The PNP-AV system produced *in vitro* results comparable to the CD-AV and Met-AV enzyme prodrug systems, with even stronger binding capabilities. Confocal microscopy of PNP-AV confirmed that binding to phosphatidylserine does indeed occur and that some enzyme is maintained on the exterior surface of the cells.

A subcutaneous MDA-MB-231 breast tumor model on the flank of SCID mice was utilized for *in vivo* evaluations. The enzyme prodrug system alone resulted in a suppression of tumor growth during the treatment period, which is a stronger response than that observed with the CD-AV system however not as strong as the tumor regression seen with the Met-AV system discussed below. As a result, Met-AV rather than PNP-AV was selected as the best candidate for reduction of immunogenicity.

The combination of docetaxel with PNP-AV did result in tumor regression during the treatment period, which provided advantage over the PNP-AV enzyme prodrug system alone. Improved efficacy is suspected to be primarily a result of enhanced phosphatidylserine externalization rather than synergy with 2-fluoroadenine, but failure to replicate results with the Met-AV system (discussed in upcoming section) may provide some evidence to the contrary.

While the PNP-AV system was ultimately not selected for transition to immune competent models, the system did perform with adequate proficiency in immune deficient mice and does hold continued promise, particularly with docetaxel combination strategies. Should future work be conducted with the PNP-AV system, it would be quite feasible to perform an approach similar to that of the humanized system of methioninase using CGL through the use of a humanized version of PNP, developed

for gene directed enzyme prodrug therapies at the University of California, Los Angeles [250-252].

Methionine-γ-Lyase and Selenomethionine

In Vivo Met-AV Plasma Clearance

The Met-AV fusion protein entered the blood stream and was cleared from circulation within 8 h after intraperitoneal administration, as shown in Figure 28. The pharmacokinetic profile was similar for all three fusion proteins in SCID mice.

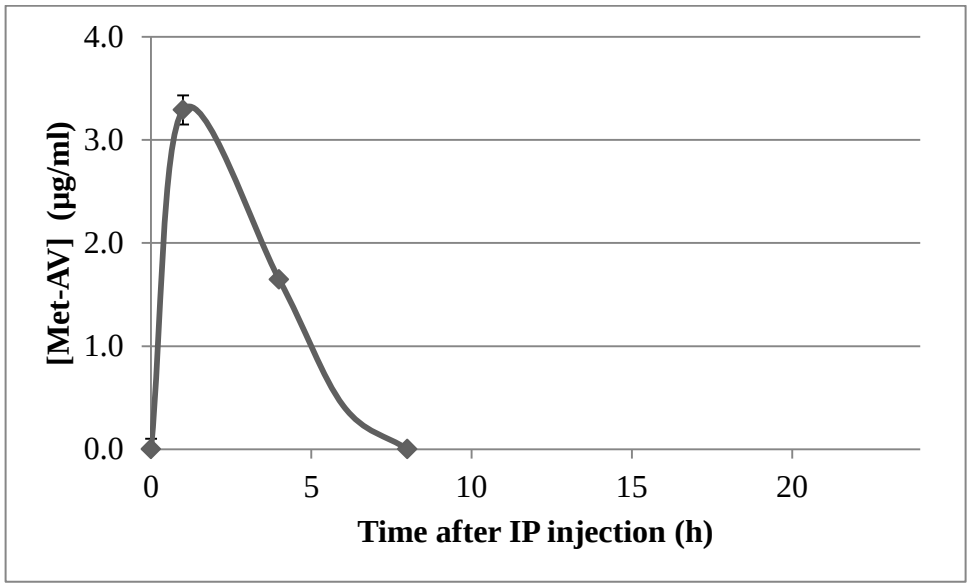

Figure 28. Met-AV clears from the circulation of SCID mice in <8 h. An ELISA assay for Met-AV was performed on serum samples at intervals following intraperitoneal administration of Met-AV at 10 mg/kg. Data is presented as mean ± standard error (n = 3).

In Vivo Evaluation of Met-AV System

The Met-AV enzyme prodrug system was first evaluated *in vivo* on the cyclic dosing regimen that consists of an intraperitoneal injection of Met-AV followed by three subsequent days of selenomethionine administration [157]. This study utilized

subcutaneous MDA-MB-231 tumors on the flank of SCID mice and evaluated tumor volume, as shown in Figure 29. Additionally, this study confirmed the vascular directed nature of the targeted enzyme prodrug therapies by showing a reduction in blood flow in the tumor as well as strong immunohistochemical evidence of Met-AV binding to tumor blood vessels [157]. The Met-AV and selenomethionine enzyme prodrug therapy significantly inhibited tumor growth and caused moderate tumor regression for the duration of the treatment period. No negative side effects or weight loss was observed as a result of treatment. The regression achieved by the Met-AV system was a significant improvement over the CD-AV system, which exhibited no detectable antitumor activity, and over the PNP-AV system, which was able to suppress growth but not cause regression without the addition of docetaxel despite a higher frequency of treatment administration.

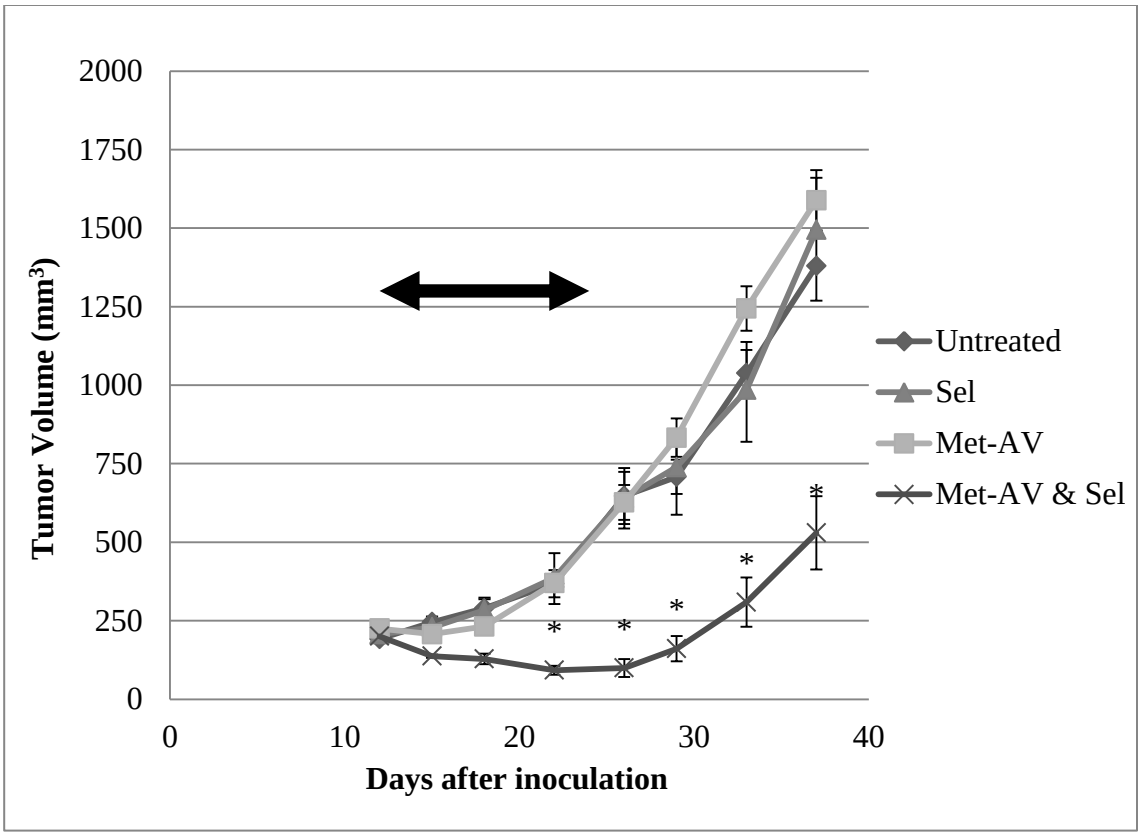

Figure 29. Met-AV and selenomethionine reduce MDA-MB-231 tumor growth on the flank of SCID mice.
Met-AV was administered every 4 days (10 mg/kg IP) with selenomethionine administered (5 mg/kg IP) each of the subsequent 3 days of the cycle for 3 cycles. Treatment period is indicated by the arrow. Data is presented as mean ± standard error (n = 7). Statistical significance compared to the untreated group is indicated by *($p < 0.001$).

Transition to Orthotopic Tumor Models

The MDA-MB-231 xenograft model is a standard system for evaluation of therapies against human breast cancer; however orthotopic implantation into the mammary fat pad is generally considered a more challenging model than the growth of the subcutaneous grafts on the flank. In comparative studies, orthotopic breast cancer xenografts showed stronger tumor growth, enhanced vascularization, and differing methylation patterns of breast cancer-related gene promoters compared to the same cells grown subcutaneously [253]. Additionally, we found that despite the aggressive and

metastatic nature of the MDA-MB-231 cell line, no metastatic formation was observed using the subcutaneous injection of the cells on the flank of SCID mice in treated or untreated mice. The targeted nature of the enzyme prodrug therapy could theoretically also inhibit metastatic growth and formation if phosphatidylserine is externalized as anticipated. The lack of metastatic formation in any experimental groups limits further analysis of the treatment; however use of an orthotopic MDA-MB-231 cell injection has been shown to result in aggressive metastatic formation at multiple locations [254].

Evaluation of the Met-AV system in SCID mice bearing orthotopically injected MDA-MB-231 tumors in the mammary fat pad number four did indeed present a more challenging model. Tumor volumes, shown in Figure 30, indicate faster and more aggressive growth than previous studies using xenograft growth on the flank of the SCID mice. Despite the significantly more aggressive model, the Met-AV system did show therapeutic effect and resulted in significantly reduced tumor volumes compared to the untreated group. As previously observed, tumor regrowth did ultimately occur following the conclusion of the treatment.

Additionally, metastases were observed on the lungs, livers, and spleens of mice, as shown in

Table 8. The treatment exhibited some beneficial effects on the metastatic formations including prevention of splenic metastasis in 75% of treated mice compared to presence of splenic metastasis in all untreated mice. The presence of liver and lung metastasis did not appear to be significantly altered by the treatment, though organs were only evaluated as positive or negative for nodules. Spread of the tumor to other mammary fat pads occurred in 100% of untreated mice and 0% of treated mice, though it was unclear if this observation was due to the significantly larger tumor volumes of

untreated mice or metastatic processes. As previously observed, no negative effects or weight loss was displayed as a result of treatment, as shown in Figure 31.

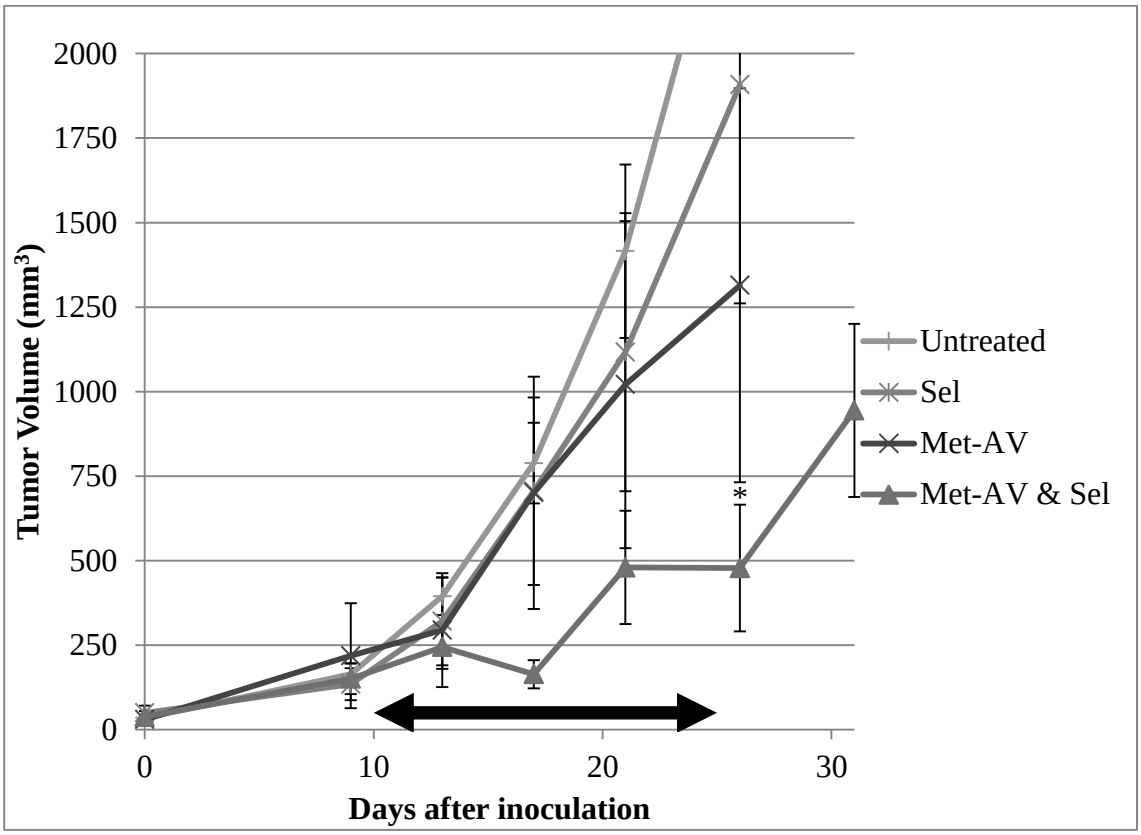

Figure 30. Met-AV and selenomethionine reduce orthotopic MDA-MB-231 tumor growth in mammary fat pad of SCID mice.
Met-AV was administered daily at 10 mg/kg IP followed 12 h later by the administration of selenomethionine at 5 mg/kg IP. Treatment period is indicated by the arrow. Data is presented as mean ± standard error (n = 6-7). Statistical significance compared to the untreated group is indicated by *($p < 0.001$).

Table 8. Metastases in SCID mice with orthotopic MDA-MB-231 tumors.
The percentage of mice with metastases to various sites is indicated.

	Spleen	Liver	Lung	Mammary Fat Pads*
Untreated	100%	50%	100%	100%
mCGL-AV & Sel	25%	58%	100%	0%

*Mammary fat pads other than the fat pad injected with cancer cells.

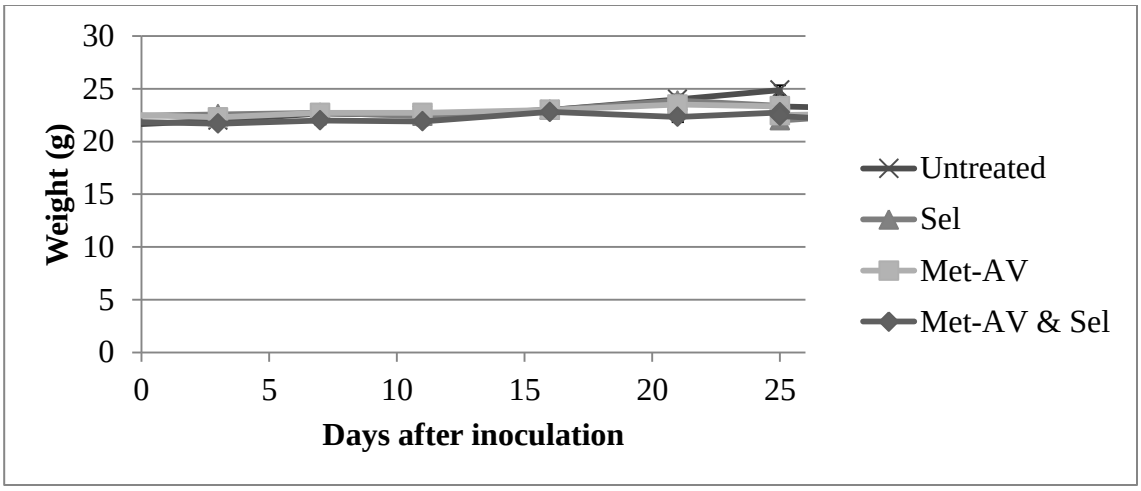

Figure 31. Minimal effect of Met-AV system on SCID mouse weight.

In Vivo Evaluation of Docetaxel Combination with Met-AV System

Significant enhancement of antitumor effects on the PNP-AV system combined with docetaxel and the theorized mechanism of increased binding of fusion protein gave rise to a reasonable optimism for an enhanced effect when combining docetaxel with the Met-AV system. Unfortunately, tumor volume data, shown in Figure 32, indicated no beneficial effect from the combination of docetaxel with Met-AV and selenomethionine. Continued observation further supported that docetaxel had no beneficial effect when combined with Met-AV and selenomethionine based on tumor volume or mouse survival.

Several variables exist between the PNP-AV system combined with docetaxel and the Met-AV system combined with docetaxel that potentially impact the conflicting results regarding the benefit of docetaxel. The most likely mechanism for differing docetaxel contributions is the transition from a subcutaneous tumor on the flank to an orthotopic tumor grown in the mammary fat pad. The differing tumor models have altered vascularization patterns [253] which would impact the presence of

phosphatidylserine directly accessible from the circulation and could even effect docetaxel induced externalization.

Alternatively, the reduced impact of docetaxel may be system specific. There is reported synergy of docetaxel with the PNP and fludarabine enzyme prodrug system [248], and if that action is the primary antitumor mechanism as opposed to the hypothesized enhancement of phosphatidylserine externalization, that effect could supersede any effect resultant from increased phosphatidylserine exposure. If the beneficial docetaxel results are actually due to a mechanistic synergy with 2-fluoroadenine, the same effect would be unlikely with the Met-AV system. Furthermore, differing cytotoxic mechanisms resultant from the systems' production of 2-fluoroadenine and methylselenol may cause a therapeutic plateau at different levels of generated drug. For example, the Met-AV system alone may already produce sufficient levels of methylselenol to achieve the maximum therapeutic effect, whereas the PNP-AV system could potentially benefit by increasing levels of 2-fluoroadenine through additional binding of PNP-AV. A number of possible explanations or combinations of explanations are feasible, and additional experimentation would be necessary to further elucidate the mechanistic responsible for the discrepancy between docetaxel efficacies.

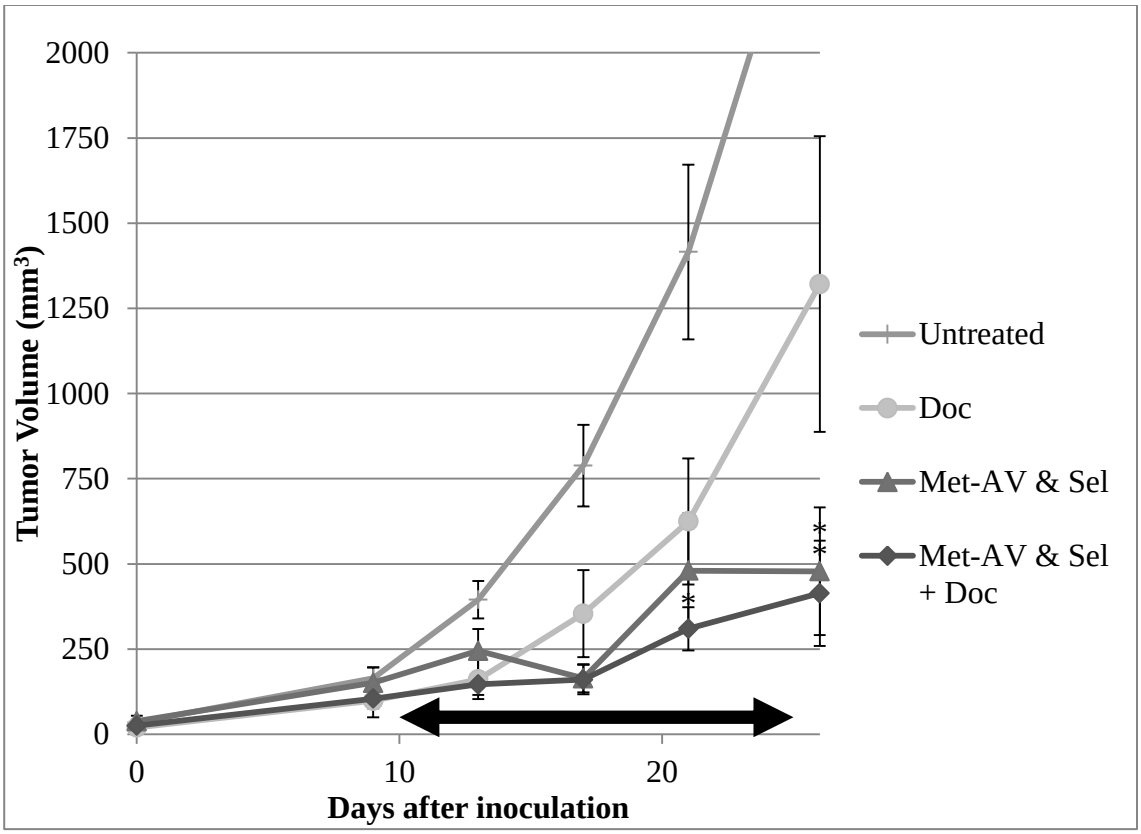

Figure 32. Docetaxel combination has no apparent enhancement of antitumor effect of Met-AV and selenomethionine for orthotopic MDA-MB-231 tumors in SCID mice.

Met-AV was administered daily at 10 mg/kg IP followed 12 h later by the administration of selenomethionine at 5 mg/kg IP. Doc was administered at 5 mg/kg IP every third day, beginning one day prior to the start of the enzyme prodrug treatment. Treatment period is indicated by the arrow. Data is presented as mean ± standard error (n = 6-7). Statistical significance compared to the untreated group is indicated by *($p <$ 0.001). No statistical significance between the Met-AV and Sel and Met-AV and Sel + Doc was observed.

Preliminary In Vivo Investigation of Rapamycin Combination Therapy

Failed enhancement of the Met-AV system with docetaxel suggests that the enzyme prodrug therapy alone, even with enhanced levels of protein, may not be sufficient to result in sustainable reduction of tumor volumes. Previous histological analysis, exemplified in Figure 26, suggests that incomplete tumor killing and subsequent regrowth results from the viable rim of cells surrounding the necrotic tumor core. Regrowth is hypothesized to occur as a result of the hypoxic response associated with tumor necrosis. Therefore, upon failure of the Met-AV and selenomethionine treatment, rapamycin was introduced concurrently to counter the hypoxic response while continuing to administer the enzyme prodrug therapy.

Despite beginning rapamycin treatment at large tumor volumes of approximately 5% of total body mass, a strong therapeutic effect was achieved when combining the Met-AV system with rapamycin, shown in Figure 33. This preliminary data suggests that the hypoxic response does indeed play a role in tumor progression following administration of the vasculature targeted enzyme prodrug systems.

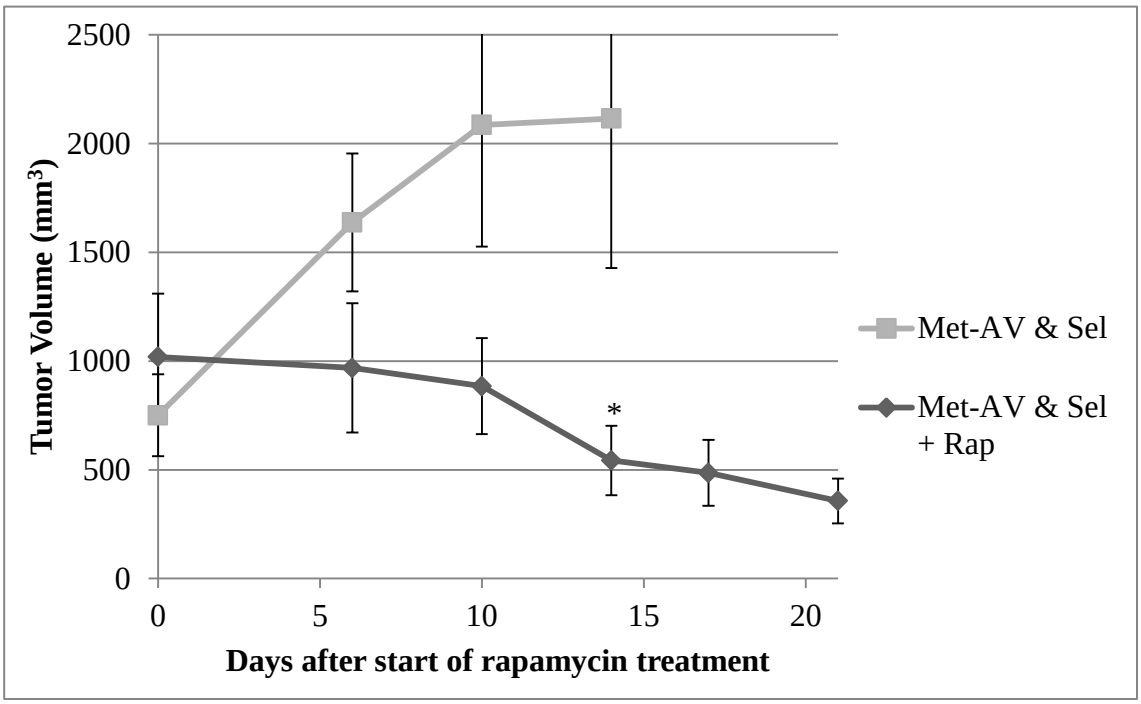

Figure 33. Preliminary enzyme prodrug combination therapy with rapamycin produces antitumor effect on large orthotopic MDA-MB-231 tumors in SCID mice.
Met-AV was administered daily at 10 mg/kg IP followed 12 h later by the administration of selenomethionine at 5 mg/kg IP. Upon strong tumor growth despite enzyme prodrug treatment, daily rapamycin co-treatment was initiated at 5 mg/kg IP. Data is presented as mean ± standard error (n = 6-9). Statistical significance is indicated by *($p < 0.05$).

Summary of Met-AV System

The Met-AV enzyme prodrug system caused tumor regression in SCID mice bearing MDA-MB-231 tumors on the flank. Regression resultant from the enzyme prodrug treatment alone provided advantage over the PNP-AV system, which could only achieve growth suppression, and the CD-AV system which produced no measureable effect. Consequently, the Met-AV system was selected as the primary candidate for transition to more advanced models, including immune competent mice.

Prior to attempting immunogenicity reduction strategies, the Met-AV system was evaluated in a different model of tumor growth utilizing orthotopic injections of cancer cells into the mammary fat pad. The orthotopic model did indeed exhibit characteristics more challenging to the treatment such as faster tumor growth and aggressive metastatic formation at multiple sites. The therapeutic effect of the Met-AV system was not as pronounced but still apparent. Combination with docetaxel did not replicate the beneficial results seen with the PNP-AV system; however it is uncertain if that is a system-specific or model-specific difference. Promising preliminary results with a rapamycin combination therapy were obtained, supporting the theory that the hypoxic response to the treatment reduction in blood flow contributes to tumor progression.

PEGylation

Optimization of conditions for PEGylation of Met-AV proved challenging, though successful conjugation was achieved with all PEG evaluated through a combination of reaction time, pH, molar ratio, and temperature variations. Figure 34 and Figure 35 represent typical results for a series of experiments evaluating reaction time and reaction temperatures of 25°C and 4°C for a maleimide PEG conjugation to Met-AV. Maleimide reactions were targeted to an available cysteine on AV used successfully in our laboratory in AV conjugation to single-walled carbon nanotubes [203]. Mono-PEGylation was desirable, as we have previously shown that maleimide conjugation to AV can leave binding to phosphatidylserine uninhibited. Poly-PEGylation likely results in conjugation to the enzyme component of the fusion protein

and interruption of enzyme activity. Additionally, larger PEGylation extents also pose greater potential for binding inhibition. Small percentages of mono-PEGylated protein make size-exclusion separations difficult as each protein contains multiple subunits with a somewhat stochastic degree of PEGylation (four subunits for Met-AV and six subunits for PNP-AV) resulting in a high polydispersity and low yields of any separable homogeneous product.

Activity analysis of PEGylated product suggests a reduction in activity with increased degree of PEGylation, though this analysis was not preceded by a size-based separation due to the previously mentioned difficulties. Samples containing mostly poly-PEGylated product generally did not retain activity, suggesting that activity present in some PEGylated samples is possibly from residual unPEGylated protein. However, some groups have shown some retention of methioninase activity for non-fused methioninase with up to eight PEGs per subunit [226, 227] and non-fused purine nucleoside phosphorylase with up to four PEGs per subunit [255]. The inability to directly reproduce or adapt existing protocols for comparable PEGylation is likely a result of the multimeric size increases of 164 kDa to 320 kDa (195% increase) for tetrameric Met [36] of 156 kDa to 390 kDa (250% increase) for hexameric PNP [210, 237, 238] upon fusion of the monomers to a 36 kDa AV and 3 kDa linker region. Accompanying the molecular mass increases are increased numbers of the targets of the PEG functional groups due to the presence of multiple AV per molecule, resulting in poor scaling of reaction conditions.

Activity retention and acceptable yield were pre-requisites to two additional gauges of an ultimately successful PEGylation: preservation of AV binding to

phosphatidylserine and reduction of immunogenicity. PEGylation of most therapeutic enzymes attempts to enhance circulation half-life and requires preservation of substrate active sites rather than continued macromolecular access to large binding domains. There is likely a very small realm of protein PEGylation strategies that effectively shield the antigenic sites of the foreign fusion proteins from immune effectors and antigen presenting cells, yet do not inhibit binding of the protein to the cell surface.

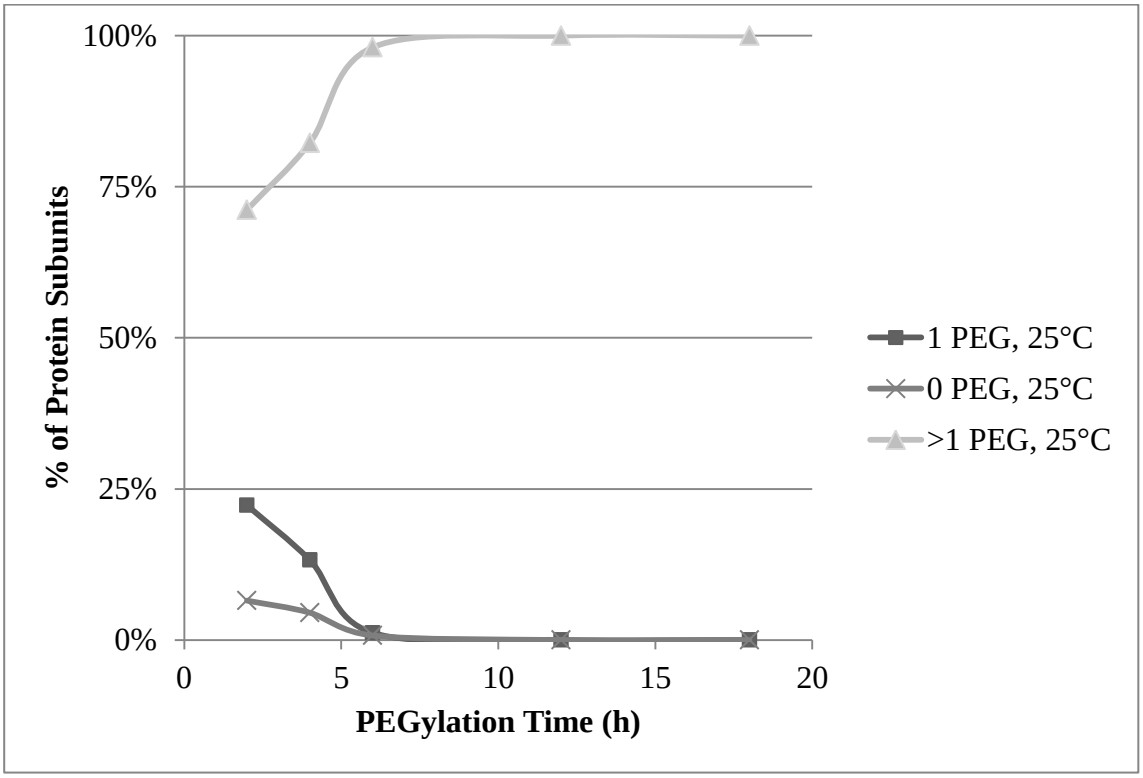

Figure 34. Met-AV Maleimide PEGylation at 25°C.
A 200:1 molar ratio of PEG to Met-AV subunits was evaluated for PEGylation per subunit for reaction times of 2 to 28 h. SDS-PAGE densitometric analysis with ImageJ was used to determine percentages of protein within bands representative of unPEGylated Met-AV, Met-AV with one PEG (desired product), and all bands showing PEGylation at more than one site per Met-AV subunit. A 10 kDa 4-arm branched PEG with a single maleimide functional group was used for conjugation.

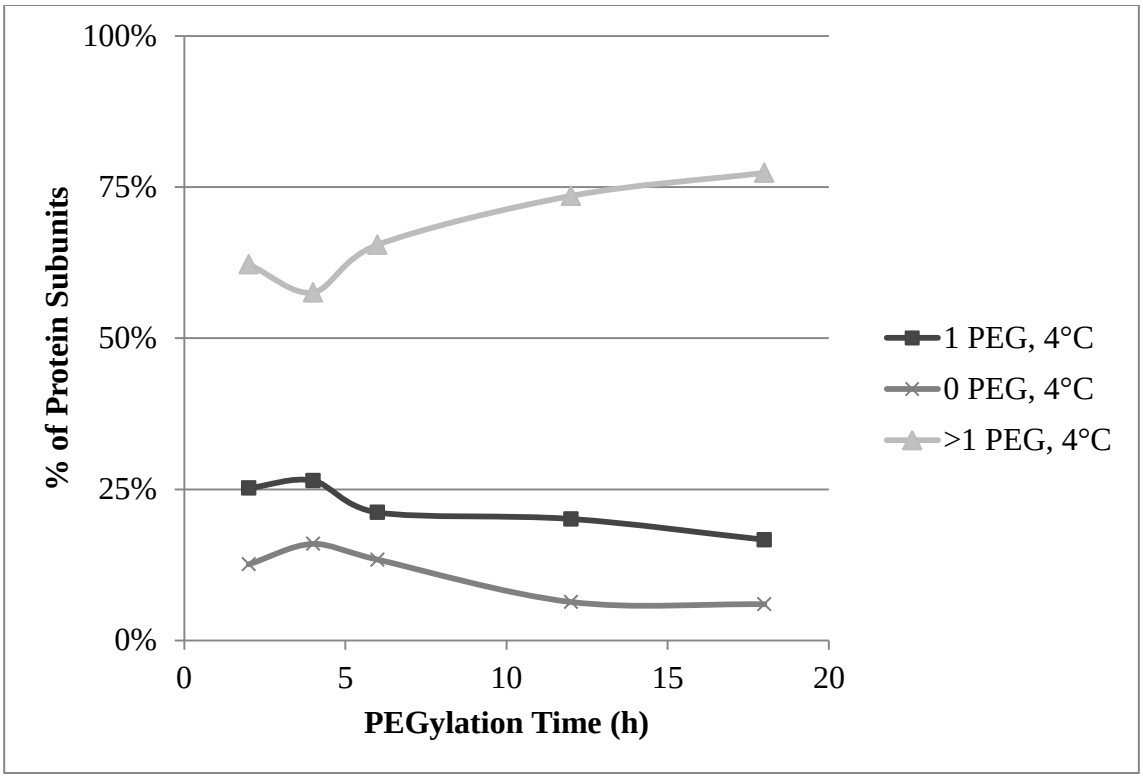

Figure 35. Met-AV Maleimide PEGylation at 4°C.
A 200:1 molar ratio of PEG to Met-AV subunits was evaluated for PEGylation per subunit for reaction times of 2 to 28 h. SDS-PAGE densitometric analysis with ImageJ was used to determine percentages of protein within bands representative of unPEGylated Met-AV, Met-AV with one PEG (desired product), and all bands showing PEGylation at more than one site per Met-AV subunit. A 10 kDa 4-arm branched PEG with a single maleimide functional group was used for conjugation.

Mouse Mutant Cystathionine-γ-Lyase and Selenomethionine

Fusion Gene Constructions with Annexin I and Annexin V

Though previous staining for extracellular protein confirmed the external binding of AV targeted proteins (see Figure 16 for external PNP-AV binding to MCF-7 cells), other studies also showed the presence of internalized AV targeted protein (see Figure 57 in Appendix A: Supplemental Data). This information motivated the comparative study of AI and AV fusion proteins, which may exhibit differing internalization properties. As a result, both mCGL-AI and mCGL-AV fusion proteins

were developed using synthetic gene fragments and the Gibson method for gene assembly. Sequencing confirmed correct assembly of genes into expression vectors bearing the T7 promoter system.

Protein Expression and Purification

Both vectors containing mCGL-AI and mCGL-AV genes were successfully transformed into BL21(DE3) *E. coli*, and protein was expressed as described for PNP-AV and the other enzyme prodrug systems. Despite codon optimization, purified protein yields ranged from 3 mg/L of culture to 20 mg/L of culture, which was sufficient for the preliminary *in vitro* and *in vivo* analysis but not for the larger-scale *in vivo* studies to follow. Upon completion of preliminary work that ultimately led to the selection of mCGL-AV for further study, that expression system was selected for optimization. Transformation into T7 Express LysY (DE3) cells was performed to enhance expression by allowing higher growth densities prior to induction, resulting from lower susceptibility to cell lysis and stronger control of the T7 RNA polymerase. Purified protein yields in excess of 120 mg/L culture were achieved after optimization with this system.

Immobilized affinity chromatography purification, including proteolytic cleavage of the 6X His-tag, was successfully performed as previously described for PNP-AV. An endotoxin removal step during chromatography was included to obtain endotoxin levels of <10 EU/mg as assessed by Limulus Amebocyte Lysate assay. The endotoxin removal step of 1% Triton X-114 with 70 column volumes was sufficient to reduce levels to below 10 EU/mg. Initial attempts with 0.1% Triton X-114 resulted in

>10 EU/mg and may have resulted in negative side effects in BALB/cJ mice after repetitive administrations. Densitometric analysis revealed >95% purity for both fusion proteins.

Enzyme Activity

Enzyme activities with the substrate L-methionine for mCGL-AI and mCGL-AV were 1.0 ± 0.1 U/mg and 1.3 ± 0.2 U/mg, respectively, compared to 1.0 U/mg for Met-AV [36]. As native CGL exhibits no detectable activity towards L-methionine [169], these results suggest that the mutations of the mouse CGL are comparable to the mutations of the human CGL engineered by the Georgiou group at the University of Texas [169]. As our enzyme prodrug therapy utilizes the conversion of L-selenomethionine to methylselenol and not L-methionine depletion alone, we evaluated the activity of the engineered mouse CGL towards L-selenomethionine which has not been previously evaluated for the engineered human or mouse CGL. mCGL-AI and mCGL-AV exhibited an activity of 0.75 ± 0.2 U/mg and 0.95 ± 0.1 U/mg, respectively.

In Vitro Binding

Dissociation constants, summarized in Table 9, were calculated from the hyperbolic regression of the binding curves (data can be found in Figure 61, Figure 62, and Figure 63 of Appendix A: Supplemental Data). Binding differences between the annexin V molecules on the different fusions can be attributed to experimental variation; however mCGL-AV does utilize mouse AV and Met-AV utilizes human AV so species differences could contribute to the minor variability observed. Interestingly,

the AI fusion exhibited stronger binding to MDA-MB-231 cancer cells than the AV fusions; however the inverse was observed with non-confluent HAAE-1 cells representative of tumor vasculature. The three fusion proteins were evaluated concurrently to avoid any experimental differences in phosphatidylserine exposure. As will be further discussed regarding *in vivo* antitumor efficacy, a phosphorylation site resulting in proteolysis of AI but not AV may play a role. It is possible that cell line specific differences in protease expression or phosphorylation capabilities result in differing binding strengths between AI and AV. The dissociation constants for describing binding strength were comparable to the other annexin targeted enzyme prodrug systems, and all three fusion proteins fell within the expected range.

Table 9. Dissociation constants of mCGL-AI, mCGL-AV, and Met-AV on MDA-MB-231 and HAAE-1 cells

Dissociation Constant (K_d) ± standard error (n = 3)		
	MDA-MB-231	**HAAE-1**
mCGL-AI	0.68 nM ± 0.3 nM	2.3 nM ± 1.1 nM
mCGL-AV	2.5 nM ± 1.7 nM	0.11 nM ± 0.02 nM
Met-AV	4.9 nM ± 0.9 nM	0.5 nM ± 0.2 nM

Binding stability was also evaluated for the three fusion proteins on MDA-MB-231 breast cancer cells, as shown in Figure 36. mCGL-AI, mCGL-AV, and Met-AV all exhibited >40% of the protein that initially bound to the cells after three days. Data is consistent with expectations based on the other enzyme prodrug systems. The decreased binding stability observed with AI, though not significant, could also be related to its potential proteolysis site.

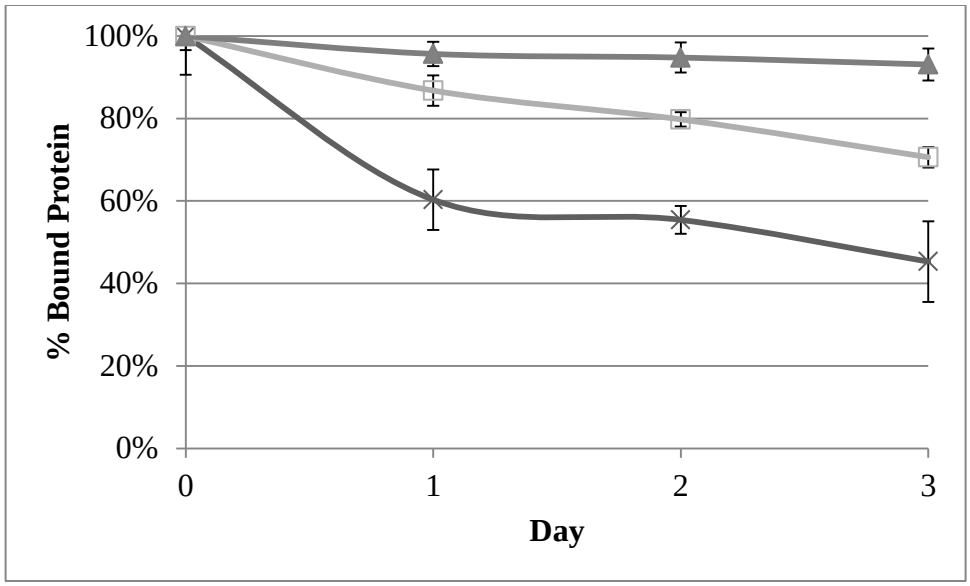

Figure 36. Binding stability of mCGL-AI, mCGL-AV, and Met-AV on MDA-MB-231 cells for 3 days.
Biotinylated mCGL-AI (x), mCGL-AV (□), and Met-AV (▲) were incubated on MDA-MB-231 cells for 2 h at 37°C and unbound protein was washed away. Streptavidin conjugated peroxidase was used to determine fusion protein present on the three following days and is presented as a percentage of fusion protein present immediately after the initial wash. Data is mean ± standard error (n = 3).

Live cell confocal microscopy was performed with fluorochrome conjugated mCGL-AI and mCGL-AV and GFP expressing MDA-MB-231 breast cancer cells. Cells were maintained at 37°C in a buffered medium without supplemental CO_2 required and monitored for viability using membrane impermeable Hoechst 33258. The cells were imaged for several hours prior to fusion protein administration, during incubation with the fusion proteins, and following a wash step to remove unbound fusion protein. Live cell imaging allowed for comparative observation of the binding and possible internalization and subsequent dissociation from the membrane of the mCGL-AI and mCGL-AV proteins without a prerequisite of an intensive kinetic

analysis. Association of both fusion proteins with the membrane was confirmed, shown in the post-wash phase in Figure 37.

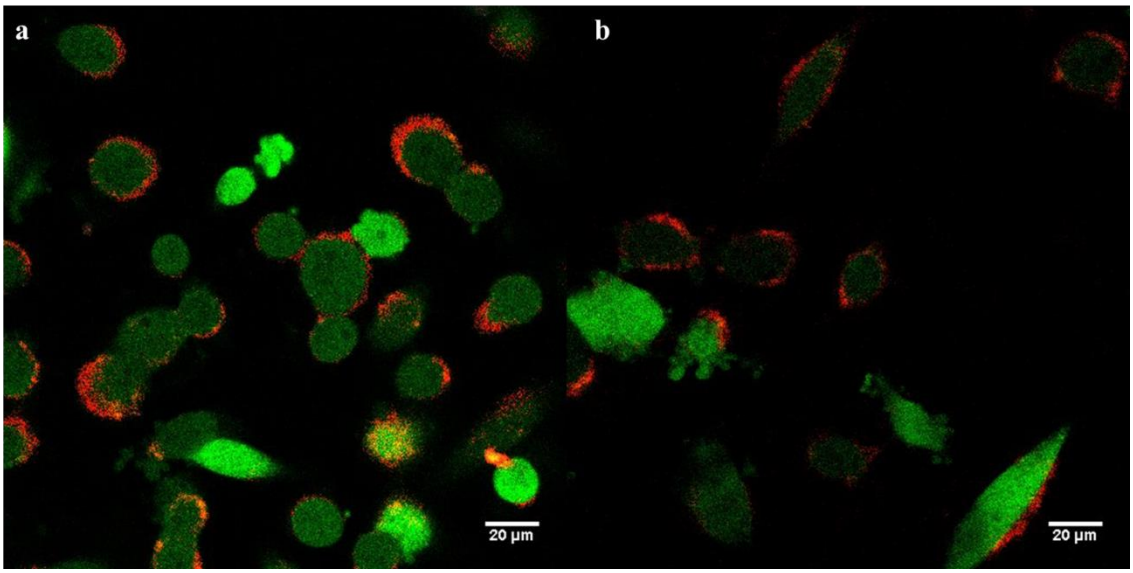

Figure 37. Live cell confocal microscopy confirms membrane binding of mCGL-AI and mCGL-AV.
(a) mCGL-AI and (b) mCGL-AV were conjugated to Dylight 680 (red) and incubated with MDA-MB-231/GFP cells (green). After 2 h at 37°C, cells were washed with culture medium to remove excess protein and imaged using a Leica SP8 confocal microscope with HyD detectors. Cells were kept at 37°C using a Peltier stage and viability was confirmed through the lack of nucleic acid staining despite inclusion of membrane impermeable Hoechst 33258 in the imaging medium.

From these images it is impossible to distinguish external membrane binding from internal membrane binding (this requires inclusion of a physical method of detecting only external or internal protein such as that described for the fixed confocal image shown in Figure 16), but internalization would likely have to occur through an endocytic pathway which is not observed (fusion protein does not appear to be present in endocytic vesicles). The membrane association remained consistent and comparable among the mCGL-AI and mCGL-AV proteins for the duration of the observation period (up to 6 h post-wash).

In Vitro Cytotoxicity

Concurrent cytotoxicity studies examined the therapeutic effect of the three fusion proteins, mCGL-AI, mCGL-AV, and Met-AV on MDA-MB-231 breast cancer cells, as shown in Figure 38. The three systems exhibited comparable cytotoxic effect over 3 days of selenomethionine administration following a single fusion protein administration at the beginning of the study. When fusion protein administration was also performed daily, the therapeutic effect was enhanced, as shown in Figure 39. Daily fusion protein administration had a particularly beneficial effect for the mCGL-AI system which elicited significantly stronger decreases in viability at lowered prodrug concentrations. Enhancement of therapeutic efficacy using higher frequency administrations of fusion protein *in vitro* also supports the transition to the daily fusion protein administration *in vivo*.

Prior to *in vivo* studies in immune competent BALB/cJ mice bearing 4T1 murine breast tumors, the cytotoxic effect was confirmed *in vitro* on 4T1 murine breast cancer cells. The data, shown in Figure 40, is consistent with the cytotoxicity results on the human MDA-MB-231 breast cancer cells. Interestingly, the mCGL-AI targeted system appeared to have a moderately stronger effect than the mCGL-AV and Met-AV systems at lowered concentrations of prodrug.

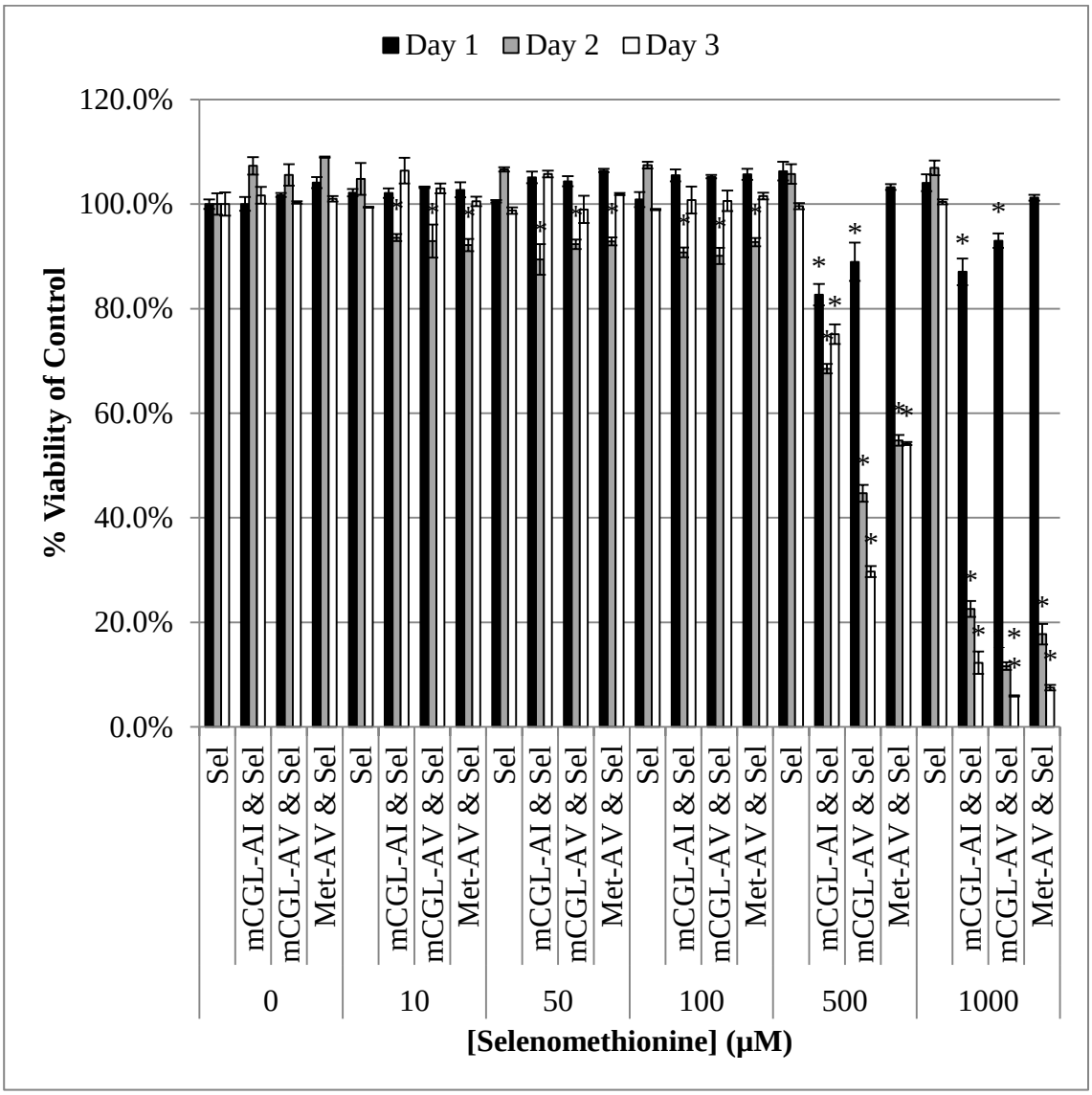

Figure 38. Comparison of the cytotoxic effect of mCGL-AI, mCGL-AV, and Met-AV enzyme prodrug therapy on MDA-MB-231 cells.
Groups that received fusion protein were treated on day 0. Selenomethionine was administered daily. Viability was determined by the Alamar Blue assay on days 1, 2, and 3 (black, gray, and white bars, respectively), and each sample was represented as a percentage of untreated control on each day. Statistical analysis was performed with a one-way ANOVA test with data presented as mean ± standard error (n = 3). Statistical significance vs. untreated control on the same day is denoted by *($p < 0.001$).

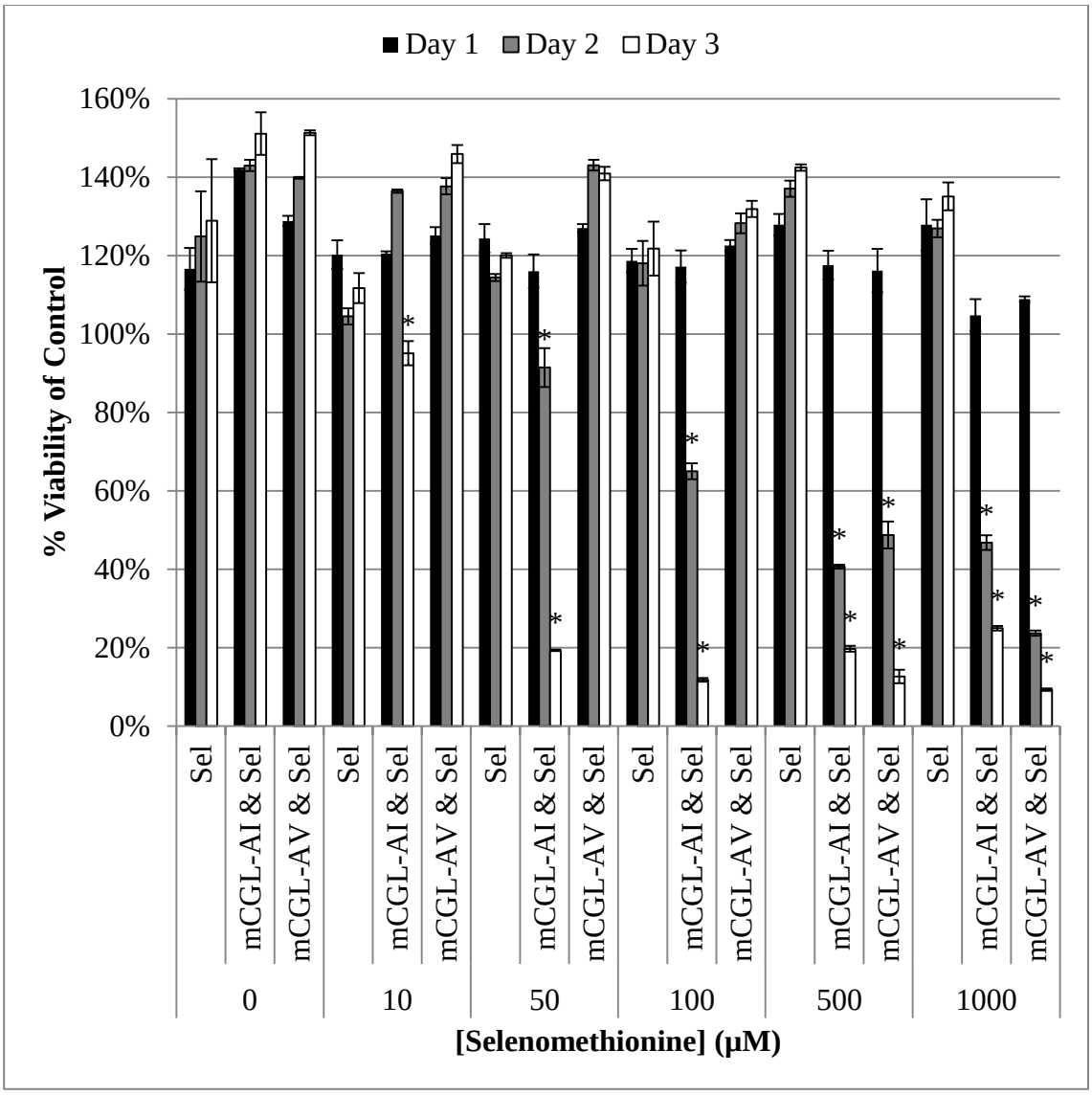

Figure 39. Comparison of the cytotoxic effect of daily administration of mCGL-AI and mCGL-AV enzyme prodrug therapy on MDA-MB-231 cells.
Fusion protein and selenomethionine was administered daily. Viability was determined by the Alamar Blue assay on days 1, 2, and 3 (black, gray, and white bars, respectively), and each sample was represented as a percentage of untreated control on each day. Statistical analysis was performed with a one-way ANOVA test with data presented as mean ± standard error (n = 3). Statistical significance vs. untreated control on the same day is denoted by *($p < 0.001$).

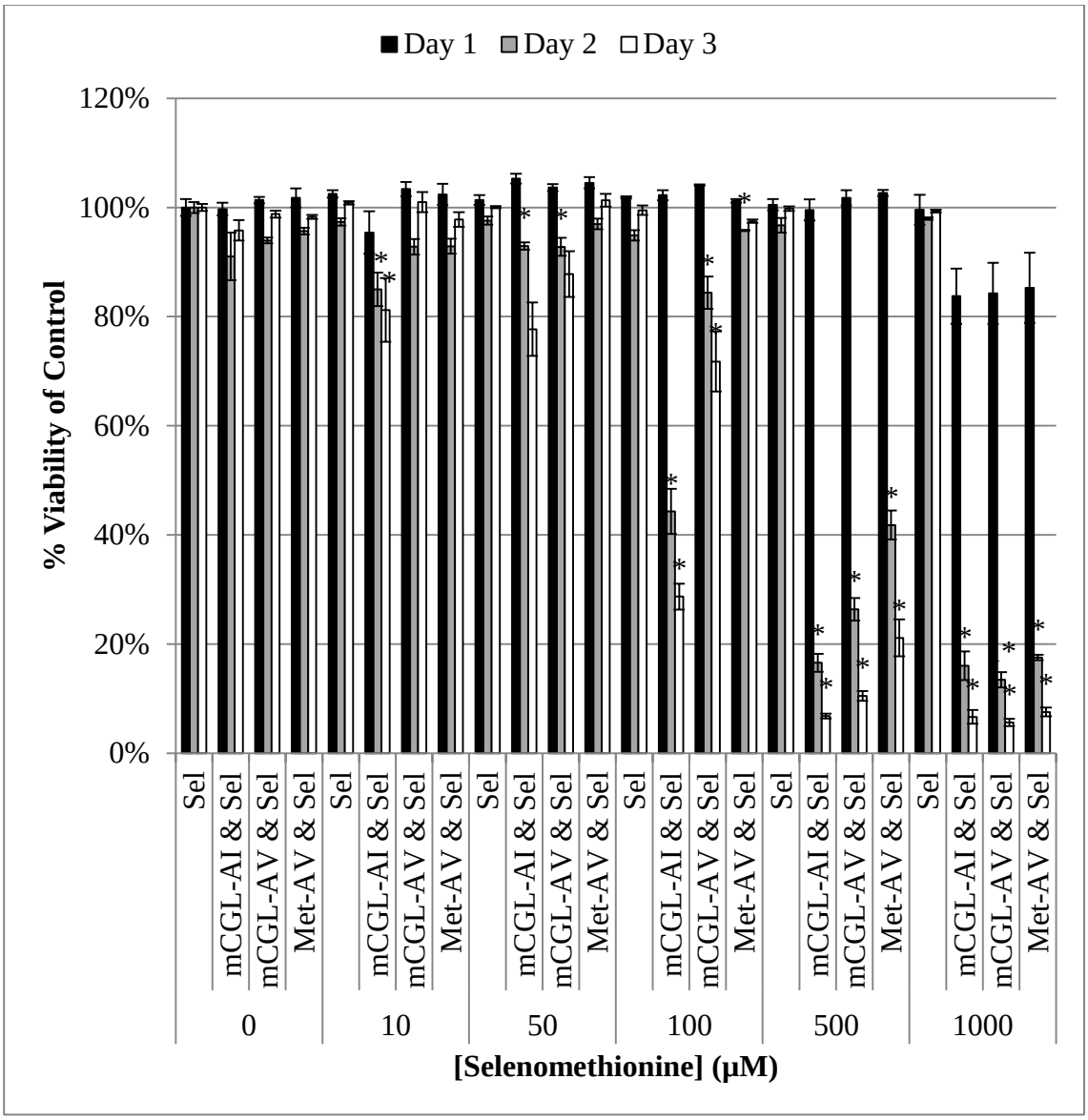

Figure 40. Comparison of the cytotoxic effect of mCGL-AI, mCGL-AV, and Met-AV enzyme prodrug therapy on 4T1 cells.
Groups that received fusion protein were treated on day 0. Selenomethionine was administered daily. Viability was determined by the Alamar Blue assay on days 1, 2, and 3 (black, gray, and white bars, respectively), and each sample was represented as a percentage of untreated control on each day. Statistical analysis was performed with a one-way ANOVA test with data presented as mean ± standard error (n = 3). Statistical significance vs. untreated control on the same day is denoted by *($p < 0.001$).

In Vivo Comparison of Annexin I and Annexin V Therapy Efficacy

Strong *in vitro* results for binding and cytotoxic effect of both mCGL-AI and mCGL-AV enzyme prodrug systems warranted a comparative *in vivo* study. Minor differences in *in vitro* binding and cytotoxicity failed to generate a clear picture of the superiority of one system over the other, especially considering how unknown effects of the tumor microenvironment may alter the therapeutic efficacies.

A small scale study was performed to examine the mCGL-AI and mCGL-AV enzyme prodrug systems for therapeutic efficacy in BALB/cJ mice bearing orthotopic 4T1 tumors. The data, shown in Figure 41, suggest that the minor advantage observed with the mCGL-AI system *in vitro* cytotoxicity studies does not translate to the *in vivo* environment. While both systems performed adequately with some growth suppression, the effect was more pronounced with the mCGL-AV system.

Despite improved binding strengths, the decreased binding stability observed with annexin I may be exacerbated *in vivo*. Annexin I, but not annexin V, contains a tyrosine phosphorylation site on the variable N terminal domain which can result in proteolytic truncation of the annexin I protein [150, 152]. The orientation of the fusion proteins (N to C) is mCGL-linker-annexin and proteolytic separation of the annexin I N terminal would release the enzymatic component of the fusion from the phosphatidylserine binding C terminal domain of the annexin. It is possible that while annexin I can exhibit improved initial binding, proteolysis ultimately occurs that releases a majority of the fusion protein. As evidenced from the strong *in vitro* cytotoxicity data, if proteolysis is limiting the therapeutic efficacy then it is likely occurring to a greater extent in the *in vivo* tumor environment.

The mildly stronger antitumor effect of the mCGL-AV system with the 4T1 *in vivo* model led to the selection of mCGL-AV as the primary candidate for further *in vivo* studies. While AI targeted systems may exhibit utility in future studies, selection of a single system for the immediate studies to follow was necessary for logistical purposes and feasibility.

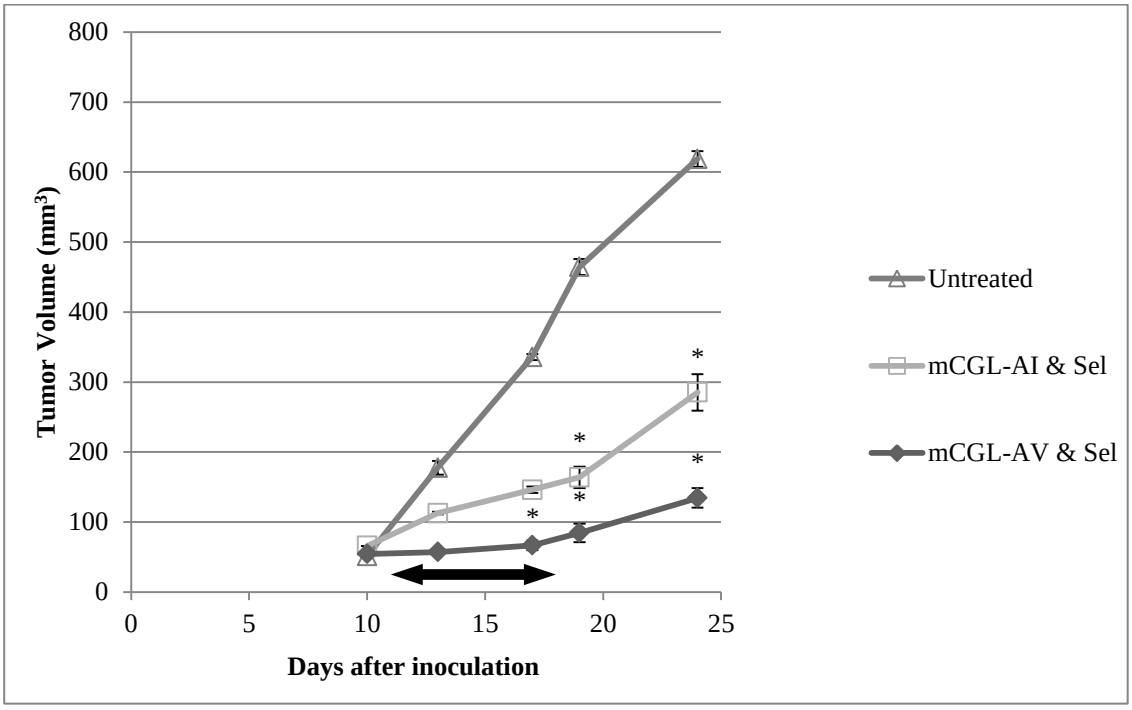

Figure 41. Comparison of efficacy of AV and AI targeted mCGL enzyme prodrug therapy with selenomethionine on orthotopic 4T1 tumors in BALB/cJ mice. mCGL-AV and mCGL-AI were administered daily (10 mg/kg IP). Selenomethionine (5 mg/kg IP) was administered 10 h post fusion protein administration. Treatment began on day 11 and continued until day 18 as indicated by the arrow. Statistical significance vs. untreated is indicated by *($p < 0.001$). No significant difference was observed between treatment groups. No negative effects were observed with either treatment. Data is presented as mean volume ± standard error (n = 6).

In Vivo Comparison of Protein Administration Method

Comparison of IV and IP administration of mCGL-AV suggested stronger efficacy using IP injections, as shown in Figure 42. It was originally anticipated that IV administration would result in more fusion protein entering circulation, hence enhancing therapeutic efficacy; however the opposite results were observed. After repeated administrations (daily), the tail vein became decreasingly accessible making this method unsuitable for daily injections. No problems were observed with daily IP administration of mCGL-AV.

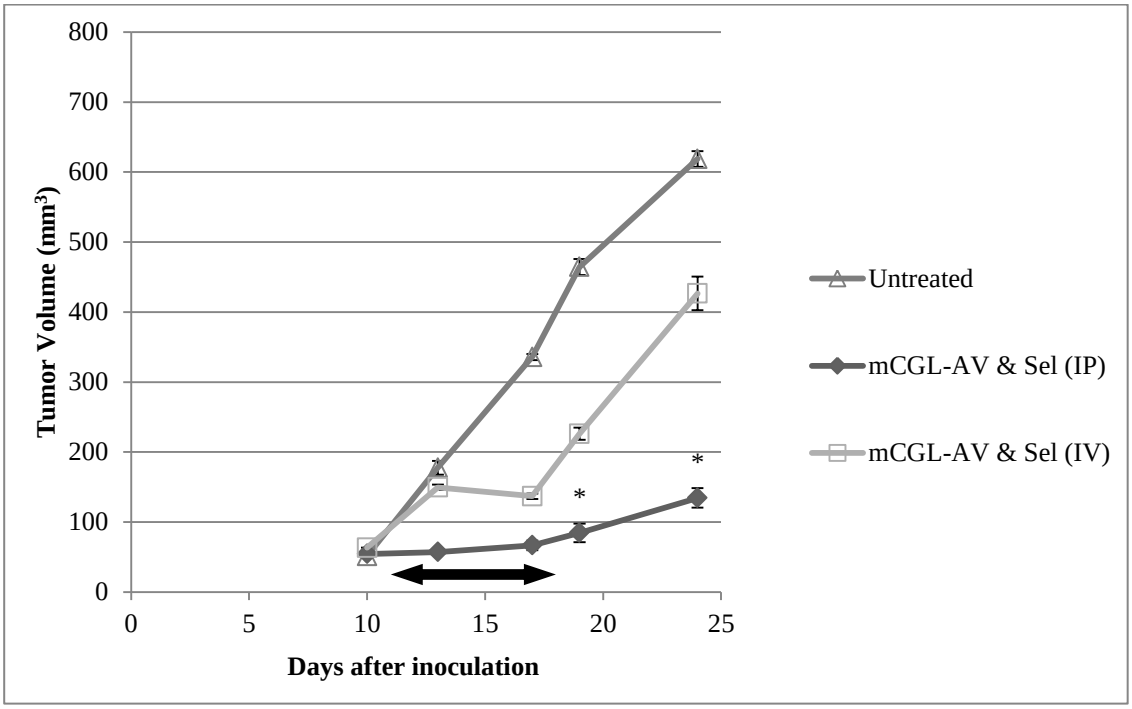

Figure 42. Intraperitoneal route of administration of fusion protein produces stronger antitumor effect than tail vein administration for orthotopic 4T1 tumors in BALB/cJ mice.
mCGL-AV was administered daily (10 mg/kg) either IP or IV. Selenomethionine (5 mg/kg IP) was administered 10 h post fusion protein administration. Treatment began on day 11 and continued until day 18 as indicated by the arrow. Statistical significance between IP and IV administration is indicated by *($p < 0.05$). Data is presented as mean volume ± standard error (n = 6).

In Vivo mCGL-AV Plasma Clearance

Clearance of the mCGL-AV protein from the circulation of BALB/cJ mice occurred with pharmacokinetics similar to the other enzyme prodrug systems in SCID mice. Complete clearance occurred within 10 h of a 10 mg/kg intraperitoneal administration of mCGL-AV (Figure 43). Interestingly, a higher peak concentration of mCGL-AV was observed when compared to other enzyme prodrug systems. This difference is most likely mouse strain dependent since the protein properties are similar. Alternatively, insufficient peak resolution could be a factor causing observed but not actual differences that could be resolved with higher frequency sampling; however the pharmacokinetic study was simply designed for confirmation of protein entrance into circulation and clearance by a specific time point (10 h).

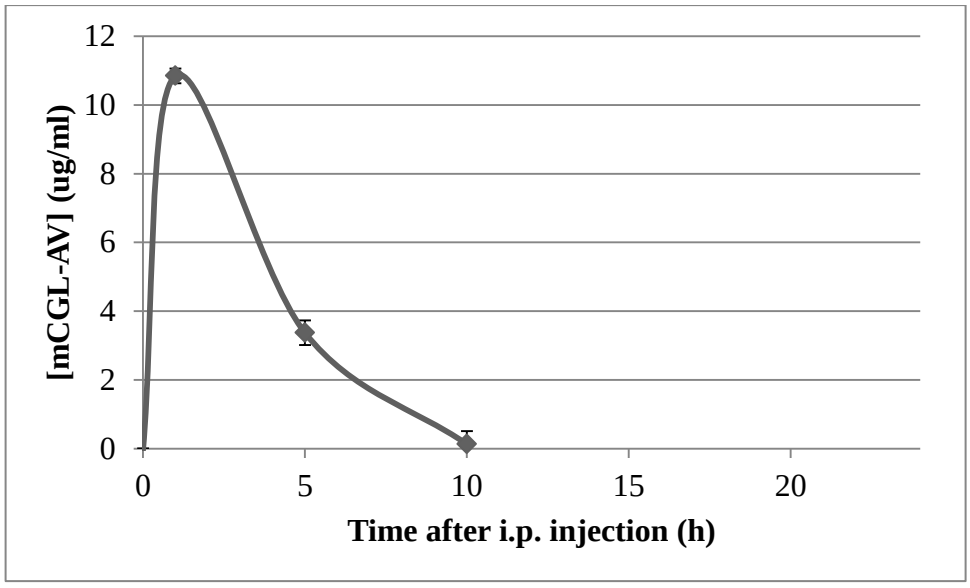

Figure 43. mCGL-AV clears from the circulation of BALBC/cJ mice in <10 h.
An ELISA assay for mCGL-AV was performed on serum samples at intervals following intraperitoneal administration of mCGL-AV at 10 mg/kg. Data is presented as mean ± standard error (n = 3).

Efficacy and Immunogenicity of Met-AV vs. mCGL-AV

The reasoning behind the development of the mCGL-AV system, consisting entirely of native protein with the exception of the three amino acid mutations, was the theorized immunogenicity in mice and anticipated immune reaction in humans of the comparable bacterial Met-AV system. A reduction of immunogenicity was a prerequisite for any consideration of clinical trials regardless of Met-AV enzyme prodrug system performance and immunogenicity in mice. The three amino acid mutations in the human CGL, equivalent to those performed in this study for the mouse CGL, are not anticipated to produce any immune response through computational analysis [169].

A basic analysis was conducted in mice to examine fusion protein specific antibody titers as well as antitumor efficacy. The Met-AV system was included as positive control, expected to elicit an immune response based on the enzyme origination from *P. putida*. The treatments were administered daily over three weeks to immune competent BALB/cJ mice bearing 4T1 orthotopic tumors. No anaphylactic response or other negative side effects were observed with either treatment group. For the mice injected daily with Met-AV, an analysis of blood samples collected weekly during the treatment revealed the presence of Met-AV specific antibodies within 7 days of the start of the treatment. By the third week, Met-AV specific antibody levels were an order of magnitude higher than after one week of treatment. Contrary to the Met-AV results, no mCGL-AV specific antibodies were detected through three weeks of treatment. Antibody titer results are summarized in Table 10.

Observation of tumor volumes showed tumor progression to occur significantly faster with the Met-AV system compared to the mCGL-AV system, as shown in Figure 44. Significant tumor progression during Met-AV and selenomethionine treatment within one week of treatment initiation suggests that the elicited antibody response has neutralizing capabilities, rendering the therapy ineffective and indistinguishable from untreated mice. The mCGL-AV system does ultimately revert from tumor growth suppression to tumor progression, as observed with the other enzyme prodrug systems in SCID mice. Eventual tumor progression is hypothesized to be a result of the hypoxic response to the vascular targeted therapy rather than the generation of neutralizing antibodies, which is supported by the antibody titer data.

BALB/c mice are considered a conventional model for immunogenicity analysis of mammalian proteins though differences between the mouse and human immune system limit utility [256]. In fact, the BALB/c model may overestimate protein immunogenicity compared to the human response [256, 257]. A more comprehensive immunogenicity analysis could include computational analysis and use of HLA-transgenic mice that have a stronger correlation with human T-cell responses [258]. Any animal or computational immunogenicity analysis though has limited utility, as the human response remains unpredictable and even non-human primate models provide inadequate comparisons [162, 258]. The ultimate evaluation for immunogenicity would require FDA regulated trials [168], which would first look for the development of a specific antibody response [161]. The lack of a specific antibody response in mice is certainly an important achievement and the first criterion should any adaptation of the therapy advance beyond preclinical studies in the future.

Table 10. Fusion protein specific IgG + IgM titers in BALB/cJ mice improved with daily administration of mCGL-AV over Met-AV (10 mg/kg IP)

	Day 0	Day 7	Day 14	Day 21
mCGL-AV	Not detected	Not detected	Not detected	Not detected
Met-AV	Not detected	10^{-4}	10^{-4}	10^{-5}

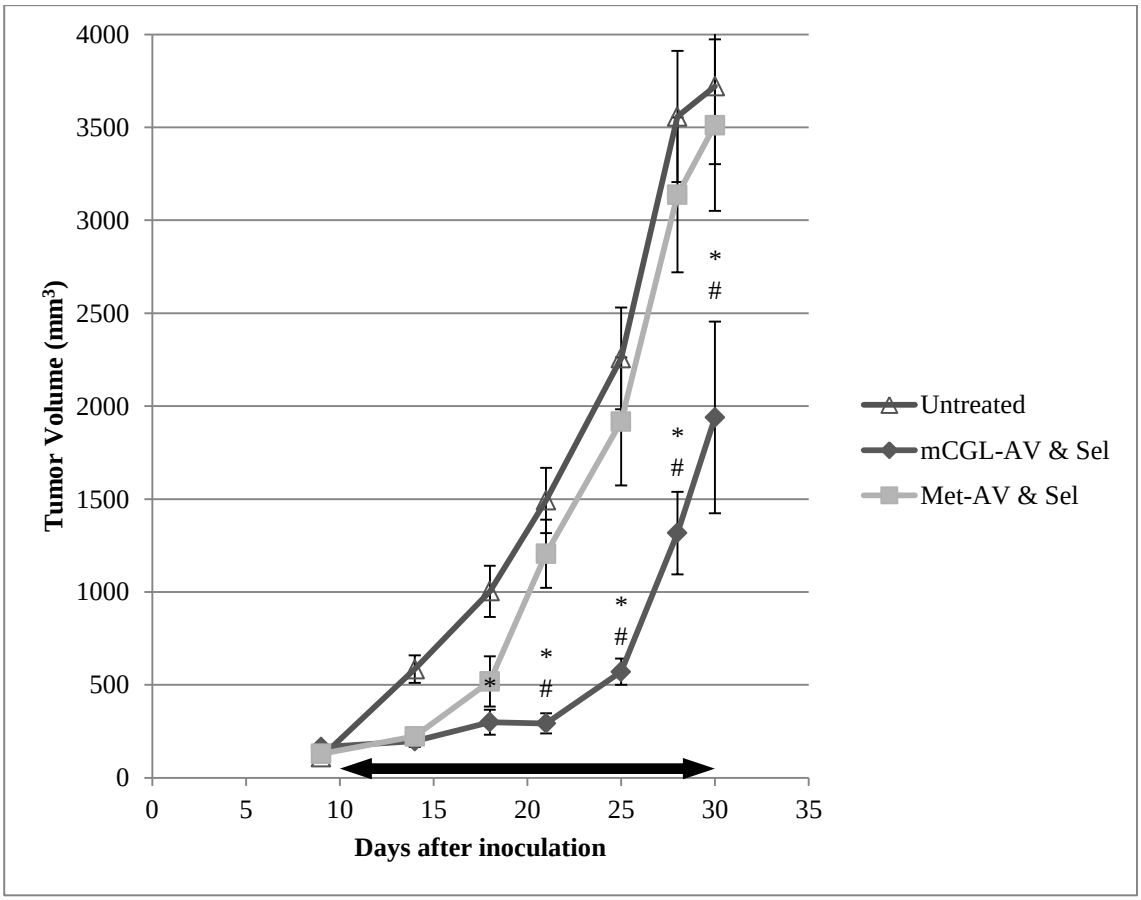

Figure 44. Comparison of efficacy of mCGL-AV and Met-AV enzyme prodrug therapy with selenomethionine on 4T1 tumors in BALB/c mice.
mCGL-AV and Met-AV were administered daily (10 mg/kg IP). Selenomethionine (5 mg/kg IP) was administered 10 h post fusion protein administration. Treatment began on day 10 and continued until day 30 as indicated by the arrow. Statistical significance vs. untreated is indicated by *($p < 0.001$). Statistical significance of mCGL-AV and Sel vs. Met-AV and Sel is indicated by #($p < 0.001$). No negative effects were observed with either treatment. Data is presented as mean volume ± standard error (n = 5-10).

Rapamycin and Cyclophosphamide Combination Therapies

Despite a lack of neutralizing antibodies and a model with a functional immune system, the mCGL-AV and selenomethionine enzyme prodrug system failed to eliminate 4T1 tumors from the mammary fat pad of BALB/cJ mice. Genomic instability significantly contributes to a tumor's adeptness at immune evasion and development of treatment resistance. As genetic variation accumulates over time, so does the tumor's ability to avoid immune detection or therapeutic destruction [259]. Delayed and incomplete antitumor responses beyond the early stages of tumor development fail to eliminate small populations of cells that have adapted to the immune response and other therapeutic conditions. Tumor repopulation occurs according to Darwinian logic in which the cancer cells that have successfully adapted to treatment conditions and any immune response proliferate to a greater extent than other cells. Tumor regrowth results despite the continuance of initially successful treatment conditions. These properties of cancer cells result in the development of the biological hallmarks of cancer and necessitate early and effective elimination of the cancer, likely through multiple mechanisms.

The hypoxic response, theorized to be augmented due to the vascular targeted approach of the therapy and resultant reduction in blood flow [157], was addressed through the incorporation of rapamycin with the enzyme prodrug therapy. Additionally, the cytotoxic effect against the tumor vasculature could allow for direct release of tumor antigens into circulation, so combination with cyclophosphamide was included to enhance antitumor immunity.

When examining the rapamycin and cyclophosphamide combinations with the enzyme prodrug therapy in BALB/cJ mice bearing aggressive 4T1 mammary tumors, shown in Figure 45, it is apparent that the rapamycin combined with the enzyme prodrug therapy produces beneficial antitumor effects. The mCGL-AV and selenomethionine system alone do produce a significant improvement in tumor volume over untreated mice; however the effect is not sustainable as previously observed. Rapamycin without the mCGL-AV system does exhibit some effect alone; however the advantage of the combined therapies produces the strongest antitumor results. Cyclophosphamide alone or in combination with the mCGL-AV system or rapamycin does not appear to have a significantly beneficial effect on tumor volumes, though its inclusion does not seem to negatively impact the therapies' capacities to restrict tumor progression. Neither rapamycin, cyclophosphamide, nor the mCGL-AV system were administered at doses high enough to elicit side effects or weight loss in the mice, as shown in Figure 46.

The injection of 4T1 cells into the mammary fat pad results in the formation of highly aggressive tumors that rapidly form pulmonary metastases. For the majority of mice, metastases are the limiting factor for survival rather than the growth of the primary tumor. Upon examining the survival curves, shown in Figure 47, and median survivals of each group, shown in Table 11, it is apparent that cyclophosphamide exhibits a beneficial effect on survival even to some degree without any combination treatment, though significance is established only when combined with the enzyme prodrug therapy and rapamycin. The enhanced median survival suggests that cyclophosphamide may indeed be stimulating an antitumor immune response that limits

the progression of the metastases, since improved median survival is not only a function of primary tumor volume, particularly in the case of cyclophosphamide alone.

The mCGL-AV enzyme prodrug system also exhibits an enhancement of median survival to a degree similar to that with the presence of cyclophosphamide. With this particular 4T1 tumor model where death is predominantly a function of metastatic progression, an increased survival with the mCGL-AV system suggests some anti-metastatic action, either through phosphatidylserine exposure on metastatic lesions or action on the primary tumor limiting metastatic formation. Minimal enhancement of survival is observed with the mCGL-AV system combined with cyclophosphamide when compared to either cyclophosphamide or the enzyme prodrug system alone. As expected, the individual constituents of the enzyme prodrug system itself do not have a significant impact on survival.

The main intended mechanism of action for rapamycin is against the primary tumor and the hypoxic response and was not theorized to have reducing effect on metastatic progression (in fact some studies report the contrary, likely from the immunosuppressive properties of rapamycin [178]). Interestingly, rapamycin combined with the enzyme prodrug therapy did enhance survival compared to the untreated group.

The complete combination of rapamycin, cyclophosphamide, and the mCGL-AV enzyme prodrug system does have a significant beneficial effect on survival, exceeding the benefit seen with any of the individual components or combinations of the individual components. Primary tumor volume for the complete combination is similar to the combination lacking cyclophosphamide; however the inclusion of cyclophosphamide clearly enhances survival benefits. When examining both primary

tumor volume and survival, the two primary designators of preclinical therapeutic success, the combination of cyclophosphamide, rapamycin, and mCGL-AV and selenomethionine provide greatest benefit.

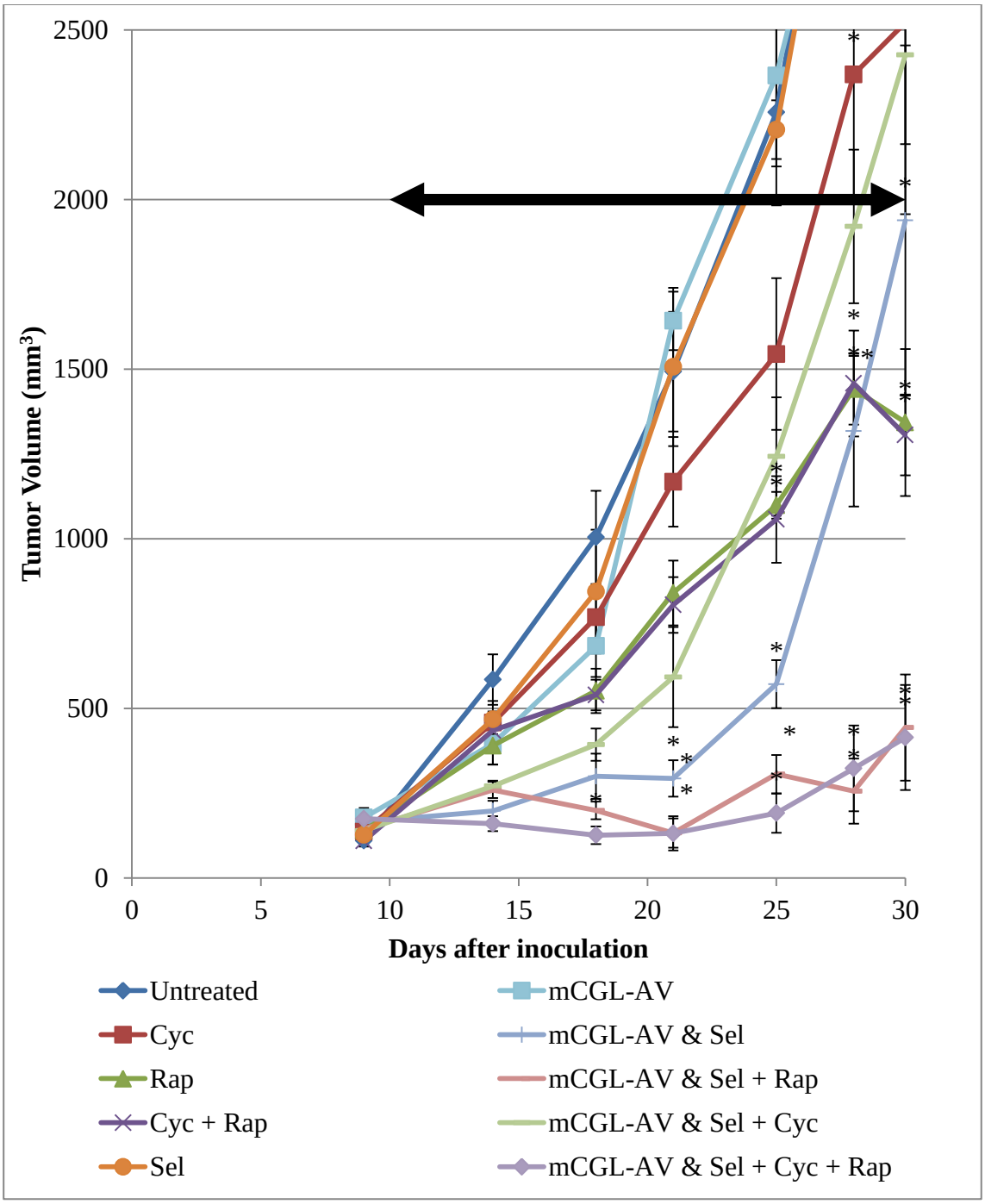

Figure 45. Combination therapy effects on orthotopic 4T1 tumor volume in BALB/cJ mice.

mCGL-AV was administered daily (10 mg/kg IP). Selenomethionine (5 mg/kg IP) was administered 10 h post fusion protein administration. Rapamycin (5 mg/kg IP) and cyclophosphamide (10 mg/kg IP) are administered daily. Treatment began on day 10 and continued until day 30 as indicated by the arrow. Statistical significance vs. untreated is indicated by *($p < 0.001$). Data is presented as mean volume ± standard error (n = 5 to10 initially, though does drop to as low as 2 as survival decreases towards the conclusion of the study).

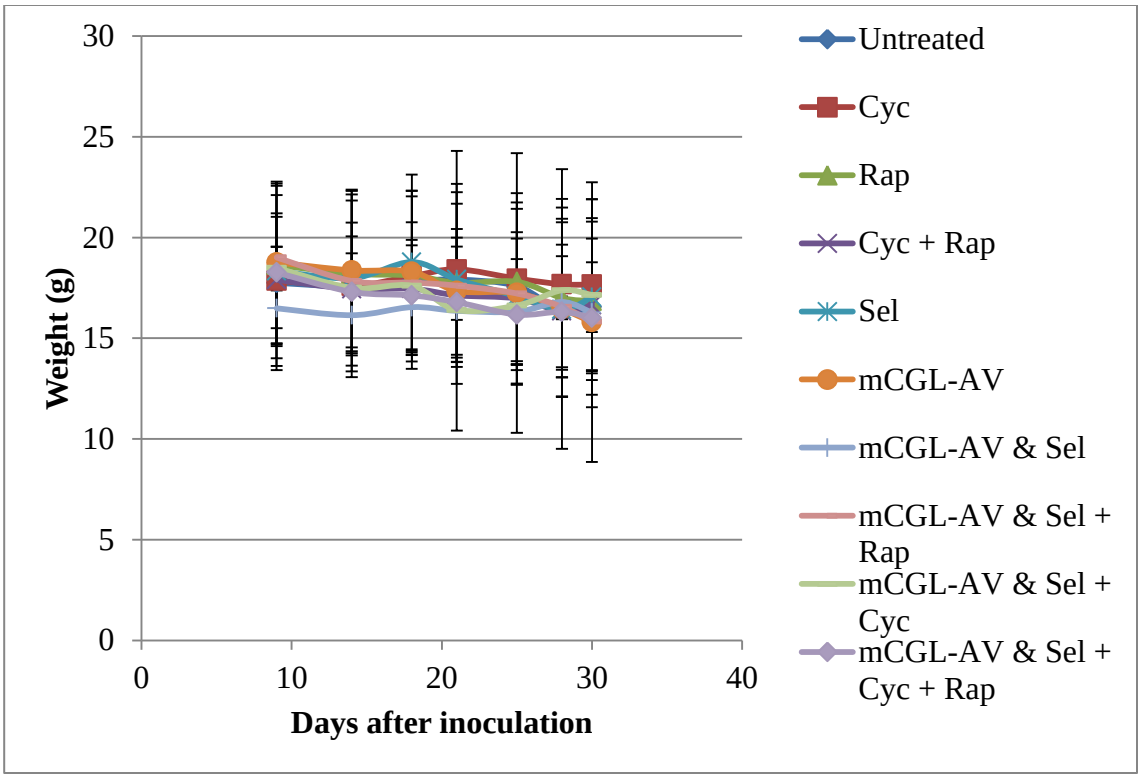

Figure 46. Minimal effect of mCGL-AV system and combination therapies on BALB/cJ mouse weight.

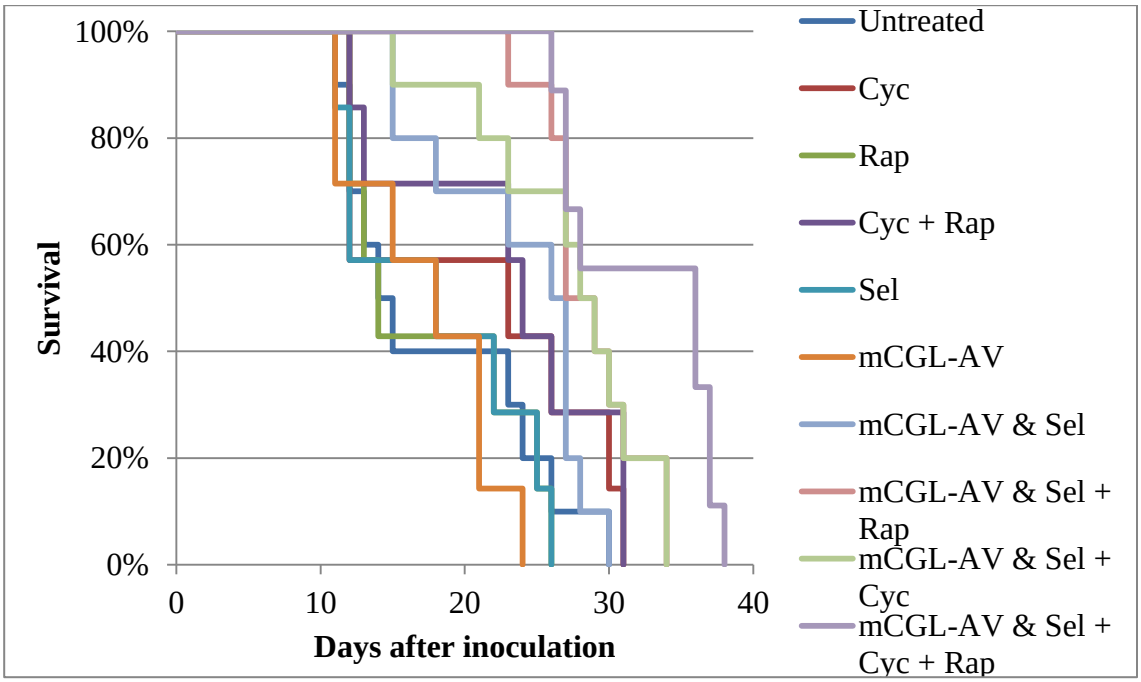

Figure 47. Kaplan-Meier survival curves for combination therapies.

Table 11. Median mouse survival and log-rank *p*-values of Kaplan-Meier survival curves with indicated significance (*).

	Median Survival	*P*-value (vs. Untreated)	*P*-value (vs. mCGL-AV & Sel)
Untreated	14 days		
Cyc	23 days	0.2739	
Rap	14 days	0.7830	
Cyc + Rap	24 days	0.1315	
Sel	18 days	0.8813	
mCGL-AV	18 days	0.5215	
mCGL-AV & Sel	26 days	0.1005	
mCGL-AV & Sel + Rap	27 days	* 0.0015	0.0303
mCGL-AV & Sel + Cyc	28 days	0.0079	0.0560
mCGL-AV & Sel + Cyc + Rap	36 days	* 0.0002	* 0.0014

Therapeutic Contributions of Combination Constituents

Further analysis, primarily comprised of immunohistochemistry studies, was performed to confirm the general hypothesized mechanisms of the antitumor responses. The degree to which the targeted mechanisms are successful or unsuccessful could help guide the design of future combination studies. The cytotoxic effect on the cancer cells, theorized to result primarily from the action of the enzyme prodrug therapy, was further evaluated with immunohistochemical staining for apoptosis (activated caspase-3) and proliferation (ki-67). The reduction of the hypoxic response, the reason for inclusion of rapamycin, was evaluated through immunohistochemical staining of HIF-1α and quantification of tumor necrosis. Representative images from each of these experimental approaches are presented in Figure 48. Evaluation of cyclophosphamide's immunostimulatory and anti-metastatic effects was performed through the quantification of regulatory T cells in the spleen and metastatic nodules in the lungs.

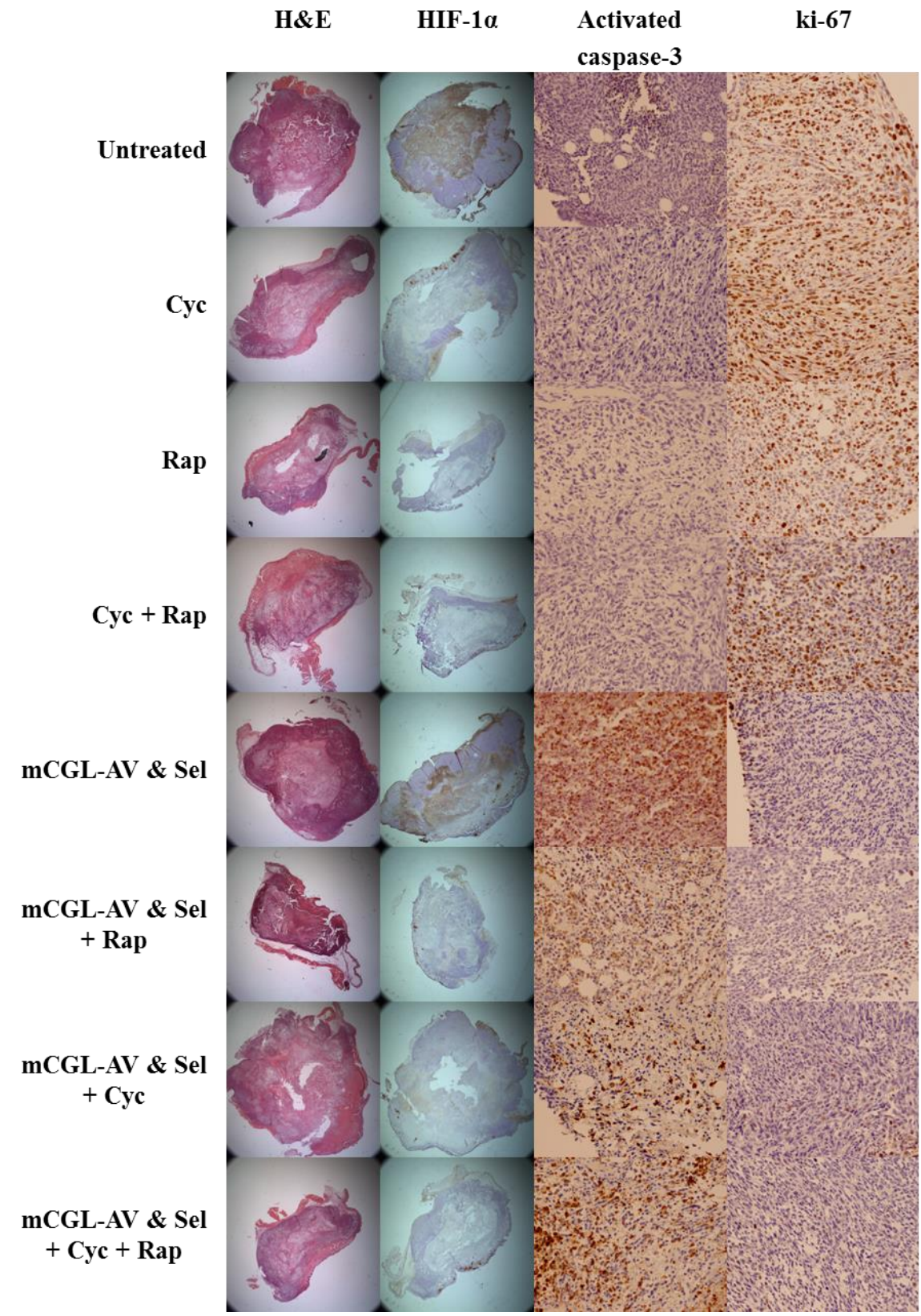

Figure 48. Representative immunohistochemistry images.

The extrinsic and intrinsic apoptotic pathways, extrinsic involving the death receptors and the intrinsic involving cell stress causing mitochondrial release of cytochrome c, converge with the proteolytic cascade and activation of caspase-3 [260]. The presence of activated caspase-3 indicates forthcoming apoptosis (though necrosis is possible), and the data in Figure 49 suggest the enzyme prodrug therapy results in increased activation of apoptotic pathways. Evidence also exists that while cell death does occur, caspase-3 activation also results in a mechanism that stimulates the repopulation of the tumor from the small proportion of surviving cells [261], suggesting that this response could be further explored in the prevention of tumor regrowth.

Staining for ki-67, a common marker for proliferative activity [262, 263], displayed the inverse trend of that observed with activated caspase-3, as anticipated. The quantification of ki-67 staining is presented in Figure 50. Based on the data showing increased levels of apoptosis in mCGL-AV and selenomethionine treated groups, decreased levels of proliferation in the enzyme prodrug treated groups is unsurprising.

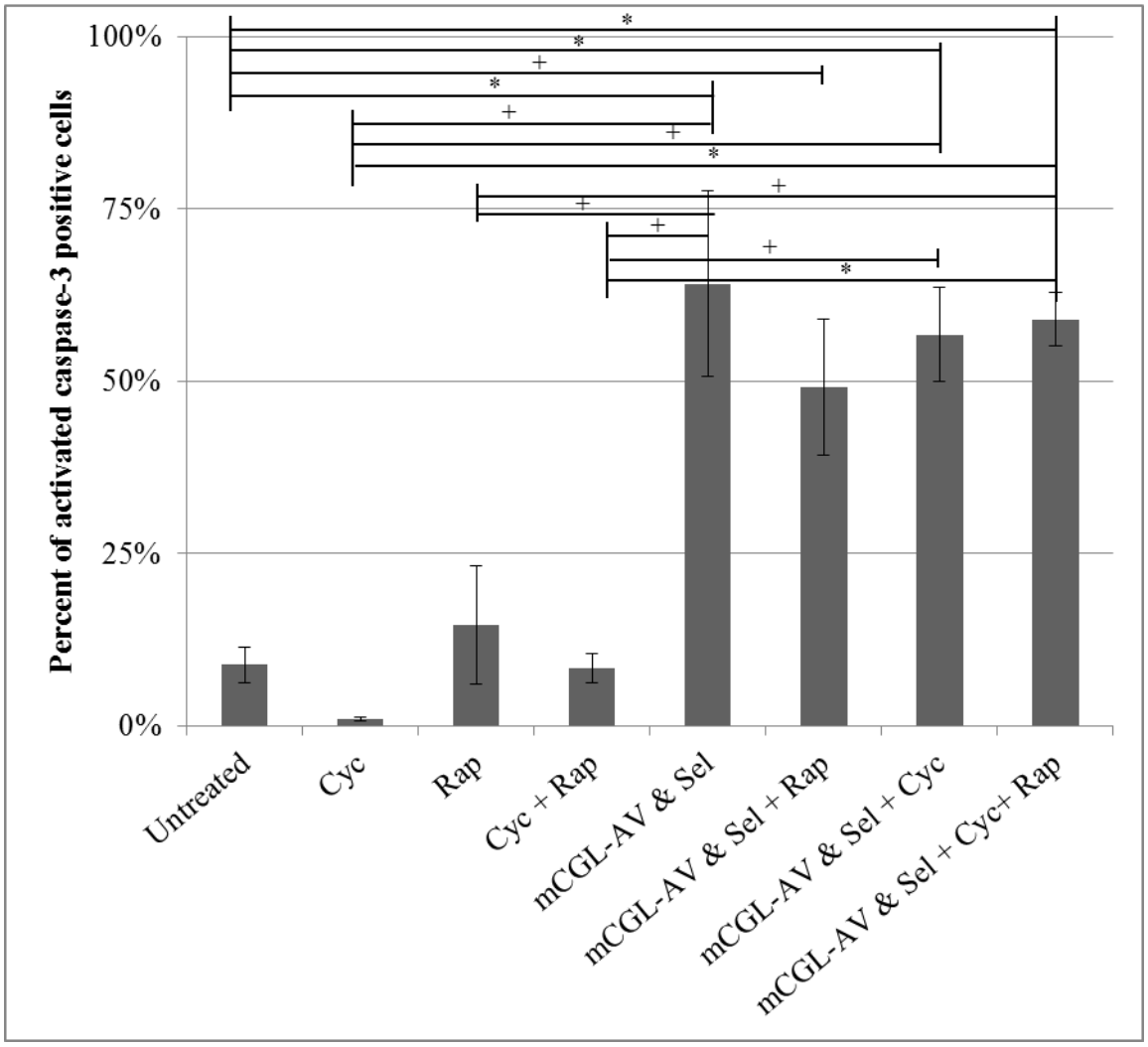

Figure 49. Enzyme prodrug treatment for 3 weeks results in increased staining of apoptosis marker activated caspase-3 in mice with orthotopic 4T1 tumors.
A Nikon Eclipse E800 compound microscope was used to capture 15 fields of view of tumor sections from 3 mice per group (necrotic tumor cores were excluded). Immunostaining for activated caspase-3 was quantified as percent of cells (hematoxylin counterstain) with DAB and is presented as mean ± standard error. Statistical significance between groups is indicated by +($p < 0.01$) or *($p < 0.001$).

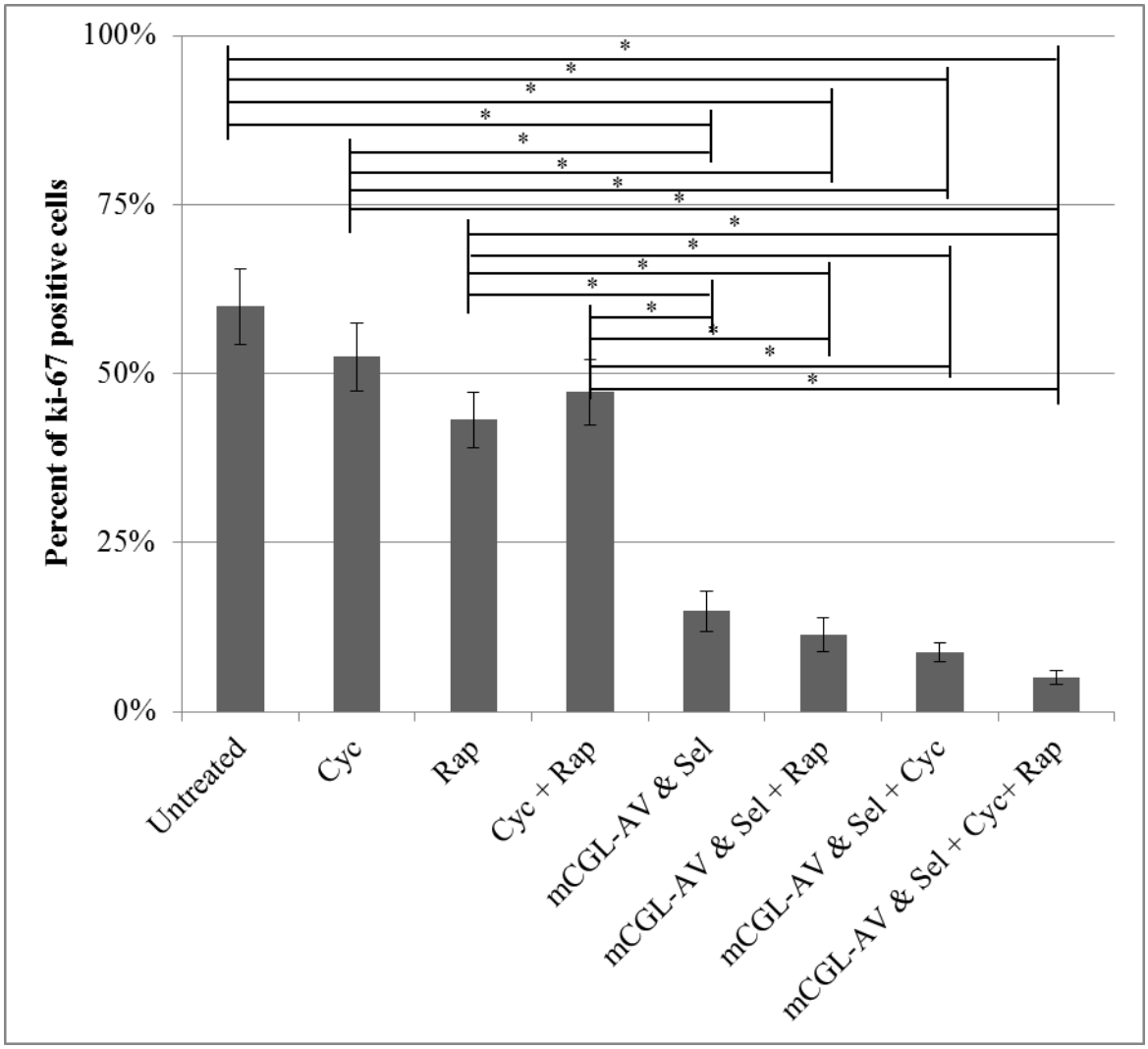

Figure 50. Enzyme prodrug treatment for 3 weeks results in decreased staining of proliferation marker ki-67 in mice with orthotopic 4T1 tumors.
A Nikon Eclipse E800 compound microscope was used to capture 15 fields of view of tumor sections from 3 mice per group (necrotic tumor cores were excluded). Immunostaining for ki-67 was quantified as percent of cells (hematoxylin counterstain) with DAB and is presented as mean ± standard error. Statistical significance between groups is indicated by *($p < 0.001$).

Intratumoral hypoxia frequently results in necrotic tumor cores, particularly with *in vivo* models bearing tumor grafts. Some degree of coagulative necrosis was apparent in tumor sections from all treated and untreated groups, with the quantification shown in Figure 51. The fast-growing and aggressiveness of the 4T1 mammary tumors results in

high necrotic percentages in untreated tumors as the tumor mass outgrows its blood supply. The targeted mCGL-AV enzyme prodrug therapy may be expected to actually increase necrosis since it is known to reduce tumor blood flow [157], however minimal increase of necrotic percentage compared to untreated mice was observed. Reduced necrosis in tumor sections treated with rapamycin is unsurprising given the role of mTOR-dependent tumor necrosis factor-α (TNF-α) related necrosis [189, 264], potentially through the inhibition of TNF-α production [265]. The rapamycin induced reduction of necrosis remains independent from the enzyme prodrug therapy effects on apoptosis and proliferation. Reduced necrosis appears to be entirely dependent on the rapamycin treatment, and apoptosis and proliferation effects appear to be solely a function of the administration of the enzyme prodrug therapy.

The primary intended downstream target of mTOR inhibition with rapamycin and the main controller of the hypoxic response is HIF-1α. Necrosis is a strong indicator of hypoxia and the subsequent enhanced expression of HIF-1α, which is expected to be highest in the surrounding viable cancer tissue [4]. Quantification of HIF-1α staining of tumor sections is shown in Figure 52. The decreased levels of HIF-1α in rapamycin treated mice correlate with the observed decreased necrotic region, as anticipated. Unexpectedly, low dose cyclophosphamide also resulted in a drastic reduction of HIF-1α expression in the tumor sections. The effect was not as pronounced when combined with the enzyme prodrug therapy, though results were variable. Implications of these observations are unknown as the necrotic tumor percentages were not reflective of a cyclophosphamide induced reduction in HIF-1α expression. Additionally, the quantitative data presented in Figure 52 represents HIF-

1α staining as a regional percentage of tumor area and does not adequately quantify the small but strong HIF-1α "hot spots" apparent in the cyclophosphamide group shown in Figure 48.

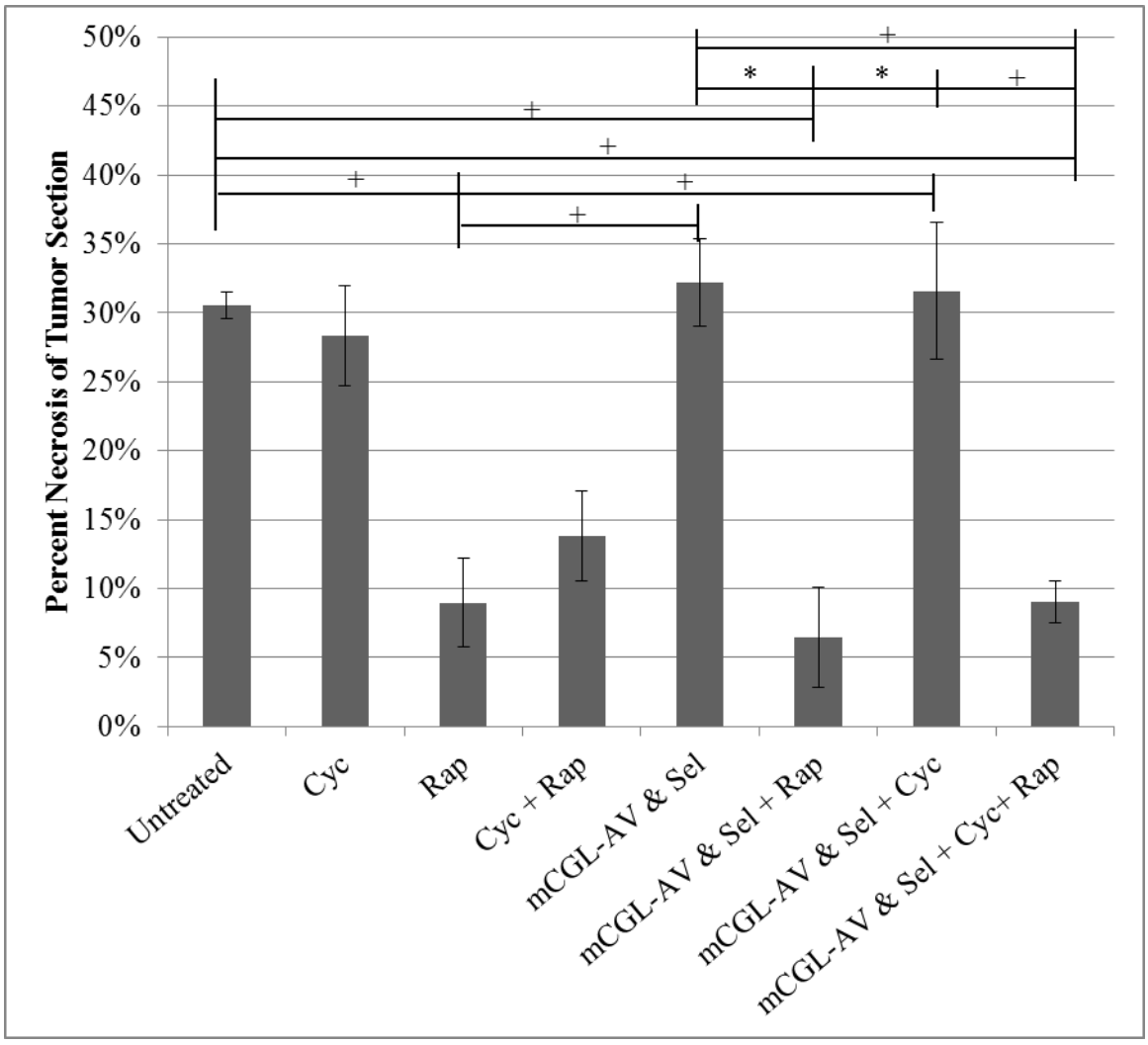

Figure 51. Rapamycin reduces percent necrosis in 4T1 tumor sections.
Necrotic regions were determined from hematoxylin and eosin stained tumor sections and quantified from whole section images of mice sacrificed after 3 weeks of treatment. Data is presented as mean ± standard error (n = 3 mice). Statistical significance between groups is indicated by +($p < 0.01$) or *($p < 0.001$).

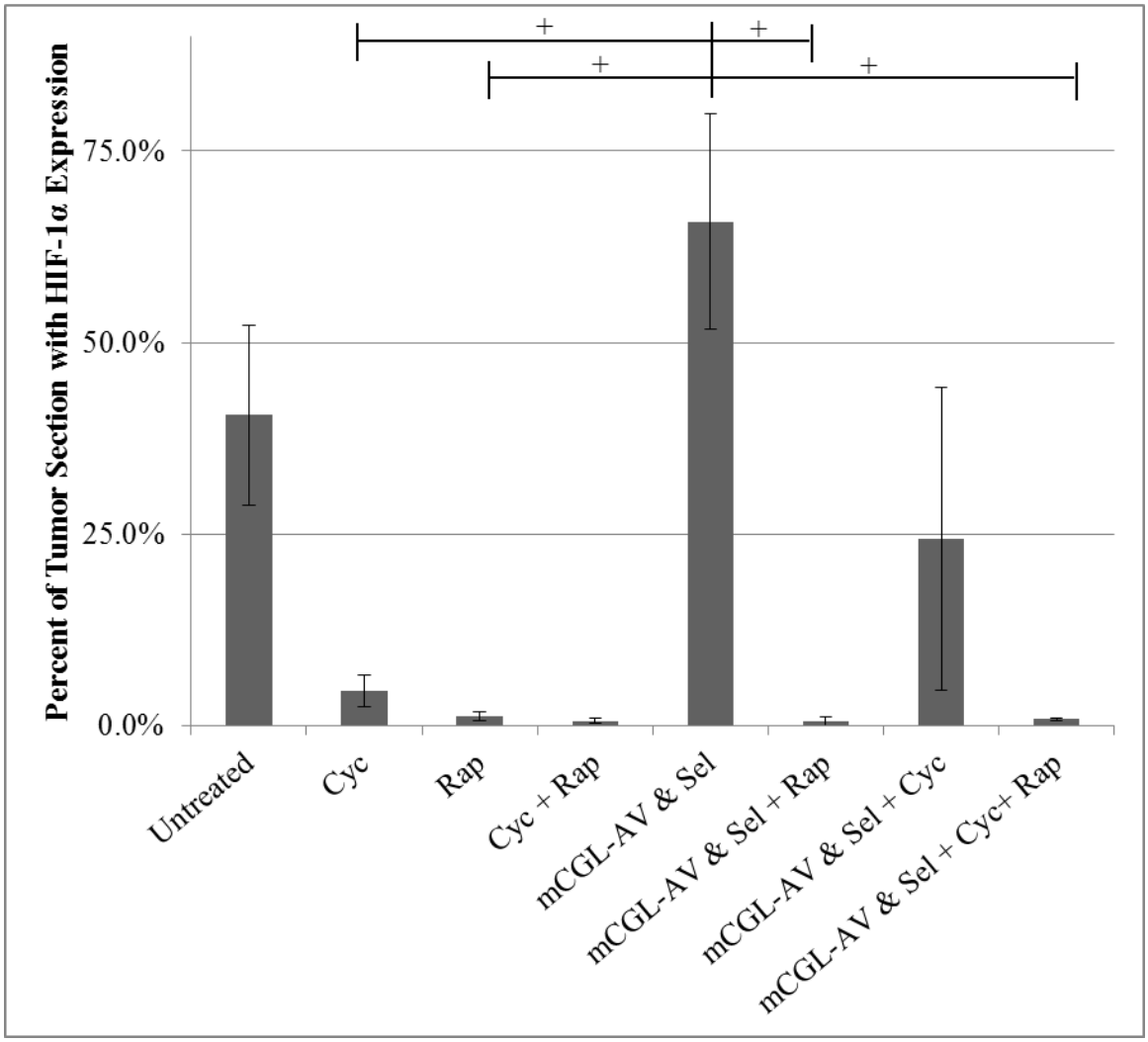

Figure 52. Rapamycin reduces percent of tumor expressing HIF-1α. Immunohistochemistry staining of HIF-1α with DAB development was quantified from whole section images of mice sacrificed after 3 weeks of treatment. Data is presented as mean ± standard error (n = 3 mice). Statistical significance between groups is indicated by +($p < 0.01$) or *($p < 0.001$).

Metastatic progression is hypothesized as the predominant cause of death in the mice bearing 4T1 mammary tumors; hence determination of the presence of metastatic nodules holds predictive therapeutic value [266]. Individual metastatic nodules on the lungs of tumor bearing mice are graphically presented as a function of nodule size, with nodule quantities summarized in Figure 53. A logarithmic scale is utilized for the

graphical display of metastatic nodules, as the sizes are fairly normally distributed on the logarithmic scale, explained by the expected exponential growth of the cells at the metastatic sites [267, 268]. The quantities of metastatic nodules observed for each experimental group correlate well with the observed survival data for all groups except the mCGL-AV and Sel + Rap group.

Cyclophosphamide provides clear benefit through reduced numbers of metastases. The enzyme prodrug therapy also shows reduced numbers and size of metastatic nodules. Rapamycin, however, exhibits no benefit regarding metastatic size or quantity. When rapamycin is combined with the enzyme prodrug therapy, metastatic progression is actually enhanced compared to the enzyme prodrug therapy alone, contrary to the observed survival data. Enhanced metastatic formation with rapamycin, likely a result of its immunosuppressive properties, can be attenuated with a reduced dose (reduction from 5 mg/kg to 1.5 mg/kg eliminated metastatic progression, though the antitumor effect at the reduced dose is unreported) [178]. Fortunately, rapamycin does not act in an antagonistic manner with cyclophosphamide and the complete combination of rapamycin, cyclophosphamide, and mCGL-AV and selenomethionine resulted overall in a strong reduction of metastatic nodules.

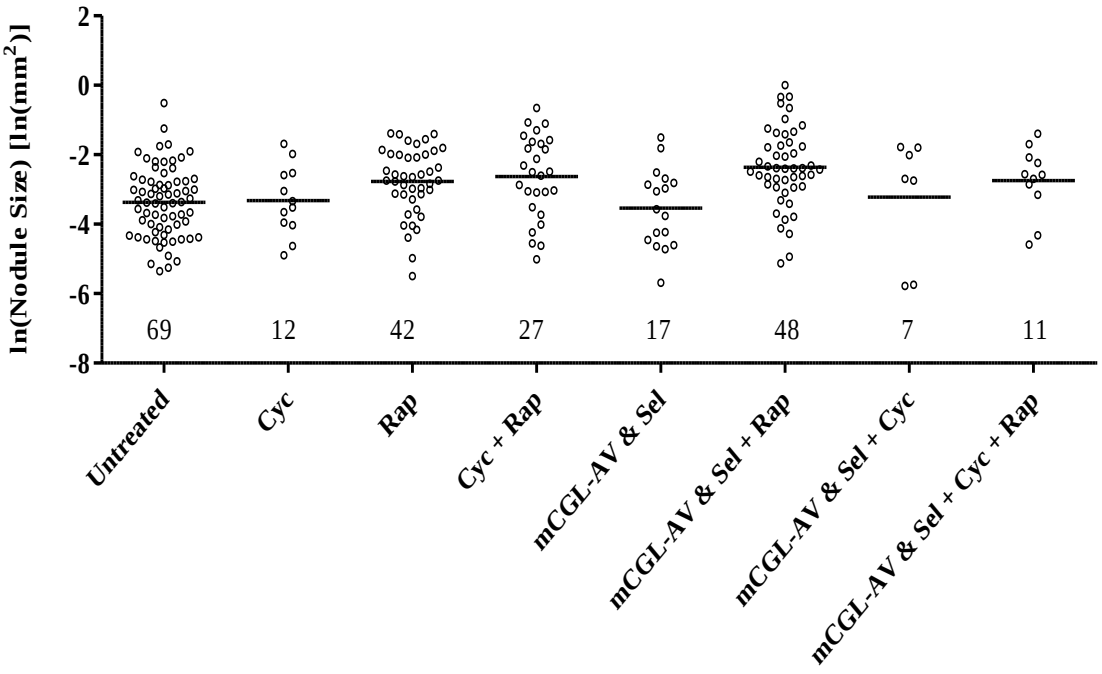

Figure 53. Cyclophosphamide reduces number of pulmonary metastasis in orthotopic 4T1-TdTomato BALB/cJ model.
A Leica stereomicroscope with an automated ImageJ macro was used to quantify fluorescent nodules in the lung. Data is shown as individual nodules from the lungs of three mice per group after 3 weeks of treatment on a log-normal scale, as the nodule sizes were logarithmically distributed. Median nodule size on the log scale is marked. Total nodules per group (n = 3 mice) is summed and shown.

To confirm cyclophosphamide's anti-metastatic activity as a result of reduced regulatory T cell numbers, flow cytometry of the spleens of the mice was performed. Representative raw flow cytometry data, as well as gating methodology for the quantification of the regulatory T cells, is presented in Figure 54. The quantification of the regulatory T cell levels for each experimental condition is shown in Figure 55. A drastic reduction in regulatory T cell levels upon cyclophosphamide treatment was not observed as expected to corroborate the anti-metastatic activity of cyclophosphamide.

Perhaps, the most viable comparisons presented in Figure 55 are actually between the mCGL-AV& Sel, mCGL-AV & Sel + Cyc, and mCGL-AV & Sel + Cyc + Rap, as those experimental groups presented with similar levels of metastases and in a similar state of health at the time of data collection. Among those groups, cyclophosphamide did cause a mild reduction in regulatory T cell levels.

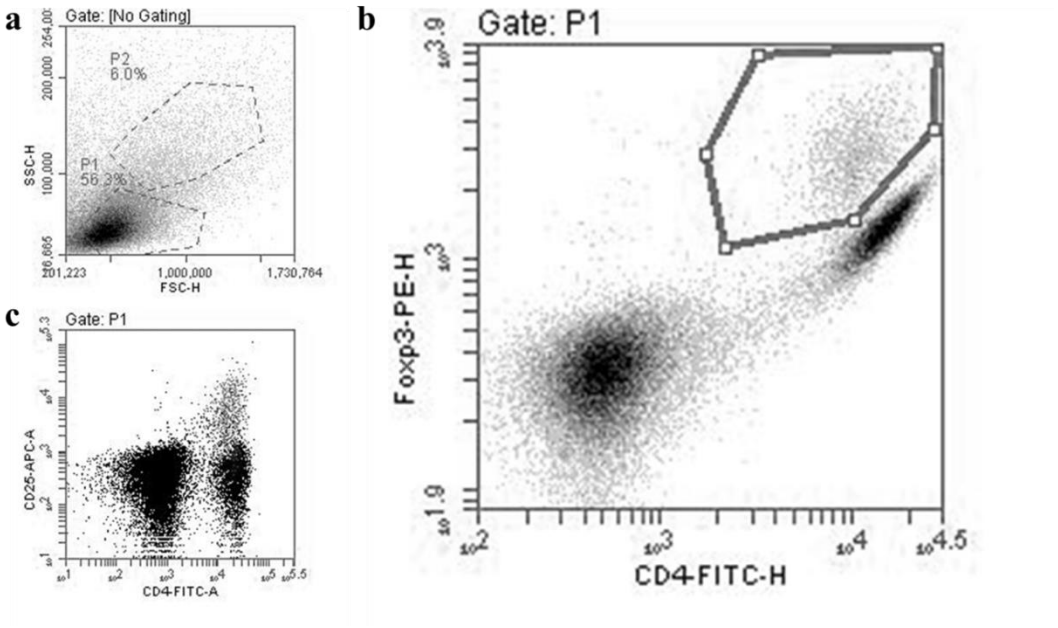

Figure 54. Flow cytometry gating of regulatory T cells from the spleens of BALB/cJ mice.
Lymphocytes were first gated with forward and side scatter (a, P1). Regulatory T cells were considered to be CD4+ and FoxP3+ and quantified (b). CD+ FoxP3+ (c, light gray) are >90% CD25+.

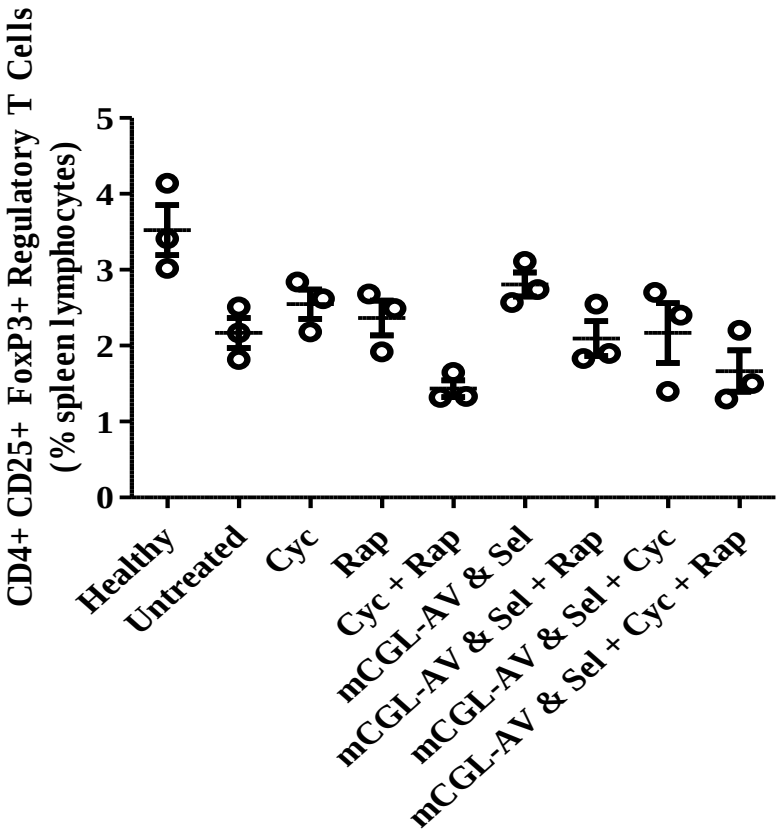

Figure 55. Effects of combination treatments of regulatory T cell levels in the spleen.
CD4+ CD25+ FoxP3+ regulatory T cell levels were quantified with flow cytometry and are presented as a percentage of spleen lymphocytes in BALB/cJ mice with 4T1 grafts after 3 weeks of treatment or healthy BALB/cJ mice with no tumor. Data is mean ± standard error (n = 3 mice). Statistical significance was observed compared with healthy mice, but no statistical significance was observed between groups bearing tumors.

Despite similar levels of regulatory T cells, rapamycin clearly does not impart the anti-metastatic properties exhibited by cyclophosphamide treated groups. Taken together, Figure 53 and Figure 55 support the expectation that regulatory T cell quantities alone are not entirely responsible for the success or failure of pulmonary metastatic formations. High quantities and sizes of metastatic nodules of rapamycin

treated groups in Figure 53 raise concerns regarding the documented immunosuppressive properties of rapamycin; however near complete attenuation of these observations with the addition of cyclophosphamide allow for continued positive speculation of combinatory treatments. Rapamycin, generally considered a cytostatic agent, can be viewed as immunosuppressive considering the requirement for constant expansion of immune cells, though the anti-proliferative effects on cancer cells may prove to be a more dominant action [269].

Unexpectedly, rapamycin combination had a similar, though mild, effect on splenic regulatory T cell levels to cyclophosphamide combinations. When used together, rapamycin and cyclophosphamide appear to exhibit a complementary downregulation of regulatory T cells compared to the enzyme prodrug treatment alone. The hypoxic promotion of regulatory T cell activity has been established [270-272], therefore the reduction of hypoxia with rapamycin may indirectly result in decreased levels of regulatory T cells. To my knowledge the phenomenon of rapamycin reduction of regulatory T cell levels has not been observed, though mTOR inhibition with rapamycin does result in the blockade of IL-2 signaling [269], which is necessary for the development and maturation of regulatory T cells [273-275]. Note that regulatory T cell levels in Figure 55 are reported as a percentage of spleen lymphocytes, so rapamycin related reductions are not attributed simply to the general immunosuppressive properties of rapamycin.

Interestingly, mice bearing 4T1 tumors had decreased levels of CD4+ CD25+ FoxP3+ regulatory T cells compared to healthy mice. This is in opposition to other tumor models that show increasing regulatory T cell levels with tumor progression

[276], though some other work corroborates the lack of increased regulatory T cells in the tumor and spleen of BALB/c mice bearing 4T1 tumors [277]. It is possible that 4T1 tumor development results in immune tolerance through the expansion of myeloid-derived suppressor cells rather than expansion of regulatory T cells, indicating there may be more effective means for immunostimulation of this model. Important to note however is that the criteria of interest is actually the prevalence of metastatic nodules and the theorized reduction of regulatory T cells was a means to that end. While cyclophosphamide and rapamycin both caused mild reductions in regulatory T cell levels, only cyclophosphamide produced beneficial results regarding prevalence of metastatic nodules in the lung. This observation, combined with the higher regulatory T cell levels in healthy mice suggest that low dose cyclophosphamide plays an additional role in metastatic progression in addition to the documented effect on regulatory T cells.

An alternative mechanism to the beneficial impact of cyclophosphamide on pulmonary metastatic prevalence is the increased presence of regulatory T cells local to the metastasis. This phenomenon has been previously observed with bone metastasis of 4T1 cells and provides a plausible explanation to the therapeutic advantage of cyclophosphamide despite negligible effects on spleen regulatory T cells [278]. Additionally, some evidence exists for the 4T1 model that low levels of regulatory T cells persist, though they maintained strong immunosuppressive activity and even minor depletions caused significant improvements in antitumor immunity [279]. A further extension of that possibility is the cyclophosphamide related reduction in activity, not necessarily quantity, of regulatory T cells. Essentially, a flow cytometry analysis of spleen regulatory T cells was insufficient to confirm that cyclophosphamide did in fact

improve antitumor immunity and the conflicting literature suggests that a full immunological workup including quantification of tumor infiltrating immune cells, metastases-localized immune cells, and levels of immune-regulatory cytokines would be necessary to further elucidate the mechanism of cyclophosphamide efficacy against metastases.

Commentary on 4T1 Mouse Model

The 4T1 tumor model was intentionally selected for its highly aggressive nature, poor immunogenicity, and low treatment response rates. The moderate success of the presented treatment strategies could potentially show significantly stronger effects and possibly result in tumor cure in other less aggressive and more immunogenic models. The triple negative status of the 4T1 model also contributes to its challenging nature, as a result of altered signaling pathways. Specifically, lack of the estrogen receptor reduces PI3K/Akt/mTOR pathway activation and hence rapamycin sensitivity [186].

Even a reduced growth rate, possible with injection of fewer cancer cells initially could enhance therapeutic efficacy as this particular model produces extremely immature vasculature, as shown in Figure 56. No vasculature was visible in treated tumors. Slower growth may be a stronger representation of human tumor development [280] and may allow stronger angiogenesis, effectively allowing enhanced drug delivery and increasing the presence of a primary therapeutic target, phosphatidylserine. Additional studies would be interesting that evaluate a slower growth model, for example, injection of only 10^3 4T1 cells rather than 10^6 cells. Possibly even more applicable for furthering this research would be evaluation in genetically engineered

mouse models with spontaneous tumorigenesis to better represent the pathologies in humans, including not only primary tumor development but also metastatic formation and antitumor immunity [280].

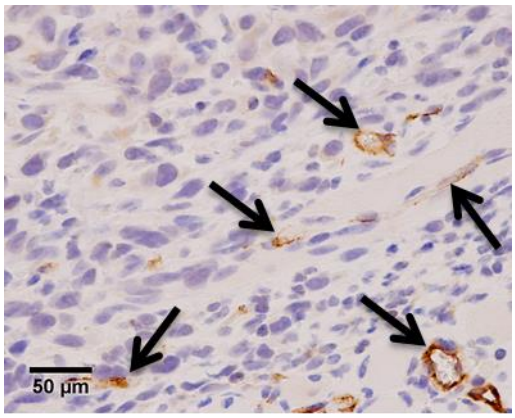

Figure 56. Low vasculature density in untreated 4T1 tumors in BALB/cJ mice. Immunohistochemistry staining of CD31 with DAB development (brown) and hematoxylin counterstain (purple) revealed minimal vasculature presence in untreated tumor sections (shown above) and no vasculature presence in any treated group. Tumor sections from three mice from each experimental group were examined. Arrows indicate CD31 staining.

Analysis of Combination Therapies for Synergism

The definition of drug synergy can be vague and application dependent, though in general an enhanced effect achieved through the combination of two compounds beyond the sum of the two effects is considered superadditive or synergistic [281]. Assessment of drug synergy is typically approached using different variations of the Bliss independence and Loewe additivity models [232, 233]. The Bliss independence model is more relevant for examination of treatment effect enhancement and applies to mechanistically independent combination approaches [232, 233]. Alternatively, the Loewe additivity model applies more directly to competing compounds and efforts towards dose reduction [232, 233].

The implication of synergism of the combination therapy as opposed to purely additive effects stems from the design of the combination therapy in which each therapeutic component acts upon separate mechanisms and pathways. The full combination therapy (mCGL-AV and selenomethionine, cyclophosphamide, rapamycin) is a three-pronged anticancer approach that introduces targeted cytotoxicity to promote tumor death, immune stimulation for reduction of metastases, and attenuation of the hypoxic response to prevent tumor regrowth. The primary means for evaluating treatment efficacy, survival and tumor volume, and the independent mechanisms of drug action implicate the Bliss independence approach as the most relevant methodology to analyze potential synergism.

Using this approach, the predicted response of a combination therapy can be achieved using the additivity of probability theory for independent mechanisms (A and B) which can be applied to inhibition of tumor growth using the equation below [232]. The predicted percent inhibition of a combination therapy is determined using the experimentally observed percent inhibitions of the combination therapy constituents.

$$Predicted_{\%\ Inhibition} = A_{\%\ Inhibition} + B_{\%\ Inhibition} - A_{\%\ Inhibition} * B_{\%\ Inhibition}$$

Subtracting the predicted effect value from the actual observed value generates a "synergism assessment factor" introduced by [233], adapted to simply define synergism as values greater than 0, additive effects equal to 0, and antagonistic effects less than 0. For example, to evaluate the synergism of selenomethionine with mCGL-AV, the measured values for tumor growth percent inhibition at a determined time point for mCGL-AV alone and for selenomethionine alone would replace A and B in the above equation. That calculated value would then be subtracted from the measured value for

the selenomethionine and mCGL-AV group to obtain the synergism assessment factor. Table 12 displays the synergism assessment factors for the different combinations for the first two weeks of treatment, after which the values become skewed by plateaued tumor volumes of untreated mice rapidly reaching the end points of the study. The ampersand indicates grouped components and the plus sign indicates the separation of the constituents undergoing evaluation for synergism. For example, "mCGL-AV + Sel" represents the evaluation of mCGL-AV and selenomethionine for synergism whereas the other representation "mCGL-AV & Sel" classifies the enzyme prodrug therapy as its own constituent to provide a stronger comparison for the evaluation of rapamycin and cyclophosphamide synergism.

Table 12. Synergism assessment factors for tumor growth inhibition

	Day of Treatment				
	0	*2*	*6*	*9*	*13*
Rap + Cyc	0.00	-0.03	**0.06**	-0.10	-0.02
mCGL-AV + Sel	0.00	**0.12**	**0.07**	**0.06**	**0.04**
mCGL-AV & Sel + Rap	0.00	-0.23	**0.10**	**0.06**	**0.20**
mCGL-AV & Sel + Cyc	0.00	**0.09**	-0.01	0.00	**0.12**
mCGL-AV & Sel + Rap & Cyc	0.00	-0.03	**0.07**	**0.15**	**0.19**

Evaluation of tumor growth inhibition at the conclusion of the treatment period using the Bliss independence model for synergy indicates that combination of the mCGL-AV enzyme prodrug system with rapamycin produced a synergistic effect. The mCGL-AV system combined with rapamycin and cyclophosphamide also exhibits synergism compared to the effects of the enzyme prodrug system alone and rapamycin and cyclophosphamide effects together. Cyclophosphamide combined with the enzyme prodrug treatment does not have a consistent synergistic effect on inhibition of tumor growth. Notably, the combination of rapamycin and cyclophosphamide without the

enzyme prodrug therapy is also not synergistic. Strong synergism of mCGL-AV and selenomethionine was apparent through the duration of the treatment.

The synergistic effect on tumor growth inhibition exhibited by the combination of rapamycin with the enzyme prodrug therapy likely results from the cytotoxic effect of the enzyme prodrug therapy combined with the inhibition of the hypoxic response by rapamycin. Alone, rapamycin reduces HIF-1α expression as expected; however it is only through combination with the enzyme prodrug therapy that a significant inhibition of tumor growth occurs. The enzyme prodrug therapy alone does achieve tumor growth inhibition; however continuous regrowth of cancer cells, presumably increased through the hypoxic response, contributes to the eventual progression of the tumor. Enzyme prodrug therapy related killing of the tumor cells combined with the modulation of tumor regrowth resulting from rapamycin inhibition of the hypoxic response produce the synergistic effect on tumor growth inhibition.

The theorized utility of the enzyme prodrug combination with cyclophosphamide is an enhancement of mouse survival through reduction of pulmonary metastases by stimulating the immune system. Hence, a lack of synergistic inhibition of tumor growth with cyclophosphamide and the enzyme prodrug therapy is unsurprising. Evaluation of primary tumor growth is a standard strategy for the evaluation of an antitumor therapy; however survival is a function of metastatic formation in addition to tumor growth. Metastatic formation is perhaps a more vital indicator of treatment efficacy, as evidenced by the enhanced survival with cyclophosphamide and cyclophosphamide combination therapies and the related reduction in metastases. The synergistic antitumor effect of rapamycin with the enzyme

prodrug therapy produces an enhanced survival as anticipated, however does not significantly reduce metastatic formation. Further enhancement of survival with the enzyme prodrug therapy combined with rapamycin and cyclophosphamide occurs as a result of the antitumor growth effects as well as metastatic reductions. The total combined advantage is not obvious and, in fact, opposes the reasonable theory that rapamycin, an immunosuppressive drug, would have an antagonistic effect when combined with cyclophosphamide used at immunostimulatory doses.

Summary of mCGL System and Combination Therapies

The mCGL enzyme was successfully designed and fused to annexin I and annexin V and confirmed to have methioninase activity that allows for the conversion of selenomethionine to methylselenol. *In vitro* results with mCGL-AI and mCGL-AV were obtained as expected based on the Met-AV system. Strong binding and cytotoxic efficacy was apparent and comparable among the three systems: mCGL-AI, mCGL-AV, and Met-AV.

In BALB/cJ mice bearing orthotopic 4T1 mammary tumors, the mCGL-AV system showed improved efficacy over the mCGL-AI system and was selected for further study. mCGL-AV and selenomethionine effectively suppressed tumor growth but only on a temporary basis. Immunohistochemical analysis confirmed that the enzyme prodrug therapy did enhance apoptosis and reduced proliferation within the tumor. Additionally, mCGL-AV showed strong improvement over Met-AV when compared in the BALB/cJ model. Daily administration led to the generation of neutralizing antibodies for Met-AV, but not for mCGL-AV. Despite a lack of any negative immune reaction, mCGL-AV and selenomethionine were not sufficient for tumor cure, stimulating the evaluation of combination therapies.

Rapamycin was included to reduce the hypoxic response theorized to augmented by the enzyme prodrug therapy. The addition of rapamycin to mCGL-AV and selenomethionine significantly reduced primary tumor volumes in a synergistic fashion. Cyclophosphamide was included with the intention of reducing regulatory T cell levels to stimulate an antitumor and anti-metastatic immune response. While regulatory T cell

levels were not significantly reduced, the number of metastatic nodules dropped drastically with the addition of cyclophosphamide.

Together, cyclophosphamide, rapamycin, and mCGL-AV and selenomethionine reduce primary tumor volumes, reduce metastatic progression, enhance survival, increase apoptosis, decrease proliferation, and decrease necrosis and the hypoxic response. The three pronged approach involving a cytotoxic mechanism, an immunostimulatory mechanism, and an anti-hypoxic response mechanism addresses many of the challenges presented with the highly aggressive and metastatic, poorly immunogenic, treatment resistant, triple-negative 4T1 tumor model.

Chapter IV: Conclusions and Future Directions

The first objective of this work was to develop the PNP-AV enzyme prodrug system. The PNP-AV fusion protein was successfully produced and purified, resulting in strong *in vitro* binding and promising cytotoxicity results.

The second objective was to assess the CD-AV, PNP-AV, and Met-AV enzyme prodrug systems *in vivo* and select the best candidate for transition into immune competent models. The CD-AV system yielded underwhelming results. The PNP-AV system was able to achieve some tumor growth suppression; however the Met-AV system outperformed the other enzyme prodrug systems and achieved temporary tumor regression. Resultantly, Met-AV was selected for work aimed at reducing immunogenicity.

The third objective, reduced immunogenicity for the highest performing system, was first attempted through various protein PEGylation methods. Ultimately, however, a protein engineering method was determined to be more effective. Native mouse CGL was mutated in three amino acid positions to impart methioninase activity, eliminating the foreign component of the fusion protein.

The central goal of the project was to effectively treat breast cancer in mice with a targeted enzyme prodrug therapy. The single cytotoxic mechanism presented by each of the therapies individually was not sufficient for sustained tumor regression or suppression, spurring work with combination therapies. Cyclophosphamide was evaluated to enhance antitumor immunity, and rapamycin was included to prevent the hypoxic response of the tumor with allowed for continued progression and regrowth.

The combination of cyclophosphamide, rapamycin, mCGL-AV, and selenomethionine effectively reduced tumor volumes and enhanced mouse survival.

Moving forward, there is much room for dosing improvements as a result of the complications of combining multiple drugs. None of the combination constituents could be considered to be optimally dosed. It is possible that a higher dose of fusion protein is required to saturate tumoral phosphatidylserine. Additionally, a higher dose of rapamycin may prove to exhibit a stronger effect on primary tumor volume, yet a lower dose may further improve the metastasis data.

The dosing schedule may also require optimization. It was originally hypothesized that maximizing the frequency of fusion protein administration would provide the greatest cytotoxic effect, which was supported by *in vitro* data. However, the daily saturation of phosphatidylserine may not prove to be entirely advantageous, given phosphatidylserine's role in non-inflammatory clearance of apoptotic cells. Fusion protein binding to phosphatidylserine could inhibit clearance of dying cells and cellular debris. Less frequent administrations may actually allow for natural clearance mechanisms to play a role in cell removal and could allow for increased tumor antigen presentation. The perceived *in vitro* benefit of daily fusion protein administration may not translate to the *in vivo* environment since dying cells are not able to be simply washed off of a plate. *In vivo* data with Met-AV fusion protein administration occurring once every 4 days displayed a strong effect, originally attributed to slower tumor growth overall among the groups. Regardless, enough evidence and literature support exist to warrant some evaluation with altered dosing schedules.

In addition to dosing considerations, alternative compounds may exhibit higher bioactivities utilizing the same or similar mechanisms. A number of rapamycin analogues and derivatives exist and are under current clinical and preclinical evaluations for slightly different activities, including Everolimus for breast cancer. Cyclophosphamide activity was hypothesized to lower regulatory T cell levels, which can also be altered through a variety of mechanisms, including Ipilimumab (anti-CTLA-4).

Immunostimulation with anti-CTLA-4 (cytotoxic T lymphocyte antigen 4) therapies in combination with the enzyme prodrug system may enhance the antitumor response in the 4T1 model. It has been shown to successfully elicit an antitumor immune response in the 4T1 model when combined with radiation therapies[266]. CTLA-4 plays a role in the maintenance of peripheral tolerance through the inhibition of T cell activation and contributes to tumor evasion of the immune system [282]. The blockade of CTLA-4 –related inhibition of T cells is an immunostimulatory mechanism independent from the cyclophosphamide-induced preferential depletion of regulatory T cells. Use of an anti-CTLA-4 antibody with the enzyme prodrug therapy may prove to significantly enhance survival, even with the 4T1 model, either in conjunction with cyclophosphamide or as an alternative approach.

Improvements to the enzyme prodrug system itself are also possible. CGL is a mammalian protein that is granted full methioninase activity towards selenomethionine from essentially zero activity with only three amino acid substitutions. It is possible that additional protein engineering could further enhance CGL activity towards selenomethionine.

Performing follow-up studies in additional immune competent breast cancer models would likely validate the therapeutic value of the enzyme prodrug therapy and the combination approaches. The 4T1 model is highly aggressive, metastatic, and poorly immunogenic with a histology characteristic of high-grade human breast cancer; all of which make it a valuable model for evaluation of immunotherapies [266]. A more immunogenic tumor model, while less representative of human breast cancers, would yield valuable information in the evaluation of the immunostimulatory approaches used in combination with the enzyme prodrug therapy. For example, the EMT6 murine breast cancer cell line implanted into BALB/c mice can elicit an immune response leading to a T cell mediated regression of the tumor [283] and enhanced survival even with multiple tumor rechallenges [284]. Additionally, the EMT6 model produces lymphatic, pulmonary, and hepatic metastasis allowing for evaluation of the anti-metastatic nature of the immunotherapies at multiple sites [285]. Alternatively, models exhibiting slower growth could provide additional insight into the efficacy of the vasculature directed enzyme prodrug therapy, since our current models grow at a rate too fast for significant development of tumor vasculature. A simple approach would be to reduce the quantity of implanted cells, either 4T1 or EMT6. Another strategy would be to utilize a transgenic mouse strain that develops highly vascularized spontaneous tumors (for example, Jackson Laboratory's FVB/N-Tg(MMTV-PyVT)634Mul/J strain which develops spontaneous mammary tumors in 100% of mice within 5 weeks with spontaneous pulmonary metastasis in 80-94% of mice).

Overall, the mCGL-AV system has demonstrated efficacy in very challenging mouse models, particularly when combined with rapamycin and cyclophosphamide.

The therapeutic system appears to be quite promising but requires significant optimization to progress beyond preclinical studies and may benefit specifically with insight from a cancer immunologist.

References

1. *The Breast Cancer Landscape*. 2013, Department of Defense Breast Cancer Research Program.

2. Altekruse, S.F., C.L. Kosary, M. Krapcho, N. Neyman, R. Aminou, W. Waldron, et al. *SEER Cancer Statistics Review 1975-2007*. 2010:[Available from: http://seer.cancer.gov/archive/csr/1975_2007/.

3. DeSantis, C., R. Siegel, P. Bandi, and A. Jemal, *Breast cancer statistics, 2011*. CA Cancer J Clin, 2011. **61**(6): p. 409-18.

4. Semenza, G.L., *Molecular mechanisms mediating metastasis of hypoxic breast cancer cells.* Trends Mol Med, 2012. **18**(9): p. 534-43.

5. *Breast Cancer*. 2014, American Cancer Society: http://www.cancer.org/cancer/breastcancer/detailedguide/breast-cancer-key-statistics.

6. Bleyer, A. and H.G. Welch, *Effect of three decades of screening mammography on breast-cancer incidence.* N Engl J Med, 2012. **367**(21): p. 1998-2005.

7. Baum, M., *Harms from breast cancer screening outweigh benefits if death caused by treatment is included.* BMJ, 2013. **346**: p. f385.

8. *Breast Cancer Treatment (PDQ)*. 2014, National Cancer Institute, National Institutes of Health: http://www.cancer.gov/cancertopics/pdq/treatment/breast/patient/.

9. Abrams, R.A. and L.B. Grochow, *Adjuvant therapy with chemotherapy and radiation therapy in the management of carcinoma of the pancreatic head.* Surg Clin North Am, 1995. **75**(5): p. 925-38.

10. Howard, T.J., *Pancreatic adenocarcinoma.* Curr Probl Cancer, 1996. **20**(5): p. 281-328.

11. Lohr, M., P. Muller, P. Karle, J. Stange, S. Mitzner, R. Jesnowski, et al., *Targeted chemotherapy by intratumour injection of encapsulated cells*

engineered to produce CYP2B1, an ifosfamide activating cytochrome P450. Gene Ther, 1998. **5**(8): p. 1070-8.

12. Chabot, G.G., *Factors involved in clinical pharmacology variability in oncology (review).* Anticancer Res, 1994. **14**(6A): p. 2269-72.

13. Ardiani, A., A.J. Johnson, H. Ruan, M. Sanchez-Bonilla, K. Serve, and M.E. Black, *Enzymes to die for: exploiting nucleotide metabolizing enzymes for cancer gene therapy.* Curr Gene Ther, 2012. **12**(2): p. 77-91.

14. Glennie, M.J. and J.G. van de Winkel, *Renaissance of cancer therapeutic antibodies.* Drug Discov Today, 2003. **8**(11): p. 503-10.

15. Brannon-Peppas, L. and J.O. Blanchette, *Nanoparticle and targeted systems for cancer therapy.* Adv Drug Deliv Rev, 2012. **64**: p. 206-212.

16. Sawyers, C., *Targeted cancer therapy.* Nature, 2004. **432**(7015): p. 294-7.

17. Greco, O. and G.U. Dachs, *Gene directed enzyme/prodrug therapy of cancer: historical appraisal and future prospectives.* J Cell Physiol, 2001. **187**(1): p. 22-36.

18. Bhaumik, S., T.V. Sekar, J. Depuy, J. Klimash, and R. Paulmurugan, *Noninvasive optical imaging of nitroreductase gene-directed enzyme prodrug therapy system in living animals.* Gene Ther, 2012. **19**(3): p. 295-302.

19. Both, G.W., *Recent progress in gene-directed enzyme prodrug therapy: an emerging cancer treatment.* Curr Opin Mol Ther, 2009. **11**(4): p. 421-32.

20. Bagshawe, K.D., *Antibody-directed enzyme prodrug therapy (ADEPT) for cancer.* Expert Rev Anticancer Ther, 2006. **6**(10): p. 1421-31.

21. Tietze, L.F. and B. Krewer, *Antibody-directed enzyme prodrug therapy: a promising approach for a selective treatment of cancer based on prodrugs and monoclonal antibodies.* Chem Biol Drug Des, 2009. **74**(3): p. 205-11.

22. Aboody, K.S., J. Najbauer, M.Z. Metz, M. D'Apuzzo, M. Gutova, A.J. Annala, et al., *Neural stem cell-mediated enzyme/prodrug therapy for glioma: preclinical studies.* Sci Transl Med, 2013. **5**(184): p. 184ra59.

23. Muller, P., R. Jesnowski, P. Karle, R. Renz, R. Saller, H. Stein, et al., *Injection of encapsulated cells producing an ifosfamide-activating cytochrome P450 for targeted chemotherapy to pancreatic tumors.* Ann N Y Acad Sci, 1999. **880**: p. 337-51.

24. Patterson, A. and A.L. Harris, *Molecular chemotherapy for breast cancer.* Drugs Aging, 1999. **14**(2): p. 75-90.

25. Xu, G. and H.L. McLeod, *Strategies for enzyme/prodrug cancer therapy.* Clin Cancer Res, 2001. **7**(11): p. 3314-24.

26. Rigg, A. and K. Sikora, *Genetic prodrug activation therapy.* Mol Med Today, 1997. **3**(8): p. 359-66.

27. Niculescu-Duvaz, I., R. Spooner, R. Marais, and C.J. Springer, *Gene-directed enzyme prodrug therapy.* Bioconjug Chem, 1998. **9**(1): p. 4-22.

28. Mahato, R., W. Tai, and K. Cheng, *Prodrugs for improving tumor targetability and efficiency.* Adv Drug Deliv Rev, 2011. **63**(8): p. 659-70.

29. Cheng, T.L., S.L. Wei, B.M. Chen, J.W. Chern, M.F. Wu, P.W. Liu, et al., *Bystander killing of tumour cells by antibody-targeted enzymatic activation of a glucuronide prodrug.* Br J Cancer, 1999. **79**(9-10): p. 1378-85.

30. Huber, B.E., E.A. Austin, C.A. Richards, S.T. Davis, and S.S. Good, *Metabolism of 5-fluorocytosine to 5-fluorouracil in human colorectal tumor cells transduced with the cytosine deaminase gene: significant antitumor effects when only a small percentage of tumor cells express cytosine deaminase.* Proc Natl Acad Sci U S A, 1994. **91**(17): p. 8302-6.

31. Wei, M.X., T. Tamiya, R.J. Rhee, X.O. Breakefield, and E.A. Chiocca, *Diffusible cytotoxic metabolites contribute to the in vitro bystander effect associated with the cyclophosphamide/cytochrome P450 2B1 cancer gene therapy paradigm.* Clin Cancer Res, 1995. **1**(10): p. 1171-7.

32. Bridgewater, J.A., R.J. Knox, J.D. Pitts, M.K. Collins, and C.J. Springer, *The bystander effect of the nitroreductase/CB1954 enzyme/prodrug system is due to a cell-permeable metabolite.* Hum Gene Ther, 1997. **8**(6): p. 709-17.

33. Lawrence, T.S., A. Rehemtulla, E.Y. Ng, M. Wilson, J.E. Trosko, and P.L. Stetson, *Preferential cytotoxicity of cells transduced with cytosine deaminase compared to bystander cells after treatment with 5-flucytosine.* Cancer Res, 1998. **58**(12): p. 2588-93.

34. Greco, O., L.K. Folkes, P. Wardman, G.M. Tozer, and G.U. Dachs, *Development of a novel enzyme/prodrug combination for gene therapy of cancer: horseradish peroxidase/indole-3-acetic acid.* Cancer Gene Ther, 2000. **7**(11): p. 1414-20.

35. Stribbling, S.M., F. Friedlos, J. Martin, L. Davies, R.A. Spooner, R. Marais, et al., *Regressions of established breast carcinoma xenografts by carboxypeptidase G2 suicide gene therapy and the prodrug CMDA are due to a bystander effect.* Hum Gene Ther, 2000. **11**(2): p. 285-92.

36. Van Rite, B.D., Y.A. Lazrak, M.L. Pagnon, N.R. Palwai, L.F. Neves, P.S. McFetridge, et al., *Enzyme prodrug therapy designed to target L-methioninase to the tumor vasculature.* Cancer Lett, 2011. **301**(2): p. 177-84.

37. Van Rite, B.D. and R.G. Harrison, *Annexin V-targeted enzyme prodrug therapy using cytosine deaminase in combination with 5-fluorocytosine.* Cancer Lett, 2011. **307**(1): p. 53-61.

38. Longley, D.B., D.P. Harkin, and P.G. Johnston, *5-fluorouracil: mechanisms of action and clinical strategies.* Nat Rev Cancer, 2003. **3**(5): p. 330-8.

39. Niculescu-Duvaz, D., I. Niculescu-Duvaz, F. Friedlos, J. Martin, R. Spooner, L. Davies, et al., *Self-immolative nitrogen mustard prodrugs for suicide gene therapy.* J Med Chem, 1998. **41**(26): p. 5297-309.

40. McGinn, C.J. and T.J. Kinsella, *The clinical rationale for S-phase radiosensitization in human tumors.* Curr Probl Cancer, 1993. **17**(5): p. 273-321.

41. Wyatt, M.D. and D.M. Wilson, 3rd, *Participation of DNA repair in the response to 5-fluorouracil.* Cell Mol Life Sci, 2009. **66**(5): p. 788-99.

42. Cheung, W.Y., R.A. Fralick, and S. Cheng, *The confused cancer patient: a case of 5-fluorouracil-induced encephalopathy.* Curr Oncol, 2008. **15**(5): p. 234-6.

43. Vauthey, J.N., W. Marsh Rde, J.C. Cendan, N.M. Chu, and E.M. Copeland, *Arterial therapy of hepatic colorectal metastases.* Br J Surg, 1996. **83**(4): p. 447-55.

44. Yang;, Y.-h., H. Aloysius;, D. Inoyama;, Y. Chen;, and L.-q. Hu, *Enzyme-mediated hydrolytic activation of prodrugs.* Acta Pharmaceutica Sinica B, 2011. **1**(3): p. 143-159.

45. Baley, J.E., C. Meyers, R.M. Kliegman, M.R. Jacobs, and J.L. Blumer, *Pharmacokinetics, outcome of treatment, and toxic effects of amphotericin B and 5-fluorocytosine in neonates.* J Pediatr, 1990. **116**(5): p. 791-7.

46. Ge, K., L. Xu, Z. Zheng, D. Xu, L. Sun, and X. Liu, *Transduction of cytosine deaminase gene makes rat glioma cells highly sensitive to 5-fluorocytosine.* Int J Cancer, 1997. **71**(4): p. 675-9.

47. Domin, B.A., W.B. Mahony, and T.P. Zimmerman, *Membrane permeation mechanisms of 2',3'-dideoxynucleosides.* Biochem Pharmacol, 1993. **46**(4): p. 725-9.

48. Domin, B.A., W.B. Mahony, and T.P. Zimmerman, *Transport of 5-fluorouracil and uracil into human erythrocytes.* Biochem Pharmacol, 1993. **46**(3): p. 503-10.

49. Zamboni, S., A. Mallano, M. Flego, A. Ascione, M.L. Dupuis, M. Gellini, et al., *Genetic construction, expression, and characterization of a single chain anti-CEA antibody fused to cytosine deaminase from yeast.* Int J Oncol, 2008. **32**(6): p. 1245-51.

50. Panjideh, H., V.C. Da Silva Coelho, J. Dernedde, C. Bachran, G.J. Forster, J. Franke, et al., *Biodistribution and efficacy of [131I]A33scFv::CDy, a recombinant antibody-enzyme protein for colon cancer.* Int J Oncol, 2008. **32**(4): p. 925-30.

51. Coelho, V., J. Dernedde, U. Petrausch, H. Panjideh, H. Fuchs, C. Menzel, et al., *Design, construction, and in vitro analysis of A33scFv::CDy, a recombinant*

fusion protein for antibody-directed enzyme prodrug therapy in colon cancer. Int J Oncol, 2007. **31**(4): p. 951-7.

52. Huber, B.E., C.A. Richards, and E.A. Austin, *Virus-directed enzyme/prodrug therapy (VDEPT). Selectively engineering drug sensitivity into tumors.* Ann N Y Acad Sci, 1994. **716**: p. 104-14; discussion 140-3.

53. Zeng, H., Q. Wei, R. Huang, N. Chen, Q. Dong, Y. Yang, et al., *Recombinant adenovirus mediated prostate-specific enzyme pro-drug gene therapy regulated by prostate-specific membrane antigen (PSMA) enhancer/promoter.* J Androl, 2007. **28**(6): p. 827-35.

54. Chaszczewska-Markowska, M., K. Stebelska, A. Sikorski, J. Madej, A. Opolski, and M. Ugorski, *Liposomal formulation of 5-fluorocytosine in suicide gene therapy with cytosine deaminase--for colorectal cancer.* Cancer Lett, 2008. **262**(2): p. 164-72.

55. Kievit, E., E. Bershad, E. Ng, P. Sethna, I. Dev, T.S. Lawrence, et al., *Superiority of yeast over bacterial cytosine deaminase for enzyme/prodrug gene therapy in colon cancer xenografts.* Cancer Res, 1999. **59**(7): p. 1417-21.

56. Boogaerts, M.A., *Oral fludarabine therapy in chronic lymphocytic leukemia--increased convenience.* Hematol J, 2004. **5 Suppl 1**: p. S31-7.

57. Casper, E.S., A. Mittelman, D. Kelson, and C.W. Young, *Phase I clinical trial of fludarabine phosphate (F-ara-AMP).* Cancer Chemother Pharmacol, 1985. **15**(3): p. 233-5.

58. Pierige, F., C. De Marco, N. Orlotti, S. Dominici, S. Biagiotti, S. Serafini, et al., *Cytotoxic activity of 2-Fluoro-ara-AMP and 2-Fluoro-ara-AMP-loaded erythrocytes against human breast carcinoma cell lines.* Int J Oncol, 2010. **37**(1): p. 133-42.

59. Ding, X., A.A. Herzlich, R. Bishop, J. Tuo, and C.C. Chan, *Ocular toxicity of fludarabine: a purine analog.* Expert Rev Ophthalmol, 2008. **3**(1): p. 97-109.

60. Von Hoff, D.D., *Phase I clinical trials with fludarabine phosphate.* Semin Oncol, 1990. **17**(5 Suppl 8): p. 33-8.

61. Hong, J.S., W.R. Waud, D.N. Levasseur, T.M. Townes, H. Wen, S.A. McPherson, et al., *Excellent in vivo bystander activity of fludarabine phosphate against human glioma xenografts that express the escherichia coli purine nucleoside phosphorylase gene.* Cancer Res, 2004. **64**(18): p. 6610-5.

62. Xie, X., J. Guo, Y. Kong, G.X. Xie, L. Li, N. Lv, et al., *Targeted expression of E. coli purine nucleoside phosphorylase and Fludara for prostate cancer therapy.* J Gene Med, 2011.

63. Martiniello-Wilks, R., X.Y. Wang, D.J. Voeks, A. Dane, J.M. Shaw, E. Mortensen, et al., *Purine nucleoside phosphorylase and fludarabine phosphate gene-directed enzyme prodrug therapy suppresses primary tumour growth and pseudo-metastases in a mouse model of prostate cancer.* J Gene Med, 2004. **6**(12): p. 1343-57.

64. Kikuchi, E., S. Menendez, C. Ozu, M. Ohori, C. Cordon-Cardo, C.R. Logg, et al., *Delivery of replication-competent retrovirus expressing Escherichia coli purine nucleoside phosphorylase increases the metabolism of the prodrug, fludarabine phosphate and suppresses the growth of bladder tumor xenografts.* Cancer Gene Ther, 2007. **14**(3): p. 279-86.

65. Mohr, L., S. Shankara, S.K. Yoon, T.U. Krohne, M. Geissler, B. Roberts, et al., *Gene therapy of hepatocellular carcinoma in vitro and in vivo in nude mice by adenoviral transfer of the Escherichia coli purine nucleoside phosphorylase gene.* Hepatology, 2000. **31**(3): p. 606-14.

66. Parker, W.B., S.A. King, P.W. Allan, L.L. Bennett, Jr., J.A. Secrist, 3rd, J.A. Montgomery, et al., *In vivo gene therapy of cancer with E. coli purine nucleoside phosphorylase.* Hum Gene Ther, 1997. **8**(14): p. 1637-44.

67. Gray, N. [cited 2014 May 30 2014]; Available from: www.pnptherapeutics.com.

68. Lee, J., S. Filosa, J. Bonvin, S. Guyon, R.A. Aponte, and J.L. Turnbull, *Expression, purification, and characterization of recombinant purine nucleoside phosphorylase from Escherichia coli.* Protein Expr Purif, 2001. **22**(2): p. 180-8.

69. Mao, C., W.J. Cook, M. Zhou, G.W. Koszalka, T.A. Krenitsky, and S.E. Ealick, *The crystal structure of Escherichia coli purine nucleoside phosphorylase: a comparison with the human enzyme reveals a conserved topology.* Structure, 1997. **5**(10): p. 1373-83.

70. Parker, W.B., P.W. Allan, S.C. Shaddix, L.M. Rose, H.F. Speegle, G.Y. Gillespie, et al., *Metabolism and metabolic actions of 6-methylpurine and 2-fluoroadenine in human cells.* Biochem Pharmacol, 1998. **55**(10): p. 1673-81.

71. Lockett, L.J., P.L. Molloy, P.J. Russell, and G.W. Both, *Relative efficiency of tumor cell killing in vitro by two enzyme-prodrug systems delivered by identical adenovirus vectors.* Clin Cancer Res, 1997. **3**(11): p. 2075-80.

72. Jensen, K.F. and P. Nygaard, *Purine nucleoside phosphorylase from Escherichia coli and Salmonella typhimurium. Purification and some properties.* Eur J Biochem, 1975. **51**(1): p. 253-65.

73. Montgomery, J.A. and K. Hewson, *Nucleosides of 2-fluoroadenine.* J Med Chem, 1969. **12**(3): p. 498-504.

74. Sorscher, E.J., S. Peng, Z. Bebok, P.W. Allan, L.L. Bennett, Jr., and W.B. Parker, *Tumor cell bystander killing in colonic carcinoma utilizing the Escherichia coli DeoD gene to generate toxic purines.* Gene Ther, 1994. **1**(4): p. 233-8.

75. Van den Neste, E., S. Cardoen, F. Offner, and F. Bontemps, *Old and new insights into the mechanisms of action of two nucleoside analogs active in lymphoid malignancies: fludarabine and cladribine (review).* Int J Oncol, 2005. **27**(4): p. 1113-24.

76. Esaki, N. and K. Soda, *L-methionine gamma-lyase from Pseudomonas putida and Aeromonas.* Methods Enzymol, 1987. **143**: p. 459-65.

77. Esaki, N., H. Tanaka, S. Uemura, T. Suzuki, and K. Soda, *Catalytic action of L-methionine gamma-lyase on selenomethionine and selenols.* Biochemistry, 1979. **18**(3): p. 407-10.

78. Dias, B. and B. Weimer, *Purification and characterization of L-methionine gamma-lyase from brevibacterium linens BL2.* Appl Environ Microbiol, 1998. **64**(9): p. 3327-31.

79. Ito, S., T. Nakamura, and Y. Eguchi, *Purification and characterization of methioninase from Pseudomonas putida.* J Biochem, 1976. **79**(6): p. 1263-72.

80. El-Sayed, A.S., *Microbial L-methioninase: production, molecular characterization, and therapeutic applications.* Appl Microbiol Biotechnol, 2010. **86**(2): p. 445-67.

81. Takakura, T., K. Mitsushima, S. Yagi, K. Inagaki, H. Tanaka, N. Esaki, et al., *Assay method for antitumor L-methionine gamma-lyase: comprehensive kinetic analysis of the complex reaction with L-methionine.* Anal Biochem, 2004. **327**(2): p. 233-40.

82. Klimberg, V.S. and J.L. McClellan, *Claude H. Organ, Jr. Honorary Lectureship. Glutamine, cancer, and its therapy.* Am J Surg, 1996. **172**(5): p. 418-24.

83. Agrawal, N.R., R.M. Bukowski, L.A. Rybicki, J. Kurtzberg, L.J. Cohen, and M.A. Hussein, *A Phase I-II trial of polyethylene glycol-conjugated L-asparaginase in patients with multiple myeloma.* Cancer, 2003. **98**(1): p. 94-9.

84. Tan, Y., M. Xu, X. Tan, X. Tan, X. Wang, Y. Saikawa, et al., *Overexpression and large-scale production of recombinant L-methionine-alpha-deamino-gamma-mercaptomethane-lyase for novel anticancer therapy.* Protein Expr Purif, 1997. **9**(2): p. 233-45.

85. Yoshioka, T., T. Wada, N. Uchida, H. Maki, H. Yoshida, N. Ide, et al., *Anticancer efficacy in vivo and in vitro, synergy with 5-fluorouracil, and safety of recombinant methioninase.* Cancer Res, 1998. **58**(12): p. 2583-7.

86. Tan, Y., M. Xu, H. Guo, X. Sun, T. Kubota, and R.M. Hoffman, *Anticancer efficacy of methioninase in vivo.* Anticancer Res, 1996. **16**(6C): p. 3931-6.

87. Miki, K., W. Al-Refaie, M. Xu, P. Jiang, Y. Tan, M. Bouvet, et al., *Methioninase gene therapy of human cancer cells is synergistic with recombinant methioninase treatment.* Cancer Res, 2000. **60**(10): p. 2696-702.

88. Tan, Y., M. Xu, and R.M. Hoffman, *Broad selective efficacy of recombinant methioninase and polyethylene glycol-modified recombinant methioninase on cancer cells In Vitro.* Anticancer Res, 2010. **30**(4): p. 1041-6.

89. Hoffman, R.M., *Altered methionine metabolism, DNA methylation and oncogene expression in carcinogenesis. A review and synthesis.* Biochim Biophys Acta, 1984. **738**(1-2): p. 49-87.

90. Mecham, J.O., D. Rowitch, C.D. Wallace, P.H. Stern, and R.M. Hoffman, *The metabolic defect of methionine dependence occurs frequently in human tumor cell lines.* Biochem Biophys Res Commun, 1983. **117**(2): p. 429-34.

91. Guo, H.Y., H. Herrera, A. Groce, and R.M. Hoffman, *Expression of the biochemical defect of methionine dependence in fresh patient tumors in primary histoculture.* Cancer Res, 1993. **53**(11): p. 2479-83.

92. Hoffman, R.M., *Altered methionine metabolism and transmethylation in cancer.* Anticancer Res, 1985. **5**(1): p. 1-30.

93. Halpern, B.C., B.R. Clark, D.N. Hardy, R.M. Halpern, and R.A. Smith, *The effect of replacement of methionine by homocystine on survival of malignant and normal adult mammalian cells in culture.* Proc Natl Acad Sci U S A, 1974. **71**(4): p. 1133-6.

94. Hoffman, R.M., *Methioninase: a therapeutic for diseases related to altered methionine metabolism and transmethylation: cancer, heart disease, obesity, aging, and Parkinson's disease.* Hum Cell, 1997. **10**(1): p. 69-80.

95. Kokkinakis, D.M., R.M. Hoffman, E.P. Frenkel, J.B. Wick, Q. Han, M. Xu, et al., *Synergy between methionine stress and chemotherapy in the treatment of brain tumor xenografts in athymic mice.* Cancer Res, 2001. **61**(10): p. 4017-23.

96. Kokkinakis, D.M., *Methionine-stress: a pleiotropic approach in enhancing the efficacy of chemotherapy.* Cancer Lett, 2006. **233**(2): p. 195-207.

97. Hoffman, R.M., *Methionine dependence in cancer cells - a review.* In Vitro, 1982. **18**(5): p. 421-8.

98. Kano, Y., S. Sakamoto, T. Kasahara, K. Kusumoto, K. Hida, K. Suda, et al., *Methionine dependency of cell growth in normal and malignant hematopoietic cells.* Cancer Res, 1982. **42**(8): p. 3090-2.

99. Kenyon, S.H., T. Ast, A. Nicolaou, and W.A. Gibbons, *Polyamines can regulate vitamin B12 dependent methionine synthase activity.* Biochem Soc Trans, 1995. **23**(3): p. 444S.

100. Kenyon, S.H., C.J. Waterfield, J.A. Timbrell, and A. Nicolaou, *Methionine synthase activity and sulphur amino acid levels in the rat liver tumour cells HTC and Phi-1.* Biochem Pharmacol, 2002. **63**(3): p. 381-91.

101. Cavuoto, P. and M.F. Fenech, *A review of methionine dependency and the role of methionine restriction in cancer growth control and life-span extension.* Cancer Treat Rev, 2012. **38**(6): p. 726-36.

102. Cooper, A.J., *Biochemistry of sulfur-containing amino acids.* Annu Rev Biochem, 1983. **52**: p. 187-222.

103. Yamamoto, N., A. Gupta, M. Xu, K. Miki, Y. Tsujimoto, H. Tsuchiya, et al., *Methioninase gene therapy with selenomethionine induces apoptosis in bcl-2-overproducing lung cancer cells.* Cancer Gene Ther, 2003. **10**(6): p. 445-50.

104. Kim, A., J.H. Oh, J.M. Park, and A.S. Chung, *Methylselenol generated from selenomethionine by methioninase downregulates integrin expression and induces caspase-mediated apoptosis of B16F10 melanoma cells.* J Cell Physiol, 2007. **212**(2): p. 386-400.

105. Zeng, H., M. Wu, and J.H. Botnen, *Methylselenol, a selenium metabolite, induces cell cycle arrest in G1 phase and apoptosis via the extracellular-regulated kinase 1/2 pathway and other cancer signaling genes.* J Nutr, 2009. **139**(9): p. 1613-8.

106. Rayman, M.P., *Selenium in cancer prevention: a review of the evidence and mechanism of action.* Proc Nutr Soc, 2005. **64**(4): p. 527-42.

107. Zeng, H., *Selenium as an essential micronutrient: roles in cell cycle and apoptosis.* Molecules, 2009. **14**(3): p. 1263-78.

108. Chaudiere, J., O. Courtin, and J. Leclaire, *Glutathione oxidase activity of selenocystamine: a mechanistic study.* Arch Biochem Biophys, 1992. **296**(1): p. 328-36.

109. Yan, L. and J.E. Spallholz, *Generation of reactive oxygen species from the reaction of selenium compounds with thiols and mammary tumor cells.* Biochem Pharmacol, 1993. **45**(2): p. 429-37.

110. Green, D.R. and J.C. Reed, *Mitochondria and apoptosis.* Science, 1998. **281**(5381): p. 1309-12.

111. Cai, J., J. Yang, and D.P. Jones, *Mitochondrial control of apoptosis: the role of cytochrome c.* Biochim Biophys Acta, 1998. **1366**(1-2): p. 139-49.

112. Li, P., D. Nijhawan, I. Budihardjo, S.M. Srinivasula, M. Ahmad, E.S. Alnemri, et al., *Cytochrome c and dATP-dependent formation of Apaf-1/caspase-9 complex initiates an apoptotic protease cascade.* Cell, 1997. **91**(4): p. 479-89.

113. Spallholz, J.E., *On the nature of selenium toxicity and carcinostatic activity.* Free Radic Biol Med, 1994. **17**(1): p. 45-64.

114. Stewart, M.S., J.E. Spallholz, K.H. Neldner, and B.C. Pence, *Selenium compounds have disparate abilities to impose oxidative stress and induce apoptosis.* Free Radic Biol Med, 1999. **26**(1-2): p. 42-8.

115. Schrauzer, G.N., *Selenomethionine: a review of its nutritional significance, metabolism and toxicity.* J Nutr, 2000. **130**(7): p. 1653-6.

116. Utsugi, T., A.J. Schroit, J. Connor, C.D. Bucana, and I.J. Fidler, *Elevated expression of phosphatidylserine in the outer membrane leaflet of human tumor cells and recognition by activated human blood monocytes.* Cancer Res, 1991. **51**(11): p. 3062-6.

117. Sugimura, M., R. Donato, V.V. Kakkar, and M.F. Scully, *Annexin V as a probe of the contribution of anionic phospholipids to the procoagulant activity of tumour cell surfaces.* Blood Coagul Fibrinolysis, 1994. **5**(3): p. 365-73.

118. Riedl, S., B. Rinner, M. Asslaber, H. Schaider, S. Walzer, A. Novak, et al., *In search of a novel target - phosphatidylserine exposed by non-apoptotic tumor cells and metastases of malignancies with poor treatment efficacy.* Biochim Biophys Acta, 2011. **1808**(11): p. 2638-45.

119. Ran, S., A. Downes, and P.E. Thorpe, *Increased exposure of anionic phospholipids on the surface of tumor blood vessels.* Cancer Res, 2002. **62**(21): p. 6132-40.

120. Ran, S. and P.E. Thorpe, *Phosphatidylserine is a marker of tumor vasculature and a potential target for cancer imaging and therapy.* Int J Radiat Oncol Biol Phys, 2002. **54**(5): p. 1479-84.

121. Siemann, D.W. and M.R. Horsman, *Vascular targeted therapies in oncology.* Cell Tissue Res, 2009. **335**(1): p. 241-8.

122. Hunt;, M., G. Dachs;, and M. Currie;, *Vascular Targeted Gene Therapy in Cancer Treatment*, in *New Gene Therapy and Cancer Research*, W. Gustafsson, Editor. 2008, Nova Science Publishers, Inc. p. 145-181.

123. Zwaal, R.F., P. Comfurius, and E.M. Bevers, *Surface exposure of phosphatidylserine in pathological cells.* Cell Mol Life Sci, 2005. **62**(9): p. 971-88.

124. Williamson, P. and R.A. Schlegel, *Back and forth: the regulation and function of transbilayer phospholipid movement in eukaryotic cells.* Mol Membr Biol, 1994. **11**(4): p. 199-216.

125. Zwaal, R.F. and A.J. Schroit, *Pathophysiologic implications of membrane phospholipid asymmetry in blood cells.* Blood, 1997. **89**(4): p. 1121-32.

126. Clark, M.R., *Flippin' lipids.* Nat Immunol, 2011. **12**(5): p. 373-5.

127. Daleke, D.L., *Phospholipid flippases.* J Biol Chem, 2007. **282**(2): p. 821-5.

128. Rao, L.V., *Mechanisms of activity of lupus anticoagulants.* Curr Opin Hematol, 1997. **4**(5): p. 344-50.

129. Connor, J., C.H. Pak, R.F. Zwaal, and A.J. Schroit, *Bidirectional transbilayer movement of phospholipid analogs in human red blood cells. Evidence for an ATP-dependent and protein-mediated process.* J Biol Chem, 1992. **267**(27): p. 19412-7.

130. Diaz, C. and A.J. Schroit, *Role of translocases in the generation of phosphatidylserine asymmetry.* J Membr Biol, 1996. **151**(1): p. 1-9.

131. Op den Kamp, J.A., *Lipid asymmetry in membranes.* Annu Rev Biochem, 1979. **48**: p. 47-71.

132. Rothman, J.E. and J. Lenard, *Membrane asymmetry.* Science, 1977. **195**(4280): p. 743-53.

133. Rote, N.S., A.K. Ng, D.A. Dostal-Johnson, S.L. Nicholson, and R. Siekman, *Immunologic detection of phosphatidylserine externalization during thrombin-induced platelet activation.* Clin Immunol Immunopathol, 1993. **66**(3): p. 193-200.

134. Herrmann, A. and P.F. Devaux, *Alteration of the aminophospholipid translocase activity during in vivo and artificial aging of human erythrocytes.* Biochim Biophys Acta, 1990. **1027**(1): p. 41-6.

135. Demo, S.D., E. Masuda, A.B. Rossi, B.T. Throndset, A.L. Gerard, E.H. Chan, et al., *Quantitative measurement of mast cell degranulation using a novel flow cytometric annexin-V binding assay.* Cytometry, 1999. **36**(4): p. 340-8.

136. Blankenberg, F.G., P.D. Katsikis, J.F. Tait, R.E. Davis, L. Naumovski, K. Ohtsuki, et al., *In vivo detection and imaging of phosphatidylserine expression during programmed cell death.* Proc Natl Acad Sci U S A, 1998. **95**(11): p. 6349-54.

137. Soares, M.M., S.W. King, and P.E. Thorpe, *Targeting inside-out phosphatidylserine as a therapeutic strategy for viral diseases.* Nat Med, 2008. **14**(12): p. 1357-62.

138. Ran, S., J. He, X. Huang, M. Soares, D. Scothorn, and P.E. Thorpe, *Antitumor effects of a monoclonal antibody that binds anionic phospholipids on the surface of tumor blood vessels in mice.* Clin Cancer Res, 2005. **11**(4): p. 1551-62.

139. Touraine, R.L., N. Vahanian, W.J. Ramsey, and R.M. Blaese, *Enhancement of the herpes simplex virus thymidine kinase/ganciclovir bystander effect and its antitumor efficacy in vivo by pharmacologic manipulation of gap junctions.* Hum Gene Ther, 1998. **9**(16): p. 2385-91.

140. Connor, J., C. Bucana, I.J. Fidler, and A.J. Schroit, *Differentiation-dependent expression of phosphatidylserine in mammalian plasma membranes:*

quantitative assessment of outer-leaflet lipid by prothrombinase complex formation. Proc Natl Acad Sci U S A, 1989. **86**(9): p. 3184-8.

141. Rao, L.V., J.F. Tait, and A.D. Hoang, *Binding of annexin V to a human ovarian carcinoma cell line (OC-2008). Contrasting effects on cell surface factor VIIa/tissue factor activity and prothrombinase activity.* Thromb Res, 1992. **67**(5): p. 517-31.

142. Woehlecke, H., A. Pohl, N. Alder-Baerens, H. Lage, and A. Herrmann, *Enhanced exposure of phosphatidylserine in human gastric carcinoma cells overexpressing the half-size ABC transporter BCRP (ABCG2).* Biochem J, 2003. **376**(Pt 2): p. 489-95.

143. Fadeel, B., B. Gleiss, K. Hogstrand, J. Chandra, T. Wiedmer, P.J. Sims, et al., *Phosphatidylserine exposure during apoptosis is a cell-type-specific event and does not correlate with plasma membrane phospholipid scramblase expression.* Biochem Biophys Res Commun, 1999. **266**(2): p. 504-11.

144. Wiegand, U.K., S. Corbach, A.R. Prescott, J. Savill, and B.A. Spruce, *The trigger to cell death determines the efficiency with which dying cells are cleared by neighbours.* Cell Death Differ, 2001. **8**(7): p. 734-46.

145. Yan, X., K. Doffek, C. Yin, M. Krein, M. Phillips, S.L. Sugg, et al., *Annexin-V promotes anti-tumor immunity and inhibits neuroblastoma growth in vivo.* Cancer Immunol Immunother, 2012. **61**(11): p. 1917-27.

146. Yin, Y., X. Huang, K.D. Lynn, and P.E. Thorpe, *Phosphatidylserine-targeting antibody induces M1 macrophage polarization and promotes myeloid-derived suppressor cell differentiation.* Cancer Immunol Res, 2013. **1**(4): p. 256-68.

147. Bondanza, A., V.S. Zimmermann, P. Rovere-Querini, J. Turnay, I.E. Dumitriu, C.M. Stach, et al., *Inhibition of phosphatidylserine recognition heightens the immunogenicity of irradiated lymphoma cells in vivo.* J Exp Med, 2004. **200**(9): p. 1157-65.

148. Luster, T.A., J. He, X. Huang, S.N. Maiti, A.J. Schroit, P.G. de Groot, et al., *Plasma protein beta-2-glycoprotein 1 mediates interaction between the anti-tumor monoclonal antibody 3G4 and anionic phospholipids on endothelial cells.* J Biol Chem, 2006. **281**(40): p. 29863-71.

149. Lim, L.H. and S. Pervaiz, *Annexin 1: the new face of an old molecule.* FASEB J, 2007. **21**(4): p. 968-75.

150. Raynal, P. and H.B. Pollard, *Annexins: the problem of assessing the biological role for a gene family of multifunctional calcium- and phospholipid-binding proteins.* Biochim Biophys Acta, 1994. **1197**(1): p. 63-93.

151. Moss, S.E. and R.O. Morgan, *The annexins.* Genome Biol, 2004. **5**(4): p. 219.

152. Gerke, V. and S.E. Moss, *Annexins: from structure to function.* Physiol Rev, 2002. **82**(2): p. 331-71.

153. Blume, K.E., S. Soeroes, M. Waibel, H. Keppeler, S. Wesselborg, M. Herrmann, et al., *Cell surface externalization of annexin A1 as a failsafe mechanism preventing inflammatory responses during secondary necrosis.* J Immunol, 2009. **183**(12): p. 8138-47.

154. Ohsawa, K., Y. Imai, D. Ito, and S. Kohsaka, *Molecular cloning and characterization of annexin V-binding proteins with highly hydrophilic peptide structure.* Journal of Neurochemistry, 1996. **67**(1): p. 89-97.

155. Fadeel, B. and D. Xue, *PS externalization: from corpse clearance to drug delivery.* Cell Death Differ, 2006. **13**(3): p. 360-2.

156. van Engeland, M., L.J. Nieland, F.C. Ramaekers, B. Schutte, and C.P. Reutelingsperger, *Annexin V-affinity assay: a review on an apoptosis detection system based on phosphatidylserine exposure.* Cytometry, 1998. **31**(1): p. 1-9.

157. Van Rite, B.D., J.J. Krais, M. Cherry, V.I. Sikavitsas, C. Kurkjian, and R.G. Harrison, *Antitumor activity of an enzyme prodrug therapy targeted to the breast tumor vasculature.* Cancer Invest, 2013. **31**(8): p. 505-10.

158. Dhakal, H.P., J.M. Nesland, M. Forsund, C.G. Trope, and R. Holm, *Primary tumor vascularity, HIF-1alpha and VEGF expression in vulvar squamous cell carcinomas: their relationships with clinicopathological characteristics and prognostic impact.* BMC Cancer, 2013. **13**: p. 506.

159. Folkman, J., *What is the evidence that tumors are angiogenesis dependent?* J Natl Cancer Inst, 1990. **82**(1): p. 4-6.

160. Ribatti, D., A. Vacca, and F. Dammacco, *The role of the vascular phase in solid tumor growth: a historical review.* Neoplasia, 1999. **1**(4): p. 293-302.

161. Services, U.S.D.o.H.a.H., *Guidance for Industry: Immunogenicity Assessment for Therapeutic Protein Products*, C.f.D.E.a.R. Food and Drug Administration, Center for Biologics Evaluation and Research, Editor. 2014: Silver Spring, MD.

162. Baker, M.P., H.M. Reynolds, B. Lumicisi, and C.J. Bryson, *Immunogenicity of protein therapeutics: The key causes, consequences and challenges.* Self Nonself, 2010. **1**(4): p. 314-322.

163. Pasut, G. and F.M. Veronese, *Polymer-drug conjugation, recent achievements and general strategies.* Progress in Polymer Science, 2007. **32**(8-9): p. 933-961.

164. Gallucci, R., *Lecture: Immunogens and Antigens*. 2012: University of Oklahoma Health Sciences Center.

165. Cong, Y.H., E. Pawlisz, P. Bryant, S. Balan, E. Laurine, R. Tommasi, et al., *Site-Specific PEGylation at Histidine Tags.* Bioconjugate Chemistry, 2012. **23**(2): p. 248-263.

166. Abuchowski, A., T. Vanes, N.C. Palczuk, and F.F. Davis, *Alteration of Immunological Properties of Bovine Serum-Albumin by Covalent Attachment of Polyethylene-Glycol.* Journal of Biological Chemistry, 1977. **252**(11): p. 3578-3581.

167. Jevsevar, S., M. Kunstelj, and V.G. Porekar, *PEGylation of therapeutic proteins.* Biotechnol J, 2010. **5**(1): p. 113-28.

168. Chirino, A.J., M.L. Ary, and S.A. Marshall, *Minimizing the immunogenicity of protein therapeutics.* Drug Discov Today, 2004. **9**(2): p. 82-90.

169. Stone, E., O. Paley, J. Hu, B. Ekerdt, N.K. Cheung, and G. Georgiou, *De novo engineering of a human cystathionine-gamma-lyase for systemic (L)-Methionine depletion cancer therapy.* ACS Chem Biol, 2012. **7**(11): p. 1822-9.

170. Hanahan, D. and R.A. Weinberg, *The hallmarks of cancer.* Cell, 2000. **100**(1): p. 57-70.

171. Hanahan, D. and R.A. Weinberg, *Hallmarks of cancer: the next generation.* Cell, 2011. **144**(5): p. 646-74.

172. Mayer, L.D. and A.S. Janoff, *Optimizing combination chemotherapy by controlling drug ratios.* Mol Interv, 2007. **7**(4): p. 216-23.

173. Hernandez-Vargas, H., J. Palacios, and G. Moreno-Bueno, *Molecular profiling of docetaxel cytotoxicity in breast cancer cells: uncoupling of aberrant mitosis and apoptosis.* Oncogene, 2007. **26**(20): p. 2902-13.

174. Montero, A., F. Fossella, G. Hortobagyi, and V. Valero, *Docetaxel for treatment of solid tumours: a systematic review of clinical data.* Lancet Oncol, 2005. **6**(4): p. 229-39.

175. Drucker, L., P. Ciobotaro, O. Kimchi, T. Tohami, S. Yarkoni, J. Radnay, et al., *Initial exposed phosphatidylserine levels correlate with cellular response to cytotoxic drugs.* Eur J Haematol, 2003. **70**(2): p. 98-105.

176. Huang, X., M. Bennett, and P.E. Thorpe, *A monoclonal antibody that binds anionic phospholipids on tumor blood vessels enhances the antitumor effect of docetaxel on human breast tumors in mice.* Cancer Res, 2005. **65**(10): p. 4408-16.

177. Semenza, G.L., *Hypoxia-inducible factors in physiology and medicine.* Cell, 2012. **148**(3): p. 399-408.

178. Zeng, Q., Z. Yang, Y.J. Gao, H. Yuan, K. Cui, Y. Shi, et al., *Treating triple-negative breast cancer by a combination of rapamycin and cyclophosphamide: an in vivo bioluminescence imaging study.* Eur J Cancer, 2010. **46**(6): p. 1132-43.

179. Goel, S., D.G. Duda, L. Xu, L.L. Munn, Y. Boucher, D. Fukumura, et al., *Normalization of the vasculature for treatment of cancer and other diseases.* Physiol Rev, 2011. **91**(3): p. 1071-121.

180. Sullivan, R. and C.H. Graham, *Hypoxia-driven selection of the metastatic phenotype.* Cancer Metastasis Rev, 2007. **26**(2): p. 319-31.

181. Laughner, E., P. Taghavi, K. Chiles, P.C. Mahon, and G.L. Semenza, *HER2 (neu) signaling increases the rate of hypoxia-inducible factor 1alpha (HIF-1alpha) synthesis: novel mechanism for HIF-1-mediated vascular endothelial growth factor expression.* Mol Cell Biol, 2001. **21**(12): p. 3995-4004.

182. Loboda, A., A. Jozkowicz, and J. Dulak, *HIF-1 and HIF-2 transcription factors--similar but not identical.* Mol Cells, 2010. **29**(5): p. 435-42.

183. Guba, M., P. von Breitenbuch, M. Steinbauer, G. Koehl, S. Flegel, M. Hornung, et al., *Rapamycin inhibits primary and metastatic tumor growth by antiangiogenesis: involvement of vascular endothelial growth factor.* Nat Med, 2002. **8**(2): p. 128-35.

184. Shih, T. and C. Lindley, *Bevacizumab: an angiogenesis inhibitor for the treatment of solid malignancies.* Clin Ther, 2006. **28**(11): p. 1779-802.

185. Gotink, K.J. and H.M. Verheul, *Anti-angiogenic tyrosine kinase inhibitors: what is their mechanism of action?* Angiogenesis, 2010. **13**(1): p. 1-14.

186. Chang, S.B., P. Miron, A. Miron, and J.D. Iglehart, *Rapamycin inhibits proliferation of estrogen-receptor-positive breast cancer cells.* J Surg Res, 2007. **138**(1): p. 37-44.

187. Thomas, G.V., C. Tran, I.K. Mellinghoff, D.S. Welsbie, E. Chan, B. Fueger, et al., *Hypoxia-inducible factor determines sensitivity to inhibitors of mTOR in kidney cancer.* Nat Med, 2006. **12**(1): p. 122-7.

188. Toschi, A., E. Lee, N. Gadir, M. Ohh, and D.A. Foster, *Differential dependence of hypoxia-inducible factors 1 alpha and 2 alpha on mTORC1 and mTORC2.* J Biol Chem, 2008. **283**(50): p. 34495-9.

189. Ng;, D.-L., S.-W. Tie;, P.-C. Ong;, W.-S. Lim;, T.-S. Tengku-Muhammad;, and Q.-C. Choo, *Rapamycin pre-treatment abrogates Tumour Necrosis Factor-1a down-regulatory effects on LXR-a and PXR mRNA expression via inhibition of c-Jun N-terminal kinase 1 activation in HepG2 cells.* Electronic Journal of Biotechnology, 2011. **12**(3).

190. Moeller, B.J., Y. Cao, C.Y. Li, and M.W. Dewhirst, *Radiation activates HIF-1 to regulate vascular radiosensitivity in tumors: role of reoxygenation, free radicals, and stress granules.* Cancer Cell, 2004. **5**(5): p. 429-41.

191. Facciabene, A., G.T. Motz, and G. Coukos, *T-regulatory cells: key players in tumor immune escape and angiogenesis.* Cancer Res, 2012. **72**(9): p. 2162-71.

192. Parham, P., *The Immune System*. 3 ed. The Development of T Lymphocytes. 2009, New York, NY.

193. Li, X., E. Kostareli, J. Suffner, N. Garbi, and G.J. Hammerling, *Efficient Treg depletion induces T-cell infiltration and rejection of large tumors.* Eur J Immunol, 2010. **40**(12): p. 3325-35.

194. Corthay, A., *How do regulatory T cells work?* Scand J Immunol, 2009. **70**(4): p. 326-36.

195. Vignali, D.A., L.W. Collison, and C.J. Workman, *How regulatory T cells work.* Nat Rev Immunol, 2008. **8**(7): p. 523-32.

196. Onizuka, S., I. Tawara, J. Shimizu, S. Sakaguchi, T. Fujita, and E. Nakayama, *Tumor rejection by in vivo administration of anti-CD25 (interleukin-2 receptor alpha) monoclonal antibody.* Cancer Res, 1999. **59**(13): p. 3128-33.

197. Shimizu, J., S. Yamazaki, and S. Sakaguchi, *Induction of tumor immunity by removing CD25+CD4+ T cells: a common basis between tumor immunity and autoimmunity.* J Immunol, 1999. **163**(10): p. 5211-8.

198. Lutsiak, M.E., R.T. Semnani, R. De Pascalis, S.V. Kashmiri, J. Schlom, and H. Sabzevari, *Inhibition of CD4(+)25+ T regulatory cell function implicated in enhanced immune response by low-dose cyclophosphamide.* Blood, 2005. **105**(7): p. 2862-8.

199. Heylmann, D., M. Bauer, H. Becker, S. van Gool, N. Bacher, K. Steinbrink, et al., *Human CD4+CD25+ regulatory T cells are sensitive to low dose cyclophosphamide: implications for the immune response.* PLoS One, 2013. **8**(12): p. e83384.

200. Sharabi, A. and N. Haran-Ghera, *Immune recovery after cyclophosphamide treatment in multiple myeloma: implication for maintenance immunotherapy.* Bone Marrow Res, 2011. **2011**: p. 269519.

201. Barbon, C.M., M. Yang, G.D. Wands, R. Ramesh, B.S. Slusher, M.L. Hedley, et al., *Consecutive low doses of cyclophosphamide preferentially target Tregs and potentiate T cell responses induced by DNA PLG microparticle immunization.* Cell Immunol, 2010. **262**(2): p. 150-61.

202. Castano, A.P., P. Mroz, M.X. Wu, and M.R. Hamblin, *Photodynamic therapy plus low-dose cyclophosphamide generates antitumor immunity in a mouse model.* Proc Natl Acad Sci U S A, 2008. **105**(14): p. 5495-500.

203. Neves, L.F., J.J. Krais, B.D. Van Rite, R. Ramesh, D.E. Resasco, and R.G. Harrison, *Targeting single-walled carbon nanotubes for the treatment of breast cancer using photothermal therapy.* Nanotechnology, 2013. **24**(37): p. 375104.

204. Nowak, A.K., R.A. Lake, A.L. Marzo, B. Scott, W.R. Heath, E.J. Collins, et al., *Induction of tumor cell apoptosis in vivo increases tumor antigen cross-presentation, cross-priming rather than cross-tolerizing host tumor-specific CD8 T cells.* J Immunol, 2003. **170**(10): p. 4905-13.

205. Gibson, D.G., H.O. Smith, C.A. Hutchison, 3rd, J.C. Venter, and C. Merryman, *Chemical synthesis of the mouse mitochondrial genome.* Nat Methods, 2010. **7**(11): p. 901-3.

206. Gibson, D.G., L. Young, R.Y. Chuang, J.C. Venter, C.A. Hutchison, 3rd, and H.O. Smith, *Enzymatic assembly of DNA molecules up to several hundred kilobases.* Nat Methods, 2009. **6**(5): p. 343-5.

207. Zang, X.P., N.R. Palwai, M.R. Lerner, D.J. Brackett, J.T. Pento, and R.G. Harrison, *Targeting a methioninase-containing fusion protein to breast cancer urokinase receptors inhibits growth and migration.* Anticancer Res, 2006. **26**(3A): p. 1745-51.

208. Laemmli, U.K., *Cleavage of structural proteins during the assembly of the head of bacteriophage T4.* Nature, 1970. **227**(5259): p. 680-5.

209. Senter, P.D., P.C. Su, T. Katsuragi, T. Sakai, W.L. Cosand, I. Hellstrom, et al., *Generation of 5-fluorouracil from 5-fluorocytosine by monoclonal antibody-cytosine deaminase conjugates.* Bioconjug Chem, 1991. **2**(6): p. 447-51.

210. Krais, J.J., O. De Crescenzo, and R.G. Harrison, *Purine nucleoside phosphorylase targeted by annexin v to breast cancer vasculature for enzyme prodrug therapy.* PLoS One, 2013. **8**(10): p. e76403.

211. Nichols, W.W., E.B. Buynak, C. Bradt, R. Hill, M. Aronson, B.E. Jarrell, et al., *Cytogenetic evaluation of human endothelial cell cultures.* J Cell Physiol, 1987. **132**(3): p. 453-62.

212. Kremmidiotis, G., A.F. Leske, T.C. Lavranos, D. Beaumont, J. Gasic, A. Hall, et al., *BNC105: a novel tubulin polymerization inhibitor that selectively disrupts tumor vasculature and displays single-agent antitumor efficacy.* Mol Cancer Ther, 2010. **9**(6): p. 1562-73.

213. Doraiswamy, A. and R.J. Narayan, *Vascular tissue engineering by computer-aided laser micromachining.* Philos Trans A Math Phys Eng Sci, 2010. **368**(1917): p. 1891-912.

214. Chen, L., T.G. Huang, M. Meseck, J. Mandeli, J. Fallon, and S.L. Woo, *Rejection of metastatic 4T1 breast cancer by attenuation of Treg cells in combination with immune stimulation.* Mol Ther, 2007. **15**(12): p. 2194-202.

215. Ho, B.Y., C.H. Lin, M.K. Apaya, W.W. Chao, and L.F. Shyur, *Silibinin and Paclitaxel Cotreatment Significantly Suppress the Activity and Lung Metastasis of Triple Negative 4T1 Mammary Tumor Cell in Mice.* J Tradit Complement Med, 2012. **2**(4): p. 301-11.

216. Pulaski, B.A., D.S. Terman, S. Khan, E. Muller, and S. Ostrand-Rosenberg, *Cooperativity of Staphylococcal aureus enterotoxin B superantigen, major histocompatibility complex class II, and CD80 for immunotherapy of advanced spontaneous metastases in a clinically relevant postoperative mouse breast cancer model.* Cancer Res, 2000. **60**(10): p. 2710-5.

217. Pulaski, B.A. and S. Ostrand-Rosenberg, *Mouse 4T1 breast tumor model.* Curr Protoc Immunol, 2001. **Chapter 20**: p. Unit 20 2.

218. Heppner, G.H., F.R. Miller, and P.M. Shekhar, *Nontransgenic models of breast cancer.* Breast Cancer Res, 2000. **2**(5): p. 331-4.

219. Pulaski, B.A. and S. Ostrand-Rosenberg, *Reduction of established spontaneous mammary carcinoma metastases following immunotherapy with major*

histocompatibility complex class II and B7.1 cell-based tumor vaccines. Cancer Res, 1998. **58**(7): p. 1486-93.

220. Chan, G.N. and R. Bendayan, *Molecular and functional characterization of P-glycoprotein in vitro.* Methods Mol Biol, 2011. **686**: p. 313-36.

221. Levelt, C.N. and K. Eichmann, *Streptavidin-tricolor is a reliable marker for nonviable cells subjected to permeabilization or fixation.* Cytometry, 1994. **15**(1): p. 84-6.

222. O'Brien, J., I. Wilson, T. Orton, and F. Pognan, *Investigation of the Alamar Blue (resazurin) fluorescent dye for the assessment of mammalian cell cytotoxicity.* Eur J Biochem, 2000. **267**(17): p. 5421-6.

223. Mikus, J. and D. Steverding, *A simple colorimetric method to screen drug cytotoxicity against Leishmania using the dye Alamar Blue.* Parasitol Int, 2000. **48**(3): p. 265-9.

224. Franzblau, S., *A rapid, microplate-based assay for evaluating the activity of drugs against Mycobacterium leprae, employing the reduction of Alamar Blue.* Lepr Rev, 2000. **71 Suppl**: p. S74-5; discussion S76.

225. Lou, Y., P.C. McDonald, A. Oloumi, S. Chia, C. Ostlund, A. Ahmadi, et al., *Targeting tumor hypoxia: suppression of breast tumor growth and metastasis by novel carbonic anhydrase IX inhibitors.* Cancer Res, 2011. **71**(9): p. 3364-76.

226. Yang, Z., J. Wang, Q. Lu, J. Xu, Y. Kobayashi, T. Takakura, et al., *PEGylation confers greatly extended half-life and attenuated immunogenicity to recombinant methioninase in primates.* Cancer Res, 2004. **64**(18): p. 6673-8.

227. Sun, X., Z. Yang, S. Li, Y. Tan, N. Zhang, X. Wang, et al., *In vivo efficacy of recombinant methioninase is enhanced by the combination of polyethylene glycol conjugation and pyridoxal 5'-phosphate supplementation.* Cancer Res, 2003. **63**(23): p. 8377-83.

228. Olszewski, M.A., G.B. Huffnagle, R.A. McDonald, D.M. Lindell, B.B. Moore, D.N. Cook, et al., *The role of macrophage inflammatory protein-1 alpha/CCL3 in regulation of T cell-mediated immunity to Cryptococcus neoformans infection.* J Immunol, 2000. **165**(11): p. 6429-36.

229. Law, J.P., D.F. Hirschkorn, R.E. Owen, H.H. Biswas, P.J. Norris, and M.C. Lanteri, *The importance of Foxp3 antibody and fixation/permeabilization buffer combinations in identifying CD4+CD25+Foxp3+ regulatory T cells.* Cytometry A, 2009. **75**(12): p. 1040-50.

230. Peng, S., S. Lyford-Pike, B. Akpeng, A. Wu, C.F. Hung, D. Hannaman, et al., *Low-dose cyclophosphamide administered as daily or single dose enhances the antitumor effects of a therapeutic HPV vaccine.* Cancer Immunol Immunother, 2013. **62**(1): p. 171-82.

231. Oliveira, L.J. and P.J. Hansen, *Deviations in populations of peripheral blood mononuclear cells and endometrial macrophages in the cow during pregnancy.* Reproduction, 2008. **136**(4): p. 481-90.

232. Zhao, W., K. Sachsenmeier, L. Zhang, E. Sult, R.E. Hollingsworth, and H. Yang, *A New Bliss Independence Model to Analyze Drug Combination Data.* J Biomol Screen, 2014. **19**(5): p. 817-821.

233. Yan, H., B. Zhang, S. Li, and Q. Zhao, *A formal model for analyzing drug combination effects and its application in TNF-alpha-induced NFkappaB pathway.* BMC Syst Biol, 2010. **4**: p. 50.

234. Grunberg, E., E. Titsworth, and M. Bennett, *Chemotherapeutic Activity of 5-Fluorocytosine.* Antimicrob Agents Chemother (Bethesda), 1963. **161**: p. 566-8.

235. King, I., D. Bermudes, S. Lin, M. Belcourt, J. Pike, K. Troy, et al., *Tumor-targeted Salmonella expressing cytosine deaminase as an anticancer agent.* Hum Gene Ther, 2002. **13**(10): p. 1225-33.

236. Leveille, S., S. Samuel, M.L. Goulet, and J. Hiscott, *Enhancing VSV oncolytic activity with an improved cytosine deaminase suicide gene strategy.* Cancer Gene Ther, 2011. **18**(6): p. 435-43.

237. Modrak-Wojcik, A., K. Stepniak, V. Akoev, M. Zolkiewski, and A. Bzowska, *Molecular architecture of E. coli purine nucleoside phosphorylase studied by analytical ultracentrifugation and CD spectroscopy.* Protein Sci, 2006. **15**(7): p. 1794-800.

238. Koellner, G., A. Bzowska, B. Wielgus-Kutrowska, M. Luic, T. Steiner, W. Saenger, et al., *Open and closed conformation of the E. coli purine nucleoside*

phosphorylase active center and implications for the catalytic mechanism. J Mol Biol, 2002. **315**(3): p. 351-71.

239. Arur, S., U.E. Uche, K. Rezaul, M. Fong, V. Scranton, A.E. Cowan, et al., *Annexin I is an endogenous ligand that mediates apoptotic cell engulfment.* Developmental Cell, 2003. **4**(4): p. 587-598.

240. Danhauser, L., W. Plunkett, M. Keating, and F. Cabanillas, *9-beta-D-arabinofuranosyl-2-fluoroadenine 5'-monophosphate pharmacokinetics in plasma and tumor cells of patients with relapsed leukemia and lymphoma.* Cancer Chemother Pharmacol, 1986. **18**(2): p. 145-52.

241. Voeks, D., R. Martiniello-Wilks, V. Madden, K. Smith, E. Bennetts, G.W. Both, et al., *Gene therapy for prostate cancer delivered by ovine adenovirus and mediated by purine nucleoside phosphorylase and fludarabine in mouse models.* Gene Ther, 2002. **9**(12): p. 759-68.

242. Xie, X., J. Guo, Y. Kong, G.X. Xie, L. Li, N. Lv, et al., *Targeted expression of Escherichia coli purine nucleoside phosphorylase and Fludara(R) for prostate cancer therapy.* J Gene Med, 2011. **13**(12): p. 680-91.

243. Parker, W.B., P.W. Allan, W.R. Waud, J.S. Hong, and E.J. Sorscher, *Effect of expression of adenine phosphoribosyltransferase on the in vivo anti-tumor activity of prodrugs activated by E. coli purine nucleoside phosphorylase.* Cancer Gene Ther, 2011. **18**(6): p. 390-8.

244. Ham, D.Y.L., *Pharmacology/Toxicology Review and Evaluation: Oral Fludarabine Phosphate*, C.f.D.E.a.R. Food and Drug Administration, Division of Oncology Drug Products, Editor. 2008.

245. Mason, K.A., K. Kishi, N. Hunter, L. Buchmiller, T. Akimoto, R. Komaki, et al., *Effect of docetaxel on the therapeutic ratio of fractionated radiotherapy in vivo.* Clin Cancer Res, 1999. **5**(12): p. 4191-8.

246. Vanhoefer, U., S. Cao, A. Harstrick, S. Seeber, and Y.M. Rustum, *Comparative antitumor efficacy of docetaxel and paclitaxel in nude mice bearing human tumor xenografts that overexpress the multidrug resistance protein (MRP).* Ann Oncol, 1997. **8**(12): p. 1221-8.

247. Fizazi, K., C.R. Sikes, J. Kim, J. Yang, L.A. Martinez, M.C. Olive, et al., *High efficacy of docetaxel with and without androgen deprivation and estramustine in preclinical models of advanced prostate cancer.* Anticancer Research, 2004. **24**(5A): p. 2897-2903.

248. Singh, P.P., S. Joshi, P.J. Russell, S. Nair, and A. Khatri, *Purine Nucleoside Phosphorylase mediated molecular chemotherapy and conventional chemotherapy: a tangible union against chemoresistant cancer.* BMC Cancer, 2011. **11**: p. 368.

249. Thorpe, P.E., *Vascular targeting agents as cancer therapeutics.* Clin Cancer Res, 2004. **10**(2): p. 415-27.

250. Afshar, S., M.R. Sawaya, and S.L. Morrison, *Structure of a mutant human purine nucleoside phosphorylase with the prodrug, 2-fluoro-2'-deoxyadenosine and the cytotoxic drug, 2-fluoroadenine.* Protein Sci, 2009. **18**(5): p. 1107-14.

251. Afshar, S., T. Olafsen, A.M. Wu, and S.L. Morrison, *Characterization of an engineered human purine nucleoside phosphorylase fused to an anti-her2/neu single chain Fv for use in ADEPT.* J Exp Clin Cancer Res, 2009. **28**: p. 147.

252. Afshar, S., T. Asai, and S.L. Morrison, *Humanized ADEPT comprised of an engineered human purine nucleoside phosphorylase and a tumor targeting peptide for treatment of cancer.* Mol Cancer Ther, 2009. **8**(1): p. 185-93.

253. Fleming, J.M., T.C. Miller, M.J. Meyer, E. Ginsburg, and B.K. Vonderhaar, *Local regulation of human breast xenograft models.* J Cell Physiol, 2010. **224**(3): p. 795-806.

254. Iorns, E., K. Drews-Elger, T.M. Ward, S. Dean, J. Clarke, D. Berry, et al., *A new mouse model for the study of human breast cancer metastasis.* PLoS One, 2012. **7**(10): p. e47995.

255. Brewerton, L.J., E. Fung, and F.F. Snyder, *Polyethylene glycol-conjugated adenosine phosphorylase: development of alternative enzyme therapy for adenosine deaminase deficiency.* Biochim Biophys Acta, 2003. **1637**(2): p. 171-7.

256. Brinks, V., W. Jiskoot, and H. Schellekens, *Immunogenicity of therapeutic proteins: the use of animal models.* Pharm Res, 2011. **28**(10): p. 2379-85.

257. Koren, E., L.A. Zuckerman, and A.R. Mire-Sluis, *Immune responses to therapeutic proteins in humans--clinical significance, assessment and prediction.* Curr Pharm Biotechnol, 2002. **3**(4): p. 349-60.

258. De Groot, A.S. and L. Moise, *Prediction of immunogenicity for therapeutic proteins: state of the art.* Curr Opin Drug Discov Devel, 2007. **10**(3): p. 332-40.

259. Parham, P., *The Immune System*. 3 ed. Cancer and Its Interactions with the Immune System. 2009, New York, NY.

260. Kolenko, V., R.G. Uzzo, R. Bukowski, N.H. Bander, A.C. Novick, E.D. Hsi, et al., *Dead or dying: necrosis versus apoptosis in caspase-deficient human renal cell carcinoma.* Cancer Res, 1999. **59**(12): p. 2838-42.

261. Huang, Q., F. Li, X. Liu, W. Li, W. Shi, F.F. Liu, et al., *Caspase 3-mediated stimulation of tumor cell repopulation during cancer radiotherapy.* Nat Med, 2011. **17**(7): p. 860-6.

262. Zhang, X., G. Barile, S. Chang, A. Hays, S. Pachydaki, W. Schiff, et al., *Apoptosis and cell proliferation in proliferative retinal disorders: PCNA, Ki-67, caspase-3, and PARP expression.* Curr Eye Res, 2005. **30**(5): p. 395-403.

263. Urruticoechea, A., I.E. Smith, and M. Dowsett, *Proliferation marker Ki-67 in early breast cancer.* J Clin Oncol, 2005. **23**(28): p. 7212-20.

264. Liu, Q., J. Qiu, M. Liang, J. Golinski, K. van Leyen, J.E. Jung, et al., *Akt and mTOR mediate programmed necrosis in neurons.* Cell Death Dis, 2014. **5**: p. e1084.

265. Adkins, J.R., M.R. Castresana, Z. Wang, and W.H. Newman, *Rapamycin inhibits release of tumor necrosis factor-alpha from human vascular smooth muscle cells.* Am Surg, 2004. **70**(5): p. 384-7; discussion 387-8.

266. Demaria, S., N. Kawashima, A.M. Yang, M.L. Devitt, J.S. Babb, J.P. Allison, et al., *Immune-mediated inhibition of metastases after treatment with local radiation and CTLA-4 blockade in a mouse model of breast cancer.* Clin Cancer Res, 2005. **11**(2 Pt 1): p. 728-34.

267. Limpert, E., W.A. Stahel, and M. Abbt, *Log-normal distributions across the sciences: Keys and clues.* Bioscience, 2001. **51**(5): p. 341-352.

268. Heitjan, D.F., *Biology, models, and the analysis of tumor xenograft experiments.* Clin Cancer Res, 2011. **17**(5): p. 949-51.

269. Law, B.K., *Rapamycin: an anti-cancer immunosuppressant?* Crit Rev Oncol Hematol, 2005. **56**(1): p. 47-60.

270. Motz, G.T. and G. Coukos, *The parallel lives of angiogenesis and immunosuppression: cancer and other tales.* Nat Rev Immunol, 2011. **11**(10): p. 702-11.

271. Ben-Shoshan, J., S. Maysel-Auslender, A. Mor, G. Keren, and J. George, *Hypoxia controls CD4+CD25+ regulatory T-cell homeostasis via hypoxia-inducible factor-1alpha.* Eur J Immunol, 2008. **38**(9): p. 2412-8.

272. Yan, M., N. Jene, D. Byrne, E.K. Millar, S.A. O'Toole, C.M. McNeil, et al., *Recruitment of regulatory T cells is correlated with hypoxia-induced CXCR4 expression, and is associated with poor prognosis in basal-like breast cancers.* Breast Cancer Res, 2011. **13**(2): p. R47.

273. Sakaguchi, S., N. Sakaguchi, M. Asano, M. Itoh, and M. Toda, *Immunologic self-tolerance maintained by activated T cells expressing IL-2 receptor alpha-chains (CD25). Breakdown of a single mechanism of self-tolerance causes various autoimmune diseases.* J Immunol, 1995. **155**(3): p. 1151-64.

274. Thornton, A.M. and E.M. Shevach, *CD4+CD25+ immunoregulatory T cells suppress polyclonal T cell activation in vitro by inhibiting interleukin 2 production.* J Exp Med, 1998. **188**(2): p. 287-96.

275. Cheng, G., A. Yu, M.J. Dee, and T.R. Malek, *IL-2R signaling is essential for functional maturation of regulatory T cells during thymic development.* J Immunol, 2013. **190**(4): p. 1567-75.

276. Ghiringhelli, F., N. Larmonier, E. Schmitt, A. Parcellier, D. Cathelin, C. Garrido, et al., *CD4+CD25+ regulatory T cells suppress tumor immunity but are sensitive to cyclophosphamide which allows immunotherapy of established tumors to be curative.* Eur J Immunol, 2004. **34**(2): p. 336-44.

277. Wang, C., J.H. Lee, and C.H. Kim, *Optimal population of FoxP3+ T cells in tumors requires an antigen priming-dependent trafficking receptor switch.* PLoS One, 2012. **7**(1): p. e30793.

278. Fournier;, P., P. Juarez;, H. Davis;, M. Riggins;, M. Niewolna;, X. Peng;, et al., *T cells and myeloid-derived suppressor cells in breast cancer bone metastasis: regulation of osteoclastogenesis and immunosuppression.*

279. Chaput, N., G. Darrasse-Jeze, A.S. Bergot, C. Cordier, S. Ngo-Abdalla, D. Klatzmann, et al., *Regulatory T cells prevent CD8 T cell maturation by inhibiting CD4 Th cells at tumor sites.* J Immunol, 2007. **179**(8): p. 4969-78.

280. Francia, G., W. Cruz-Munoz, S. Man, P. Xu, and R.S. Kerbel, *Mouse models of advanced spontaneous metastasis for experimental therapeutics.* Nat Rev Cancer, 2011. **11**(2): p. 135-41.

281. Tallarida, R.J., *Quantitative methods for assessing drug synergism.* Genes Cancer, 2011. **2**(11): p. 1003-8.

282. Smyth, M.J., D.I. Godfrey, and J.A. Trapani, *A fresh look at tumor immunosurveillance and immunotherapy.* Nat Immunol, 2001. **2**(4): p. 293-9.

283. Kurt, R.A., J.A. Park, M.C. Panelli, S.F. Schluter, J.J. Marchalonis, B. Carolus, et al., *T lymphocytes infiltrating sites of tumor rejection and progression display identical V beta usage but different cytotoxic activities.* J Immunol, 1995. **154**(8): p. 3969-74.

284. Li, X., H. Le, R.F. Wolf, V.A. Chen, A. Sarkar, R.E. Nordquist, et al., *Long-term effect on EMT6 tumors in mice induced by combination of laser immunotherapy and surgery.* Integr Cancer Ther, 2011. **10**(4): p. 368-73.

285. Gorczynski, R.M., Z. Chen, I. Khatri, A. Podnos, and K. Yu, *Cure of metastatic growth of EMT6 tumor cells in mice following manipulation of CD200:CD200R signaling.* Breast Cancer Res Treat, 2013. **142**(2): p. 271-82.

Appendix A: Supplemental Data

PNP-AV *In Vitro* Binding Data

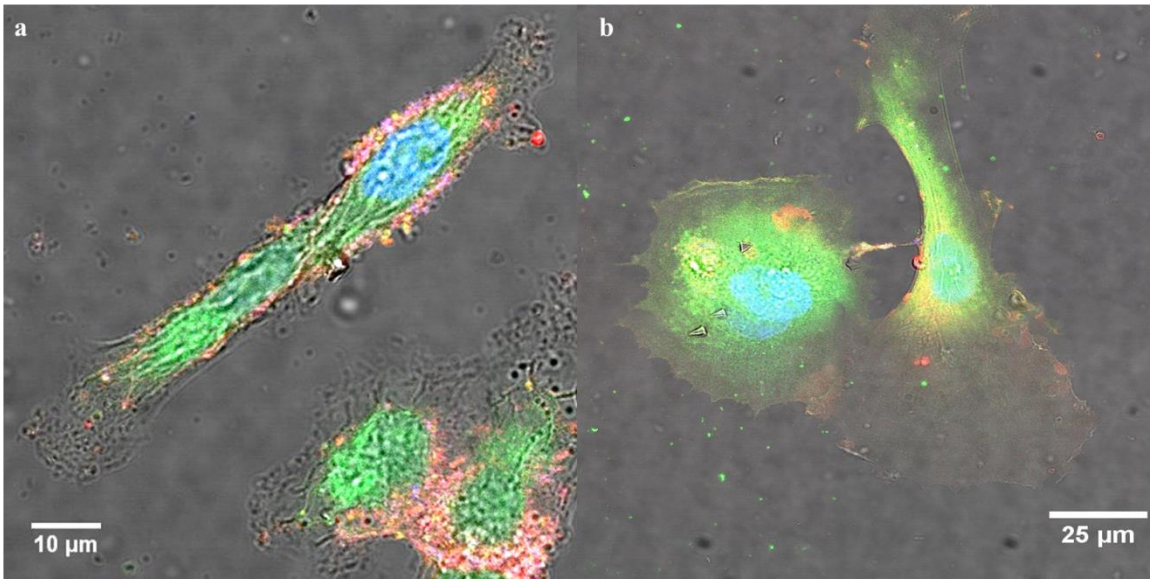

Figure 57. Fixed cell confocal imaging with differential interference contrast (DIC).
Confocal fluorescence microscopy overlaid on a DIC image confirms association of PNP-AV with MDA-MB-231 cells. Representative cells are shown in (a and b). FITC-conjugated PNP-AV is shown in green, CellMask stain of the plasma membrane in red, and Hoechst 33258 nucleic acid stain in blue.

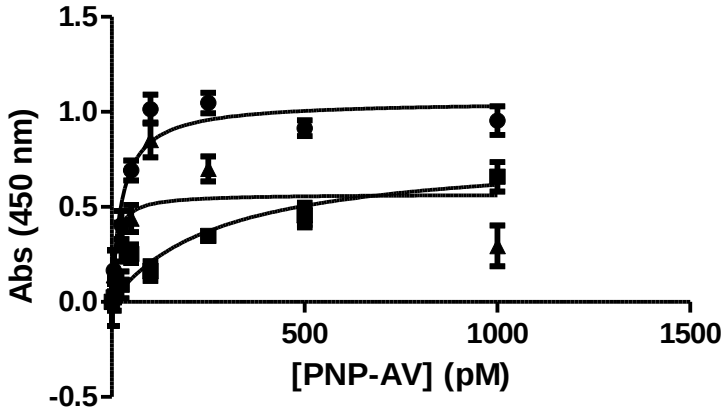

Figure 58. PNP-AV dissociation constant binding data on non-confluent HAAE-1 cells.
Specific binding (▲) was determined by subtracting total binding (●) in calcium supplemented medium from nonspecific binding (■) in calcium deficient medium. Binding was quantified with biotinylated protein and HRP-conjugated streptavidin, developed with OPD. Data are presented as mean ± standard error (n = 3).

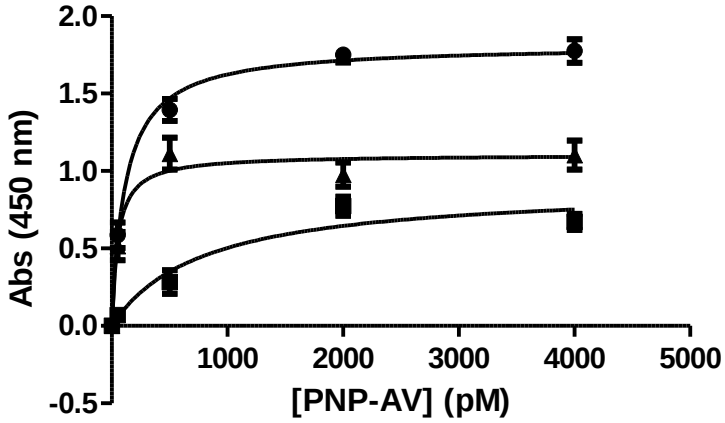

Figure 59. PNP-AV dissociation constant binding data on MCF-7 cells. Specific binding (▲) was determined by subtracting total binding (●) in calcium supplemented medium from nonspecific binding (■) in calcium deficient medium. Binding was quantified with biotinylated protein and HRP-conjugated streptavidin, developed with OPD. Data are presented as mean ± standard error (n = 3).

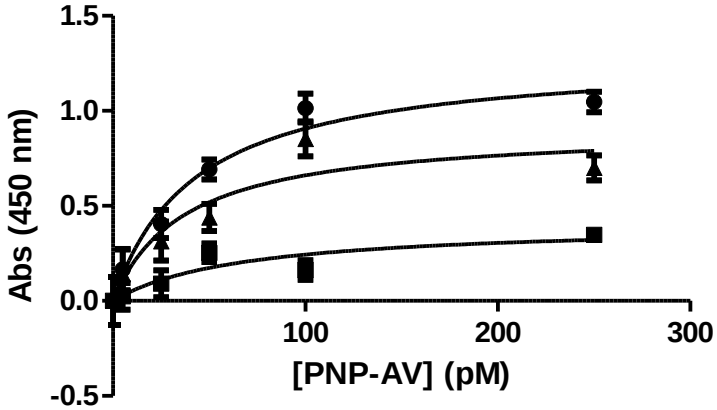

Figure 60. PNP-AV dissociation constant binding data on MDA-MB-231 cells. Specific binding (▲) was determined by subtracting total binding (●) in calcium supplemented medium from nonspecific binding (■) in calcium deficient medium. Binding was quantified with biotinylated protein and HRP-conjugated streptavidin, developed with OPD. Data are presented as mean ± standard error (n = 3).

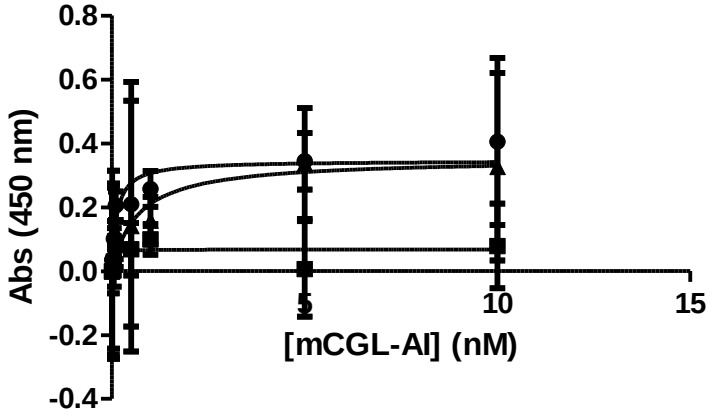

Figure 61. mCGL-AI dissociation constant binding data on MDA-MB-231 cells. Specific binding (▲) was determined by subtracting total binding (○) in calcium supplemented medium from nonspecific binding (□) in calcium deficient medium. Binding was quantified with biotinylated protein and HRP-conjugated streptavidin, developed with OPD. Data are presented as mean ± standard error (n = 3).

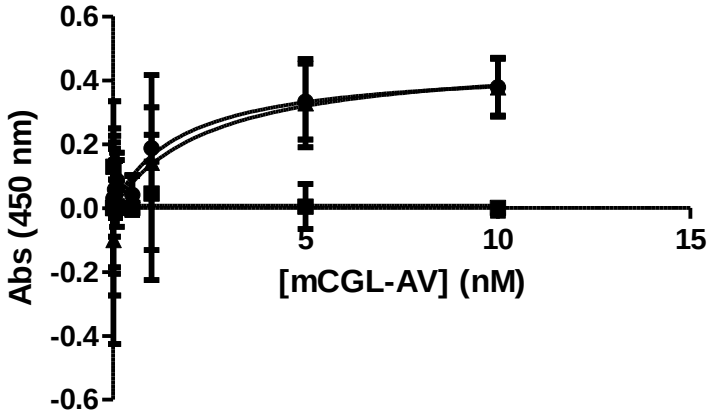

Figure 62. mCGL-AV dissociation constant binding data on MDA-MB-231 cells. Specific binding (▲) was determined by subtracting total binding (●) in calcium supplemented medium from nonspecific binding (■) in calcium deficient medium. Binding was quantified with biotinylated protein and HRP-conjugated streptavidin, developed with OPD. Data are presented as mean ± standard error (n = 3).

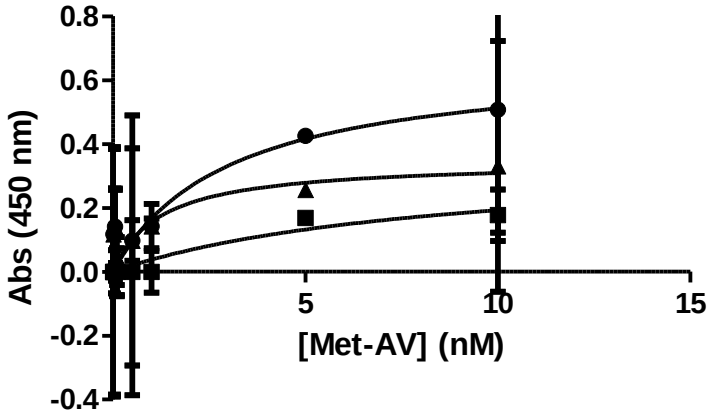

Figure 63. Met-AV dissociation constant binding data on MDA-MB-231 cells.
Specific binding (▲) was determined by subtracting total binding (●) in calcium supplemented medium from nonspecific binding (■) in calcium deficient medium. Binding was quantified with biotinylated protein and HRP-conjugated streptavidin, developed with OPD. Data are presented as mean ± standard error (n = 3).

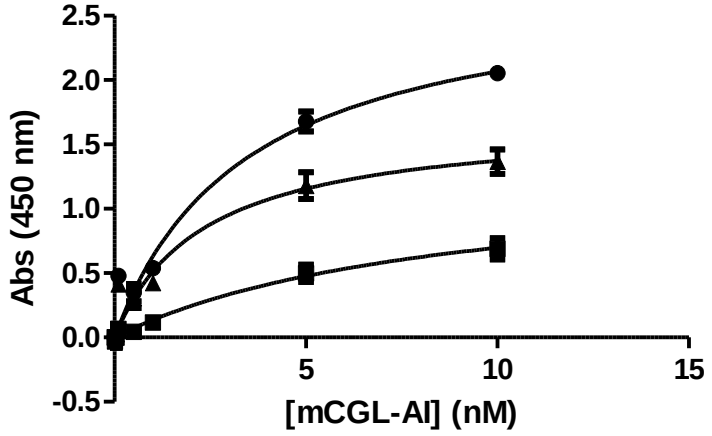

Figure 64. mCGL-AI dissociation constant binding data on non-confluent HAAE-1 cells.
Specific binding (▲) was determined by subtracting total binding (●) in calcium supplemented medium from nonspecific binding (■) in calcium deficient medium. Binding was quantified with biotinylated protein and HRP-conjugated streptavidin, developed with OPD. Data are presented as mean ± standard error (n = 3).

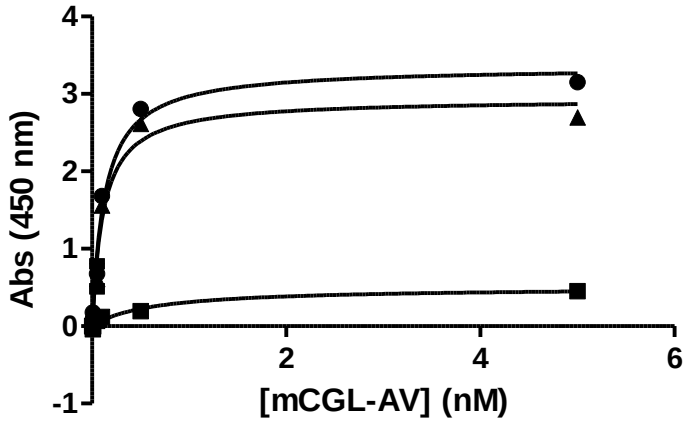

Figure 65. mCGL-AV dissociation constant binding data on non-confluent HAAE-1 cells.
Specific binding (▲) was determined by subtracting total binding (●) in calcium supplemented medium from nonspecific binding (■) in calcium deficient medium. Binding was quantified with biotinylated protein and HRP-conjugated streptavidin, developed with OPD. Data are presented as mean ± standard error (n = 3).

Appendix B: Laboratory Protocols

Protein Design and Vector Construction

PNP-AV Fusion Gene Construction and Transformation

1. Culture cells containing PNP-AV gene in 5 mL LB Medium for 16 h at 37°C and 250 rpm.
    - LB Medium (500 mL)
        - 10 g/L Tryptone (5.0 g)
        - 5 g/L Yeast Extract (2.5 g)
        - 5 g/L NaCl (2.5 g)
2. Perform miniprep of plasmid using QIAprep spin columns (protocol included in Appendix B: Laboratory Protocols)
3. Perform PCR to amplify PNP-AV gene using the PNP-AV fusion primers in Appendix C: Fusion Gene Construction and the conditions below.
    - Combine components on ice (add Phusion DNA Polymerase last).
    - Mix and centrifuge.
    - Cycle.

Table 13. PNP-AV Fusion Gene Amplification PCR Components

	Volume (µl)	**Stock Concentration**	**Final Concentration**
dNTPs	1	10 mM	200 µM
Sense primer	1	100 µM	2.0 µM
Antisense primer	1	100 µM	2.0 µM
Template DNA	1		<250 ng
HF Buffer	10	5x	1x
DMSO	1.5		3%
PCR Grade Water	34		
Phusion Polymerase	0.5		1 U/50mL rxn
TOTAL	**50**		

Table 14. PNP-AV Fusion Gene Amplification PCR Conditions

Step	# of Cycles	Temperature	Time
Initial Denaturation	1	98°C	60 sec
Amplification	31		
- Denaturation		98°C	10 sec
- Annealing		60°C	30 sec
- Elongation		72°C	60 sec
Final Elongation	1	72°C	7 min
Cooling	1	4°C	∞

4. Cleanup PCR products with QIAquick (protocol included in Appendix B: Laboratory Protocols, PCR Product Purification).
5. Isolate PNP-AV gene fragment using DNA gel electrophoresis and gel extraction with QIAquick (protocol included in Appendix B: Laboratory Protocols).
6. Perform restriction digest of purified PNP-AV gene with Xho1 and Xba1 according to conditions below.
    - Pipet mixture up and down or flick to mix.
    - Allow digestion to occur for 1 hour at 37°C. (1 unit of enzyme will digest 1 µg of DNA in 1 hour at 37°C [in a total reaction volume of 50 µl])

      Note: DNA estimated based on QIAquick max binding as 10 µg, eluted in 48 µL, resulting in 0.208 µg/µL.

Table 15. PNP-AV Restriction Digest Components

Component	Volume (µL)	Stock Concentration	Final Concentration
FP gene	15.8	0.208 µg/µL *	3 µg
NEB Buffer #4	5	10x	1x
BSA	0.5	100x	1x
Xho1	1	20 U/µL	20 U/rxn
Xba1	1	20 U/uL	20 U/rxn
PCR grade H_2O	26.7		
Total	**50**		

7. Digest pET303/CT-His plasmid with Xho1 and Xba1 according to conditions below.

    - Pipet mixture up and down or flick to mix.
        - Allow digestion to occur for 1 hour at 37°C. (1 unit of enzyme will digest 1 µg of DNA in 1 hour at 37°C [in a total reaction volume of 50 µl])

Table 16. pET303/CT-His Backbone Restriction Digest Components

Component	Volume (µL)	Stock Concentration	Final Concentration
pET303/CT-His plasmid	6.6	0.15 µg/µL	1 µg
NEB Buffer #4	5	10x	1x
BSA	0.5	100x	1x
Xho1	1	20 U/µL	20 U/rxn
Xba1	1	20 U/µL	20 U/rxn
PCR grade H_2O	35.9		
Total	**50**		

8. Dephosphorylate pET303/CT-His (to prevent intramolecular reclosure) after restriction digest.

- Heat pET303/CT-His digest mixture for 20 minutes at 65°C to heat deactivate restriction enzymes
    - Add 0.5 units of Calf Intestinal Alkaline Phosphatase (CIP) (New England Biolabs; M0290S) per µg vector DNA (1.0 µL)
    - Incubate 60 minutes at 37°C

9. Purify DNA using PCR product purification protocol for the PNP-AV gene and pET303/CT-His backbone. Use 20 µL elutions.
10. Ligate PNP-AV gene into pET303/CT-His backbone using the conditions below.
    - Combine all components (ligase last) in microcentrifuge tube on ice.
    - Incubate overnight at 16°C.

Table 17. Components for PNP-AV Ligation into pET303/CT-His

Component	**Volume (µL)**	**Stock Concentration**	**Final Concentration**
pET303/CT-His plasmid	1.3	39 ng/µL *	0.025 pmol (50 ng)
FP gene	2.9	**	0.076 pmol (50 ng)
Ligase Buffer	2	10x	1x
T4 DNA Ligase	1	400,000U/mL	400 U/rxn
PCR grade H_2O	12.8		
Total	**20**		

Note: DNA concentrations were estimated as shown below.

* (Mass DNA in digest)(Xho1 Efficiency)(Xba1 Efficiency)(Purification Recovery) = (3.3 µg)(0.95)(0.95)(0.9*0.7) = 1.88 µg in 48 µL = 39 ng/µL

** (Mass DNA in digest)(Xho1 Efficiency)(Xba1 Efficiency)(Purification Recovery) = (1.0 µg)(0.95)(0.95)(0.9*0.7) = 0.81 µg in 48 µL = 17 ng/µL

11. Transform plasmid into NovaBlue Gigasingles competent cells (protocol included in Appendix B: Laboratory Protocols) and culture for amplification of plasmid.
12. Using a flame sterilized, blunt glass pipet, select several colonies and culture each colony in 15 mL of LB medium with antibiotic at 37°C and 250 rpm for 16 h.
13. Collect cells through centrifugation at 1000 x *g* and discard supernatant.
14. Perform a miniprep using the QIAprep spin columns and submit for sequencing.
    - T7 promoter, T7 terminator, and PNP sequencing primers were used. Primer sequences are included in Appendix C: Fusion Gene Construction.

      Note: PNP Sequencing primer needed to be diluted from 100 µM to 5 µM
    - Plasmid DNA should be submitted at approximately 100 ng/µL and primers at 3-5 µM.
15. After confirming correct sequence, transform plasmid miniprep into BL21(DE3) competent cells (protocol included in Appendix B: Laboratory Protocols) and culture for expression.

mCGL-AI, mCGL-AV Fusion Gene Constructions and Transformations

1. Resuspend Life Technologies gene fragments to 40 ng/ul (come as ~2000 ng powder)
    - Centrifuge for 2-5 sec at >3000 x *g*.

- Add x µl nuclease free water (final concentration of 40 ng/µl)
    - F1 (1000 bp) – add 49 µl water
    - A1-F2 (1000 bp) – add 38 µl water
    - A1-F3 (452 bp) – add 61 µl water
    - A5-F2 (1000 bp) – add 21 µ water
    - A5-F3 (371 bp) – add 31 µl water
- Incubate 1 h at room temperature, then resuspend gently with pipet.
- Aliquot and store at -20°C (2 yr stability)

2. Combine reagents for Gibson assembly.
    - Use 50 ng of plasmid and 0.2 pmol of each fragment (equimolar)
        - Reaction 1 (total = 9.3 µl)
            - 1 ul pET-30 Ek/LIC (at 50 ng/µl)
            - 3.3 µl F1
            - 3.3 µl F2
            - 1.7 µl F3
    - 10 µl Gibson Master Mix (2X)
    - Nuclease free DI (adjust to final volume of 20 µl)
3. Incubate at 50°C for 1 h, then keep on ice (or -20°C) until transformation
    - Exonuclease removes nucleotides at 5’ end leaving single stranded 3’ overhang. Complementary fragments anneal and DNA polymerase fills in gaps followed by ligation with DNA ligase.

4. Transform NEB 5-alpha competent cells (included in Gibson Assembly kit) with Gibson Assembly reaction product (protocol included in Appendix B: Laboratory Protocols).
5. Using a flame sterilized, blunt glass pipet, select several colonies and culture each colony in 15 mL of LB medium with antibiotic at 37°C and 250 rpm for 16 h.
6. Collect cells through centrifugation at 1000 x *g* and discard supernatant.
7. Perform a miniprep using the QIAprep spin columns and submit for sequencing.
    - T7 promoter, T7 terminator, and mCGL-AI and mCGL-AV sequencing primers were used. Primer sequences are included in Appendix C: Fusion Gene Construction.
    - Plasmid DNA should be submitted at approximately 100 ng/µL and primers at 3-5 µM.
8. After confirming correct sequence, transform plasmid miniprep for mCGL-AI into BL21(DE3) competent cells and plasmid miniprep for mCGL-AV into T7 Express lysY competent cells (protocols included in Appendix B: Laboratory Protocols) and culture for expression.

Plasmid Miniprep

Note: Miniprep performed with QIAprep Spin Columns (Qiagen; 27104)

1. Resuspend pelleted bacterial cells in 250 uL Buffer P1 and transfer to microcentrifuge tube (make sure RNase A has been added to Buffer P1).
2. Add 250 uL Buffer P2 and mix thoroughly by inverting the tube 4-6 times.

3. Add 350 uL Buffer N3 and mix immediately and thoroughly by inverting the tube 4-6 times.
4. Centrifuge for 10 min at 13,000 rpm in microcentrifuge.
5. Apply the supernatants from step 4 to the QIAprep spin column by decanting or pipetting.
6. Centrifuge for 30-60 seconds. Discard flow through.
7. Wash QIAprep spin column by adding 0.5 mL Buffer PB and centrifuge for 30-60 seconds. Discard flow through.
8. Wash QIAprep spin column by adding 0.75 mL Buffer PE and centrifuging for 30-60 seconds.
9. Discard the flow through and centrifuge for an additional 1 minute to remove residual wash buffer.
10. Place QIAprep column in a clean 1.5 mL microcentrifuge tube. To elute DNA, add 50uL Buffer EB to the center of each QIAprep spin column, let stand for 1 min, then centrifuge for 1 min.

PCR Product Purification

Note: PCR product cleanup performed with QIAquick PCR Purification Kit (Qiagen; 28104)

1. Add 120 µl of pH indicator I to 30 ml Buffer PB (if not previously completed).
2. Add 5 volumes of Buffer PB to 1 volume of PCR sample & mix. (ie. Add 500 µl Buffer PB to 100 µl PCR sample).
3. Check to make sure mixture is yellow. If not, read manual.

4. Place QIAquick spin column in a provided 2 ml collection tube.
5. Apply sample to QIAquick column and centrifuge for 30-60 seconds at 13,000 rpm.
6. Discard flow-through. Replace column back into same tube.
7. Wash by adding 0.75 ml Buffer PE to column & centrifuge for 30-60 seconds.
8. Discard flow-through. Replace column in same tube & centrifuge for an additional minute. (This additional centrifugation will ensure all residual ethanol will be removed).
9. Place QIAquick column in a clean 1.5 ml microcentrifuge tube.
10. Elute DNA by adding 50 µl Buffer EB to center of QIAquick membrane & centrifuge column for 1 minute.

DNA Gel Electrophoresis and Extraction

Note: Gel extraction performed with QIAquick Gel Extraction Kit (Qiagen; 28704).

1. Weigh out 1.0g agarose and dissolve in 50 ml of 1X TE buffer (40 mM Tris, 1 mM EDTA). Microwave 5 times in 20 second intervals on power level 5 with cap loosely on (cap will pop off and contents will spill out or glass will break otherwise).
    - 10X TE Buffer (1 L)
        - 10 mM EDTA (3.722 g)
        - 400 mM Tris (48.456 g)
        - DI water (1 L)

2. Let the solution cool to 55oC and add 2.5 µl of 10 mg/ml of ethidium bromide stock to the 50 ml volume (mix the solution well to evenly distribute the ethidium bromide). Pour the gel into the electrophoretic cell (up to the blue line on the comb) and wait 60 min for solidification.
3. Once the gel has solidified pour the TE buffer over the gel until it covers the gel by about 1 mm. The gel is now ready to be loaded.
4. To each DNA sample to be loaded, add 2 µl of sample DNA to 1 µl loading dye (Qiagen; 239901). The maximum volume of DNA sample is 20 µl for each well of the 8 comb gel which has a total volume of 25 µl.
    - Mix 2 µl DNA from PCR and 1 µl loading dye with pipet, and then load into each well (for samples).
5. For the marker lane, add 2 µl of 500 bp ladder (Bio-Rad Laboratories Inc.; 170-8203) to 1 µl loading dye.
6. Run the gel at 100 V (low) until the first band gets ¾ of the way to the bottom of the gel.
7. View the gel using the UV box and cut appropriate fragment from the gel with a clean scalpel for extraction.
8. Weigh the gel slice in a colorless tube.
9. Add 3 volumes of Buffer QG to 1 volume of gel. (ie. 300 µl Buffer QG to 100 mg gel)
10. Incubate at 50°C for 10 minutes (or until gel slice is completely dissolved). To help dissolve, vortex the tube every 2-3 minutes during incubation.

11. After gel is dissolved, check to see that the color of the mixture is yellow, similar to Buffer QG. It not, refer to manufacturer instructions.
12. Add 1 gel volume of isopropanol to the sample & mix. (ie. Add 100 µl isopropanol to 100 mg of gel).
13. Place a QIAquick spin column in a provided 2 ml collection tube. Bind DNA by applying sample to column.
14. Centrifuge at 13,000 rpm for 1 minute. Discard flow-through & replace column in same tube.
15. Add 0.5 ml of Buffer QG to column & centrifuge for 1 minute.
16. Wash by adding 0.75 ml of Buffer PE to column & centrifuge for 1 minute.
17. Discard flow-through & centrifuge for an additional minute. Residual ethanol from Buffer PE will not be completely removed unless the flow-through is discarded before additional centrifugation.
18. Place column in a clean 1.5 ml microcentrifuge tube.
19. Elute DNA by adding 50 µl Buffer EB to center of QIAquick membrane & centrifuge for 1 minute.

NovaBlue Gigasingles Competent Cell Transformation

1. Thaw NovaBlue GigaSingles cells on ice for 5 minutes (with all but the cap surrounded by ice)
2. Resuspend cells by pipetting up and down and transfer 50 µL to transform tube.
3. Add 1 µL of ligation reaction directly to cells and stir gently (Also add 1 µL of test plasmid to second vial of cells).

4. Incubate on ice for 5 min
5. Heat tubes for exactly 30 sec in 42°C water bath.
6. Place tubes on ice for 2 min.
7. Add 250 µL SOC medium (at room temperature) to each tube and keep tubes on ice.
8. Incubate at 37°C while shaking at 250 rpm for 60 min prior to plating.
9. Concurrently, heat LB agar plates (made in advance) to 37°C for ~20 min prior to plating.
    - Make LB Agar solution (at least one day prior to transformation) and autoclave.
        - LB Agar (250 mL; 25 mL per dish, 10 dishes)
            - 10 g/L Tryptone (2.5 g)
            - 5 g/L Yeast Extract (1.25 g)
            - 5 g/L NaCl (1.25 g)
            - 15 g/L Agar (3.75 g)
    - Allow solution to cool slightly after autoclave and add antibiotic.
    - Pipet 25 mL into each petri dish by flame. Allow dishes to sit with small amount of ventilation facing burner. Once solidified, refrigerate overnight until ready for transformation.
10. Spread 50 µL cell solutions on plates using flame/EtOH sterilized glass pipette at several dilutions (1:1 to 1:100) in SOC medium.
11. Allow plates to sit on benchtop for several minutes (for liquid to be absorbed), invert, and incubate overnight at 37°C.

BL21(DE3) Competent Cell Transformation

1. Resuspend cells and then add 1 uL of selected colony miniprep to 20 µL BL21(DE3) cells in transformation tube on ice.
2. Incubate the tube on ice for 5 minutes.
3. Heat the tube for exactly 30 seconds in 42°C water bath.
4. Incubate tube for 2 min on ice.
5. Add 80 µL room temperature SOC medium to tube on ice.
6. Incubate for 60 minutes at 37°C while shaking at 250 rpm.
7. Concurrently, heat LB agar + antibiotic plates to 37°C for ~20 min prior to plating.
8. Spread 50 µL cell solution on plates using flame/EtOH sterilized glass pipette at several dilutions (1:1 to 1:100) in SOC medium.
9. Allow plates to sit on benchtop for several minutes (for liquid to be absorbed), invert, and incubate overnight at 37°C.

NEB 5-alpa Competent Cell Transformation

1. Thaw NEB 5-alpha competent cells on ice for 2-5 min.
2. Resuspend cells and then add 2 uL of Gibson Assembly reaction to 50 µL cells in transformation tube on ice.
3. Incubate the tube on ice for 30 minutes.
4. Heat the tube for exactly 30 seconds in 42°C water bath.
5. Incubate tube for 2 min on ice.
6. Add 950 µL room temperature SOC medium to tube on ice.

7. Incubate for 60 minutes at 37°C while shaking at 250 rpm.
8. Concurrently, heat LB agar + antibiotic plates to 37°C for ~20 min prior to plating.
9. Spread 100 µL cell solution on plates using flame/EtOH sterilized glass pipette at several dilutions (1:1 to 1:100) in SOC medium. Use kanamycin plates to select for plasmid and ampicillin plates as a control.
10. Allow plates to sit on benchtop for several minutes (for liquid to be absorbed), invert, and incubate overnight at 37°C.

T7 Express lysY Competent Cell Transformation

1. Thaw T7 Express lysY competent cells on ice for 20 min.
2. Resuspend cells and then add 1 uL of plasmid miniprep to 50 µL cells in transformation tube on ice. Flick the tube gently 4-5 times to mix the cells and DNA.
3. Incubate the tube on ice for 30 minutes.
4. Heat the tube for exactly 10 seconds in 42°C water bath.
5. Incubate tube for 5min on ice.
6. Add 950 µL room temperature SOC medium to tube on ice.
7. Incubate for 60 minutes at 37°C while shaking at 250 rpm.
8. Concurrently, heat LB agar + antibiotic plates to 37°C for ~20 min prior to plating.

9. Spread 100 µL cell solution on plates using flame/EtOH sterilized glass pipette at several dilutions (1:1 to 1:100) in SOC medium. Use kanamycin plates to select for plasmid and ampicillin plates as a control.
10. Allow plates to sit on benchtop for several minutes (for liquid to be absorbed), invert, and incubate overnight at 37°C.

Protein Expression and Purification

BL21(DE3) Expression of CD-AV, PNP-AV, Met-AV, and mCGL-AI

1. Culture 5 µl of *E. coli* BL21(DE3) harboring vector with fusion gene in 10 mL of LB medium containing antibiotic in a 125 mL Erlenmeyer flask overnight at 37^{o}C with shaking at 200 rpm.
    - LB Medium
        - 10 g Tryptone
        - 5 g Yeast Extract
        - 5 g NaCl
        - 1 L DI water
    - Autoclave LB Medium.
    - Add antibiotic to the 1 L of LB medium before taking out the 10 mL for the initial culture. Note: CD-AV, Met-AV, and mCGL-AI require 35 µg/ml kanamycin and PNP-AV requires 100 µg/ml carbenicillin.
    - Incubate.
2. Add 10 mL of the cell culture to 1 L of fresh LB medium with antibiotic and incubate at 37^{o}C with shaking (200 rpm). Take 1.5 mL of medium before adding the bacteria, as a blank. This cell culture was grown to mid-log phase (OD_{600} = 0.6).
    - Transfer 10 mL of bacteria to 1 L LB medium.
    - Transfer entire volume of medium to four 1 L flasks.
    - Put in shaker at 37^{o} C at 200 rpm.

- Measure optical density at 600 nm (absorbance) at regular intervals (1.5 h) using a clear 96 well plate and microtiter plate reader of sample (using 250 µL samples). When $OD_{600nm} = 0.6$, proceed to next step.

3. Add IPTG to a final concentration of 0.4 mM (96 mg IPTG) to solutions in four 1 L flasks and incubate at 30^{o}C with shaking (180 rpm) for 6 h to induce protein expression.
    - Put back in shaker at 30^{o}C for 5 hours.
    - IPTG stimulates the production of fusion protein (IPTG activates the promoter in the plasmid that will start the transcription of the gene that follows the promoter).

T7 Express lysY (DE3) Expression of mCGL-AV

1. Culture 10 µL of *E. coli* T7 Express lysY (DE3) harboring the fusion gene mCGL-AV in 10 mL of TB medium containing 35 µg/mL kanamycin in a 125 mL Erlenmeyer flask for 6 h at 37^{o}C with shaking at 220 rpm.
    - TB Medium Nutrients
        - 12 g Tryptone
        - 24 g Yeast Extract
        - 4 mL glycerol
        - 900 mL DI

- TB Medium Buffering
    - 2.31 g KH_2PO_4
    - 12.54 g K_2HPO_4
    - 100 mL DI
- Autoclave TB components separately then combine once at room temperature
- Add 35 mg kanamycin to the 1 L of TB medium before taking out the 10 mL for the initial culture
- Incubate

2. Add 10 ml of the cell culture to 1 L of fresh culture medium with kanamycin and incubate at 37^{o}C with shaking (220 rpm). Take 1.5 mL of medium before adding the bacteria, as a blank. This cell culture was grown to mid-log phase (OD_{600} = 0.5).
    - Transfer 10 mL of bacteria to 1 L TB medium.
    - Transfer entire volume of medium to four 1 L flasks.
    - Put in shaker at 37^{o} C at 220 rpm for 9 h.
    - Measure optical density at 600 nm (absorbance) at regular intervals using a clear 96 well plate and microtiter plate reader of sample (using 250 µL samples). Adjustment of 9 h incubation time may be necessary. When OD_{600nm} = 1.2, proceed to next step.
3. Add IPTG to a final concentration of 1 mM (238 mg IPTG total) to solutions in four 1 L flasks and incubate at 25^{o}C with shaking (200 rpm) to induce protein expression.

- Put back in shaker at 25°C for 19 h.

- IPTG stimulates the production of fusion protein (IPTG activates the promoter in the plasmid that will start the transcription of the gene that follows the promoter).

Fusion Protein Purification

Note: Include 0.02 mM pyridoxal phosphate in all buffers for Met and mCGL fusion proteins.

1. Harvest the cells by centrifugation for 10 min at 1000 x *g*, at 4ºC.
2. Resuspend the cell pellet in 40 mL of sonication buffer.
    - Vortex to resuspend cell pellets.
    - Sonication Buffer (40 mL)
        - 0.05 mM N- *p*-tosyl-L-phenylalanine chloromethyl ketone (TPCK) (0.704 mg)
        - 1 mM phenylmethylsulfonyl fluoride (PMSF) (6.968 mg)
        - 1% HPLC ethanol (400 µL)
        - 0.01% β-mercaptoethanol (4 µL)
        - 0.02 M sodium phosphate dibasic (113.6 mg)
        - 40 mL DI
        - Dissolve TPCK and PMSF in ethanol in microcentrifuge tube, and then add to beaker.
        - Make this buffer in the 100 mL beaker.
        - Adjust to pH 7.4

3. Lyse the cells by sonication at 4^{o}C for 30 sec at 4.5 watts then allow it to cool for 30 sec on ice. This cycle was repeated 4 times (5 times total) for a total sonication time of 2.5 min on power level 4.
    - Clean sonicator tip with ethanol before use.
    - Put beaker in tub with ice while sonicating.
4. Centrifuge the lysate obtained at 12,000 x *g* for 30 min to remove the cell debris and take the supernatant. The protein will be in the supernatant and the cell debris in the pellet.
5. After taking supernatant sample, add Imidazole (40 mM) and NaCl (500 mM) to the lysate to reduce non-specific protein binding.
    - 40 mM imidazole (0.0817 g for 40 mL)
    - 500 mM NaCl (1.168 g for 40 mL)
6. Equilibrate a 5 mL HisTrap chromatography column using Wash Buffer 1.
    - Feed wash buffer through column until the output reaches baseline
    - <u>WASH BUFFER 1</u> (500 mL)
        - 20 mM sodium phosphate dibasic (1.42 g)
        - 40 mM imidazole (1.362 g)
        - 500 mM NaCl (14.61 g)
        - Adjust to pH 7.4
7. Feed the soluble protein fraction into the column (load entire sample – avoid air in column).
    - Discard flow through – contains unwanted proteins

8. Wash the column with 60 column volumes (350 mL) of Wash Buffer 2 to remove unwanted proteins and endotoxin. (Run Wash 2 for a minimum of 1.5 h)
    - ➢ Discard flow through – contains unwanted proteins
    - o <u>WASH BUFFER 2</u> (300 mL)
        - 20 mM sodium phosphate dibasic (0.8517 g)
        - 40 mM imidazole (0.817 g)
        - 500 mM NaCl (8.766 g)
        - 1.0% Triton X-114 (3 mL)
        - ➢ Adjust to pH 7.4
9. Wash the column with 20 column volumes (100 mL) of Wash Buffer 1 to wash the protein until the pen reaches the baseline. (Run Wash 1 for a minimum of 1 h)
    - ➢ Discard flow through – contains unwanted proteins
10. Elute the protein using elution buffer.
    - ➢ Collect the elution – contains fusion protein– Begin collection once peak starts to rise and end once peak begins to level off, note there is a delay from detector to output
    - o <u>ELUTION BUFFER</u> (300 mL)
        - 20 mM sodium phosphate dibasic (0.8517 g)
        - 500 mM imidazole (10.212 g)
        - 500 mM NaCl (8.766 g)
        - ➢ Adjust to pH 7

11. Clean column for future use.
    - Normally just run enough elution buffer through (without collecting) to get a good baseline. All proteins should be cleared from the column.
    - If column is dirty/clogged, regenerate the column using this procedure:
        - 25 mL of 1 M KCl (make 200 mL, use 14.91 g)
        - 25 mL of 1 M NaOH (make 200 mL, use 8.0 g)
        - 25 mL of DI Water
        - 25 mL of 1 M Ethanol (1.5 mL ethanol + 23.5 mL DI Water)
12. Dialyze eluted protein for 3 hours against 2 liters of dialysis buffer containing 20 mM sodium phosphate at pH 7.4 to remove NaCl and imidazole from the protein solution and make it suitable for His-tag cleavage.
    - Note: volumes greater than 20 mL will typically need 2 dialysis bags
    - <u>DIALYSIS 1 BUFFER</u> (2 L)
        - 20 mM sodium phosphate dibasic (5.678 g)
        - Adjust to pH 7.4
13. Measure the concentration of protein (Bradford Protein assay).
14. Cleave the His-tag by adding HRV-3C protease at 10 U/mg of protein with the recommended 10X buffer provided. Incubate for 18h at 4^{o}C at 30 rpm in dark.
15. Equilibrate the HisTrap column with Wash Buffer 1.
    - Feed through the column until stable baseline is reached.

16. Add imidazole (40 mM) and NaCl (500 mM) to the cleaved protein solution (mass depends on volume after overnight cleavage incubation).
17. Feed the cleaved solution to the HisTrap column and collect protein.
    - Collect first peak solution from the column (flow-through). This contains our protein.
18. Push remainder of cleaved solution through column and tubing with Wash 1 and collect until signal approaches baseline.
19. Elute uncleaved protein with imidazole.
    - Allow elution to reach baseline so that all protein is cleared from column
    - Discard elution – any protein is the protease or uncleaved FP
20. Dialyze purified protein for 3 hours against 2 liters of dialysis buffer.
    - Note: volumes greater than 20 ml will typically need 2 dialysis bags
    - <u>DIALYSIS 2 BUFFER</u> (2 L)
        - 20 mM sodium phosphate dibasic (5.5678 g)
        - 100 mM NaCl (11.688 g)
        - Adjust to pH 7.4
21. Prepare column for storage. After reaching a baseline with elution buffer, equilibrate column with 1 M EtOH to prevent bacterial growth. If column is very dirty, clean using the procedure above.
22. Pass the sample through a 0.2 µm cellulose-acetate filter in biohood (now sterile practice)
23. Perform Bradford assay and record final protein yield

24. Aliquot purified protein into cryovials (2 mL per vial), flash freeze in liquid nitrogen, lyophilize, and store at -80°C.

Protein Analysis

Bradford Protein Concentration Assay

1. Add 5 µL sample to each well.
   - Include blank using DI water
   - Include at least a 2x protein dilution (2.5 µL protein, 2.5 µL DI water). Note: Further dilution may be required to obtain values within calibration curve.
2. Add 250 ul Bradford reagent to each well and incubate at room temperature for 5 min.
3. Take absorbance at 595 nm and subtract out blank
4. Calculate protein concentration (µg/mL) using calibration curve below.

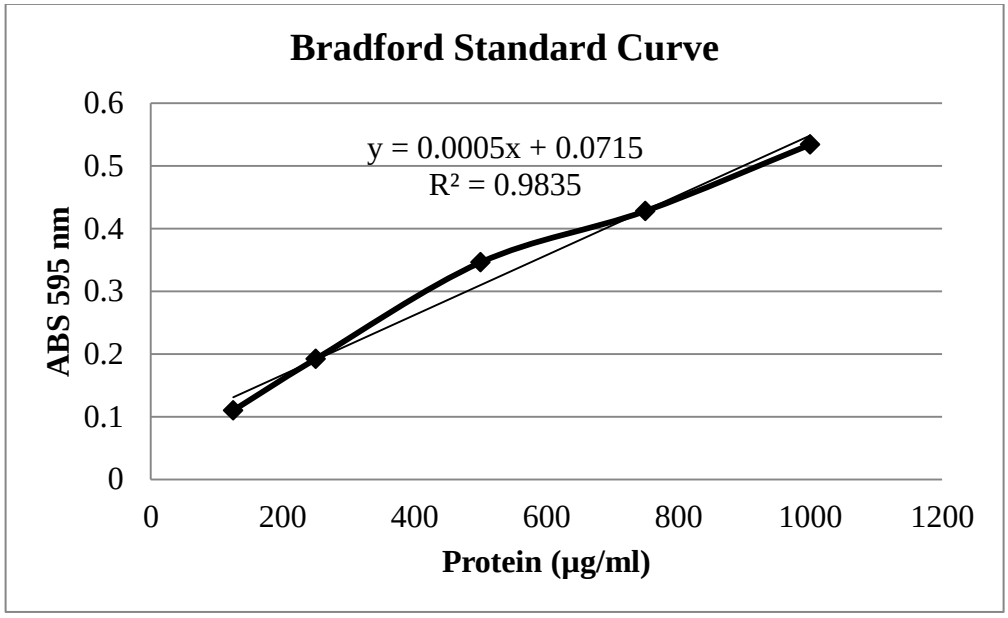

Figure 66. Bradford protein concentration assay calibration curve using bovine serum albumin.

SDS-PAGE

Electrophoresis and Coomassie staining

1. Make solutions if necessary.
    - 10x Running Buffer (1 L)
        - 30.3 g Tris
        - 144.1 g glycine
        - 10 g SDS
        - pH 8.5
    - Loading Buffer
        - 95 µL Laemmli buffer
        - 5 µL β-mercaptoethanol
    - Destain (4 L)
        - 1.8 L DI
        - 1.8 L methanol (45% w/v)
        - 0.4 L acetic acid (10% w/v)
2. Mix 15 µL sample, 25 µL loading buffer in microcentrifuge tube
3. Heat for 2 min at 100°C.
4. Cool at room temperature for 1 min.
5. Load gel with 10 µL sample and 5 µL ladder (dependent on manufacturer recommendation). Precast gels can be purchased or produced according to the protocol below.
6. Run gel at 150V for 45 min.

7. Add stain to gel (0.25% w/v Coomassie Brilliant Blue R250 in destain solution), microwave in 15 s intervals until it just starts to boil
8. Shake at room temperature for 5 min
9. Rinse gel gently with DI to remove as much stain as possible and discard liquid.
10. Add destain, shake for 4 h at room temperature.
11. Discard old destain, add new destain, and shake for 4 h at room temperature.
12. For analysis, obtain an image and process using ImageJ densitometric analysis.

Gel Casting Procedure

1. Assemble the glass plates on the gel casting stand and fill with water to ensure that they are sealed.
2. Mix the components of separating gel, adding the TEMED last. Mix well and immediately fill the glass plates, leaving a 1.5 cm gap at the top (for the stacking gel).

Table 18. SDS-PAGE gel casting components

Gel Components	Stacking 4%	Separating 12%	Separating 10%	Separating 8%
DI	1.82 mL	1.67 mL	1.70 mL	1.74 mL
1.5 M Tris-HCL pH 8.8	-	1.25 mL	1.25 mL	1.25 mL
1 M Tris-HCL pH 6.8	312.5 µL	-	-	-
10 % (w/v) SDS	25 µL	50 µL	50 µL	50 µL
Acrylamide (29%) Bis (1%)	333 µL	2 mL	1.97 mL	1.93 mL
Ammonium persulfate 10%	12.5 µL	25 µL	25 µL	25 µL
TEMED	2.5 µL	5 µL	5 µL	5 µL
Total	**2.5 mL**	**5 mL**	**5 mL**	**5 mL**

Table 19. Gel selection based on monomer molecular weight

Gel	Molecular Weight
7%	50 kDa - 500 kDa
10%	20 kDa - 300 kDa
12%	10 kDa - 200 kDa
15%	3 kDa - 100 kDa

3. Immediately add 1 mL of isopropanol on top of the gel to prevent oxygen from inhibiting the polymerization. Wait 20 min for solidification.
4. Pour off the isopropanol and rinse with dH_2O to remove any residual isopropanol. Mix the components for the 4% staking gel and pour on top of the separating gel. Insert the well-comb and wait 20 min for solidification.

Cytosine Deaminase Activity Assay

1. Prepare stock of 0.5 mg/mL of 5-FC diluted in PBS buffer (8 g/L NaCl, 1.15 g/L Sodium Phosphate Dibasic, 0.2 g/L KCl, 0.2 g/L Potassium Phosphate Monobasic, pH 7.4).
2. Add 775 µL of PBS to the appropriate number of microcentrifuge tubes where reaction will take place.
3. Add 225 µL of enzyme sample to the tubes. (The following dilution example can be done for a 4.5x dilution: add 50 µL enzyme sample + 175 µL PBS. When doing a dilution, add the PBS prior to enzyme sample).
4. Incubate the reaction at 37^{o}C for 30 minutes.
5. Remove 50 µL of sample and quench it in 1 ml of 0.1 N HCl.
6. Transfer 250 µL to a clear 96-well plate.
7. Read absorbance at 255 & 290 nm using a microtiter plate reader.

Definition of unit: One unit of enzyme is defined as the amount of enzyme that forms 1 µmol 5-FU per min at 37°C. In a 30 minute enzymatic reaction, 1 U of undiluted enzyme would produce 30 µmol in 225 µL of undiluted enzyme sample, hence the concentration of 5-FU, determined from the absorbances and the equation below, can be multiplied by 0.148 (determined by $\frac{1}{30\ \mu mol} * \frac{1}{225\ \mu L} * \frac{1000\ \mu L}{1\ mL}$) to obtain activity (U/mL).

$$[\text{5-FU}] = 0.185 * A_{255nm} - 0.049 * A_{290nm}$$

Purine Nucleoside Phosphorylase Activity Assay

1. Make solutions for assay.
    - 100 mM Potassium Phosphate pH 7.4
        - 0.13609 g Photassium phosphate monobasic
        - 10 mL DI
        - ➢ Adjust pH to 7.4
    - 7.5 mM Inosine
        - 0.00201 g Inosine
        - 1 mL DI
    - 10 U/mL xanthine oxidase
        - ➢ Aliquot to 100 uL vials upon arrival
        - ➢ Keep solution on ice
    - PNP solution (roughly .125 U/mL)
        - Note: need roughly 0.005 mg/mL protein
        - Keep solutions on ice
2. Combine reagents (except PNP), mix well by inversion, and allow to reach room temperature.

Table 20. PNP activity assay components

Buffer	270 µL
Inosine	10 µL
Xanthine Oxidase	10 µL
PNP	10 µL

3. Add to appropriate wells in a 96 well plate.

4. Perform kinetic run (A = 293 nm) on plate reader for 3 min or until values are constant.
5. Add PNP solution (DI for blanks).
6. Perform kinetic run for 5 min (A = 293 nm).
7. Use maximum linear rates to determine slope.

Definition of unit: One unit of enzyme is defined as the phosphorolysis of 1.0 µmol of inosine to hypoxanthine and ribose 1-phosphate per min at pH 7.4 and 25°C. The difference between rate of change of absorbance (uric acid), the uric acid millimolar extinction coefficient at 293 nm (12.0), and PNP concentration is used to calculate specific activity.

*Note: PNP concentration in equation is final concentration of reaction mix.

$$\frac{U}{mg} = \frac{\frac{\Delta A_{293} PNP}{min} - \frac{\Delta A_{293} Blank}{\text{min}}}{12 * PNP\ concentration}$$

Methionine-γ-Lyase Activity Assay

1. Make solutions for assay.
    - Buffer: 0.05 M Potassium Phosphate, 0.02 mM PLP
        - 50 mL DI
        - 0.435 g potassium phosphate dibasic
        - 500 uL 100X PLP (24.2 mg in 50 ml)
        - pH to 8

- 0.1 M L-methionine
    - 3 mL buffer
    - 0.04476 g L-methionine
- 50% (w/v) trichloro-acetic acid
    - 10 mL DI
    - 5.0 g trichloro-acetic acid
- 1 M Sodium Acetate
    - 30 mL DI
    - 2.46 g sodium acetate
    - pH to 5
- 0.1% 3-Methyl-2-benzo-thiazolinone hydrazone hydrochloride hydrate (MBTH)
    - 15 mL DI
    - 15 mg MBTH

2. Mix:
    - 125 μL of buffer
    - 125 μL of L-methionine solution
    - 200 μL of enzyme sample (dilutions in buffer) [Note: blank with buffer only]
3. Incubate the mixture at 37°C for 10 min.
4. Add 62.5 μL of 50 % (w/v) trichloro-acetic acid to terminate the reaction of Methioninase
5. Centrifuge at maximum speed for 2 min.

6. Mix in transparent 96-well plate
    - 65.8 µL of the supernatant
    - 131.6 µL of sodium acetate
    - 52.6 µL of MBTH 0.1% (= 1 mg/ml MBTH). MBTH reacts with the ketobutyrate to produce the color change that we measure.
7. Incubate at 50°C for 30 min (PCH-2 Peltier Cooler/Heater, Grant-bio).
8. Add 250 µL of sample to 96 well plate and measure the absorbance at 320 nm against the blank using a microtiter plate reader.

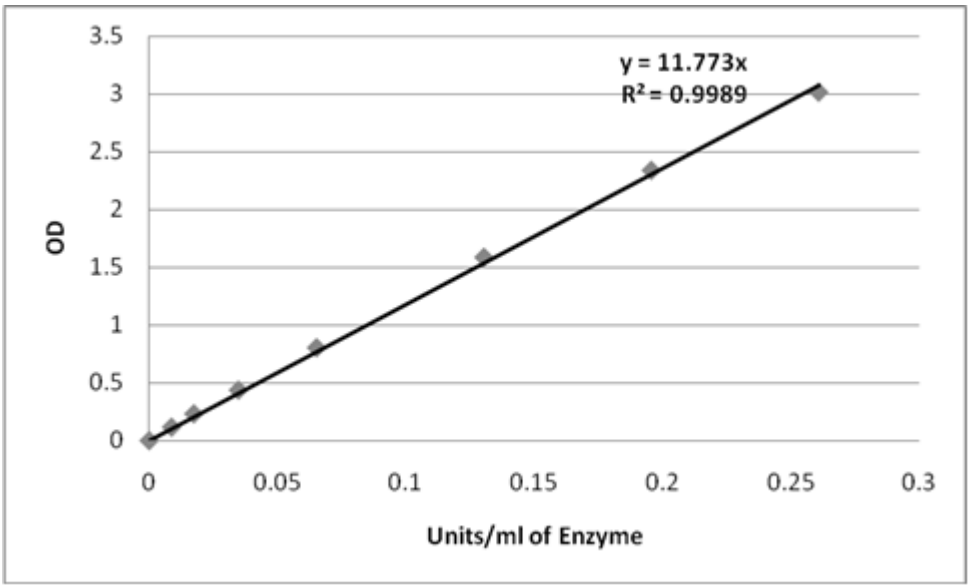

Figure 67. Standard curve for methioninase assay using α-ketobutyrate and MTBH.

Definition of unit: One unit of enzyme is defined as the amount that catalyzes the formation of 1 µmol of α-ketobutyrate per minute. Specific activity is expressed as units per milligram protein. $\frac{U}{mL} = \frac{(dilution\ factor)(OD_{320nm})}{11.73}$

Chromogenic Limulus Amebocyte Lysate Endotoxin Assay

The principle used to determine endotoxin quantities is the following: Step 1: a proenzyme is converted to an enzyme by the endotoxin. Step 2: the enzyme converts a substrate + water to a peptide and p-nitroaniline. The p-nitroaniline is then measured at 405 nm, and an endotoxin concentration can be calculated from a standard curve made using known amounts of *E. coli* endotoxin.

1. Reconstitute 1 vial containing lyophilized Limulus Amebocyte Lysate using 1.4 ml reagent water/vial of LAL. Once reconstituted, it is stable up to 1 week when stored at -20^{o}C immediately following reconstitution. Thaw and use only once. Keep in a dark place.
2. Reconstitute the *E. coli* endotoxin vial using 1.0 ml of LAL Reagent Water warmed to room temperature. Prior to use, vigorously mix for 15 minutes because the endotoxin tends to attach to glass. Our kit contained 30 EU of lyophilized endotoxin. Once reconstituted, it is stable for 4 weeks when stored at 4^{o}C. Keep in a dark place.
3. Reconstitute the chromogenic substrate by adding 6.5 ml of LAL Reagent Water to obtain a final concentration of roughly 2 mM. Once reconstituted, it is stable for 4 weeks when stored at 4^{o}C. Keep in a dark place.
4. Prepare the stop reagent => 10 g Sodium Dodecyl Sulfate (SDS) in 100 ml of DI Water.
5. Prepare the endotoxin sample dilutions that will be used to construct the standard curve. Make dilutions in glass tubes.

Table 21: LAL Endotoxin Assay Standard Curve

[Endotoxin] (EU/ml)	Endotoxin Stock Solution	Endotoxin Standard (1 EU/ml)	LAL Reagent Water
1.0	0.1 ml	-	(30-1)/10 ml = 2.9 ml
0.5	-	0.5 ml	0.5 ml
0.25	-	0.5 ml	1.5 ml
0.1	-	0.1 ml	0.9 ml

* NOTE: the bottom 3 standards are made from the 1.0 EU/ml solution made first. Vigorously vortex each dilution for at least 1 minute before proceeding to the next dilution. Also 30 EU is variable depending on the kit received – check literature with product for proper value to use.

6. Using a clear 96-well plate, add 50 µl of each standard and diluted sample into appropriate wells (running all samples in triplicate). Starting dilution is 1:10 dilution of each sample, followed by 1:100 and 1:1000. The BLANK wells should receive 50 µl of LAL Reagent Water in place of sample. When adding to wells, use the same pattern of addition throughout the assay to be consistent.
7. Add 50 µl of LAL to each well and then tap on the side of the plate to facilitate mixing.
8. Incubate for 10 minutes at 37^{o}C.
9. Add 100 µl of substrate solution (pre-warmed to 37^{o}C) to each well. Tap the side of the plate to facilitate mixing.
10. Incubate for 6 minutes at 37^{o}C.
11. Add 50 µl of stop reagent (SDS). Tap the side of the plate to facilitate mixing.
12. Read absorbance at 405 nm.

Protein Conjugations

Biotinylation

1. Dissolve biotin (SureLINK Chromophoric Biotin) in anhydrous DMF immediately prior to use at 20 mg/ml.
2. Using a 60-fold molar excess of biotin for conjugation, add the appropriate volume of 20 mg/ml SureLINK Chromophoric Biotin to the protein solution (should be at 0.2-5.0 mg/ml).

   Note: % DMF of total reaction volume should be < 5%
3. Incubate at 4^{o}C for 4 hours with gentle agitation.
4. Remove the unconjugated biotin by dialysis using a 3.5-5.0 kDa membrane in 2L 1X modification buffer. Run dialysis for 4 hours. Change dialysate and run another dialysis for 4 hours. Change dialysate and run another overnight. Done at 4^{o}C with gentle stir.
   - Dialysis Buffer (2 L)
     - 100 mM sodium phosphate dibasic (use 28.392 g)
     - 150 mM NaCl (use 17.532 g)
     - pH to 7.3
5. Flash freeze in liquid nitrogen and store at -80^{o}C in the dark.

Determine Degree of Biotinylation

6. Perform Bradford assay to determine [biotinylated protein] (mg/ml) and calculate molar concentration.
   a. [Protein] = (mg/ml)/MW

7. Measure absorbance of biotinylated protein at 280 and 354 nm in plate reader (must be between 0.05 and 2 – dilute if necessary).
8. Calculate biotin concentration.
    a. [Biotin] = $(D*A_{354})/(29000*L)$
    b. 290000: molar extinction coefficient
    c. L: pathlength (1)
9. MSR = [Biotin] / [Protein]

DyLight 680 Conjugation

1. To protect reagents from moisture, allow DyLight NHS Esters and DMF to equilibrate to room temperature before opening the vials.
2. Add 100 µL of DMF to the DyLight NHS Ester. Pipette up and down or vortex until it is completely dissolved.

   Note: Allow the dye to completely dissolve for 5 minutes and then vortex again.
3. Suspend fusion protein in 0.05 M sodium borate buffer, pH 8.5 (or 0.1 M sodium phosphate, 0.15 M NaCl, pH 7.2-7.5) to be in the range of 1-10 mg/mL.
4. Transfer the appropriate amount of reagent (based on calculations) to the reaction tube containing the protein. Mix well and incubate at room temperature for 1 hour.

Calculate the amount (mg) of DyLight NHS Ester Dye to be added to the labeling reaction:

$$\frac{\text{total amount of protein } (mg)}{MW \text{ of protein}} \times 10 \text{ molar excess} \times MW \text{ of DyLight } 680$$

= ___ mg of DyLight 680

Ex: .5 mg/ 330000 g/mol * 10 * 950 g/mol * 100 µL/mg = 1.4 µL

[Dylight 680 has a molecular weight of 950 g/mol]

Calculate the microliters of NHS-ester dye solution to add to the reaction:

$$\_\_\_ mg\ of\ DyLight\ 680 \text{ (from previous calculation)} \times \frac{100\ \mu L}{1\ mg} =$$

= ___ µL of DyLight 680 NHS-ester solution at 10 mg/mL

5. Remove non-reacted reagent from the protein by dialysis against 2 L of 20 mM sodium phosphate dibasic pH 7.4, using a 12-14k MWCO dialysis membrane for 4 hr at 4°C. (5.678 g for 2 L DI H_2O).

   Note: Wrap the beakers being used for dialysis to protect the DyLight 680 from the light.
6. Transfer the dialysis cassette to new dialysis buffer and allow 4 hr dialysis at 4°C.
7. Transfer the dialysis cassette to new dialysis buffer and allow overnight dialysis at 4°C.
8. Remove labeled protein sample from dialysis cassette. Store at 4°C protected from light or lyophilize to powder and store at -80°C.

In Vitro Studies

Binding Stability Assay

1. [Day -1] Seed 5 x 10^4 cells in wells on 4 plates and grow until 70-80% confluent (using growth medium). Create 3 blanks (just media).
2. [Day 0] Add 300 µL FP suitable medium with 100 nM biotinylated FP to three wells on each plate.
3. Incubate for 2 hours at 37°C.
4. Wash 3 times with 250 µL FP suitable medium (standard growth medium with supplemental 2 mM Ca^{2+}).
5. Add 1 mL FP suitable medium.
6. [Day 0, 1, 2, 3] Take one plate (6 wells), remove medium and replace with 300 µL FP suitable medium.
7. Perform Alamar Blue assay
    a. Add 10% (30 uL) Alamar Blue.
    b. Incubate for 4 hours at 37°C.
    c. Transfer 250 µL to opaque 96 well plate.
    d. Measure fluorescence (530 nm excitation, 590 nm emmision).
8. Wash 3 times with 250 µL FP suitable medium.
9. Fix cells.
    a. Add 150 µL FP suitable medium with 0.25% glutaradlehyde to each well.
    b. Incubate for 5 min at room temperature.
    c. Remove medium.

d. Add 150 µL FP suitable medium with 50 mM ammonium chloride.

e. Incubate for 5 min at room temperature.

f. Remove medium.

10. Wash 3 times with 250 µL FP suitable medium.
11. Add 300 µL Streptavidin/HRP (2 µg/mL – stored in glass fridge).
12. Incubate for 1 hour at room temperature.
13. Wash 3 times with 250 µL FP suitable medium.
14. Add 300 µL of the chromogenic substrate O-phenylenediamine (OPD) to each well. (OPD is in -20^{o}C freezer in aluminum foil coated tube). The OPD solution is made with phosphate citrate buffer (1 capsule in 100 mL DI water). Prior to use, add 40 µL of 30% H_2O_2. Weigh out the desired amount of OPD with a concentration of 0.4 mg/ml.

    - OPD Solution – keep out of light and use immediately
        - Add one capsule of phosphate-citrate buffer to 100 mL DI in beaker and stir (no more than 30 min prior to use of OPD)
        - Weigh 0.4 mg/mL OPD and place in foil coated tube (6.4 mg for 16 mL buffer)
        - Add 40 µL of 30% H_2O_2 (glass fridge) to buffer
        - Mix for 30 seconds
        - Add required amount of buffer to OPD (16 mL) (use within 5 min)
        - Mix by inversion

15. Incubate for 30 minutes at room temperature and in the dark to minimize OPD color change.

16. Transfer 100 µL of the supernatant to 96-well plates and measure absorbance at 450 nm.

Binding Strength Assay

1. Seed 5 x 10^4 cells in 48 wells on 2 plates (per protein) and grow until 70% confluent (using growth medium).
2. Fix the cells in all wells by adding 200 µL/well PBS buffer containing 0.25% glutaraldehyde for 5 min. Remove before proceeding.
3. Quench excess aldehyde groups by incubating with 200 µL/well of 50 mM NH_4Cl, diluted in PBS buffer for 5 min at room temperature. Remove after incubation period.
4. Dilute biotinylated FP conjugate in 0.5% BSA diluted in PBS buffer. Add 300 µL to wells in Sets 1 and 2, using triplicates of each concentration. The blank for each set will receive no FP.
    - Set 2 (21 wells) gets PBS + BSA + 2 mM Ca^{+2} + FP (varying concentrations)
    - Blank (3 wells) gets PBS + BSA + 2 mM Ca^{+2}
    - Set 1 (21 wells) gets PBS + BSA + 5 mM EDTA + FP (varying concentrations)
    - Blank (3 wells) gets PBS + BSA + 5 mM EDTA
5. Incubate for 2 hours at 37^{o}C, 5% CO_2.
6. Wash 3 times with 250 µL of 0.5% BSA diluted in PBS buffer.
    - Set 2 (21 wells) gets PBS + BSA + 2 mM Ca^{+2}

- Blank (3 wells) gets PBS + BSA + 2 mM Ca^{+2}
- Set 1 (21 wells) gets PBS + BSA + 5 mM EDTA
- Blank (3 wells) gets PBS + BSA + 5 mM EDTA

7. Add 300 µL of Streptavidin-HRP (2 µg/mL) and incubate for 1 hour at room temperature. (Streptavidin-HRP is in 4^{o}C glass fridge)
8. Wash 4 times with 250 µL of PBS buffer.
    - Set 1 (21 wells) gets PBS + 5 mM EDTA
    - Blank (3 wells) gets PBS + 5 mM EDTA
    - Set 2 (21 wells) gets PBS + 2 mM Ca^{+2}
    - Blank (3 wells) gets PBS + 2 mM Ca^{+2}
9. Add 300 µL of the chromogenic substrate O-phenylenediamine (OPD) to each well. (OPD is in -20^{o}C freezer). The OPD solution is made with phosphate citrate buffer (1 capsule in 100 ml DI water). Prior to use, add 40 µL of 30% H_2O_2. Weigh out the desired amount of OPD with a concentration of 0.4 mg/ml.
    - Add one capsule of phosphate-citrate buffer to 100 mL DI in beaker and stir (no more than 30 min prior to use of OPD)
    - Weigh .4 mg/mL OPD and place in foil coated tube (6.4 mg for 16 mL buffer)
    - Add 40 µL of 30% H_2O_2 (glass fridge) to buffer
    - Mix for 30 seconds
    - Add required amount of buffer to OPD (16 mL) (use within 5 min)
    - Mix by inversion

10. Incubate for 30 minutes at room temperature and in the dark to minimize OPD color change.
11. Transfer 100 µL of the supernatant to 96-well plates.
12. Measure absorbance at 450 nm.

Fixed Cell Confocal Microscopy

1. Plate cells on chambered slide or coverslip in petri dish.
2. Fix cells
    a. Fix the cells in all wells by adding 200 µL/well PBS buffer containing 0.25% glutaraldehyde and 2mM Ca^{2+} for 5 min. Remove before proceeding.
    b. Quench excess aldehyde groups by incubating with 200 µL/well of 50 mM NH_4Cl, diluted in PBS buffer for 5 min at room temperature. Remove after incubation period.
3. Incubate the cells with 100 nM biotinylated FP/SWNT with calcium supplementation and 0.5% BSA.
4. Rinse cells with PBS + Ca
5. Add Streptavidin-Alexa 488 at 4 µg/mL (stored at 20 µg/mL) for 1 h
6. Stain the cells with CellMask plasma membrane stain (stored at 10 µg/mL) at 2 µg/mL. Submerge in stain solution for 5 min at 37°C, rinse and repeat 3 times
7. Stain cells with Hoechst 33258 for 30 min at 10 µg/mL.
8. Wash cells with medium and allow to air dry.
9. Attach coverslip to slide with fluorogel.
10. Image with confocal Leica SP8 microscope.

Live Cell Confocal Microscopy

1. Grow cells to 70% confluence in 35 mm petri dish under standard growth conditions.
2. Add growth medium with 2 mM Ca^{2+} for fusion protein binding and 1 µM DAPI (membrane impermeable) to distinguish live and dead cells.
3. Maintain 37°C using a Peltier stage and image prior to adding fusion protein.
4. Add fusion protein conjugated to Dylight 680 to petri dish and continue imaging for 2 h.
5. Wash cells 6 times with the calcium and DAPI supplemented growth medium.
6. Continue live imaging for 2 h post-wash.

Cytotoxicity Assay

1. [Day -1] Seed cells on 24-well plates and grow them until they reach 70-80% confluence using growth medium.

   Note: Methioninase systems require the separation of experimental groups on different plates to avoid effects of gaseous methylselenol.
2. Incubate for 24 hours.
3. [Day 0, 1, 2, 3] Replace growth medium with 300 µL of FP suitable medium (standard growth medium with supplemental 2 mM Ca^{2+}). Perform an Alamar Blue assay to determine cell viability.
   a. Add 10% (30 µL) of Alamar Blue.
   b. Incubate for 4 hours at 37°C.
   c. Transfer 250 µL to an opaque 96-well plate
   d. Read fluorescence: excitation – 530 nm; emission – 590 nm.
   e. NO CELLS well is blank, 0 µM on 2 plates without FP is 100% viability
4. [Day 0] Wash 3 times using 300 µL of FP suitable medium.
5. [Day 0] Add 300 µL of FP suitable media containing 100 nM fusion protein to 21 wells.
6. [Day 0] Incubate for 2 hours at 37°C.
7. [Day 0, 1, 2, 3] Wash 3 times using 300 µL of FP suitable medium.
8. [Day 0, 1, 2, 3] Remove medium from wells. Add 300 µL /well of FP suitable medium containing varying concentrations of the prodrug.

In Vivo Studies and Follow-up Analysis

Protein Specific Antibody Titers

Sample collection

1. Collect samples at week 0, 1, 2, 3.
2. Collect 3 drops of blood (about 150 µL) from mice (submandibular bleed) and isolate plasma using capiject collection tubes.
3. Store plasma at -80°C.

Bioassay (Sandwich ELISA)

1. Add 100 µL 20 ug/ml FP in 0.1 M carbonate coating buffer and incubate overnight at 4°C with plate cover.
    - Carbonate coating buffer
        - 0.08 g Na_2CO_3
        - 0.15 g $NaHCO_3$
        - 25 mL DI
        - pH to 9.6
2. Wash plate 2 times with 200 µL PBS.
3. Block for 2 h at room temperature with 200 µL blocking buffer.
    - Blocking buffer
        - PBS
        - 10% FBS
        - pH to 7.4
4. Wash plate 2 times with 200 µL PBS.

5. Add 100 µL of plasma samples (10x, 100x, etc. dilutions in PBS) and incubate overnight at 4°C.
6. Wash plate 4 times with 200 µL PBS.
7. Add 100 µL diluted goat anti-mouse IgG IgM conjugated to HRP and incubate for 1 h at room temperature.
    - HRP conjugated Rabbit anti-mouse IgG IgM (Jackson Immuno 315-035-044)
        - Reconstitute lyophilized Ab with 1.5 mL DI and centrifuge if not clear
        - Dilute 1:25,000 for assay (2 µL in 50 mL PBS)
8. Wash three times.
9. Add 100 µL OPD, H_2O_2 solution and incubate for 30 min at room temperature in the dark.
        - Add one capsule of phosphate-citrate buffer to 100 mL DI in beaker and stir (no more than 30 min prior to use of OPD)
        - Weigh 0.4 mg/mL OPD and place in foil coated tube (6.4 mg for 16 mL buffer)
        - Add 40 µL of 30% H_2O_2 (glass fridge) to buffer
        - Mix for 30 seconds
        - Add required amount of buffer to OPD (16 mL) (use within 5 min)
        - Mix by inversion
10. Transfer 100 µL of the supernatant to 96-well plates.
11. Measure absorbance at 450 nm.

Fusion Protein Plasma Clearance

Sample Collection

1. Biotinylate fusion protein.
2. Inject 10 mg/kg IP into mice (t = 0 h controls do not receive injection).
3. Perform cardiac draws at appropriate time (t = 0 h to 24 h). Use 3 mL 21 gauge needle for draw and collect in clot activating capiject blood collection vial.
4. Allow 20 minutes for clots to form before centrifugation.
5. Centrifuge at 3500 x *g* for 90 s.
6. Remove serum with pipet and freeze (cryovial) at -80°C.

Bioassay (ELISA)

1. Prepare biotinylated fusion protein samples for calibration curve (typically between 0 µg/mL and 10 µg/mL) and assay solutions.
    - Diluting Buffer (1 L)
        - 0.5 g Tween 20 (0.005%)
        - 2.5 g BSA (0.25%)
        - 1 L PBS
    - Wash Buffer
        - 5 g Tween 20 (0.05%)
        - 1 L PBS
2. Add 50 µL of each serum sample to wells. Use streptavidin-coated 96 well plates.
3. Cover the plate with adhesive cover and incubate for 60 min at 37^{o}C.

4. Shake out the plates into a sink. Wash the plates with wash buffer 4 times by adding 200 µL and shaking out the wash buffer into a sink. Pat plates dry by inverting on paper towel.
5. Add 50 µL of Annexin V polyclonal antibody (rabbit) diluted to 1.25 µg/mL in diluting buffer to each well.
6. Cover the plate with adhesive cover and incubate for 60 min at 37^{o}C.
7. Shake out the plates into a sink. Wash the plates with wash buffer 4 times by adding 200 µL and shaking out the wash buffer into a sink. Pat plates dry by inverting on paper towel.
8. Add 50 µL of anti-rabbit IgG-HRP conjugate (secondary antibody) diluted to 1:1,000 (initially at about 1 mg/mL) using diluting buffer to each well.
9. Cover the plate with adhesive cover and incubate for 60 min at 37^{o}C.
10. Shake out the plates into a sink. Wash the plates with wash buffer 4 times by adding 200 µL and shaking out the Wash buffer into a sink. Pat plates dry by inverting on paper towel.
11. Add 50 µL of OPD solution to each well.
    - Add one capsule of phosphate-citrate buffer to 100 mL DI in beaker and stir (no more than 30 min prior to use of OPD)
    - Weigh 0.4 mg/mL OPD and place in foil coated tube (6.4 mg for 16 mL buffer)
    - Add 40 µL of 30% H_2O_2 (glass fridge) to buffer
    - Mix for 30 seconds
    - Add required amount of buffer to OPD (16 mL) (use within 5 min)

- Mix by inversion

12. Cover the plate with adhesive cover and incubate for 30 minutes at room temperature in the dark.
13. Read absorbance at 450 nm.

Fluorescent Lung Metastasis Image Processing and Quantification

An automated image processing macro was developed in ImageJ (National Institutes of Health) to clean up fluorescence images of whole lungs removed from BALB/cJ mice. The macro code is included below. Image cleanup first occurs through the subtraction of a Gaussian blur of the fluorescence image from the fluorescence image to highlight the high frequency information, particularly to separate fluorescence signal from background noise. A median filter is then applied to remove speckling from the image. User input is requested to select the region of interest, specifically to avoid analysis of lung boundary regions which are also high frequency information. User input is also requested to finalize the automated thresholding to ensure appropriate processing. The "Analyze Particles" function in ImageJ (FIJI build) is then utilized to identify and quantify nodules based on size and circularity.

```
//begin of ImageJ lung nodule processing macro
//JJ Krais – July 21, 2014

input = "enter input file path here (use'\\' in place of '\')";
output = "enter output file path here (use'\\' in place of
'\')";
var current_image="";

//Go through image directory, apply 'action' to directory
one at a time.
list = getFileList(input);
for (i = 0; i < list.length; i++) {
```

```
  current_image="";
  print("processing image #" + i+1 + " of " + list.length);
   image_cleanup(input, output, list[i]);
  print("image cleanup complete");
   user_inputs(output);
  print("beginning nodule analysis");
  analyze_nodules();
}

print("Processing complete");

function image_cleanup(input, output, filename)   {

    //Open file and apply Gaussian Blur
    open(input + filename);
    print("blurring...");
    run("Gaussian Blur...", "sigma=40");
    output_file = "blur " + filename;
    saveAs("Tiff", output + output_file);
    close();

     //Re-open images, this is necessary for image calculator
     to work.
    open(input + filename);
    open(output + output_file);
    wait(100);

    //Subtract blurred image from original
    print("subtracting blur...");
    imageCalculator("Subtract create", filename,output_file);
    selectWindow("Result of " + filename);
    current_image = filename + "-background subtracted";

    //Save and close all images
    saveAs("Tiff", output + current_image);
    close();
    selectWindow(filename);
    close();
    wait(100);
    selectWindow(output_file);
    close();

    //reopen and apply median filter
   print("removing speckling...");
   open(output + current_image + ".tif");
   run("Median...", "radius=20");
```

```
   selectWindow(current_image +".tif");
   current_image=current_image + "-despeckled";
   saveAs("Tiff", output + current_image);
   wait(100);
   close();
    }

function user_inputs(output) {
  open(output + current_image + ".tif");

//user selects region of interest and it is cleared
   print("waiting on user selection...");
   setTool("freehand");
   run("Invert");
  beep();
   waitForUser("Select region of interest. \nClick OK when
complete.");
   run("Clear Outside");

   //thresholding
   print("waiting on user thresholding...");
   run("Threshold...");
   waitForUser("Adjust threshold value. \nClick OK when
complete.");
   run("Convert to Mask");

   //save
   current_image=current_image + "-thresh";
   saveAs("Tiff", output + current_image);
   wait(100);
   close();
}

function analyze_nodules()  {
  open(output + current_image + ".tif");

 //analyze particles
   run("Analyze Particles...", "size=50-Infinity
circularity=0.20-1.00 Nothing display clear summarize add
in_situ");
   roiManager("Show All with labels");
   roiManager("Show All");
   saveAs("Results", output +
current_image+"_datafile.xls");
   close();
}
```

Immunohistochemistry Image Processing and Quantification

An automated image processing macro was developed in ImageJ to quantify DAB staining on immunohistochemistry stained tumor sections counter stained with hematoxylin. The macro code is included below. The background is first subtracted with the ImageJ background subtraction function, and then the hematoxylin and DAB stains are separated using a color deconvolution. Masks of the DAB and hematoxylin images are generated using a user applied threshold. DAB positive and hematoxylin positive cells are quantified using the "Analyze Particles" function of ImageJ (FIJI build).

```
//begin of ImageJ DAB quantification macro
//JJ Krais – July 21, 2014

input = "enter input file path here (use'\\' in place of '\')";
output = "enter output file path here (use'\\' in place of '\')";
var current_image="";

//Go through image directory, apply 'action' to directory one at a time.
list = getFileList(input);
for (i = 0; i < list.length; i++) {
  current_image="";
  print("processing image #" + i+1 + " of " + list.length);
  subtract_background(input, output, list[i]);
  print("background subtracted");

  separate_stains(output);
  print("stains separated");

  print("beginning DAB thresholding...");
  stain_file=output + current_image + " DAB.tif";
  generate_masks(stain_file);
  print("beginning H thresholding...");
  stain_file=output + current_image + " H.tif";
  generate_masks(stain_file);

  window_name=current_image+" DAB.tif mask";
  mask_file=output+window_name;
  print("quantifying DAB positive cells...");
```

```
  quantify_cells(mask_file, window_name);
  window_name=current_image+" H.tif mask";
  mask_file=output+window_name;
  print("quantifying H positive cells...");
  quantify_cells(mask_file, window_name);

  selectWindow("Summary");
  saveAs("Text", output + "summary.xls");

  outline_file=current_image + " DAB.tif mask outlines";
  create_overlay(outline_file);
   print("file #" + i+1 + " processing is complete");
}

print("Processing complete, saving data...");
print("Data saved.");

function subtract_background(input, output, filename)   {
    //Open file
    open(input + filename);

    //Subtract background
    run("Subtract Background...", "rolling=50 light separate");

    //Save and close all images
    current_image=filename +"-bg";
    saveAs("Tiff", output + current_image);
    close();
  }

function separate_stains(output){
   open(output + current_image + ".tif");
   run("Colour Deconvolution", "vectors=[H DAB]");
   selectWindow(current_image + ".tif-(Colour_3)");
   run("Close");

   selectWindow(current_image + ".tif-(Colour_2)");
   saveAs("Tiff", output + current_image + " DAB");
   close();

   selectWindow(current_image + ".tif-(Colour_1)");
   saveAs("Tiff", output + current_image + " H");
   close();

   selectWindow(current_image + ".tif");
   close();
```

```
  selectWindow("Colour Deconvolution");
  close();
}

function generate_masks(stain){
  open(stain);

  //convert to grayscale
  run("8-bit");

   //thresholding
   print("waiting on user thresholding...");
   run("Threshold...");
   waitForUser("Adjust threshold value. \nClick OK when complete.");
   run("Convert to Mask");

  saveAs("Tiff", stain + " mask");
  close();
}

function quantify_cells(mask_file, window_name){
  open(mask_file +".tif");

  run("Watershed");

  run("Analyze Particles...", "size=75-Infinity circularity=0.30-1.00
  show=[Bare Outlines] display clear summarize");

  selectWindow("Drawing of " + window_name +".tif");
  saveAs("Tiff", mask_file + " outlines");
  close();

  selectWindow(window_name + ".tif");
  close();
}

function create_overlay(outline_file){
  open(output+current_image+".tif");
  open(output+outline_file+".tif");

  selectWindow(current_image+".tif");

  arg2="image=["+outline_file+".tif] x=0 y=0 opacity=50";
  run("Add Image...",arg2);
  run("Brightness/Contrast...");
```

```
    run("Enhance Contrast", "saturated=0.35");

    saveAs("TIff", output+current_image+" DAB selection overlay.tif");
    close();

    selectWindow(outline_file + ".tif");
    close();
}
```

Quantification of Regulatory T Cells in Spleen

1. Mechanically separate spleen in petri dish using a syringe (3 mL) plunger.
2. Add 7 mL FACS buffer (PBS, 10% FBS, 0.1% NaN_3 Sodium Azide; make ahead of time – alternatively use FACS buffer in kit).
3. Pass cells through cell strainer (70 µm) and rinse strainer with 3 mL FACS buffer.
4. Centrifuge 5 min at 1100 x *g* at 4°C and discard supernatant.
5. Wash cells with 1 mL flow cytometry staining buffer, count cells, centrifuge.
6. Resuspend cells in 1 mL flow cytometry staining buffer to get ~10 million cells/mL (Should be about 1mL).
7. Add 0.5 µg anti-mouse CD16/CD32 to 50 µL sample in flow cytometry staining buffer for blocking and incubate for 20 min at 4°C
8. Make anti-CD4 and anti-CD25 mix solution using 0.125 µg CD4 and 0.06 µg per sample in 50 µL per sample and add 50 µL antibodies to 50 µL cells
9. Vortex gently to mix and incubate at 4°C for 30 min.
10. Wash cells twice in flow cytometry staining buffer. Add 1 mL staining buffer, centrifuge 1100 x *g* for 5 min, discard supernatant, and repeat.

11. Discard supernatant and gently pulse vortex the pellet to cause dissociation of the pellet.
12. Add 1 mL Foxp3 fixation/permeabilization working solution to each tube and pulse vortex.
    - Dilute Foxp3 fixation/permeabilization concentrate with Foxp3 fixation/permeabilization diluent in 1:3 ratio to get working solution
13. Incubate 1 h at 4°C in dark.
14. Add (do not wash) 1 mL 1x permeabilization buffer.
    - Dilute 10x concentrate with DI
15. Centrifuge at 1100 x *g* for 5 min.
16. Resuspend pellet in 100 µL 1x permeabilization buffer (usually the remaining volume).
17. Add (do not wash) 0.5 µg (2.5 µL) anti-Foxp3 (or isotype control PE) to each sample and incubate in dark for 30 min at room temperature.
18. Add 1 mL 1x permeabilization buffer to each tube.
19. Centrifuge at 1100xg for 5 min and discard supernatant.
20. Add 1 mL 1x permeabilization buffer to each tube.
21. Centrifuge at 1100 x *g* for 5 min and discard supernatant.
22. Add 1 mL flow cytometry staining buffer.
23. Centrifuge at 1100 x *g* for 5 min and discard supernatant.
24. Resuspend cells in flow cytometry staining buffer (add 350 µL to residual volume for total volume of 400-500 µL) and acquire data on flow cytometer.

Appendix C: Fusion Gene Construction

PNP-AV Primers

PNP and AV Amplification Primers

PNP gene sense primer:
5'-GAC GAC GAC AAG ATG CCC **GCT ACC CCA CAC ATT AAT GCA G**-3'

PNP gene antisense primer:
5'-CGC G|GA TCC AGA ACC GGA GCC **CTC TTT ATC GCC CAG CAG AAC**-3'

Annexin V sense primer:
5'-CGC G|GA TCC **GCA CAG GTT CTC AGA GGC**-3'

Annexin V antisense primer:
5'-GA GGA GAA GCC CGG **TTA GTC ATC TTC TCC ACA GAG C**-3'

Legend: **Gene complementary region**, BamHI restriction site (cut indicated |), linker segment

PNP-AV Fusion Primers

Fusion gene sense primer:
5'-CGC T|CT AGA ATG **GCT ACC CCA CAC ATT AAT GCA G**-3'

Fusion gene antisense primer:
5'-CGC C|TCGAG *CGG ACC CTG GAA CAG AAC TTC CAG* **GTC ATC TTC TCC ACA GAG CAG C**-3'

Legend: **Gene complementary region**, Xba1 (sense) restriction site (cut indicated |) or Xho1 (antisense) restriction site (cut indicated |), *HRV-3C protease cleavage site*

PNP-AV Sequences

PNP-AV DNA Sequence

ATGGCTACCCCACACATTAATGCAGAAATGGGCGATTTCGCTGACGTAGTTTTGATGC
CAGGCGACCCGCTGCGTGCGAAGTATATTGCTGAAACTTTCCTTGAAGATGCCCGTGA
AGTGAACAACGTTCGCGGTATGCTGGGCTTCACCGGTACTTACAAAGGCCGCAAAATT
TCCGTAATGGGTCACGGTATGGGTATCCCGTCCTGCTCCATCTACACCAAAGAACTGA
TCACCGATTTCGGCGTGAAGAAAATTATCCGCGTGGGTTCCTGTGGCGCAGTTCTGCC
GCACGTAAAACTGCGCGACGTCGTTATCGGTATGGGTGCCTGCACCGATTCCAAAGTT
AACCGCATCCGTTTTAAAGACCATGACTTTGCCGCTATCGCTGACTTCGACATGGTGCG
TAACGCAGTAGATGCAGCTAAAGCACTGGGTATTGATGCTCGCGTGGGTAACCTGTTC
TCCGCTGACCTGTTCTACTCTCCGGACGGCGAAATGTTCGACGTGATGGAAAAATACG
GCATTCTCGGCGTGGAAATGGAAGCGGCTGGTATCTACGGCGTCGCTGCAGAATTTGG
CGCGAAAGCCCTGACCATCTGCACCGTATCTGACCACATCCGCACTCACGAGCAGACC
ACTGCCGCTGAGCGTCAGACTACCTTCAACGACATGATCAAAATCGCACTGGAATCCG
TTCTGCTGGGCGATAAAGAGGGCTCCGGTTCTGGATCC*GCACAGGTTCTCAGAGGCACTGTG*
ACTGACTTCCCTGGATTTGATGAGCGGGCTGATGCAGAAACTCTTCGGAAGGCTATGAAAGGCTTG
GGCACAGATGAGGAGAGCATCCTGACTCTGTTGACATCCCGAAGTAATGCTCAGCGCCAGGAAAT
CTCTGCAGCTTTTAAGACTCTGTTTGGCAGGGATCTTCTGGATGACCTGAAATCAGAACTAACTGGA
AAATTTGAAAAATTAATTGTGGCTCTGATGAAACCCTCTCGGCTTTATGATGCTTATGAACTGAAACA
TGCCTTGAAGGGAGCTGGAACAAATGAAAAAGTACTGACAGAAATTATTGCTTCAAGGACACCTGA
AGAACTGAGAGCCATCAAACAAGTTTATGAAGAAGAATATGGCTCAAGCCTGGAAGATGACGTGGT
GGGGGACACTTCAGGGTACTACCAGCGGATGTTGGTGGTTCTCCTTCAGGCTAACAGAGACCCTG
ATGCTGGAATCGATGAAGCTCAAGTTGAACAAGATGCTCAGGCTTTATTTCAGGCTGGAGAACTTAA
ATGGGGGACAGATGAAGAAAAGTTTATCACCATCTTTGGAACACGAAGTGTGTCTCATTTGAGAAA
GGTGTTTGACAAGTACATGACTATATCAGGATTTCAAATTGAGGAAACCATTGACCGCGAGACTTCT
GGCAATTTAGAGCAACTACTCCTTGCTGTTGTGAAATCTATTCGAAGTATACCTGCCTACCTTGCAG
AGACCCTCTATTATGCTATGAAGGGAGCTGGGACAGATGATCATACCCTCATCAGAGTCATGGTTT
CCAGGAGTGAGATTGATCTGTTTAACATCAGGAAGGAGTTTAGGAAGAATTTTGCCACCTCTCTTTA
TTCCATGATTAAGGGAGATACATCTGGGGACTATAAGAAAGCTCTTCTGCTGCTCTGTGGAGAAGA
*TGAC*CTGGAAGTTCTGTTCCAGGGTCCGCTCGAGCACCACCACCACCACCACTGA

Legend: **PNP**, linker, *AV*, HRV-3C protease site, 6X His-tag

PNP-AV Amino Acid Sequence (Pre-Cleavage)

MATPHINAEMGDFADVVLMPGDPLRAKYIAETFLEDAREVNNVRGMLGFT
GTYKGRKISVMGHGMGIPSCSIYTKELITDFGVKKIIRVGSCGAVLPHVKL
RDVVIGMGACTDSKVNRIRFKDHDFAAIADFDMVRNAVDAAKALGIDARV
GNLFSADLFYSPDGEMFDVMEKYGILGVEMEAAGIYGVAAEFGAKALTIC
TVSDHIRTHEQTTAAERQTTFNDMIKIALESVLLGDKEGSGSGS*AQVLRGTVT*
DFPGFDERADAETLRKAMKGLGTDEESILTLLTSRSNAQRQEISAAFKTLFGRDLLD
DLKSELTGKFEKLIVALMKPSRLYDAYELKHALKGAGTNEKVLTEIIASRTPEELRAIK
QVYEEEYGSSLEDDVVGDTSGYYQRMLVVLLQANRDPDAGIDEAQVEQDAQALFQA
GELKWGTDEEKFITIFGTRSVSHLRKVFDKYMTISGFQIEETIDRETSGNLEQLLLAV
VKSIRSIPAYLAETLYYAMKGAGTDDHTLIRVMVSRSEIDLFNIRKEFRKNFATSLYSMI
*KGDTSGDYKKALLLLCGEDD*LEVLFQGPLEHHHHHH

Legend: **PNP**, linker, *AV*, HRV-3C protease site, 6X His-tag

PNP-AV Amino Acid Sequence (Post-Cleavage)

MATPHINAEMGDFADVVLMPGDPLRAKYIAETFLEDAREVNNVRGMLGFT
GTYKGRKISVMGHGMGIPSCSIYTKELITDFGVKKIIRVGSCGAVLPHVKL
RDVVIGMGACTDSKVNRIRFKDHDFAAIADFDMVRNAVDAAKALGIDARV
GNLFSADLFYSPDGEMFDVMEKYGILGVEMEAAGIYGVAAEFGAKALTIC
TVSDHIRTHEQTTAAERQTTFNDMIKIALESVLLGDKEGSGSGS*AQVLRGTVT*
DFPGFDERADAETLRKAMKGLGTDEESILTLLTSRSNAQRQEISAAFKTLFGRDLLD
DLKSELTGKFEKLIVALMKPSRLYDAYELKHALKGAGTNEKVLTEIIASRTPEELRAIK
QVYEEEYGSSLEDDVVGDTSGYYQRMLVVLLQANRDPDAGIDEAQVEQDAQALFQA
GELKWGTDEEKFITIFGTRSVSHLRKVFDKYMTISGFQIEETIDRETSGNLEQLLLAV
VKSIRSIPAYLAETLYYAMKGAGTDDHTLIRVMVSRSEIDLFNIRKEFRKNFATSLYSMI
*KGDTSGDYKKALLLLCGEDD*LEVLFQ

Legend: **PNP**, linker, *AV*

PNP-AV NCBI BLAST Results

Table 22. NCBI BLAST Result Summary for PNP-AV

Protein	Species	Ident	Accession
Annexin A5	*Homo sapiens*	100%	NP 001145.1
Purine nucleoside phosphorylase	*Escherichia coli*	100%	WP 001322562.1

Mutant CGL Sequences

Engineered Mouse and Human CGL Sequence Comparison

Table 23. mCGL and hCGL NCBI BLAST Results and Sequences with Highlighted Site of Mutation

Protein	Species	Ident	Accession
Cystathionine γ-lyase	*Mus musculus*	99%	NP 666065.1
	Homo sapiens		AAB24700.1

Identities	Positives	Gaps
340/397 (86%)	364/397 (91%)	0/397 (0%)

Query (mCGL; wild type)
Subjct (hCGL; wild type)

Query 2
QKDASLSGFLPSFQHFATQAIHVGQEPEQWNSRAVVLPISLATTFKQDFPGQSSGFEYSR 61
EKDASSQGFLPHFQHFATQAIHVGQDPEQWTSRAVVPPISLSTTFKQGAPGQHSGFEYSR 62
Sbjct 3

Query 62
SGNPTRNCLEKAVAALDGAKHSLAFASGLAATITITHLLKAGDEIICMDEVYGGTNRYFR 121
SGNPTRNCLEKAVAALDGAKYCLAFASGLAATVTITHLLKAGDQIICMDDVYGGTNRYFR 122
Sbjct 63

Query 122
RVASEFGLKISFVDCSKTKLLEAAITPQTKLVWIETPTNPTLKLADIGACAQIVHKRGDI 181
QVASEFGLKISFVDCSKIKLLEAAITPETKLVWIETPTNPTQKVIDIEGCAHIVHKHGDI 182
Sbjct 123

Query 182
ILVVDNTFMSAYFQRPLALGADICMCSATKYMNGHSDVVMGLVSVNSDDLNSRLRFLQNS 241
ILVVDNTFMSPYFQRPLALGADISMYSATKYMNGHSDVVMGLVSVNCESLHNRLRFLQNS 242
Sbjct 183

Query 242
LGAVPSPFDCYLCCRGLKTLQVRMEKHFKNGMAVARFLETNPRVEKVVYPGLPSHPQHEL 301
LGAVPSPIDCYLCNRGLKTLHVRMEKHFKNGMAVAQFLESNPWVEKVIYPGLPSHPQHEL 302
Sbjct 243

Query 302
AKRQCSGCPGMVSFYIKGALQHAKAFLKNLKLFTLAESLGGYESLAELPAIMTHASVPEK 361
VKRQCTGCTGMVTFYIKGTLQHAEIFLKNLKLFTLAESLGGFESLAELPAIMTHASVLKN 362
Sbjct 303

Query 362
DRATLGINDTLIRLSVGLEDEQDLLEDLDRALKAAHP 398
DRDVLGISDTLIRLSVGLEDEEDLLEDLDQALKAAHP 399
Sbjct 363

Table 24. Mutant mCGL NCBI BLAST Results and Sequence with Highlighted Mutations

Protein	Species	Ident	Accession
Cystathionine γ-lyase	*Mus musculus*	99%	NP 666065.1
	Identities	**Positives**	**Gaps**
	395/398 (99%)	395/398 (99%)	0/398 (0%)

Query (mutant)
Subjct (wild type)

```
Query  1
MQKDASLSGFLPSFQHFATQAIHVGQEPEQWNSRAVVLPISLATTFKQDFPGQSSGFNYS  60
MQKDASLSGFLPSFQHFATQAIHVGQEPEQWNSRAVVLPISLATTFKQDFPGQSSGFEYS  60
Sbjct  1

Query  61
RSGNPTRNCLEKAVAALDGAKHSLAFASGLAATITITHLLKAGDEIICMDEVYGGTNLYF  120
RSGNPTRNCLEKAVAALDGAKHSLAFASGLAATITITHLLKAGDEIICMDEVYGGTNRYF  120
Sbjct  61

Query  121
RRVASEFGLKISFVDCSKTKLLEAAITPQTKLVWIETPTNPTLKLADIGACAQIVHKRGD  180
RRVASEFGLKISFVDCSKTKLLEAAITPQTKLVWIETPTNPTLKLADIGACAQIVHKRGD  180
Sbjct  121

Query  181
IILVVDNTFMSAYFQRPLALGADICMCSATKYMNGHSDVVMGLVSVNSDDLNSRLRFLQN  240
IILVVDNTFMSAYFQRPLALGADICMCSATKYMNGHSDVVMGLVSVNSDDLNSRLRFLQN  240
Sbjct  181

Query  241
SLGAVPSPFDCYLCCRGLKTLQVRMEKHFKNGMAVARFLETNPRVEKVVYPGLPSHPQHE  300
SLGAVPSPFDCYLCCRGLKTLQVRMEKHFKNGMAVARFLETNPRVEKVVYPGLPSHPQHE  300
Sbjct  241

Query  301
LAKRQCSGCPGMVSFYIKGALQHAKAFLKNLKLFTLAVSLGGYESLAELPAIMTHASVPE  360
LAKRQCSGCPGMVSFYIKGALQHAKAFLKNLKLFTLAESLGGYESLAELPAIMTHASVPE  360
Sbjct  301

Query  361
KDRATLGINDTLIRLSVGLEDEQDLLEDLDRALKAAHP  398
KDRATLGINDTLIRLSVGLEDEQDLLEDLDRALKAAHP  398
Sbjct  361
```

mCGL Fusions Gibson Fragments

The mCGL fusion proteins, mCGL-AI and mCGL-AV, were each constructed via Gibson Assembly using three fragments each and assembled directly into the vector (pET-30 Ek/LIC). The first fragment consists exclusively of the vector overlap and mCGL and therefore was able to be used for both fusions. Underlined regions indicate overlapping sections of fragment, either with the adjacent fragment or vector sequence. Fragment overlaps were designed at 40 bp according to manufacturer recommendations for the extended incubation protocol for Gibson Assembly of 3+ fragments.

mCGL-AI Gibson Fragments

mCGL-AI Fragment 1:

CATGGACAGCCCAGATCTGGGTACCGATGACGACGACAAGATGCTGGAAGTTCTGTTCCAG
GGTCCGATGCAGAAAGACGCGAGCCTGTCTGGCTTCCTGCCGTCTTTTCAGCACTTCGCAAC
TCAGGCGATCCACGTTGGTCAGGAGCCTGAACAATGGAACTCTCGTGCGGTTGTTCTGCCGA
TCAGCCTCGCCACGACCTTCAAACAGGATTTCCCGGGTCAGTCTTCTGGTTTCAACTACTCCC
GTTCTGGCAATCCGACCCGTAACTGCCTGGAAAAAGCGGTAGCCGCGCTGGACGGTGCGAA
ACACTCTCTGGCGTTCGCCTCTGGTCTCGCGGCGACCATCACGATCACCCATCTGCTCAAGG
CCGGTGACGAAATCATCTGTATGGACGAAGTTTACGGTGGCACCAACCTGTATTTTCGTCGT
GTTGCGTCTGAATTCGGTCTGAAAATCTCTTTCGTTGACTGCTCTAAAACCAAACTCCTGGAG
GCAGCAATTACTCCGCAGACGAAACTCGTTTGGATCGAAACCCCGACCAACCCGACCCTGA
AGCTCGCCGACATCGGTGCGTGCGCTCAAATCGTTCACAAACGTGGTGACATCATCCTGGTT
GTTGATAATACCTTCATGTCTGCGTACTTTCAGCGTCCGCTGGCGCTGGGCGCTGACATCTGC
ATGTGCTCCGCGACCAAATACATGAACGGTCACTCTGACGTAGTTATGGGTCTGGTTAGCGT
TAACAGCGACGATCTCAATTCCCGCCTGCGTTTCCTGCAGAACTCCCTCGGCGCAGTACCGT
CCCCGTTCGACTGCTATCTCTGCTGCCGTGGTCTCAAAACGCTGCAGGTTCGTATGGAAAAG
CATTTCAAGAACGGTATGGCGGTGGCGCGCTTCCTCGAAACGAACCCGCGTGTTGAAAAAG
TTGTTTACCCTGGCCTCCCGTCCCACCCGCAGCACGAACTGGCGAAACGTCAGTGCTCTGGT
TGCCCTGGC

mCGL-AI Fragment 2:

GCACGAACTGGCGAAACGTCAGTGCTCTGGTTGCCCTGGCATGGTTTCCTTCTACATCAAAG
GTGCCCTCCAGCACGCGAAAGCCTTCCTGAAAAACCTGAAACTGTTCACCCTCGCGGTTTCT
CTGGGTGGTTACGAATCTCTCGCTGAACTGCCGGCGATCATGACCCACGCTTCTGTACCTGA
AAAAGACCGTGCGACCCTCGGTATCAACGATACCCTGATCCGTCTGTCTGTTGGTCTGGAGG
ACGAACAGGACCTGCTGGAAGACCTGGATCGTGCTCTCAAAGCGGCGCACCCGAGCGGTGG
TGGTGGTAGTGGTGGCGGTGGTATGGCAATGGTTAGCGAATTTCTGAAACAGGCACGTTTTC
TGGAAAACCAAGAACAAGAATATGTTCAGGCCGTGAAAAGCTATAAAGGTGGTCCGGGTAG
CGCAGTTAGCCCGTATCCGAGCTTTAATGTTAGCAGTGATGTTGCAGCACTGCATAAAGCCA
TTATGGTTAAAGGTGTTGATGAAGCCACCATCATTGATATTCTGACCAAACGTACCAATGCA
CAGCGTCAGCAGATTAAAGCAGCATATCTGCAAGAAAATGGTAAACCGCTGGATGAAGTTC
TGCGTAAAGCACTGACAGGTCATCTGGAAGAGGTTGTTCTGGCAATGCTGAAAACACCGGC
ACAGTTTGATGCAGATGAACTGCGTGGTGCAATGAAAGGTCTGGGCACCGATGAAGATACA
CTGATTGAAATCCTGACCACCCGTAGCAATGAGCAGATTCGTGAAATTAATCGTGTGTATCG
CGAAGAACTGAAACGTGATCTGGCAAAAGATATCACCAGCGATACCAGCGGTGATTTTCGT
AAAGCCCTGCTGGCACTGGCCAAAGGTGATCGTTGTCAGGATCTGAGCGTTAACCAGGATCT
GGCAGATACCGATGCACGTGCCCTGTATGAAGCCGGTGAGCGTCGTAAAGGTACTGATGTG
AACGTTTTCACTACG

mCGL-AI Fragment 3:

TGAGCGTCGTAAAGGTACTGATGTGAACGTTTTCACTACGATTCTGACCTCCCGTTCTTTCCC
GCATCTCCGTCGTGTGTTCCAGAACTATGGTAAGTACTCTCAGCACGACATGAACAAAGCGC
TGGACCTGGAACTCAAAGGTGACATTGAAAAGTGCCTCACCACCATCGTTAAATGCGCGAC
CTCTACCCCTGCTTTCTTCGCGGAAAAACTGTATGAGGCCATGAAGGGTGCGGGCACTCGTC
ACAAGGCTCTGATCCGTATTATGGTTTCCCGTAGCGAGATTGATATGAACGAAATTAAGGTT
TTCTACCAGAAAAAGTACGGTATCAGCCTGTGCCAGGCGATCCTGGACGAAACCAAAGGCG
ACTACGAAAAGATTCTGGTTGCGCTGTGCGGTGGTAACTGACCGGGCTTCTCCTCAACCATG
GCGATATCGGATCCGAATT

mCGL-AV Gibson Fragments

mCGL-AV Fragment 1:

CATGGACAGCCCAGATCTGGGTACCGATGACGACGACAAGATGCTGGAAGTTCTGTTCCAG
GGTCCGATGCAGAAAGACGCGAGCCTGTCTGGCTTCCTGCCGTCTTTTCAGCACTTCGCAAC
TCAGGCGATCCACGTTGGTCAGGAGCCTGAACAATGGAACTCTCGTGCGGTTGTTCTGCCGA
TCAGCCTCGCCACGACCTTCAAACAGGATTTCCCGGGTCAGTCTTCTGGTTTCAACTACTCCC
GTTCTGGCAATCCGACCCGTAACTGCCTGGAAAAAGCGGTAGCCGCGCTGGACGGTGCGAA
ACACTCTCTGGCGTTCGCCTCTGGTCTCGCGGCGACCATCACGATCACCCATCTGCTCAAGG
CCGGTGACGAAATCATCTGTATGGACGAAGTTTACGGTGGCACCAACCTGTATTTTCGTCGT
GTTGCGTCTGAATTCGGTCTGAAAATCTCTTTCGTTGACTGCTCTAAAACCAAACTCCTGGAG
GCAGCAATTACTCCGCAGACGAAACTCGTTTGGATCGAAACCCCGACCAACCCGACCCTGA
AGCTCGCCGACATCGGTGCGTGCGCTCAAATCGTTCACAAACGTGGTGACATCATCCTGGTT
GTTGATAATACCTTCATGTCTGCGTACTTTCAGCGTCCGCTGGCGCTGGGCGCTGACATCTGC
ATGTGCTCCGCGACCAAATACATGAACGGTCACTCTGACGTAGTTATGGGTCTGGTTAGCGT
TAACAGCGACGATCTCAATTCCCGCCTGCGTTTCCTGCAGAACTCCCTCGGCGCAGTACCGT
CCCCGTTCGACTGCTATCTCTGCTGCCGTGGTCTCAAAACGCTGCAGGTTCGTATGGAAAAG
CATTTCAAGAACGGTATGGCGGTGGCGCGCTTCCTCGAAACGAACCCGCGTGTTGAAAAAG
TTGTTTACCCTGGCCTCCCGTCCCACCCGCAGCACGAACTGGCGAAACGTCAGTGCTCTGGT
TGCCCTGGC

mCGL-AV Fragment 2:

GCACGAACTGGCGAAACGTCAGTGCTCTGGTTGCCCTGGCATGGTTTCCTTCTACATCAAAG
GTGCCCTCCAGCACGCGAAAGCCTTCCTGAAAAACCTGAAACTGTTCACCCTCGCGGTTTCT
CTGGGTGGTTACGAATCTCTCGCTGAACTGCCGGCGATCATGACCCACGCTTCTGTACCTGA
AAAAGACCGTGCGACCCTCGGTATCAACGATACCCTGATCCGTCTGTCTGTTGGTCTGGAGG
ACGAACAGGACCTGCTGGAAGACCTGGATCGTGCTCTCAAAGCGGCGCACCCGAGCGGTGG
TGGTGGTAGTGGTGGCGGTGGTATGGCGACCCGTGGTACCGTTACTGATTTCCCGGGTTTCG
ACGGTCGTGCGGACGCGGAAGTTCTGCGTAAAGCGATGAAAGGCCTGGGTACGGATGAAGA
TTCTATCCTGAACCTGCTGACGTCTCGTTCTAACGCGCAACGCCAGGAAATCGCGCAGGAGT
TCAAAACGCTGTTTGGCCGCGACCTGGTGGACGACCTCAAGTCCGAGCTGACCGGTAAATTC
GAAAAACTGATTGTTGCCATGATGAAGCCGTCCCGTCTGTATGACGCGTACGAGCTCAAGCA
TGCGCTGAAAGGTGCTGGCACCGACGAAAAGGTTCTGACCGAGATCATCGCCTCTCGTACCC
CGGAAGAACTGTCTGCGATTAAACAGGTTTACGAGGAAGAATACGGTTCTAATCTGGAGGA
CGACGTGGTCGGCGATACTTCTGGTTACTATCAGCGTATGCTCGTTGTCCTGCTCCAGGCCA
ATCGTGATCCGGACACTGCGATCGACGATGCGCAAGTTGAGCTGGACGCACAGGCGCTCTTC
CAGGCTGGTGAACTGAAATGGGGCACGGACGAGGAGAAGTTCATCACCATCTTCGGCACGC
GTTCTGTTAGCCACCTGCGTCGTGTTTTCGACAAATACATGACCATCTCTGGCTTTCAGATCG
AAGAAACCATT

mCGL-AV Fragment 3:

ATACATGACCATCTCTGGCTTTCAGATCGAAGAAACCATTGACCGTGAGACCTCTGGTAACC
TGGAACAGCTGCTGCTGGCGGTTGTTAAATCTATCCGTTCTATTCCGGCGTACCTGGCGGAA
ACCCTGTACTACGCCATGAAGGGTGCGGGCACTGACGATCACACCCTGATTCGTGTTGTTGT
TTCTCGCTCCGAGATTGATCTCTTCAATATCCGTAAGGAATTTCGTAAAAACTTTGCGACTTC
CCTCTACTCTATGATCAAAGGCGACACTAGCGGCGACTACAAAAAAGCGCTGCTCCTGCTGT
GCGGTGGTGAAGACGACTGACCGGGCTTCTCCTCAACCATGGCGATATCGGATCCGAATT

mCGL Fusions Sequencing Primers and Sequences

Sequencing primers are indicated with underlines on the fusion gene to indicate the sequencing approach. In addition to the underlined primers indicated below, the sequencing facility at Oklahoma Medical Research Foundation provided T7 promoter and T7 terminator primers. All primers are oriented in the forward direction for simplicity of analysis, with the exception of the T7 terminator primer. Primer spacing was optimized to 350-500 base pairs to ensure accuracy and maximize reuse of primers for mCGL-AI and mCGL-AV. Primers were designed using Gene Designer software (DNA 2.0; Menlo Park, CA) and analyzed with OligoAnalyzer 3.1 (Integrated DNA Technologies) to the following specifications: melting temperature of 55-50°C, length of 18-24 base pairs, no hairpins with a melting temperature >50°C, no self-dimers with $\Delta G < -6$ kcal/mol, and no single base strings >4 base pairs.

mCGL-AI Sequencing Primers and DNA Sequence

ATGCACCATCATCATCATCATTCTTCTGGTCTGGTGCCACGCGGTTCTGGTATGAAAGAAAC
CGCTGCTGCTAAATTCGAACGCCAGCACATGGACAGCCCAGATCTGGGTACCGATGACGAC
GACAAGATGCTGGAAGTTCTGTTCCAGGGTCCGATGCAGAAAGACGCGAGCCTGTCTGGCTT
CCTGCCGTCTTTTCAGCACTTCGCAACTCAGGCGATCCACGTTGGTCAGGAGCCTGAACAAT
GGAACTCTCGTGCGGTTGTTCTGCCGATCAGCCTCGCCACGACCTTCAAACAGGATTTCCCG
GGTCAGTCTTCTGGTTTCAACTACTCCCGTTCTGGCAATCCGACCCGTAACTGCCTGGAAAA
AGCGGTAGCCGCGCTGGACGGTGCGAAACACTCTCTGGCGTTCGCCTCTGGTCTCGCGGCGA
CCATCACGATCACCCATCTGCTCAAGGCCGGTGACGAAATCATCTGTATGGACGAAGTTTAC
GGTGGCACCAACCTGTATTTTCGTCGTGTTGCGTCTGAATTCGGTCTGAAAATCTCTTTCGTT
GACTGCTCTAAAACCAAACTCCTGGAGGCAGCAATTACTCCGCAGACGAAACTCGTTTGGAT
CGAAACCCCGACCAACCCGACCCTGAAGCTCGCCGACATCGGTGCGTGCGCTCAAATCGTTC
ACAAACGTGGTGACATCATCCTGGTTGTTGATAATACCTTCATGTCTGCGTACTTTCAGCGTC
CGCTGGCGCTGGGCGCTGACATCTGCATGTGCTCCGCGACCAAATACATGAACGGTCACTCT
GACGTAGTTATGGGTCTGGTTAGCGTTAACAGCGACGATCTCAATTCCCGCCTGCGTTTCCT
GCAGAACTCCCTCGGCGCAGTACCGTCCCCGTTCGACTGCTATCTCTGCTGCCGTGGTCTCA
AAACGCTGCAGGTTCGTATGGAAAAGCATTTCAAGAACGGTATGGCGGTGGCGCGCTTCCTC
GAAACGAACCCGCGTGTTGAAAAAGTTGTTTACCCTGGCCTCCCGTCCCACCCGCAGCACGA
ACTGGCGAAACGTCAGTGCTCTGGTTGCCCTGGCATGGTTTCCTTCTACATCAAAGGTGCCC
TCCAGCACGCGAAAGCCTTCCTGAAAAACCTGAAACTGTTCACCCTCGCGGTTTCTCTGGGT
GGTTACGAATCTCTCGCTGAACTGCCGGCGATCATGACCCACGCTTCTGTACCTGAAAAAGA
CCGTGCGACCCTCGGTATCAACGATACCCTGATCCGTCTGTCTGTTGGTCTGGAGGACGAAC
AGGACCTGCTGGAAGACCTGGATCGTGCTCTCAAAGCGGCGCACCCGAGCGGTGGTGGTGG
TAGTGGTGGCGGTGGTATGGCAATGGTTAGCGAATTTCTGAAACAGGCACGTTTTCTGGAAA
ACCAAGAACAAGAATATGTTCAGGCCGTGAAAAGCTATAAAGGTGGTCCGGGTAGCGCAGT
TAGCCCGTATCCGAGCTTTAATGTTAGCAGTGATGTTGCAGCACTGCATAAAGCCATTATGG
TTAAAGGTGTTGATGAAGCCACCATCATTGATATTCTGACCAAACGTACCAATGCACAGCGT
CAGCAGATTAAAGCAGCATATCTGCAAGAAAATGGTAAACCGCTGGATGAAGTTCTGCGTA
AAGCACTGACAGGTCATCTGGAAGAGGTTGTTCTGGCAATGCTGAAAACACCGGCACAGTT
TGATGCAGATGAACTGCGTGGTGCAATGAAAGGTCTGGGCACCGATGAAGATACACTGATT
GAAATCCTGACCACCCGTAGCAATGAGCAGATTCGTGAAATTAATCGTGTGTATCGCGAAG
AACTGAAACGTGATCTGGCAAAAGATATCACCAGCGATACCAGCGGTGATTTTCGTAAAGC
CCTGCTGGCACTGGCCAAAGGTGATCGTTGTCAGGATCTGAGCGTTAACCAGGATCTGGCAG
ATACCGATGCACGTGCCCTGTATGAAGCCGGTGAGCGTCGTAAAGGTACTGATGTGAACGTT
TTCACTACGATTCTGACCTCCCGTTCTTTCCCGCATCTCCGTCGTGTGTTCCAGAACTATGGT
AAGTACTCTCAGCACGACATGAACAAAGCGCTGGACCTGGAACTCAAAGGTGACATTGAAA
AGTGCCTCACCACCATCGTTAAATGCGCGACCTCTACCCCTGCTTTCTTCGCGGAAAAACTG
TATGAGGCCATGAAGGGTGCGGGCACTCGTCACAAGGCTCTGATCCGTATTATGGTTTCCCG
TAGCGAGATTGATATGAACGAAATTAAGGTTTTCTACCAGAAAAAGTACGGTATCAGCCTGT
GCCAGGCGATCCTGGACGAAACCAAAGGCGACTACGAAAAGATTCTGGTTGCGCTGTGCGG
TGGTAACTGA

mCGL-AV Sequencing Primers and DNA Sequence

ATGCACCATCATCATCATCATTCTTCTGGTCTGGTGCCACGCGGTTCTGGTATGAAAGAAAC
CGCTGCTGCTAAATTCGAACGCCAGCACATGGACAGCCCAGATCTGGGTACCGATGACGAC
GACAAGATGCTGGAAGTTCTGTTCCAGGGTCCGATGCAGAAAGACGCGAGCCTGTCTGGCTT
CCTGCCGTCTTTTCAGCACTTCGCAACTCAGGCGATCCACGTTGGTCAGGAGCCTGAACAAT
GGAACTCTCGTGCGGTTGTTCTGCCGATCAGCCTCGCCACGACCTTCAAACAGGATTTCCCG
GGTCAGTCTTCTGGTTTCAACTACTCCCGTTCTGGCAATCCGACCCGTAACTGCCTGGAAAA
AGCGGTAGCCGCGCTGGACGGTGCGAAACACTCTCTGGCGTTCGCCTCTGGTCTCGCGGCGA
CCATCACGATCACCCATCTGCTCAAGGCCGGTGACGAAATCATCTGTATGGACGAAGTTTAC
GGTGGCACCAACCTGTATTTTCGTCGTGTTGCGTCTGAATTCGGTCTGAAAATCTCTTTCGTT
GACTGCTCTAAAACCAAACTCCTGGAGGCAGCAATTACTCCGCAGACGAAACTCGTTTGGAT
CGAAACCCCGACCAACCCGACCCTGAAGCTCGCCGACATCGGTGCGTGCGCTCAAATCGTTC
ACAAACGTGGTGACATCATCCTGGTTGTTGATAATACCTTCATGTCTGCGTACTTTCAGCGTC
CGCTGGCGCTGGGCGCTGACATCTGCATGTGCTCCGCGACCAAATACATGAACGGTCACTCT
GACGTAGTTATGGGTCTGGTTAGCGTTAACAGCGACGATCTCAATTCCCGCCTGCGTTTCCT
GCAGAACTCCCTCGGCGCAGTACCGTCCCCGTTCGACTGCTATCTCTGCTGCCGTGGTCTCA
AAACGCTGCAGGTTCGTATGGAAAAGCATTTCAAGAACGGTATGGCGGTGGCGCGCTTCCTC
GAAACGAACCCGCGTGTTGAAAAAGTTGTTTACCCTGGCCTCCCGTCCCACCCGCAGCACGA
ACTGGCGAAACGTCAGTGCTCTGGTTGCCCTGGCATGGTTTCCTTCTACATCAAAGGTGCCC
TCCAGCACGCGAAAGCCTTCCTGAAAAACCTGAAACTGTTCACCCTCGCGGTTTCTCTGGGT
GGTTACGAATCTCTCGCTGAACTGCCGGCGATCATGACCCACGCTTCTGTACCTGAAAAAGA
CCGTGCGACCCTCGGTATCAACGATACCCTGATCCGTCTGTCTGTTGGTCTGGAGGACGAAC
AGGACCTGCTGGAAGACCTGGATCGTGCTCTCAAAGCGGCGCACCCGAGCGGTGGTGGTGG
TAGTGGTGGCGGTGGTATGGCGACCCGTGGTACCGTTACTGATTTCCCGGGTTTCGACGGTC
GTGCGGACGCGGAAGTTCTGCGTAAAGCGATGAAAGGCCTGGGTACGGATGAAGATTCTAT
CCTGAACCTGCTGACGTCTCGTTCTAACGCGCAACGCCAGGAAATCGCGCAGGAGTTCAAA
ACGCTGTTTGGCCGCGACCTGGTGGACGACCTCAAGTCCGAGCTGACCGGTAAATTCGAAA
AACTGATTGTTGCCATGATGAAGCCGTCCCGTCTGTATGACGCGTACGAGCTCAAGCATGCG
CTGAAAGGTGCTGGCACCGACGAAAAGGTTCTGACCGAGATCATCGCCTCTCGTACCCCGG
AAGAACTGTCTGCGATTAAACAGGTTTACGAGGAAGAATACGGTTCTAATCTGGAGGACGA
CGTGGTCGGCGATACTTCTGGTTACTATCAGCGTATGCTCGTTGTCCTGCTCCAGGCCAATCG
TGATCCGGACACTGCGATCGACGATGCGCAAGTTGAGCTGGACGCACAGGCGCTCTTCCAG
GCTGGTGAACTGAAATGGGGCACGGACGAGGAGAAGTTCATCACCATCTTCGGCACGCGTT
CTGTTAGCCACCTGCGTCGTGTTTTCGACAAATACATGACCATCTCTGGCTTTCAGATCGAAG
AAACCATTGACCGTGAGACCTCTGGTAACCTGGAACAGCTGCTGCTGGCGGTTGTTAAATCT
ATCCGTTCTATTCCGGCGTACCTGGCGGAAACCCTGTACTACGCCATGAAGGGTGCGGGCAC
TGACGATCACACCCTGATTCGTGTTGTTGTTTCTCGCTCCGAGATTGATCTCTTCAATATCCG
TAAGGAATTTCGTAAAAACTTTGCGACTTCCCTCTACTCTATGATCAAAGGCGACACTAGCG
GCGACTACAAAAAAGCGCTGCTCCTGCTGTGCGGTGGTGAAGACGACTGA

mCGL-AV Amino Acid Sequence (Pre-cleavage)

MHHHHHHSSGLVPRGSGMKETAAAKFERQHMDSPDLGTDDDDKMLEVLFQ|G
P**MQKDASLSGFLPSFQHFATQAIHVGQEPEQWNSRAVVLPISLATTFKQDF**
PGQSSGFNYSRSGNPTRNCLEKAVAALDGAKHSLAFASGLAATITITHLLK
AGDEIICMDEVYGGTNLYFRRVASEFGLKISFVDCSKTKLLEAAITPQTKLV
WIETPTNPTLKLADIGACAQIVHKRGDIILVVDNTFMSAYFQRPLALGADIC
MCSATKYMNGHSDVVMGLVSVNSDDLNSRLRFLQNSLGAVPSPFDCYLCC
RGLKTLQVRMEKHFKNGMAVARFLETNPRVEKVVYPGLPSHPQHELAKR
QCSGCPGMVSFYIKGALQHAKAFLKNLKLFTLAVSLGGYESLAELPAIMT
HASVPEKDRATLGINDTLIRLSVGLEDEQDLLEDLDRALKAAHPSGGGGSG
GGG*MATRGTVTDFPGFDGRADAEVLRKAMKGLGTDEDSILNLLTSRSNAQRQEIAQ*
EFKTLFGRDLVDDLKSELTGKFEKLIVAMMKPSRLYDAYELKHALKGAGTDEKVLT
EIIASRTPEELSAIKQVYEEEYGSNLEDDVVGDTSGYYQRMLVVLLQANRDPDTAIDD
AQVELDAQALFQAGELKWGTDEEKFITIFGTRSVSHLRRVFDKYMTISGFQIEETIDR
ETSGNLEQLLLAVVKSIRSIPAYLAETLYYAMKGAGTDDHTLIRVVVSRSEIDLFNIRKE
FRKNFATSLYSMIKGDTSGDYKKALLLLCGGEDD

Legend: 6X His-tag, HRV-3C protease site, **mCGL**, linker, *AV*

mCGL-AI Amino Acid Sequence (Pre-cleavage)

MHHHHHHSSGLVPRGSGMKETAAAKFERQHMDSPDLGTDDDDKMLEVLFQ|G
P**MQKDASLSGFLPSFQHFATQAIHVGQEPEQWNSRAVVLPISLATTFKQDF**
PGQSSGFNYSRSGNPTRNCLEKAVAALDGAKHSLAFASGLAATITITHLLK
AGDEIICMDEVYGGTNLYFRRVASEFGLKISFVDCSKTKLLEAAITPQTKLV
WIETPTNPTLKLADIGACAQIVHKRGDIILVVDNTFMSAYFQRPLALGADIC
MCSATKYMNGHSDVVMGLVSVNSDDLNSRLRFLQNSLGAVPSPFDCYLCC
RGLKTLQVRMEKHFKNGMAVARFLETNPRVEKVVYPGLPSHPQHELAKR
QCSGCPGMVSFYIKGALQHAKAFLKNLKLFTLAVSLGGYESLAELPAIMT
HASVPEKDRATLGINDTLIRLSVGLEDEQDLLEDLDRALKAAHPSGGGGSG
GGG*MAMVSEFLKQARFLENQEQEYVQAVKSYKGGPGSAVSPYPSFNVSSDVAALHK*
AIMVKGVDEATIIDILTKRTNAQRQQIKAAYLQENGKPLDEVLRKALTGHLEEVVLA
MLKTPAQFDADELRGAMKGLGTDEDTLIEILTTRSNEQIREINRVYREELKRDLAKDI
TSDTSGDFRKALLALAKGDRCQDLSVNQDLADTDARALYEAGERRKGTDVNVFTTIL
TSRSFPHLRRVFQNYGKYSQHDMNKALDLELKGDIEKCLTTIVKCATSTPAFFAEKL
YEAMKGAGTRHKALIRIMVSRSEIDMNEIKVFYQKKYGISLCQAILDETKGDYEKILV
ALCGGN

Legend: 6X His-tag, HRV-3C protease site, **mCGL**, linker, *AI*

mCGL-AV Amino Acid Sequence (Post-cleavage)

GP**MQKDASLSGFLPSFQHFATQAIHVGQEPEQWNSRAVVLPISLATTFKQD
FPGQSSGFNYSRSGNPTRNCLEKAVAALDGAKHSLAFASGLAATITITHLLK
AGDEIICMDEVYGGTNLYFRRVASEFGLKISFVDCSKTKLLEAAITPQTKLV
WIETPTNPTLKLADIGACAQIVHKRGDIILVVDNTFMSAYFQRPLALGADIC
MCSATKYMNGHSDVVMGLVSVNSDDLNSRLRFLQNSLGAVPSPFDCYLCC
RGLKTLQVRMEKHFKNGMAVARFLETNPRVEKVVYPGLPSHPQHELAKR
QCSGCPGMVSFYIKGALQHAKAFLKNLKLFTLAVSLGGYESLAELPAIMT
HASVPEKDRATLGINDTLIRLSVGLEDEQDLLEDLDRALKAAHP**SGGGGSG
GGG*MATRGTVTDFPGFDGRADAEVLRKAMKGLGTDEDSILNLLTSRSNAQRQEIAQ
EFKTLFGRDLVDDLKSELTGKFEKLIVAMMKPSRLYDAYELKHALKGAGTDEKVLT
EIIASRTPEELSAIKQVYEEEYGSNLEDDVVGDTSGYYQRMLVVLLQANRDPDTAIDD
AQVELDAQALFQAGELKWGTDEEKFITIFGTRSVSHLRRVFDKYMTISGFQIEETIDR
ETSGNLEQLLLAVVKSIRSIPAYLAETLYYAMKGAGTDDHTLIRVVVSRSEIDLFNIRKE
FRKNFATSLYSMIKGDTSGDYKKALLLLCGGEDD*

Legend: **mCGL**, linker, *AV*

mCGL-AI Amino Acid Sequence (Post-cleavage)

GP**MQKDASLSGFLPSFQHFATQAIHVGQEPEQWNSRAVVLPISLATTFKQD
FPGQSSGFNYSRSGNPTRNCLEKAVAALDGAKHSLAFASGLAATITITHLLK
AGDEIICMDEVYGGTNLYFRRVASEFGLKISFVDCSKTKLLEAAITPQTKLV
WIETPTNPTLKLADIGACAQIVHKRGDIILVVDNTFMSAYFQRPLALGADIC
MCSATKYMNGHSDVVMGLVSVNSDDLNSRLRFLQNSLGAVPSPFDCYLCC
RGLKTLQVRMEKHFKNGMAVARFLETNPRVEKVVYPGLPSHPQHELAKR
QCSGCPGMVSFYIKGALQHAKAFLKNLKLFTLAVSLGGYESLAELPAIMT
HASVPEKDRATLGINDTLIRLSVGLEDEQDLLEDLDRALKAAHP**SGGGGSG
GGG*MAMVSEFLKQARFLENQEQEYVQAVKSYKGGPGSAVSPYPSFNVSSDVAALHK
AIMVKGVDEATIIDILTKRTNAQRQQIKAAYLQENGKPLDEVLRKALTGHLEEVVLA
MLKTPAQFDADELRGAMKGLGTDEDTLIEILTTRSNEQIREINRVYREELKRDLAKDI
TSDTSGDFRKALLALAKGDRCQDLSVNQDLADTDARALYEAGERRKGTDVNVFTTIL
TSRSFPHLRRVFQNYGKYSQHDMNKALDLELKGDIEKCLTTIVKCATSTPAFFAEKL
YEAMKGAGTRHKALIRIMVSRSEIDMNEIKVFYQKKYGISLCQAILDETKGDYEKILV
ALCGGN*

Legend: **mCGL**, linker, *AI*

mCGL-AV NCBI BLAST Results

For details regarding 99% identity, see the mutations outlined in Table 24, also in Appendix C: Fusion Gene Construction.

Table 25. NCBI BLAST Result Summary for mCGL-AV

Protein	Species	Ident	Accession
Cystathionine-γ-lyase	*Mus musculus*	99%	NP 666065.1
Annexin A5	*Mus musculus*	100%	NP 033803.1

mCGL-AI NCBI BLAST Results

For details regarding 99% identity, see the mutations outlined in Table 24, also in Appendix C: Fusion Gene Construction.

Table 26. NCBI BLAST Result Summary for mCGL-AI

Protein	Species	Ident	Accession
Cystathionine-γ-lyase	*Mus musculus*	99%	NP 666065.1
Annexin A1	*Mus musculus*	100%	NP 034860.2